Dipl.-Ing. Anton Tamtögl

Surface Dynamics and Structure of Bi(111) from Helium Atom Scattering

DOCTORAL THESIS

For obtaining the academic degree of

Doktor der technischen Wissenschaften

Doctoral Programme of Technical Sciences
Technical Physics

Graz University of Technology

Supervisor:
Univ.-Prof. Mag. Dr.rer.nat Wolfgang Ernst
Institute of Experimental Physics

Graz, May 2012

Acknowledgement

This PhD thesis was performed under the supervision of Prof. W. E. Ernst. The current form of this work would not have been possible without the help, support and patience of him.
It was a pleasure to work with Michael Mayrhofer-Reinhartshuber and Patrick Kraus on the same project. Besides their support they have turned into personal friends over the time and they used to build me up when things went completely wrong in the laboratory.
Moreover, I would like to thank all members of the Institute of Experimental Physics for the pleasant and cooperative working atmosphere. Without the great skills of the people in the mechanical and the electrical workshop this work would not have been possible. In addition, I would also like to thank the ladies from the secretary.
Prof. G. Benedek deserves my gratitude for teaching us the theory about helium atom scattering and especially for hosting P. Kraus at the Universita di Milano-Bicocca. Among the various useful discussions, D. Campi of his group in Milano performed several calculations in order to clarify a couple of questions.
I would like to thank Prof. J. R. Manson for his stimulating lectures in 2009 that motivated this work and for his assistance with the scattering intensity calculations and questions about the geometry of the apparatus.
I also gratefully acknowledge the transfer of Prof. K. H. Rieder's helium atom scattering machine from the FU Berlin to the University of Technology in Graz and for several discussions about the concerning physics behind the experiments.
Thanks to Prof. W. Allison from the University of Cambridge on agreeing to serve as second referee and examiner
Finally, I need to thank my family and as the most important person in my life, Lisa. Without their support this work would not have been possible.

Abstract

The surface structure and surface dynamics of Bi(111) have been studied using elastic and inelastic scattering of helium atoms. Elastic helium atom scattering experiments on Bi(111) exhibit diffraction peaks up to third order whose position is in excellent agreement with previous structure determinations.
The surface corrugation was modeled using the eikonal approximation as well as the GR-method. The surface charge density corrugation obtained from the best fit results gives rise to a corrugation height of approximately 10% of the surface lattice constant. This rather large corrugation height is not expected for a surface with metallic behavior and may be a consequence of the surface electron pocket states at the Fermi level of Bi(111).
The vibrational dynamics of Bi(111) were investigated by measurements of the Debye-Waller attenuation of the elastic diffraction peaks and a surface Debye temperature of (84 ± 8) K was determined. A decrease of the surface Debye temperature at higher sample temperatures that was recently observed on Bi nanofilms could not be confirmed in the case of the single crystal measurements.
It was shown that Bi(111) supports bound states of the helium atom on the surface from which information on the corresponding atom-surface potential could be extracted. Using the angular position of bound state resonance effects the bound state energies were determined and a 9-3 atom-surface interaction potential was fitted. The well depth $D = (8.32 \pm 0.73)$ meV of the potential is consistent with previously determined values for noble metals.
Using inelastic helium atom scattering measurements the surface phonon dispersion of Bi(111) could be determined for the first time whereupon measurements at a surface temperatures of 123 K and at room temperature were carried out. In both high-symmetry directions the phonon dispersion exhibits a Rayleigh mode, a strong longitudinal resonance and a nearly dispersionless branch at approximately 4 meV.
The Rayleigh mode shows an indication for a Kohn anomaly along $\overline{\Gamma \mathrm{K}}$ which could be related to a non-adiabatic effect. The longitudinal resonance, which is a common feature on metal surfaces, exhibits the largest amplitude in the second layer as shown by comparison of the phonon dispersion with calculations from density functional perturbation theory.
The calculations also confirm the flat phonon branch at approximately 4 meV

which seems to originate from an atomic displacement in the third layer. The observation of this subsurface mode in helium scattering is only possible due to the electron phonon-coupling. Thereby oscillations of the electron charge density above the first layer are caused by the movement of the atoms in subsurface layers.

Kurzfassung

Im Rahmen dieser Arbeit wurde die Struktur und die Dynamik der Bi(111) Oberfläche mithilfe von elastischer und inelastischer Streuung von Heliumatomen untersucht. Die elastische Streuung von Heliumatomen zeigt Beugungspeaks bis zur dritten Ordnung, deren Position genau mit vorhergehenden Strukturbestimmungen übereinstimmt.
Die Oberflächenkorrugation wurde unter Verwendung der eikonalen Approximation sowie der GR-Methode modelliert. Die hierbei erhaltene Korrugation der Oberflächenladungsdichte besitzt eine Amplitude von 10 % der Gitterkonstante an der Oberfläche. Eine dermaßen große Amplitude ist für eine Oberfläche mit metallischem Charakter in keiner Weise zu erwarten und könnte im Vorhandensein von Elektronenpockets am Fermi-Niveau der Obefläche begründet liegen.
Des weiteren wurde die Temperaturabhängigkeit der elastisch gestreuten Peaks bestimmt, um über den Debye-Waller Faktor Rückschlüsse auf die Gitterschwingungen der Bi(111) Oberfläche zu ziehen. Dabei wurde die Oberflächen-Debye-Temperatur mit (84 ± 8) K bestimmt. Eine Abnahme der Oberfläche Debye-Temperatur bei höheren Temperaturen, welche kürzlich auf Bi Nanoschichten beobachtet wurde, konnte für die Messungen am Einkristall nicht bestätigt werden.
Außerdem konnte gezeigt werden, dass gebundene Zustände des Heliumatoms auf der Bi(111) Oberfläche existieren, welche Informationen über das Wechselwirkungspotential zwischen Heliumatom und Oberfläche enthalten. Anhand der Winkelpositionen, an denen Resonanzeeffekte der gebundenen Zustände sichtbar sind, konnten die Energien der gebundene Zustände ermittelt werden und ein 9-3 Atom-Oberflächen-Wechselwirkungspotential wurde gefittet. Die Tiefe der Potentialmulde beträgt $D = (8.32 \pm 0.73)$ meV, was in guter Übereinstimmung zu den Potentialtiefen für Edelmetalle ist.
Mithilfe der inelastischen Streuung von Heliumatomen konnte zum ersten Mal die Phononendispersionsrelation der Bi(111) Oberfläche ermittelt werden. Die Messungen hierzu wurden bei einer Oberflächentemperatur von 123 K und bei Raumtemperatur durchgeführt. Die Dispersionskurve zeigt einen Rayleighmode, einen longitudinalen Resonanzmode und einen nahezu dispersionslosen Mode bei etwa 4 meV.
Die Dispersion des Rayleighmode zeigt Indizien für eine Kohn-Anomalie entlang

$\overline{\Gamma K}$, welche in einem nicht-adiabtischen Effekt begründet liegen könnte. Der longitudinale Resonanzmode, welcher ein typisches Merkmal für Metalloberflächen ist, besitzt die größte Amplitude in der zweiten Atomlage, wie durch Vergleich der Phononendispersion mit Berechnungen anhand der störungstheoretischen Dichtefunktionaltheorie gezeigt werden kann.
Diese theoretischen Rechnungen bestätigen auch den flachen Phononenmode bei etwa 4 meV, welcher sogar in der dritten Atomlage lokalisiert ist. Die Beobachtung von solchen Moden in unteren Lagen ist nur aufgrund der Elektron-Phonon-Kopplung möglich welche eine Oszillation der Ladungsdichte über der ersten Atomlage verursacht.

Deutsche Fassung:
Beschluss der Curricula-Kommission für Bachelor-, Master- und Diplomstudien vom 10.11.2008
Genehmigung des Senates am 1.12.2008

EIDESSTATTLICHE ERKLÄRUNG

Ich erkläre an Eides statt, dass ich die vorliegende Arbeit selbstständig verfasst, andere als die angegebenen Quellen/Hilfsmittel nicht benutzt, und die den benutzten Quellen wörtlich und inhaltlich entnommene Stellen als solche kenntlich gemacht habe.

Graz, am ……. ……..
(Unterschrift)

Englische Fassung:

STATUTORY DECLARATION

I declare that I have authored this thesis independently, that I have not used other than the declared sources / resources, and that I have explicitly marked all material which has been quoted either literally or by content from the used sources.

……. ……..
date (signature)

Contents

List of Figures

List of Tables

1. Introduction

An important task of surface science is the investigation of interactions between atoms or molecules with a solid surface including effects of surface layers and structures. The findings in the experimental and theoretical framework of this field of science are not only interesting in terms of interface and nanostructure science; they are also of essential importance for applied fields such as nano-electronics, catalysis and nanostructured materials[1,2].
The experimental technique of helium atom scattering is used as an advantageous tool in surface science. Among other prominent methods for the investigation of surfaces, helium atom scattering can be viewed as the only genuinely non-destructive surface sensitive diffraction method[3]. Furthermore, the impinging helium atoms exhibit momenta comparable to those of lattice vibrations and can thus provide information on surface phonons[4].
In the course of this work a helium atom scattering apparatus was characterized using measurements on the well-known lithium fluoride surface. The apparatus was then used to investigate the structural properties and the vibrational dynamics of the bismuth (111) surface.
The properties of bismuth and in particular the Bi(111) surface will be addressed at the beginning of section 6. To emphasize the increasing interest in this material an article recently published by Parameswaran et al.[5] with the title: "Unfinished bismuth" shall be cited. The authors describe anisotropies in the conductivity of bismuth and conclude with the remark "[...] it seems likely that resolving the nature of the anisotropic phase will involve a careful re-examination of several tenets of solid state theory - and some fascinating new physics"[5].

1.1. Organization of this Thesis

A first introduction to the elementary concepts of helium atom scattering from surfaces is given in the following. Section 2 then deals with the theoretical concepts in describing the surface structure and vibrations. Furthermore, the generation of a supersonic expansion and the time-of-flight principle are briefly described.
Section 3 is devoted to the theoretical background for the helium atom scattering technique. The atom-surface scattering theory is introduced and the necessary

procedures in analyzing experimental measurements are described including possible complications and pitfalls. It provides the necessary background to become familiar with this kind of measurement tool which might be helpful with respect to future students planning to work on the described apparatus.
The apparatus used in this work is briefly described in section 4 together with the vacuum setup. Section 5 deals with a first characterization of the apparatus whereupon mainly scattering experiments from a lithium fluoride surface were used. Finally, in section 6 the experimental results for scattering of helium from a bismuth (111) single crystal are presented and the new insights into the physics of this material that the measurements may provide.

1.2. Introducing the Principle of Helium Atom Scattering

Figure 1.1 shows a typical experimental setup used in a **H**elium **A**tom **S**cattering (HAS) experiment. Pure helium gas is used to create an atomic beam in a supersonic expansion whereupon the gas expands from a high pressure region (typical pressure in the experiments: 50 bar) through a small nozzle into a region of vacuum. The expansion gives rise to an adiabatic cooling of the gas whereupon the internal energy of the gas is transformed into translational kinetic energy[6].

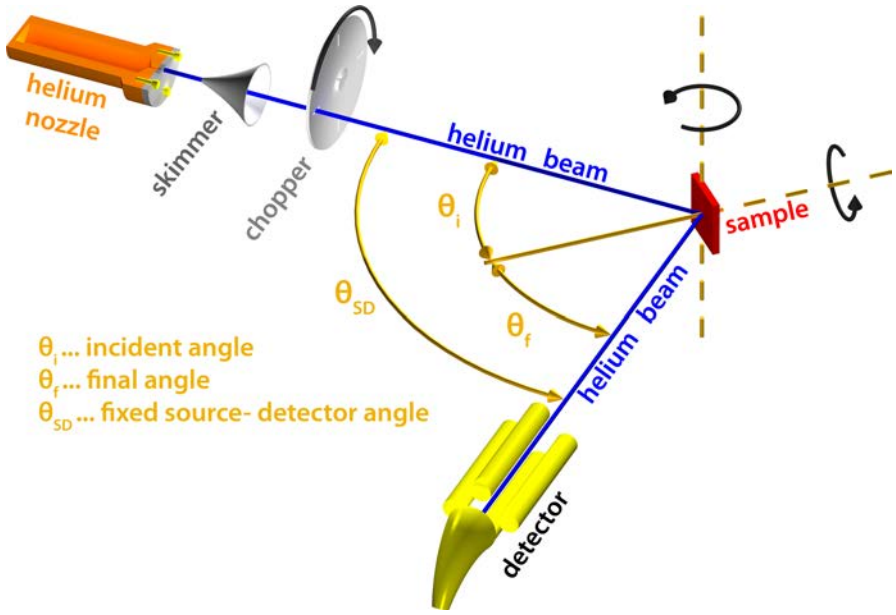

Figure 1.1.: Schematic drawing of a helium atom scattering machine

About 10 mm from the nozzle the outer part of the expanding gas cloud is separated from the forward moving atoms using a conical skimmer. Further down

the beam line a chopper can be located allowing time-of flight experiments by chopping the beam into short pulses.
The intense, nearly monoenergetic helium beam is then directed towards a target surface at a particular angle of incidence and the scattered intensity is monitored at a given angle using a mass spectrometer. Therefore the sample is mounted on a manipulator which allows to position and rotate the sample.

1.2.1. Elastic Scattering - Surface Structure

Elastic measurements i.e. measurements where the helium atoms are scattered elastically at the surface, are used to determine the surface structure.

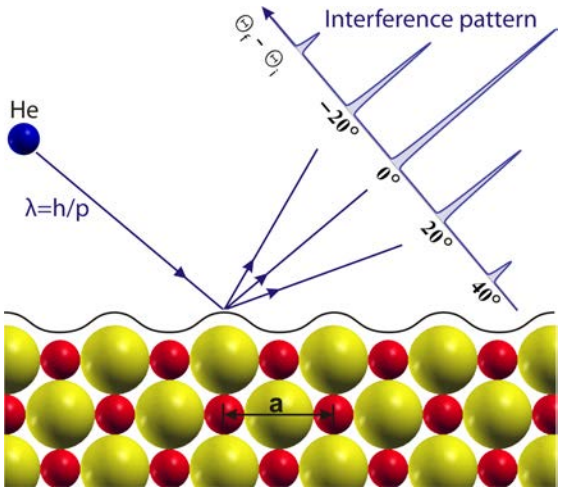

Figure 1.2.: Elastic scattering of He-atoms at the surface: The periodic arrangement of the surface atoms gives rise to an interference pattern due to the wave-particle duality. Information such as the surface structure and lattice constants may be extracted from the interference pattern.

Thus the surface structure is studied by scattering the helium beam at the surface and observing the resulting interference pattern. Interference occurs due to wave-particle duality, which states that the incident helium atoms can be described as waves giving rise to a diffraction pattern just as in the case of X-ray diffraction [3,7–9].

1.2.2. Inelastic Scattering - Surface Dynamics

Inelastic measurements include energy transfer to or from the surface which reveals information about the surface dynamics. Thus the helium atoms are scattered inelastically through excitation or deexcitation of the surface vibrational modes (phonon creation or annihilation). This process can be understood as a

diffraction from a moving lattice in analogy with the elastic diffraction from a static lattice. The alteration of the energy has the classic analogue in the change of the frequency of a wave, diffracted from a moving lattice, due to the Doppler effect [10].
Hence inelastic scattering of helium atoms is used to determine surface phonon modes located at the surface. The scattered helium atom may either loose energy by exciting a phonon or gain energy via energy transfer from a phonon to the He atom. The scattered helium atom exhibits an energy (velocity) that is lower/higher than the velocity before the interaction.

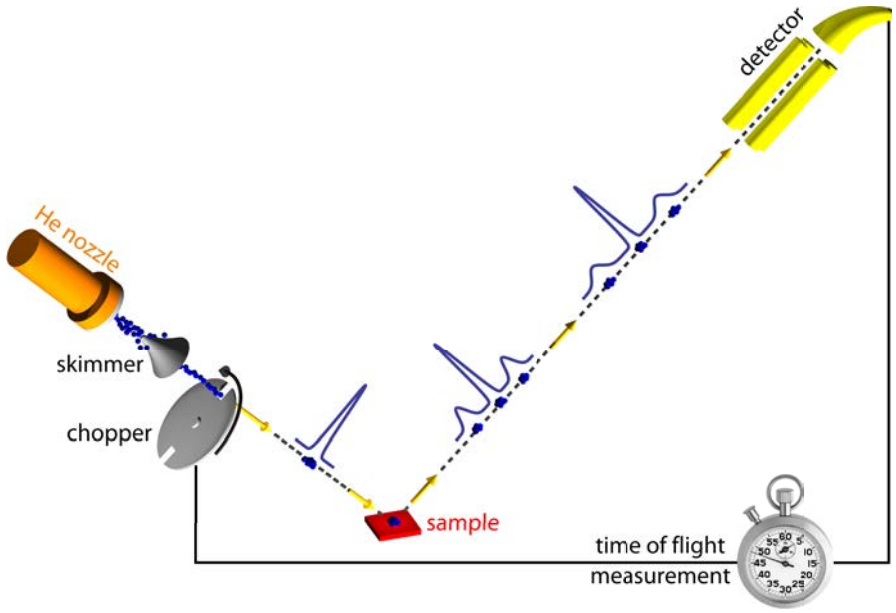

Figure 1.3.: Principle of the time-of-flight measurement: The helium beam is chopped into narrow bunches and interacts with the surface whereupon the helium atoms can change their velocity. After interaction the He atoms propagate to the detector whereupon faster atoms arrive earlier at the detector than slower particles.

To achieve information about the different velocities in the helium beam a so called time-of-flight measurement is carried out. Therefore it is necessary to modulate the beam by a rotating chopper disk: A slit in the chopper rotates past the beam and chops the beam into narrow bunches of He-atoms. The atoms in the bunch are then propagating to the detector whereby faster atoms tend to arrive earlier at the detector than slower particles [3,4,7,10–12].

1.2.3. Why Use Helium Atoms?

Using helium atoms to probe a surface holds several advantages compared with X-rays, neutrons or electrons. Hence the lightweight helium atoms in the energy range of 10-200 meV do not penetrate into the bulk material giving rise to the only surface characterization method that is strictly surface sensitive. This means in addition, that using helium atoms to probe a surface is truly non-destructive to the sample[3].

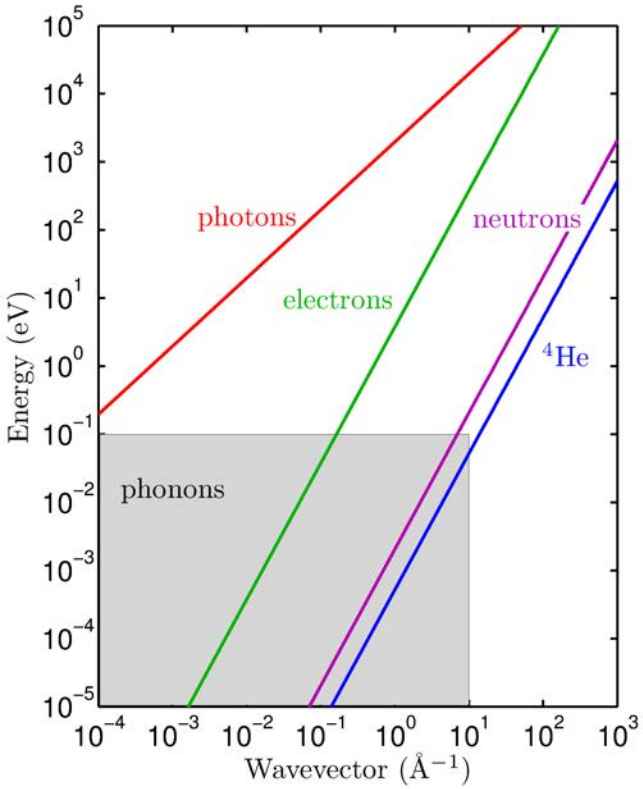

Figure 1.4.: Energy-wavevector relation for various probe particles used in studying phonons. The gray region indicates the approximate energy range of surface phonons. Neutrons are ideal for measuring bulk phonons but due to their large penetration depth those are rather insensitive to surface phonons. He atoms and low energy electrons are most suitable for the measurement of surface phonons. Whilst low energy electrons tend to penetrate into the solid for a few atomic layers, He atoms do not penetrate into the bulk at all. Furthermore, the method of inelastic X-ray scattering under gracing incidence condition can detect surface phonons as well but it is He atom scattering which provides the best resolution[13,14].

Since the helium atoms are neutral they are insensitive to surface charges thus allowing the investigation of insulating materials. Furthermore, as a noble gas, the helium atoms are chemically inert thus offering a completely inert investigation

method (chemically, electrically, magnetically and mechanically)[3].
Finally, He atom scattering provides the best resolution for the determination of phonon dispersion curves. From figure 1.4 which shows the energy-wavevector relationship of several probe particles it can be seen that the relation for neutrons and He atoms overlaps ideally with the region of phonons. However, as mentioned before, neutrons have the disadvantage of penetrating into the bulk[4,7,10,14].
Hence a helium beam is capable of studying the surface structure and dynamics for a wide range of materials, including those with reactive or metastable surfaces[3,4,7,11,12].

2. Theoretical Background

2.1. Surface Description

2.1.1. Description of Crystals

Most aspects of surface descriptions and surface crystallography are extensions of the concepts used to describe the structure of bulk materials. Since the main concepts of bulk crystallography can be found in every textbook about solid state physics (e.g[15]), these concepts will not be covered in great detail.
Usually the periodic structure of an ideal crystal is characterized in terms of a lattice. The crystal lattice is a three-dimensional arrangement of points. All the information that is necessary to describe the crystal is given by a subunit of this lattice: The unit cell. The unit cell itself is specified by three unit cell vectors $(\vec{a}, \vec{b}, \vec{c})$. A stacking of these unit cells in all three dimensions fills the space of the lattice and describes the crystal. In terms of translational symmetry, the crystal looks exactly the same when viewed from a point $\vec{r}$ as when viewed from point $\vec{r'}$

$$\vec{r'} = \vec{r} + n_1 \cdot \vec{a} + n_2 \cdot \vec{b} + n_3 \cdot \vec{c} \tag{2.1}$$

where n_1, n_2 and n_3 are integers[16]. However, the lattice is a mathematical abstraction. The crystal structure is formed when an atom or a group of atoms, the so-called basis, is attached to every lattice point[17]. Hence the basis indicates the position of the atoms within the unit cell.

2.1.2. Description of Surfaces

An ideal crystal surface is prepared via a planar cut through an ideal bulk crystal. The resulting surface structure is usually given in terms of the Miller indices of the bulk plane[16]. Consequently, crystal surfaces are in principle three-dimensional objects since the atoms of the uppermost layer are not necessarily situated in one plane. However, all symmetry properties of the surface are two-dimensional, and for the description of the surface lattice only two translation vectors are sufficient[17]:

$$\vec{r'} = \vec{r} + n_1 \cdot \vec{a} + n_2 \cdot \vec{b} \tag{2.2}$$

Table 2.1.: The common names of the 5 Bravais lattices in two dimensions together with their restrictions on the unit cell vectors $\vec{a}$ and $\vec{b}$ and the angle γ.

oblique	$\lvert\vec{a}\rvert \neq \lvert\vec{b}\rvert$	$\gamma \neq 90°$
rectangular	$\lvert\vec{a}\rvert \neq \lvert\vec{b}\rvert$	$\gamma = 90°$
centered rectangular	$\lvert\vec{a}\rvert \neq \lvert\vec{b}\rvert$	$\gamma = 90°$
square	$\lvert\vec{a}\rvert = \lvert\vec{b}\rvert$	$\gamma = 90°$
hexagonal	$\lvert\vec{a}\rvert = \lvert\vec{b}\rvert$	$\gamma = 120°$

According to the three-dimensional translation (equation 2.1), equation 2.2 corresponds to a geometry where the z-axis is perpendicular to the surface and the x- and y-axes lie in the surface plane. The unit cell is now specified by the vectors $\vec{a}$ and $\vec{b}$ or simply by the norm of the vectors and the enclosed angle γ. The convention for the choice of these unit cell vectors is the following[16]:

- $\vec{b}$ is always longer than or equal to $\vec{a}$. ($|\vec{b}| \geq |\vec{a}|$)
- The angle between $\vec{a}$ and $\vec{b}$ must always be greater than or equal to 90°. ($\gamma \geq 90°$)

In the two-dimensional case there are only five possible unit meshes which have the possibility to cover the entire plane of the lattice via translation. These distinct lattice types are commonly named as Bravais lattice[1,16]. The properties and common names of the 5 Bravais lattices for the tow-dimensional case are listed in table 2.1.

In figure 2.1 those Bravais lattices are shown. Note that for the rectangular centered lattice two types of unit cells are displayed: The rectangular unit cell which is non-primitive and the primitive unit cell which is non-rectangular. Thereby the primitive unit cell is the unit cell with the smallest area, having lattice points only at their corners[16]. Consequently in the case of the rectangular centered lattice the rectangular unit cell is non-primitive but the primitive unit cell does not reflect the full symmetry of the lattice.

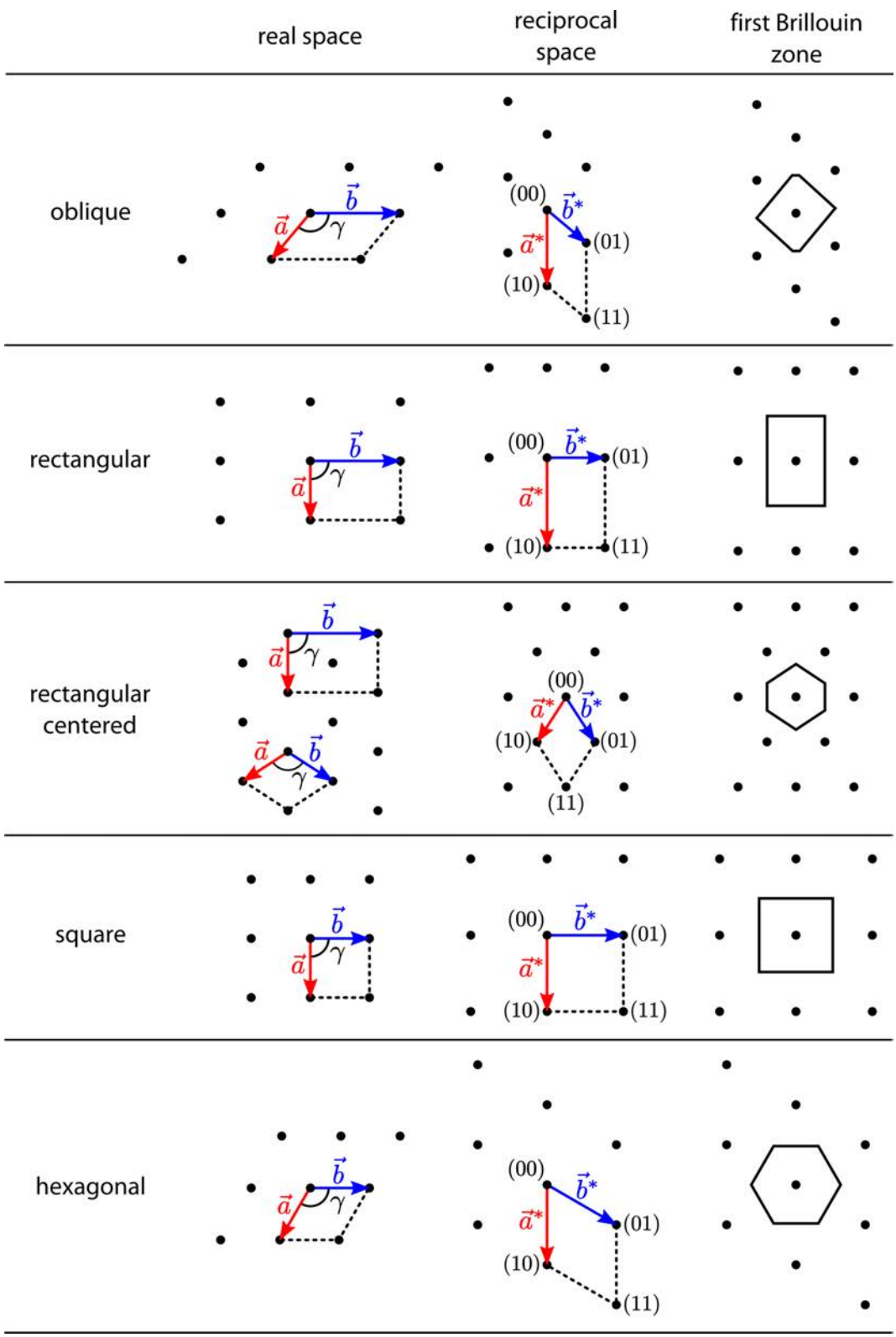

Figure 2.1.: The five two-dimensional Bravais lattices in real and reciprocal space together with the first Brillouin zone. For the rectangular centered lattice two types of unit cells are displayed in real space: The rectangular and the primitive unit cell.

2.1.3. The Reciprocal Space

Another lattice, the reciprocal lattice, has proven to be very useful when dealing with diffraction experiments[1,17]. The two-dimensional reciprocal lattice is constructed analogous to the three-dimensional one[15]. Hence the unit cell vectors of the two-dimensional reciprocal lattice $\vec{a}^*$ and $\vec{b}^*$ are defined in terms of the real-space lattice vectors $\vec{a}$ and $\vec{b}$ by

$$\vec{a}^* = 2\pi \frac{\vec{b} \times \vec{n}}{\vec{a}(\vec{b} \times \vec{n})}, \quad \vec{b}^* = 2\pi \frac{\vec{n} \times \vec{a}}{\vec{a}(\vec{b} \times \vec{n})} \tag{2.3}$$

where $\vec{n}$ is the unit vector normal to the surface. A general translation vector of the reciprocal lattice is:

$$\vec{G}_{hk} = h\vec{a^*} + k\vec{b^*} \tag{2.4}$$

where h and k are integer numbers, referred to as Miller indices. Each point of the two-dimensional reciprocal lattice can be reached by a reciprocal lattice vector $\vec{G}_{hk}$.
The reciprocal lattices of the 5 Bravais types are given in figure 2.1. Thereby, for the centered rectangular lattice the primitive unit cell should be used for the reciprocal lattice since the choice of non-primitive unit vectors results in different unit vectors in both real and reciprocal space[16].

2.1.4. The Wigner-Seitz Cell and the Brillouin Zone

The Wigner-Seitz cell is a special primitive unit cell which is defined by a unique construction instruction. The construction in real space is given by the following steps:

- The origin (00) of the lattice is taken at an arbitrarily chosen lattice point. From the origin lines are drawn to the neighboring (closest) lattice points.
- At the midpoint of each line perpendicular lines are dawn (in 3D: planes).
- The smallest area (in 3D: volume) around the (00) lattice point that is enclosed by these perpendicular lines defines the Wigner-Seitz primitive cell.

The primitive cell that is constructed in this manner has the advantage that it contains only one lattice point located at its center[17].
In reciprocal space the Wigner-Seitz cell is known as the first Brillouin zone. Note that the enclosing line segments of the first Brillouin zone are called the Brillouin zone boundary[16]. The first Brillouin zones of the two-dimensional Bravais lattices are shown in the right hand column of figure 2.1.
In reciprocal space the first Brillouin zone is the usual choice for the primitive cell.

It is used in the description of diffraction, electronic band structure and lattice vibrations[16]. The center of the Brillouin zone is labeled by Γ, whereupon high symmetry points are labeled by upper case roman letters. This notation is the BSW (Bouckaert-Smoluchowski-Wigner) notation[18].
In the case of surface Brillouin zones the symmetry points are usually written with a bar, e.g. $\overline{\Gamma}$, to distinguish them from those in the bulk[16]. The two-dimensional surface Brillouin zone can be related to the bulk Brillouin zone. Therefore the points of the three-dimensional zone are projected onto the two-dimensional zone which is shown in figure 2.2 for the fcc(111) surface.

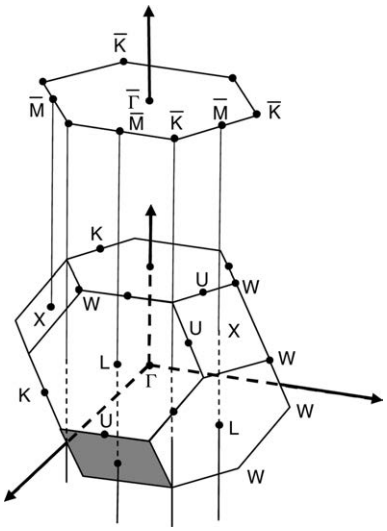

Figure 2.2.: Relation between the surface and the bulk Brillouin zone in case of the fcc(111) surface taken from[19].

2.2. Generation of a Helium Beam

As a matter of fact HAS requires the generation of an atomic He beam. In order to provide sharp diffraction peaks and to resolve small changes in the velocity of the scattered beam, the velocity distribution of the generated He beam has to be as narrow as possible. Therefore the He beam is generated in a supersonic expansion which gives rise to a quasi-monochromatic beam.
The comparison of a supersonic source with a He beam generated in an effusive source shows the advantage of a supersonic source: In an effusive beam the Maxwell-Boltzmann distribution of the source is more or less maintained in the beam. The difference of the velocity spread for both sources is illustrated in figure 2.3. It shows the measured velocity distribution of a supersonic He source and the Maxwell-Boltzmann distribution for a He gas at the same temperature. Note that the actual velocity spread of the supersonic beam is even smaller, since effects

introduced due to the measurement of the velocity distribution add to the spread of the beam (see section 2.4.1).

The principle of a supersonic expansion is as follows:[20] He gas (He 6.0 which cor-

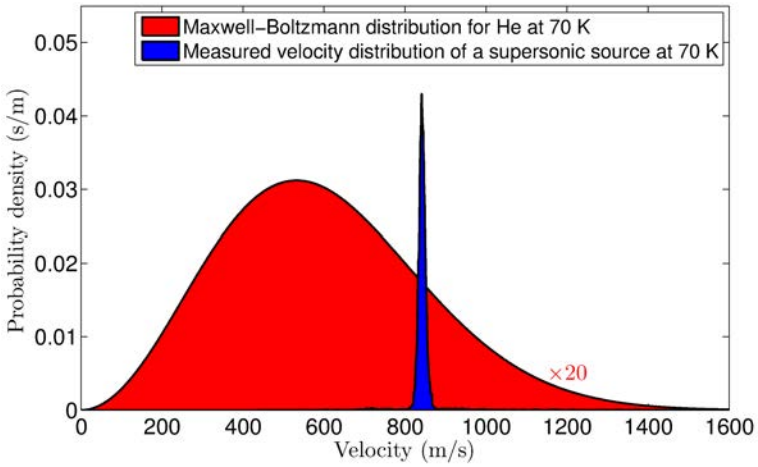

Figure 2.3.: Comparison of an effusive with a supersonic source: The measured velocity distribution of a supersonic He source at 70 K and the corresponding Maxwell-Boltzmann distribution for a He gas at the same temperature are shown.

responds to a purity $> 99.9999\%$) with a high pressure p_0 is provided and expands through a nozzle with a diameter of 10 µm into a vacuum chamber at low pressure p_a. If the ratio p_0/p_a is sufficiently large the gas flow will reach sonic speed (Mach number $M_a = 1$) at the nozzle outlet. Typical values for the experiments are $p_0 = 30$ bar up to $p_0 = 60$ bar and $p_a \leq 1 \cdot 10^{-6}$ mbar.

Due to the quick expansion the process may be considered as adiabatic, giving rise to an adiabatic cooling of the gas whereas the internal energy of the gas is transformed into translational kinetic energy. The gas leaves the nozzle in the continuum flow regime whereupon energy exchange between the He atoms is possible but with increasing expansion a transition to molecular flow occurs[21].

The skimmer, a conically shaped aperture with a certain diameter, selects a part of this expansion, usually beyond the continuous flow region to obtain a laminar flow helium beam. It also transfers the helium beam into the following vacuum chamber.

This expansion can be described by means of the theory of continuous media and equilibrium thermodynamics. A short survey will be given in the following sections.

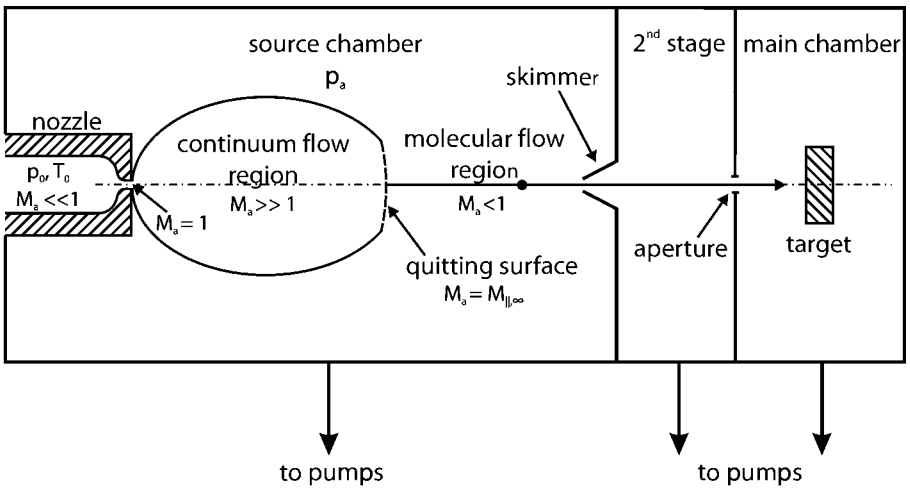

Figure 2.4.: Setup of the supersonic expansion: He gas with a high pressure p_0 expands through a nozzle into the source chamber at low vacuum pressure p_a. The skimmer selects the central part of the expanding gas beyond the continuous flow region and transfers the helium beam into the following vacuum chamber.

2.2.1. Thermodynamics of Free Jet Expansion

Since helium is a monoatomic gas, rather small and does not have a dipole moment (because it is spherical) it may be considered as quite close to an ideal gas. Starting with the specific heat capacity at constant pressure P and constant volume V which are:

$$c_P = \left(\frac{\partial h}{\partial T}\right)_P , \quad c_V = \left(\frac{\partial u}{\partial T}\right)_V \tag{2.5}$$

where u is the specific internal energy and h the specific enthalpy. Forming the total derivative of u(V,T) and h(P,T) gives:

$$du = c_V \cdot dT \;\; (V = const), \qquad dh = c_p \cdot dT \;\; (p = const) \tag{2.6}$$

For an ideal gas ($pV = nRT$):

$$c_p - c_V = R \tag{2.7}$$

holds. Due to the quick expansion the process may be considered as adiabatic. Assuming reversibility this yields an isentropic process. For an ideal gas the adiabatic exponent $\gamma = c_P/c_V$ is constant and the pressure and temperature before the expansion P_1, T_1 are related to pressure and temperature after the expansion P_2, T_2 by:

$$\frac{P_2}{P_1} = \left(\frac{T_2}{T_1}\right)^{\frac{\gamma}{\gamma-1}} \tag{2.8}$$

2.2.2. Continuum Properties of Free Jet Expansion

Treating the free jet expansion as a steady flow of a homogeneous gas wherein heat transfer and external forces are negligible, according to Pauly[20] the conservation of energy can be written as:

$$\frac{D}{Dt}\left(h + \frac{w^2}{2}\right) = 0 \tag{2.9}$$

Thus the sum of the specific enthalpy h and the specific kinetic energy $w^2/2$ is constant along a streamline which is expressed by the convective derivative D/Dt. Together with equation 2.6 this yields:

$$\frac{w_2^2 - w_1^2}{2} = h_2 - h_1 = \int_{T_2}^{T_1} c_P \cdot dT \tag{2.10}$$

If the specific heat is assumed to be constant the integration can be carried out immediately:

$$\frac{w_2^2 - w_1^2}{2} = 2c_P \cdot T_1 \left(1 - \frac{T_2}{T_1}\right) \tag{2.11}$$

The gas in the source (point 1) can be assumed as steady at the pressure p_0 and the stagnation temperature T_0 whereby the flow velocity is negligibly small ($w_1 \approx 0$). Point 2 represents any other point along the isentropic flow where the velocity $v = w_2$ is reached. Using equation 2.8 to insert the pressure relation instead of the temperature relation yields:

$$v \approx \sqrt{2 \cdot c_p \cdot T_0 \left[1 - \left(\frac{p_a}{p_0}\right)^{\frac{\gamma-1}{\gamma}}\right]} \tag{2.12}$$

Dealing with helium and thus with a monoatomic gas, $c_P = 5/2 \cdot k_B/m$ and $\gamma = 5/3$. Furthermore, due to the low background pressure p_a in the vacuum chamber $p_a/p_0 \ll 1$ and the final speed that is reached by the Helium atoms is given by:

$$v \approx \sqrt{\frac{5 \cdot k_B \cdot T_0}{m_{He}}} \tag{2.13}$$

with the atomic mass m_{He} of Helium.

Another useful variable to characterize continuum gas flow is the Mach number M_a which is defined as the speed of the gas atoms, divided by the speed of sound v_a in the gas:

$$M_a = \frac{v}{v_a} = \frac{v}{\sqrt{\gamma \frac{R \cdot T}{m_a}}} \tag{2.14}$$

with the molar mass m_a. All thermodynamic variables of the jet can also be expressed in terms of M_a [6]. Let us consider again the free jet expansion whereupon the gas in the source is at rest (pressure p_0). Given a short converging nozzle where the flow can be assumed to be isentropic and friction and heat conduction can be neglected, at the nozzle exit sonic speed ($M_a = 1$) is attained as long as the ratio p_0/p_a satisfies the condition:

$$\frac{p_0}{p_a} \geq \left(\frac{\gamma+1}{2}\right)^{\frac{\gamma}{\gamma-1}} \tag{2.15}$$

In the case of helium gas $p_0/p_a \geq 2.05$ holds. However, if the pressure ratio increases beyond the critical value the flow is said to be underexpanded and as a consequence, a further expansion toward the ambient pressure p_a occurs. Thus the flow becomes supersonic ($M_a > 1$) and the Mach number increases with increasing distance from the nozzle[20].

In the proximity of the nozzle the collisions between the gas particles are very frequent. However, as the free jet expands into vacuum the density decreases rapidly with increasing distance from the nozzle. Beyond a certain distance the number of collisions is so low that it can be neglected[21].

2.2.3. Transition to Nonequilibrium Conditions

The theoretical description of the transition from continuous flow to free molecular flow is rather difficult. A very simple but useful concept is that of an unsteady transition, the so called quitting surface model. Thereby the expansion is divided by a quitting surface into the two regions (see figure 2.5).
In the free-molecular collisionless region, the continuous media results must be modified to account for the free molecular flow. Thus the physical meaning of the Mach number gets gradually lost with decreasing gas density and is therefore often replaced by the speed ratio:

$$S = \frac{v_{||}}{v_{||w}} \tag{2.16}$$

whereupon $v_{||w}$ is the most probable speed[20]. The speed ratio is in turn related to the Mach number by

$$S = \sqrt{\frac{\gamma}{2}} M_a \tag{2.17}$$

A detailed theoretical consideration of this transition requires an approximate solution of the Boltzmann equation. Thus the velocity distribution of the beam is

described using a distribution function called the ellipsoidal drifting Maxwellian model. It takes account of the fact that the velocity components in direction parallel to the streamlines ($v_{||}$) and perpendicular to the streamlines ($v_{\perp}$) behave differently during the expansion. The velocity distribution is the product of two Maxwell-Boltzmann distributions with two temperatures $T_{||}$ and $T_{\perp}$ (see figure 2.5)[21].

In the continuum region the number of collisions between the gas particles is high

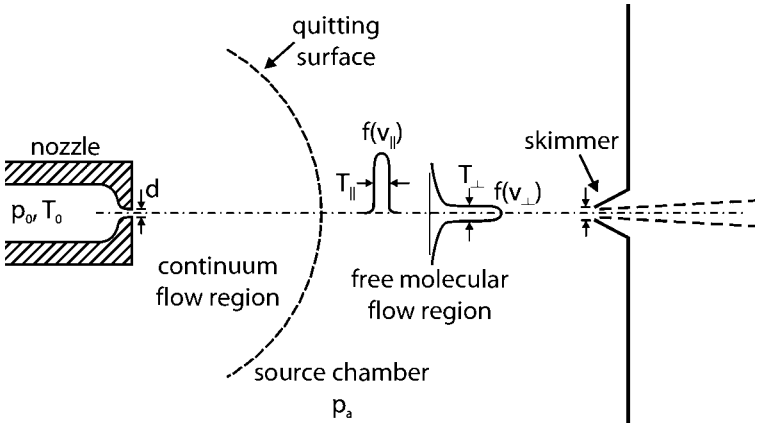

Figure 2.5.: Illustration of the quitting surface model: The continuum flow and free-molecular flow regimes are separated by the quitting surface. The spread in parallel velocities $f(v_{||})$ is characterized by $T_{||}$ and the spread in velocities perpendicular to the streamline $f(v_{\perp})$ by $T_{\perp}$.

enough to maintain local equilibrium $T_{||} = T_{\perp}$. Using the quitting surface model at distances beyond the quitting surface no collisions between the particles occur, therefore the distribution of parallel velocities does not change in this region. However, the perpendicular velocities continue to decrease which gives rise to an decreasing temperature $T_{\perp}$ whereas the temperature $T_{||}$ of the parallel velocity distribution remains constant[20].

According to Miller[6] the terminal speed ratio achieved by supersonic expansion may be estimated by

$$S_{||,\infty} = \alpha \cdot \left[\frac{\sqrt{2} \cdot p_0 \cdot d}{100 \cdot k_B \cdot T_0} \left(\frac{53 \cdot C_6}{k_B \cdot T_0} \right)^{1/3} \right]^{\beta} \tag{2.18}$$

with the pressure of the source p_0 in bar, the source temperature T_0 in K and the nozzle diameter d in mm. For a helium beam ($\gamma = 5/3$) the parameters $\alpha = 0.527$ and $\beta = 0.545$ should be chosen[6]. C_6 is the parameter of the Lennard-Jones potential with $C_6 = 2.1252 \cdot 10^{-67}\mathrm{J} \cdot \mathrm{cm}^6$.

Using equation 2.17 the terminal Mach number $M_{||,\infty}$ is given by

$$M_{||,\infty} = \sqrt{\frac{2}{\gamma}} S_{||,\infty} \tag{2.19}$$

Furthermore the distance of the quitting surface can be estimated as the distance at which the continuum expansion reaches the terminal Mach number. According to Miller[6] the distance x_q of the quitting surface with respect to the nozzle (diameter d) on the jet axis is then calculated using:

$$\frac{x_q}{d} \approx \left(\frac{S_{||,\infty}}{3.232} \right)^{3/2} \tag{2.20}$$

2.3. Kinetic Parameters of the He-Beam

According to the quantum formalism every particle may be treated as a wave with a wavelength:

$$\lambda_i = \frac{h}{p} = \frac{h}{m \cdot v} = \frac{h}{\sqrt{2mE}} \tag{2.21}$$

Given the maximum velocity which is reached after the supersonic expansion (equation 2.13 with $T_0 = T_N$) the particles impinging on the surface exhibit an energy E_i

$$E_i = \frac{1}{2} m_{He} \cdot v_{He}^2 = \frac{5}{2} k_B T_N \tag{2.22}$$

where T_N is the temperature of the helium nozzle. Since the wavevector $\vec{k}_i$ is related to the wavelength via $|\vec{k}_i| = 2\pi/\lambda_i$ the energy may also be expressed in terms of the wavevector:

$$E_i = \frac{\hbar^2}{2m_{He}} k_i^2 \tag{2.23}$$

The nozzle temperature T_N can be varied so that the energy of the impinging helium atoms changes. Some typical kinetic parameters of the He-beam at different nozzle temperatures T_N are given in table 2.2.

Table 2.2.: Kinetic parameters of a He-beam generated in supersonic expansion with different nozzle temperatures T_N:

T_N (K)	v (m/s)	E_i (meV)	λ (Å)	k_i (Å^{-1})
50	718	10.8	1.38	4.6
100	1016	21.5	0.97	6.4
200	1437	43.1	0.69	9.1
300	1759	64.6	0.56	11.2
400	2032	86.2	0.49	12.9

2.4. Time of Flight Measurements

The time-of-flight (TOF) method is based on a fairly simple principle: From a measurement of the time t required for an atom to travel a given distance L the speed of the atom is determined:

$$v = \frac{L}{t} \tag{2.24}$$

To measure the velocity distribution of a helium beam it is necessary to modulate the beam by a rotating chopper disk: A slit in the chopper rotates past the beam and chops the beam into narrow bunches of He-atoms. The atoms in the bunch are then propagating to the detector whereby faster atoms tend to arrive earlier at the detector than slower particles. By repeating this measurement many times the detector yields a distribution of flight times $g(t)$ from which the velocity distribution $f(v)$ or the energy distribution $f(E)$ may be calculated[11,20,22,23].
In practice the chopping of the beam marks the starting time of the TOF measurement and a LED/phototransistor pair mounted at the chopper slit, produces a synchronous timing pulse. This trigger pulse initiates a multichannel analyzer to store the detected beam intensity as a time histogram. The limiting restraints in the resolution of this time-of-flight measurement will be discussed in the following section.

2.4.1. TOF-Resolution

For the resolution in a TOF spectrum the width of the peaks is of importance. The velocity spread of the beam contributes to this width. It is, however, usually not the dominant factor, which is rather the time width introduced by the TOF analysis itself[3].
Firstly, the chopper modulates the beam with a frequency ν_{ch} which can be described by a chopper transmission function $C(t)$. The ideal $C(t)$ is a delta function but due to the finite slit width of the chopper it is usually described using a function with a trapezoidal shape[23]. Secondly, the resolution is limited by the detector which exhibits a finite ionization length and thus can be described by a function $D(x)$ giving the ionization probability. Both contributions by $C(t)$ and $D(x)$ can be included in an effective transmission function $T_{eff}(t)$[23].
The experimentally determined time-of-flight distribution $G(t)$ includes both the finite width of the chopper function and the finite length of the ion source. The relation of $G(t)$ to the true time-of-flight distribution $g(t)$ is mathematically expressed by means of a convolution integral:

$$G(t) \propto \int_{-\infty}^{\infty} T_{eff}(t-\tau)g(\tau)d\tau \tag{2.25}$$

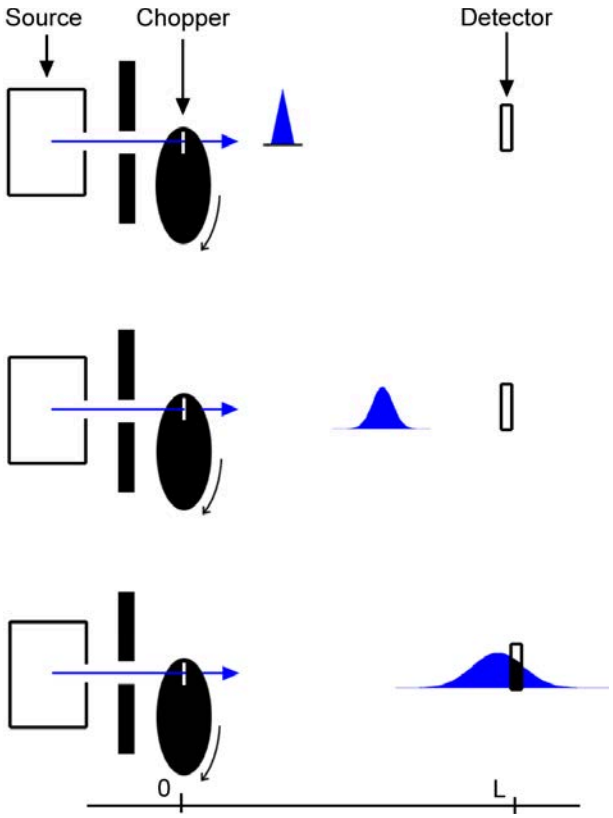

Figure 2.6.: Schematic illustration of the TOF principle from[24]: A continuous beam is chopped into particle bunches which travel along the flight path to the detector. Due to the velocity spread of the particles the narrow bunch disperses.

To determine $g(t)$ it is necessary to use the deconvolution of equation 2.25. According to Pauly[23] both $G(t)$ and $T_{eff}(t)$ can be approximated by Gaussian functions to a very high degree of accuracy. Thus the desired true time-of-flight distribution $g(t)$ is also a Gaussian function. For the corresponding halfwidths of the Gaussian functions, integration of equation 2.25 yields:

$$\Delta t_G^2 = \Delta t_g^2 + \Delta t_T^2 = \Delta t_g^2 + \underbrace{\Delta t_C^2 + \Delta t_D^2}_{=\Delta t_T^2} \tag{2.26}$$

with Δt_T, the halfwidth of $T_{eff}(t)$, Δt_C the halfwidth of $C(t)$ and Δt_D the halfwidth of $D(x)$.

2.4.2. Corrections of TOF measurements

A multichannel analyzer with a selectable channel width t_{mc} sums up the single TOF spectra during the measurement time. The rotating chopper disk triggers the starting point of the multichannel analyzer and the real time of flight t_f is composed of

$$t_f = t_p - t_c - t_{mc}/2 \tag{2.27}$$

where t_p is the peak time given in the TOF spectra and t_c is a correction which is necessary due to the influence of a delayed triggering. Hence t_c is dependent on the chopper frequency ν_{ch} by:

$$t_c = \alpha \cdot \frac{1}{\nu_{ch}} \tag{2.28}$$

with $\alpha = -(5.4 \pm 1.2)$ ms/s (see section 5.2). In addition, when using a small channel width, $t_{mc}/2$ is negligible.

2.4.3. TOF-measurements using a Pseudo Random Chopper

The use of a chopper as described so far requires two restrictions:

- A short opening time of the chopper to ensure a good resolution.
- The overlapping of different particle bunches at the detector is forbidden. Hence an adequate interval between two adjacent pulses has to be chosen to exclude that faster and slower particles of the two adjacent pulses overlap at the detector.

Both requirements give rise to a relatively small time that the chopper slit remains open for the beam. The ratio which gives the fraction of intensity that is transmitted through the chopper is called "duty factor" and is usually ≈ 0.01 for a single slit chopper disk[22]. Therefore the intensity of the helium beam is reduced to only a few percent after chopping which gives rise to rather long measuring times.
This disadvantage can be overcome using the pseudo random chopper technique that gives rise to an average beam intensity of 50% of the unmodulated beam[25]. Using this technique the beam is pulsed at time intervals that are much shorter than the spread of inelastic beams at the detector which gives rise to an overlap of TOF spectra from different chopper pulses. However, provided the beam is chopped in a specific sequence of pulses, the superposition can be deconvoluted[26]. The crucial point in using this technique is the extraction of the TOF distribution from the measured detector signal. The distribution measured at the detector

$D(t)$ is determined by the convolution of the desired TOF distribution $F(t)$ with the shutter function$Z(t)$:

$$D(t) = U(t) + (C \odot F)(t) \tag{2.29}$$

whereupon $\odot$ denotes the convolution integral:

$$D(t) = U(t) + \int C(t - t'')F(t'')dt'' \tag{2.30}$$

and $U(t)$ accounts for a background in the detector signal[23]. Given several constraints it is possible to calculate the TOF distribution via a simple algebraic transformation. Hence we gain the deconvoluted TOF distribution $F(t)$ by convoluting equation 2.29 with the chopper function $C(t)$:

$$F(t) = (C \odot D)(t) - (C \odot U)(t) \tag{2.31}$$

Assuming that the background U is constant gives rise to

$$F(t) = \int C(t')D(t + t')dt' - U \int C(t')dt' \tag{2.32}$$

This convolution integral, that is also referred as cross-correlation method, can easily be handled using the Fourier transformation[24].
The pseudo random chopping concept is now based on the fact that the cross-correlation function of a random function is a delta function[22]. In other words, modulating the beam with a random function and deconvoluting it using the same random function would give rise to the same result as modulating the beam with a delta function.
Of course, in practice it is not possible to use a random modulation since there is no random number generator which is fully uncorrelated[27]. Therefore we are looking for an experimentally realizable "pseudo-random" function that resembles a random function. This is possible using a binary pseudo-random sequence with discrete intervals, where the length of the sequence equals $N = 2^k - 1$ and the sum of the sequence equals 1. Hence the conventional single slot is replaced by a pseudo-random sequence of slots and teeth[22,28] as shown in figure 2.7.
In an experiment the function $D(t)$ measured with the detector consists of discrete values. These discrete values are delivered by the channels of the multi channel analyzer and are then deconvoluted using the above described cross correlation method. Details on this deconvolution procedure can be found in Mayrhofer-Reinhartshubers master's thesis[24] as well as in the literature[25,28].
Finally it should be noted that the pseudo-random chopper technique adds complexity to the experimental apparatus since the chopper has to be phase-locked

Figure 2.7.: Image of a chopper disc for a pseudorandom modulation. The additional slit provides a synchronization light pulse at the start of the pseudo-random sequence and the off-center hole is for balancing.

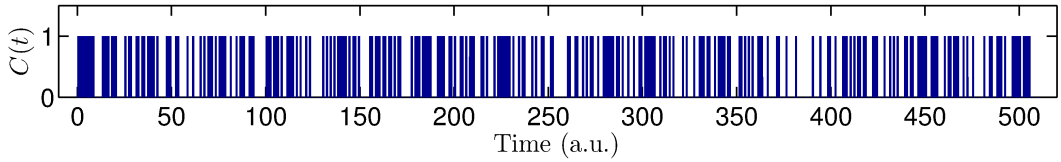

Figure 2.8.: Graphical representation of the pseudo random sequence $C(t)$ with $N = 511$ elements that is used in the TOF measurements. The binary value of 1 corresponds to a slit where the chopper is open for the helium beam whereas 0 corresponds to the time where the chopper is closed for the beam.

to the multichannel analyzer (MCA) and the chopper period must exactly match the cycle time of the MCA within a small fraction of one MCA time channel[22,26]. Yet the pseudo-random chopper technique can greatly improve the signal-to-noise ratio in TOF measurements[23] giving rise to shorter measurement times than compared to TOF measurements with a single slit chopper disc.
However, the method is not well suited in all cases. Hence pseudo-random chopping works poorly if the TOF spectra contain very small peaks in the presence of very large peaks. In that case the statistical noise of the large peaks will be distributed across the spectrum and after the deconvolution the small peaks cannot be distinguished from the noise any more[26]. Thus a key to the successful use of pseudo-random chopping is to arrange the scattering geometry in a way that only phonon peaks of comparable intensities appear in the TOF spectrum[26].

2.5. Crystal Vibrations - Phonons

In a first attempt to describe crystal vibrations, the crystal is described using a one-dimensional chain of atoms. A lot of basics about crystal vibrations in three-dimensional solids can be learned from this model, whereupon detailed descriptions are found in most solid state textbooks[15].

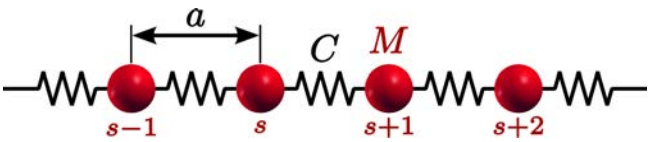

Figure 2.9.: Schematic representation of a one-dimensional crystal with one atom per unit cell. The atoms with mass M are connected by springs with the force constants C.

2.5.1. Crystals with a Monoatomic Basis

The simplest model we can think of is a one-dimensional monoatomic crystal consisting of atoms with the mass M and separated by the lattice vector of length a as shown in figure 2.9. Considering only nearest-neighbor interactions, each atom is bound to its neighbors via harmonic springs with the force constant C. The force F_s acting on the atom s is given in terms of the displacement u:[4,15]

$$F_s = C(u_{s+1} - u_s) + C(u_s - u_{s-1}) \tag{2.33}$$

Hence the force acting on the atom s is linearly dependent on the difference of the displacement u with respect to the nearest neighbors ($s-1$ and $s+1$). This expression is of the form of Hook's law and is applicable as long as the deformation is small. Thus the equation of motion for atom s becomes:

$$M\frac{d^2u_s}{dt^2} = C(u_{s+1} + u_{s-1} - 2u_s) \tag{2.34}$$

The periodic time dependence is fulfilled using $u_s(t) = u_s \cdot e^{(-i\omega t)}$ in accordance to a harmonic oscillator and equation 2.34 gives rise to:

$$-M\omega^2 u_s = C(u_{s+1} + u_{s-1} - 2u_s) \tag{2.35}$$

which is now a difference equation with respect to the displacement u. The displacement of the atoms can be described as traveling waves:[15]

$$u_{s\pm1} = u \cdot e^{(i(s\pm1)qa)} \tag{2.36}$$

where q is the wavevector. Substituting this in equation 2.35 yields:

$$\omega^2 M = -C\left(e^{(iqa)} + e^{(-iqa)} - 2\right) \tag{2.37}$$

This is a dispersion relation for the angular frequency $\omega(q)$:

$$\begin{aligned} \omega^2(q) &= \frac{2C}{M}\left(1 - \cos(qa)\right) \\ &\text{or} \\ \omega(q) &= \sqrt{\frac{4C}{M}}\left|sin\left(\frac{qa}{2}\right)\right| \end{aligned} \tag{2.38}$$

where the norm ensures only positive frequencies ω. This solution describes waves that are propagating along the chain. At $q = 0$ (the Γ-point) ω becomes 0, and for small values of q, ω is approximately linear: $\omega = \sqrt{C/M}aq$. $\omega(q)$ reaches its maximum at the zone boundary ($q = \frac{\pi}{a}$). The dispersion continues then periodically with a period equal to the reciprocal lattice vector $2\pi/a$. Hence the first Brillouin zone contains all physically relevant information[4,15].

2.5.2. Crystals with two Atoms per Unit Cell

The situation for two atoms per unit cell is very similar to the case with one atom per unit cell. Figure 2.10 illustrates the case for two different atoms with mass M_1 and M_2 whereupon the lattice spacing is again a but one atom is located at the origin and one at $a/2$.

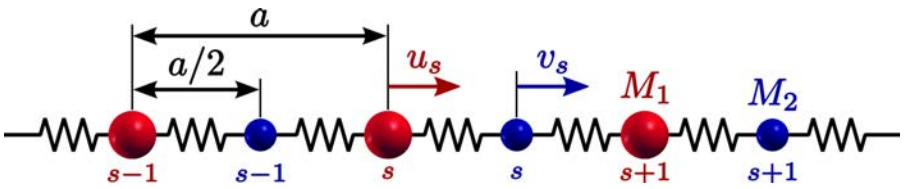

Figure 2.10.: Schematic representation of a one-dimensional crystal with two atoms of mass M_1 and M_2 per unit cell. The force acting on each atom is given in terms of the displacements u and v with respect to the equilibrium position.

Considering again only nearest-neighbor interactions the equation of motion is obtained in a similar manner as above:[15]

$$\begin{aligned} M_1 \frac{d^2 u_s}{dt^2} &= C\left(v_{s+1} + v_{s-1} - 2u_s\right) \\ M_2 \frac{d^2 v_s}{dt^2} &= C\left(u_{s+1} + u_{s-1} - 2v_s\right) \end{aligned} \tag{2.39}$$

which is a system of two coupled differential equations. Using the same ansatz for plane waves as before, a homogeneous linear system of equations for the displacements u and v is obtained. The system of equations has only a solution if

the determinant of the coefficient matrix vanishes:

$$M_1 M_2 \omega^4 - 2C\left(M_1 + M_2\right)\omega^2 + 2C^2\left(1 - \cos(qa)\right) = 0 \tag{2.40}$$

Equation 2.40 exhibits two solutions with a positive frequency ω which are referred to as the acoustical branch (ω_-) and the optical branch (ω_+):

$$\omega_\pm^2 = C\left[\left(\frac{1}{M_1} + \frac{1}{M_2}\right) \pm \sqrt{\left(\frac{1}{M_1} + \frac{1}{M_2}\right)^2 - \frac{4}{M_1 M_2}\sin^2\left(\frac{qa}{2}\right)}\right] \tag{2.41}$$

The dispersion is shown in the dispersion relation $\omega(q)$ 2.11: For each q there are two values of ω whereupon the two solutions give rise to a different kind of dispersion. The acoustical branch shows a similar behavior as the dispersion for the monoatomic case (equation 2.38). This branch goes to zero for $q = 0$ and corresponds to a vibration where all atoms of the unit cell oscillate in phase. Since it corresponds to the propagation of sound in the long wavelength limit it is called acoustic branch[15].

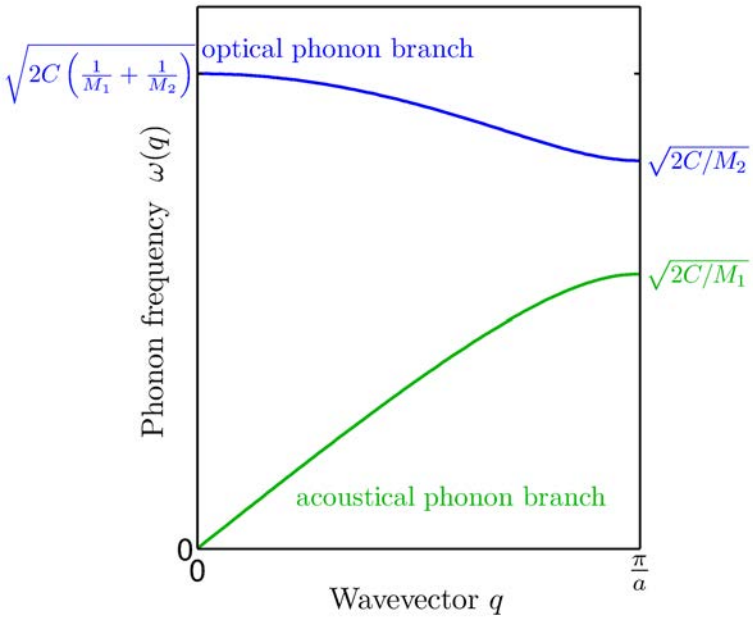

Figure 2.11.: Dispersion relation $\omega(q)$ of the one-dimensional diatomic crystal obtained by solving equation 2.40. There appear two branches: The acoustical branch and the optical branch. The acoustic branch (corresponding to the negative sign in equation 2.41) always goes to zero for $q = 0$, whereas the optical branch exhibits a finite value for $q = 0$. The gap between the optical and acoustic branch increases with increasing difference of the masses M_1 and M_2.

In the case of the optical branch ω exhibits a finite value as q approaches zero. At $q = 0$ this is a vibration in which the two atoms per unit cell move exactly out of phase. The dispersion branch is called optical due to the possibility to couple these vibrations to an electromagnetic field: If the two atoms in the unit cell carry different charges, the vibration corresponds to a changing dipole moment which in turn can be coupled to an external light source[4].
The approximations of this simple model are still just valid for a one-dimensional chain of atoms. However, in a majority of cases there are high symmetry directions in a three-dimensional crystal where the movement of a crystal plane reduces to a one-dimensional problem[29]. Moreover, the model can even be further extended to include nextnearest-neighbor interaction forces and so on[4].

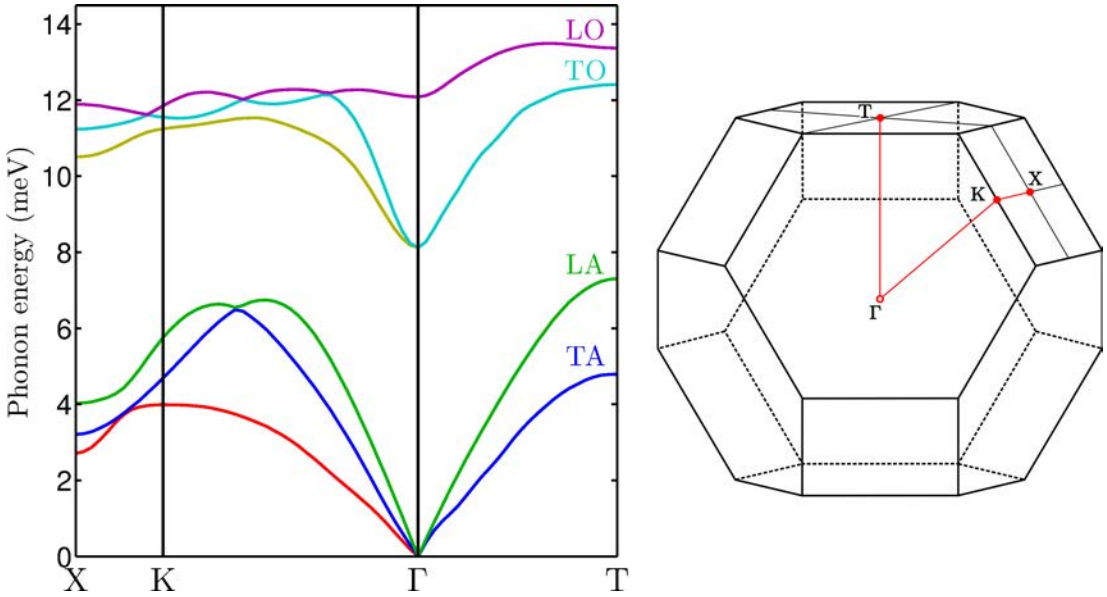

Figure 2.12.: Bulk phonon dispersion of bismuth according to the calculation of Diaz-Sanchez et al.[30]. On the right hand side the first Brillouin zone of bismuth is shown together with the directions that are plotted in the graph. The branches of the ΓT-direction are labeled as:
TA: transversal acoustic, LA: longitudinal acoustic, TO: transversal optical, LO: longitudinal optical

In this treatment only longitudinal vibrations have been considered so far. Vibrations with a transverse polarization can be treated in a similar way, with similar results but with a different force constant. The branches are then labeled as LO and LA for longitudinal polarization and TO and TA for transverse polarization. In general, for a three-dimensional crystal, each atom has three degrees of freedom corresponding to displacements in the three lateral directions x, y and z. A crystal

with n atoms per unit cell gives rise to $3n$ dispersion branches with three of them being acoustic and the remaining $3n - 3$ branches showing an optical character. Due to symmetry operations in the crystal, the branches can be degenerate in energy[15].
Figure 2.12 shows the calculated dispersion curves according to Diaz-Sanchez et al.[30] for a few high-symmetry directions of a bismuth crystal.

2.5.3. Quantized Lattice Vibrations

What has been neglected so far is the quantized character of lattice vibrations. Due to this character the quantized energy of a lattice vibration is called a phonon in analogy with the photon, the quantum of light. In a quantum mechanical treatment, these lattice vibrations are described by a Hamiltonian equivalent to the one of a harmonic oscillator. Thus, the energies of a lattice vibration with the angular frequency ω are quantized with:[15]

$$E_l = \left(l + \frac{1}{2}\right) \hbar\omega \tag{2.42}$$

with the quantum number l. The mode is excited to l, hence l is the total number of phonons in this state. The zero point energy of the mode is given by the term $1/2\hbar\omega$. As in the case of photons, phonons are bosons and are therefore not subject to the Pauli exclusion principle.
A lot of material properties are determined by the number and energy of the occupied phonon states, e.g. the heat capacity or the thermal conductivity since the thermal movement of the crystal atoms can be described in terms of phonons[15,29].

2.5.4. Surface Phonons

At the surface the altered environment with respect to the bulk modifies the dynamics to give rise to new vibrational modes[31]. This "new" vibrational modes are called surface phonons due to their localization at the surface: Their amplitude exhibits a wavelike characteristics parallel to the surface and decays rapidly into the bulk, perpendicular to the surface. This property is associated with the broken translational invariance at a surface[32].

The crystalline symmetry at the surface is reduced from three dimensions to the two dimensions in the plane parallel to the surface. The two-dimensional states at the surface are then characterized by the vector $\vec{Q} = (q_x, q_y)$. Usually for a given $\vec{Q} = (q_x, q_y)$ there exist a lot of of bulk phonon modes with different values of q_z. Hence when the bulk modes are projected onto the surface (where q_z vanishes) one obtains a whole band of bulk vibrational frequencies that appear at the surface[4]. This can be clearly seen in the dispersion relation which is illustrated in figure 2.13. For the case of a real surface, e.g. Ag(111) this procedure is shown in 2.14.

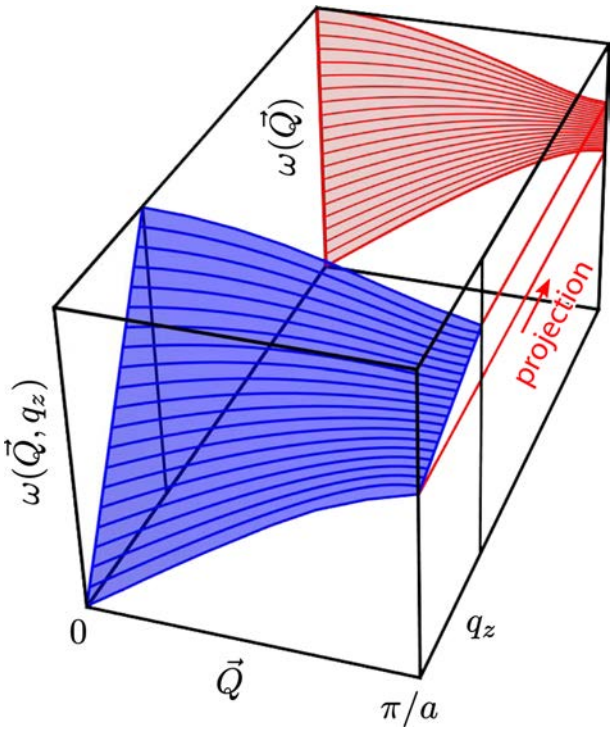

Figure 2.13.: Illustration of the projection of the bulk phonon modes onto the surface: A 3-dimensional set of dispersion curves with parallel ($\vec{Q}$) and normal (q_z) wavevector components is projected onto the surface. The set of dispersion curves is converted into a broad two-dimensional band since for every $\vec{Q}$ there exist a lot of of bulk modes with different values of q_z.

Theoretical calculations of surface phonon dispersions are usually carried out using the slab method. Therefore the crystal is considered as a slab with typically 20-50 layers. The layers are extending to infinity in the directions parallel to the surface using periodic boundary conditions.
In doing so both the bulk and the surface modes are found whereupon the surface localized modes are identified due to the decay of the vibrational amplitudes into the bulk[4,31]. Figure 2.14(d) shows such a calculation for the Ag(111) surface.

With increasing number of layers the number of dispersion curves increases and the projected bulk modes become denser, whereupon for a real crystal these curves even form a continuum. However, beyond a certain slab thickness, the position of the surface localized modes does not change with increasing number of layers[31].

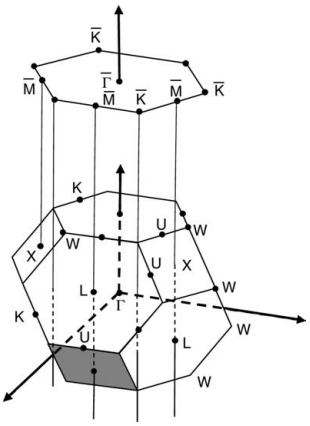

(a) Relation between the fcc(111) and the fcc bulk Brillouin zone from[19]†.

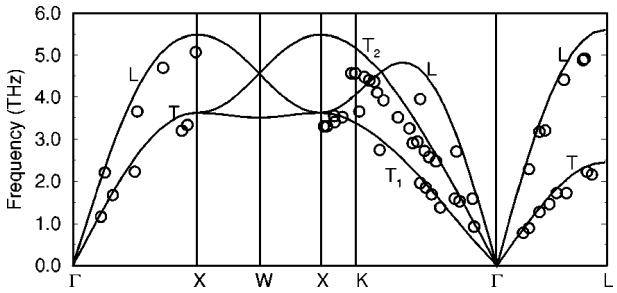

(b) The calculated phonon dispersion curves (solid lines) of silver from[33]§. The bulk values are projected onto the surface according to 2.14(a).

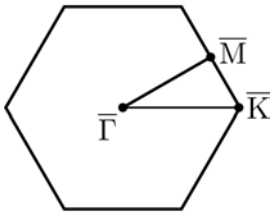

(c) Brillouin zone of the fcc(111) surface.

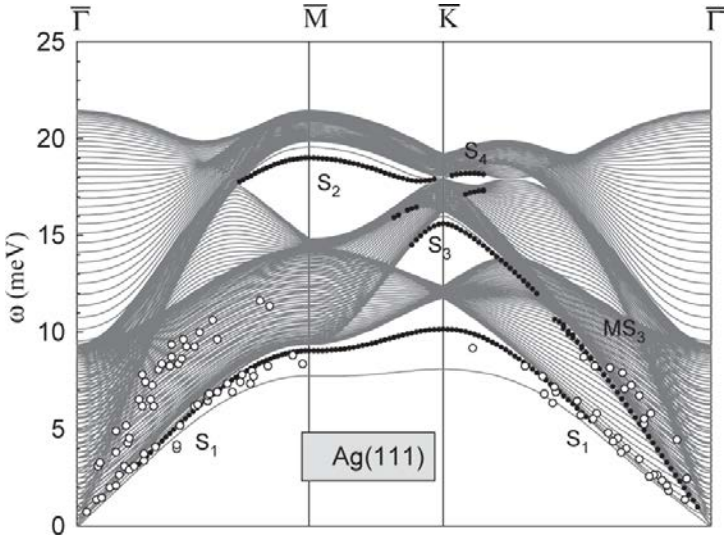

(d) Theoretical surface phonon spectrum of Ag(111) taken from[34]‖. Black dots denote theoretical surface modes and open symbols show experimental data.

Figure 2.14.: Formation of surface phonon modes exemplified for Ag(111): The phonon dispersion of the surface consists of the bulk bands, which are due to the projection of bulk phonons onto the two-dimensional Brillouin zone and the localized surface phonon modes originating in the broken translational invariance at the surface.

In most crystals, the modification of the forces at the surface is in such a way that the surface localized modes exhibit frequencies which lie below the associated projected bulk modes. They appear like a mode that is "peeled" down from the bulk band[4]. Thereby, despite the truncation of the crystal, the presence of the surface introduces another perturbation: An alteration of the force constants near the surface since the surface atoms exhibit fewer neighboring partners. In most cases this alteration gives rise to a softening of the total forces acting on the surface atoms[31].
Hence the modes are found below or in gaps of the bulk vibrational spectrum, e.g. the modes S_1, S_2 or S_3 in figure 2.14(d). If the alteration of the force constants is strong enough, several layers can be affected. Therefore the modes are labeled according to the layer in which the mode is primarily localized e.g. S_2 is primarily localized in the second layer[31].
For many materials a surface localized mode with optical character occurs in the gaps between the bulk acoustic and optical bands. The surface phonon mode with the lowest energy (S_1 in figure 2.14(d)), usually derives from the bulk transverse acoustic band. This branch is referred to as the Rayleigh mode. In this mode the vibration of the atoms is preferentially in the plane defined by the surface normal and the propagation direction[4].
Despite the modes that lie below the bulk bands or in a gap inside the bulk bands there are two other cases. Along symmetry lines that are associated with a mirror plane, a surface mode can fall into a region that is occupied by a sub-band of bulk modes to which it is orthogonal. Then it is still a surface mode. However, if the surface mode appears in a region filled by bulk modes to which it is not automatically orthogonal, it is no longer referred as a pure surface mode[31]. These modes exhibit maximum amplitudes in the surface layer but non-vanishing amplitudes in the bulk and are called mixed modes or surface resonances[32].
In figure 2.14(d) the mode labeled MS_3 is caused by such a resonance: The so-called longitudinal resonance which appears below the lower edge of the band formed by the projected longitudinal bulk modes. The origin of this anomalous resonance has been discussed controversially. It was first attributed to a large softening of the force constants in the first layer[35] which is however, unexpected since the surface shows no significant relaxation or reconstruction.
The occurrence of this resonance could then be explained by taking into account the crucial role of surface electrons which gives rise to electron-mediated force constants in the case of noble and transition metal surfaces[36–39]. In some cases it was even explained in terms of an inherent character of the He-surface interaction as a consequence of the HAS technique[34].

2.5.4.1. The Rayleigh Wave in the Continuum Limit

Surface phonons have already been mentioned by Lord Rayleigh in 1885, who predicted the existence of a surface acoustic wave with a velocity below that in the bulk. It was also him to derive an equation for the Rayleigh wave, by approximating the semi-infinite solid in terms of a continuous and isotropic medium[32,40]. An equation for surface acoustic waves propagating in the x-direction of the plane with $z = 0$ can be derived in the continuum limit using Hooke's law. In doing so the speed of the surface acoustic wave v is determined by equation:[40]

$$c_{33}c_{55}\rho^2 v^2 \left(c_{11} - \rho v^2\right) = \left(c_{55} - \rho v^2\right) \left[c_{33}\left(c_{11} - \rho v^2\right) - c_{13}^2\right]^2 \tag{2.43}$$

where ρ is the mass density of the medium and c_{ij} are the elements of the elasticity (stiffness) tensor which links the stress tensor $\overleftrightarrow{\sigma}$ with the strain tensor $\overleftrightarrow{\epsilon}$ according to Hooke's law in Voigt notation: $\sigma_i = c_{ij}\epsilon_j$. The physical solution of this equation is the phase velocity of a propagating wave with $\omega = vk$ which shall be referred to as v_{RW}.
Equation 2.43 is valid as long as either the x- or the z-axis of the crystal is along a two-fold rotation axis or perpendicular to a mirror plane[40]. The solution of this equation gives rise to a general result (for the given assumptions): The speed of a surface acoustic wave v_{RW} is always lower than the speed of the slowest bulk wave propagating in the same direction. For the special case of an isotropic medium equation 2.43 reduces to:

$$\xi^6 - 8\xi^4 + 8\xi^2\left(3 - 2\frac{v_t^2}{v_l^2}\right) - 16\left(1 - \frac{v_t^2}{v_l^2}\right) = 0 \tag{2.44}$$

with v_l and v_t the speed of sound of the longitudinal and the transverse wave in the bulk and $\xi = v_{RW}/v_t$. The displacements of such a Rayleigh wave, calculated within the continuum theory are shown in figure 2.15.
The condition for the existence of a localized wave, $\xi < 1$, is only fulfilled by the solution of equation 2.44 for ξ^2 with the smallest value[2,40]. Hence using equation 2.44 the velocity of the Rayleigh wave can be calculated from the bulk values v_l and v_t. However, it is important to keep in mind that this holds only for the case of an isotropic medium.

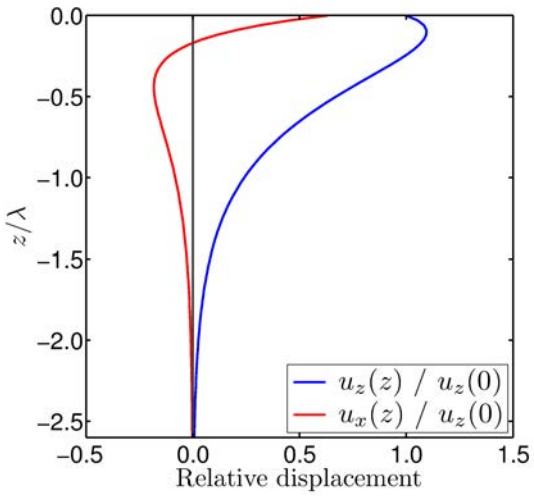

(a) Displacement components u_x and u_z. Both components decrease exponentially with distance z from the surface into the medium whereupon the decay length is proportional to the wavelength λ.

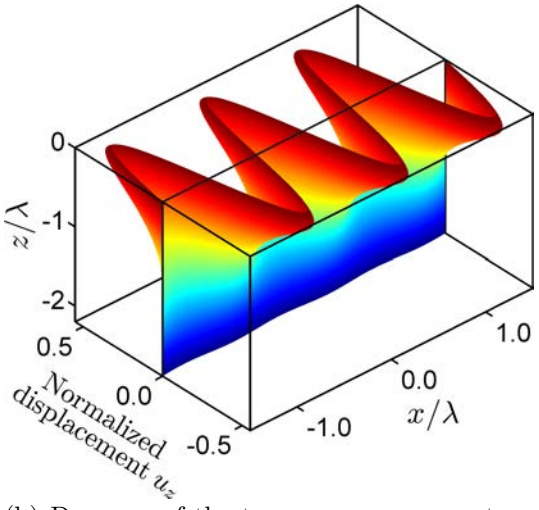

(b) Decrease of the transverse component u_z with increasing depth z.

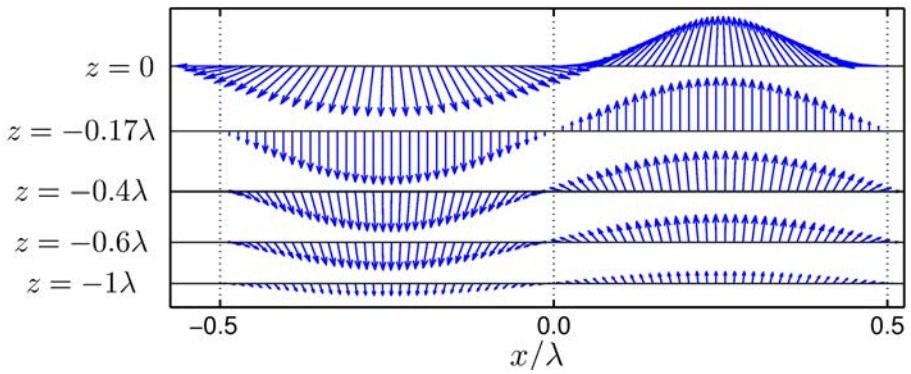

(c) Displacement pattern of the Rayleigh wave. The displacements are neither longitudinal nor transverse, but the transverse component is dominant giving rise to a quasi-transverse mode. Only in a particular depth the displacements are purely transverse.

Figure 2.15.: Displacement of the Rayleigh wave for NaCl calculated within the continuum theory and the assumption of an isotropic medium. Force constants of NaCl according to[41]. Note that the figures are just for illustration purposes since a more realistic treatment would require to account for the anisotropy of the elastic constants[2].

3. Theoretical Aspects of HAS

Figure 3.1 gives an impression of the different processes that occur for scattering of He atoms on a crystal surface. These processes will be described in the following sections. A more detailed description, which is beyond the scope of this work can be found in a lot of articles[3,4,8,9,14].

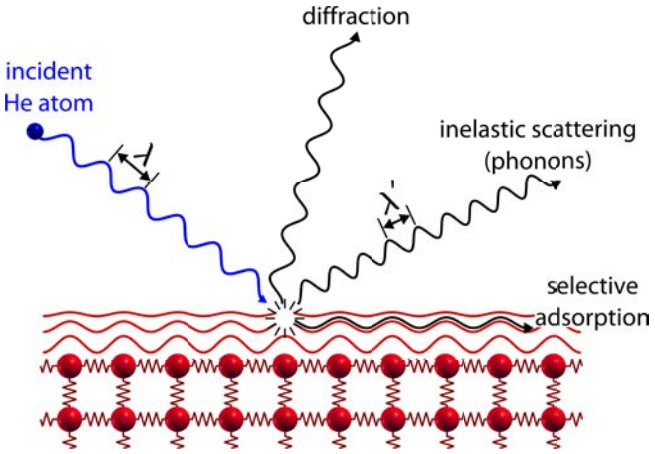

Figure 3.1.: Graphical representation of the different processes for the scattering of He atoms on a crystal surface.

3.1. The Atom-Surface Potential

As figure 3.1 already suggests, the He atom scattering process differs from the scattering mechanism of electrons, neutrons or X-rays. Hence He atoms are scattered by the electron density on the surface whereas the other probe particles are scattered by the ion cores. In the case of inelastic scattering this corresponds to a scattering of the He atom by phonon-induced electron charge oscillations[39].
The interaction of the impinging He-atom with a solid surface can be described in terms of an interaction potential. Therefore it is assumed that the He atom interacts with all surface atoms of the crystal via a total potential $V(\vec{r})$. Obviously the potential depends on the actual position of the impinging atom with respect to the surface, $\vec{r} = (\vec{R}, z)$, usually expressed in terms of coordinates in the surface plane ($\vec{R}$) and perpendicular to it (z). In principle the potential is time dependent but for the description of elastic scattering the time average of the potential $\langle V(\vec{r}, t) \rangle$

is sufficient. This average potential is determined by the surface atoms which are fixed at their equilibrium positions at a given temperature[3,29].
The interaction of a closed-shell atom like He with the surface can be divided into two parts. At distances close to the surface, the Pauli repulsion $V_{rep}(\vec{r})$ arises due to the overlap of the closed-shell electrons of the He-atom with the electrons of the surface. Further away from the surface Van-der-Waals forces give rise to an attractive potential $V_{att}(\vec{r})$: Due to quantum induced polarizations an attractive force between the impinging atom and the surface charge distribution arises. Therefore the potential can be broken down into[3,42]:

$$V(\vec{r}) = V_{rep}(\vec{r}) + V_{att}(\vec{r}) \tag{3.1}$$

To calculate the actual interaction potential of a surface with the He atom, a summation over all two-body potentials between the He atom and the atoms of the surface has to be carried out. Thereby the potentials are assumed to be identical to the corresponding gas phase two-body potentials. This method is accurate for solids with a closed-shell character (e.g. ionic crystals) but should be treated with care in the case of semiconductors and metals since the bonding is partly mediated by conduction electrons in the latter case[43,44].
Furthermore, even for the gas phase, two-body potentials are not known with high accuracy for most systems and the effective two-body potentials have to be estimated using an approximate model[3,42]. A popular choice for this two-body potential is the Lennard-Jones 12-6 potential:

$$v_{LJ} = 4\epsilon \left[\left(\frac{\sigma}{r}\right)^{12} - \left(\frac{\sigma}{r}\right)^{6} \right] \tag{3.2}$$

where r is the distance between the particles, ϵ is the well depth of the potential and σ is the distance at which the potential equals zero[9].
The resulting atom-surface potential that is achieved after summation over all individual Lennard-Jones potentials in the continuum limit, is the 9-3 potential which will be described in section 3.6.4.
Figure 3.2 shows an illustration of the He-LiF(001) interaction potential. In general the potential energy depends on the lateral position at which the impinging He atom approaches the surface. The potential as a function of the distance normal to the surface is shown for two extreme cases in figure 3.2(b): Case A corresponds to a He atom approaching on-top of a surface atom, whereas case B accounts for an approach on a bridging site between two surface atoms.

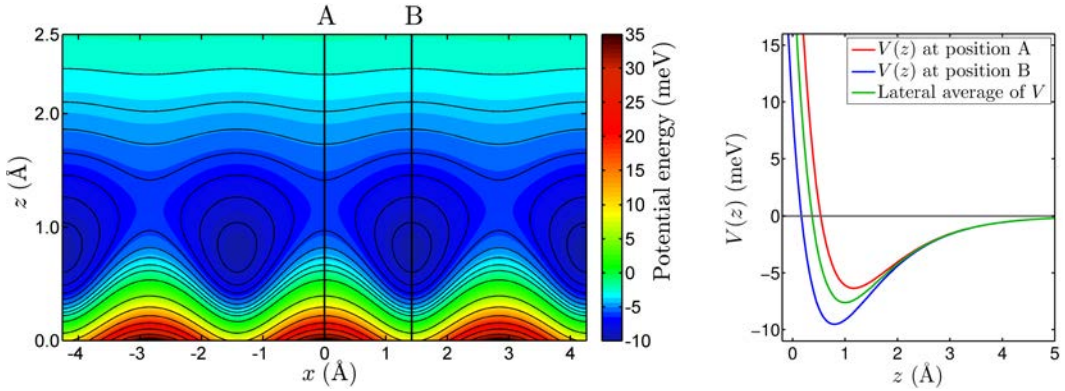

(a) Contour plot of the equipotential lines for the He-LiF(001) interaction potential.

(b) Potential energy vs. distance z normal to the surface.

Figure 3.2.: Visualization of the He-LiF(001) interaction potential (Lennard-Jones-Devonshire potential) according to the parameters determined by Celli et al.[45]. The left-hand graph shows a contour plot of the potential with z being the direction normal to the surface. The right hand graph shows the potential as a function of z for the two different positions corresponding to A and B in the left part. The laterally averaged potential is also shown.

Consequently, the potential follows the periodicity of the surface which can be seen from the contour plot in figure 3.2(a). This fact suggests that the potential $V(\vec{r})$ can be written according to the Fourier series:

$$V(\vec{r}) = V(\vec{R}, z) = \sum_{\vec{G}} V_{\vec{G}}(z) \cdot e^{i\vec{G}\vec{R}} \tag{3.3}$$

where the sum is taken over $\vec{G}$, the surface reciprocal lattice vectors[3,29,42]. At this point the discussion about the atom-surface potential is finished, though further aspects of the atom-surface potential will be addressed in section 3.6.

3.2. Elastic Scattering of He on Surfaces

A scattering process with Helium atoms is considered elastic if the energy does not change ($E_i = E_f$). Given the diffraction on a periodic structure the Laue equations give three conditions for incident waves to be diffracted by a crystal lattice. Thus the change in the momentum of the incident and the final beam has to be equal to a reciprocal lattice vector $\vec{g}$: $\Delta\vec{k} = \vec{g}$. Together this yields 4 conditions that have to be fulfilled for diffraction peaks in elastic scattering:[9,46]

$$E_i = E_f \tag{3.4}$$

$$\vec{k}_f = \vec{k}_i + \vec{g} \tag{3.5}$$

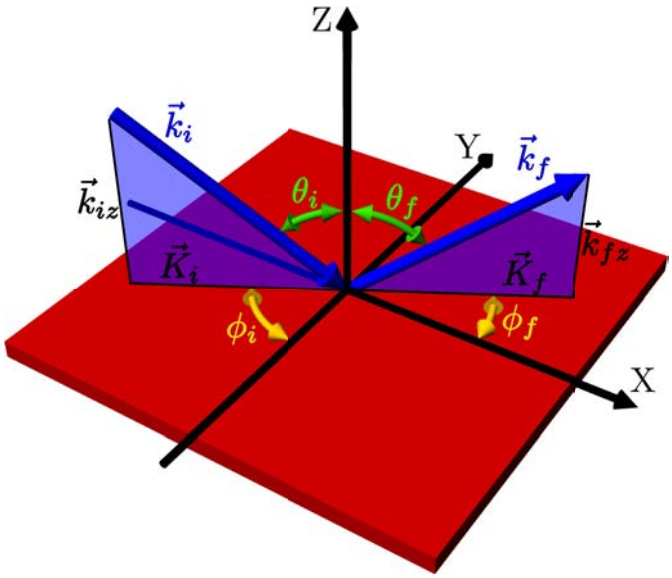

Figure 3.3.: Geometry in elastic HAS experiments: $\vec{k}_i$, $\vec{k}_f$...incoming and outgoing wavevectors, $\vec{K}_i$, $\vec{K}_f$... wavevector component parallel to the surface, θ_i, θ_f... polar angle and ϕ_i, ϕ_f... azimuthal angle.

The usual convention for the notation of directions, vectors and angles in diffraction geometries is shown in figure 3.3. The surface lies in the x - y - plane and the normal z is perpendicular to the surface. The wavevector describing the incoming beam of particles is named $\vec{k}_i$ and the outgoing one $\vec{k}_f$. Since He scattering is purely surface sensitive, the wave vectors are usually separated into wave vectors with components parallel to the surface (designated by capital letters) and components perpendicular to the surface (designated by subscript z):[9,47]

$$\vec{k}_i = (\vec{K}_i, k_{iz}), \quad \vec{k}_f = (\vec{K}_f, k_{fz}) \tag{3.6}$$

The polar angles θ_i, θ_f are defined by the incoming wavevector and z and by the outgoing wavevector and z, respectively. $\vec{K}_i$ and $\vec{K}_f$ assign the azimuthal angles ϕ_i, ϕ_f together with the x-axis. The azimuthal angle can be changed by rotating the surface along the z-axis. Furthermore, diffraction processes that lie within the plane defined by the incoming wavevector and the z-axis are called *in plane* diffraction which will always be the case for the experiments described in this work.
Using this notation the Laue condition 3.5 for scattering on a surface yields the famous Bragg condition:[9,46]

$$\Delta\vec{K} = \vec{K}_f - \vec{K}_i = \vec{G}_{hk} \tag{3.7}$$

whereupon $\vec{G}_{h,k}$ is a reciprocal surface vector with the Miller-indices h and k. The

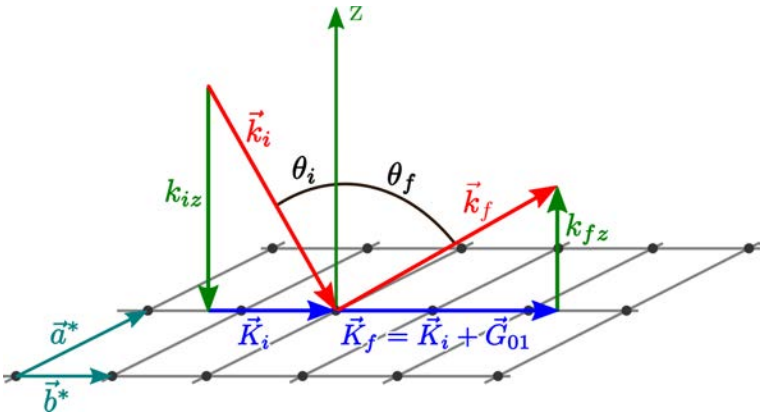

Figure 3.4.: Example of an elastic scattering process: The Bragg condition 3.7 is fulfilled for $\vec{G}_{hk} = \vec{G}_{01}$. Hence $\vec{K}_f = \vec{K}_i + \vec{G}_{01}$.

conservation of energy together with equation 2.23 yields:

$$\Delta E = E_f - E_i = \frac{\hbar^2}{2m}\left(\vec{k}_f^2 - \vec{k}_i^2\right) = 0 \quad \Rightarrow \quad \vec{k}_f^2 = \vec{k}_i^2 \tag{3.8}$$

where m is the mass of the He atom. For elastic *in plane* diffraction, the momentum transfer parallel to the surface ΔK may be expressed using the incoming wavevector $\vec{k}_i$ and the initial and final scattering angle θ_i and θ_f (see figure 3.3 and 3.6):[9,47]

$$\Delta K\left(\theta_i\right) = \left|\vec{k}_i\right|\left(\sin\theta_f - \sin\theta_i\right) = 2\left|\vec{k}_i\right| \cdot \cos\left(\frac{\theta_{SD}}{2}\right) \cdot \sin\left(\theta_i - \frac{\theta_{SD}}{2}\right) \tag{3.9}$$

with $\theta_{SD} = \theta_i + \theta_f$, the fixed source-detector angle. Combining equation 3.9 and the Bragg condition 3.7 yields:

$$\theta_i = \frac{\theta_{SD}}{2} - \arcsin\left[\frac{G_{hk}}{2 \cdot k_i \cdot \cos\left(\frac{\theta_{SD}}{2}\right)}\right] \tag{3.10}$$

This equation gives the initial scattering angle θ_i for a diffraction peak corresponding to the reciprocal lattice vector G_{hk}. Hence it may be used to calculate the position of diffraction peaks (h, k) for a given surface structure and incoming wavevector k_i. On the other hand, if the surface structure is unknown one can determine G_{hk} from the experimentally measured diffraction peak at θ_i.

3.2.1. The Ewald Sphere Construction

The well known Ewald construction can be adapted for the two-dimensional geometry given by the surface. Therefore a 2D lattice can be considered as a 3D lattice with infinite periodicity in the direction perpendicular to the surface, i.e.

for the corresponding lattice vector $\vec{c}$ holds: $|\vec{c}\,| \to \infty$. In reciprocal space this yields to $|\vec{c}^*| \to 0$. Hence the reciprocal lattice points along the surface normal are infinitely dense giving rise to the formation of lattice rods. The intersection points of these rods with the Ewald sphere define the scattered wave vectors for which diffraction occurs[17].
In other words, the restriction of the third Laue condition (along the surface normal) is relaxed: In the 3D case there are discrete reciprocal lattice points rather than rods in the 2D case, which is the source of the third Laue condition for scattering on a 3D solid[1].

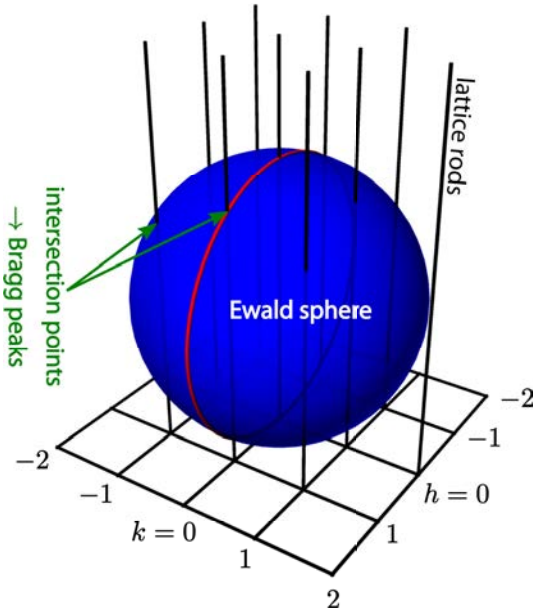

Figure 3.5.: Example of the Ewald sphere for diffraction from a square lattice. The intersection points of the lattice rods with the Ewald sphere define the scattered wave vectors for which diffraction occurs

In figure 3.5 the construction of the Ewald sphere for scattering on a 2D lattice is shown. Usually, in a typical elastic HAS experiment the angular distribution of the diffracted beam at different angles θ_i (see figure 3.3) is determined which gives rise to a one-dimensional diffraction image. Therefore the Ewald sphere is often simplified to the construction of a circle corresponding to an angular scan along a certain crystallographic direction. In figure 3.5 this would correspond to the red circle for a scan along the $\langle 10 \rangle$ direction.

The left graph in figure 3.6 illustrates an example for the construction of such a circle. The incoming angle θ_i according to the scattering geometry is given by the wavevector $\vec{k}_i$ and the surface normal whereupon the endpoint of $\vec{k}_i$ lies at the intersection of the surface with the 00 lattice rod. According to the conservation

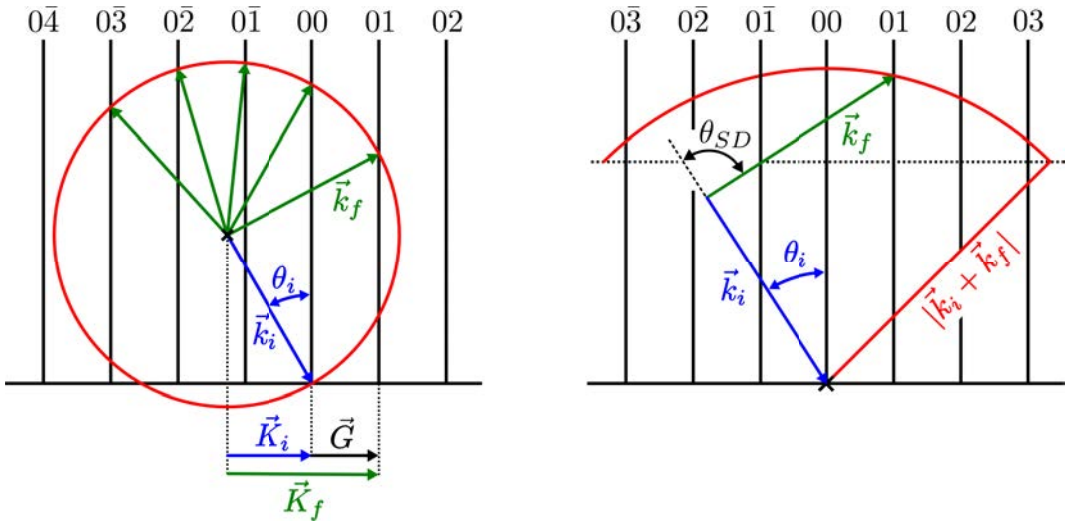

Figure 3.6.: The Ewald construction for diffraction from surfaces. On the left hand side the conventional Ewald sphere construction is shown for a fixed angle of incidence θ_i. On the right hand side the modified Ewald sphere construction for a fixed source detector angle θ_{SD}, which is the case in our apparatus, is shown.

of energy (equation 3.8), $|\vec{k}_i| = |\vec{k}_f|$ holds which corresponds to a circle of radius $|\vec{k}_i|$ around the origin of $\vec{k}_i$. Possible diffraction peaks are given by the Bragg condition 3.7: At the intersection points of the circle with the reciprocal lattice rods in the graphical representation.
The scattering geometry in the apparatus used for this work is somewhat different since the source-detector angle, $\theta_{SD} = \theta_i + \theta_f$, is kept constant and the surface is rotated. The right graph in figure 3.6 shows the graphical representation for this situation. Again, conservation of energy gives rise to $|\vec{k}_i| = |\vec{k}_f|$ but since θ_{SD} = constant, the wavevectors $\vec{k}_i$ and $\vec{k}_f$ enclose a fixed angle. Thus, if the incoming angle θ_i is changed, the incoming and outgoing angle have to be rotated simultaneously. This corresponds to a circle of radius $|\vec{k}_i + \vec{k}_f|$ around the endpoint of $\vec{k}_i$. The direction for diffraction peaks is again given by the Bragg condition which corresponds to intersection points of the circle with the reciprocal lattice rods. Note that only a part of the circle is drawn in figure 3.6 since θ_i can only be varied within $0 < \theta_i < 90°$.

3.3. Inelastic Scattering of He on Surfaces

In the case of inelastic scattering the impinging particle interacts with surface phonons. As described in section 2.5.4 phonons are quantized modes of crystal lattice vibrations and surface phonons are vibrational modes localized at the

surface.

3.3.1. Classification of Surface Phonons

Surface phonon modes are usually classified according to their polarization, very much in the same manner as for bulk modes. The polarization is referred to the sagittal plane which is defined by the incident wave vector $\vec{k}_i$ and the surface normal[4,10,14].

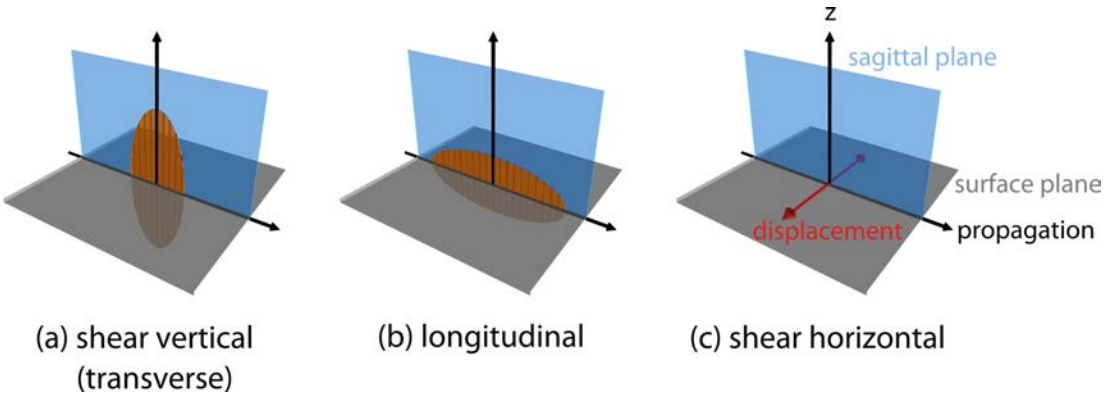

Figure 3.7.: The three types of polarization of surface phonon modes[14]:
(a) transverse: Polarization parallel to the sagittal plane, mainly perpendicular to the propagation direction. (b) longitudinal: Polarization parallel to the sagittal plane, mainly in propagation direction. (c) shear horizontal: Polarization within the surface plane.

Each surface branch reflects approximately the polarization of its "parent" bulk band from which it originates, although it may be strongly affected by symmetry constraints at the surface. Due to these symmetry constraints, surface phonons propagating in a high-symmetry direction must either be polarized in the sagittal plane or parallel to the surface plane (in the plane perpendicular to the sagittal plane)[4,10,14]. Figure 3.7 shows the classification for these surface modes.
Surface phonon modes that are polarized within the surface plane (case (c) in figure 3.7) are called shear horizontal (SH) since they are perfectly transverse and parallel to the surface plane. The modes that are oscillating in the sagittal plane are called sagittal (case (a) and (b) in figure 3.7). These modes usually exhibit shear vertical (transverse) and longitudinal components of the displacements giving rise to an elliptical polarization. Their name indicates which is the dominant component in the sagittal plane[4,14]. Hence they are either designated as quasi-transverse (shear vertical, ∼SV) corresponding to case (a) of figure 3.7 or as quasi-longitudinal (∼L) illustrated in case (b) of figure 3.7.

Only at high symmetry points of the reciprocal space these sagittal modes recover an exactly linear polarization. This is the case either at the origin or the boundaries of the Brillouin zone, where the group velocity of the sagittal modes vanishes. The Rayleigh wave which was already described in section 2.5.4 has a quasi-transverse (∼SV) polarization in the sagittal plane. However, the polarization of the Rayleigh wave remains elliptical even at the $\overline{\Gamma}$-point which is consistent with the finite value of the group velocity at this point. Furthermore, there can be surface phonons with optical or acoustic characteristics for each of the above mentioned polarizations[4,10,14].
The experiments presented in this work have always been performed for in plane scattering along a high-symmetry direction of the crystal. In this case the sagittal plane coincides with the scattering plane. If the sagittal plane is also a mirror plane for the crystal, SH modes cannot be excited because they are anti-symmetric with respect to the sagittal plane. In this scattering geometry the incident He-atoms can only couple with phonons that exhibit a displacement field which is symmetric with respect to the sagittal plane[4,10].

3.3.2. Measuring Surface Phonons by means of TOF

Since the interaction with surface phonons includes energy transfer to or from the surface it is important to gain information about the energy of the scattered helium atoms. Therefor a chopped beam allows to measure differences in the time-of-flight of scattered helium atoms (see section 2.4). Therewith the energy exchange between helium atoms and the surface can be determined to identify surface phonons.
In the event of inelastic scattering the He-atom looses or gains energy via energy transfer to or from the surface phonons. However, conservation of energy and momentum still holds if the whole system is considered: The energy and momentum exchange due to the phonon have to be taken into account. For simplification only single phonon events (in each inelastic scattering event only one phonon is created or annihilated) and in plane inelastic scattering will be considered in this work. Thus conservation of energy becomes:

$$E_f = E_i + \Delta E = E_i \pm \hbar\omega \tag{3.11}$$

where $\hbar\omega$ states the energy of a phonon with the frequency ω. $+\hbar\omega$ holds for the annihilation of a phonon and $-\hbar\omega$ for the creation[3,11,48,49]. The alteration of the Ewald construction due to the creation or annihilation of phonons is shown in the right hand graph of figure 3.8. Using equation 2.23 the conservation of energy can

also be written as:

$$\frac{\hbar^2}{2m}k_f^2 = \frac{\hbar^2}{2m}k_i^2 \pm \hbar\omega \tag{3.12}$$

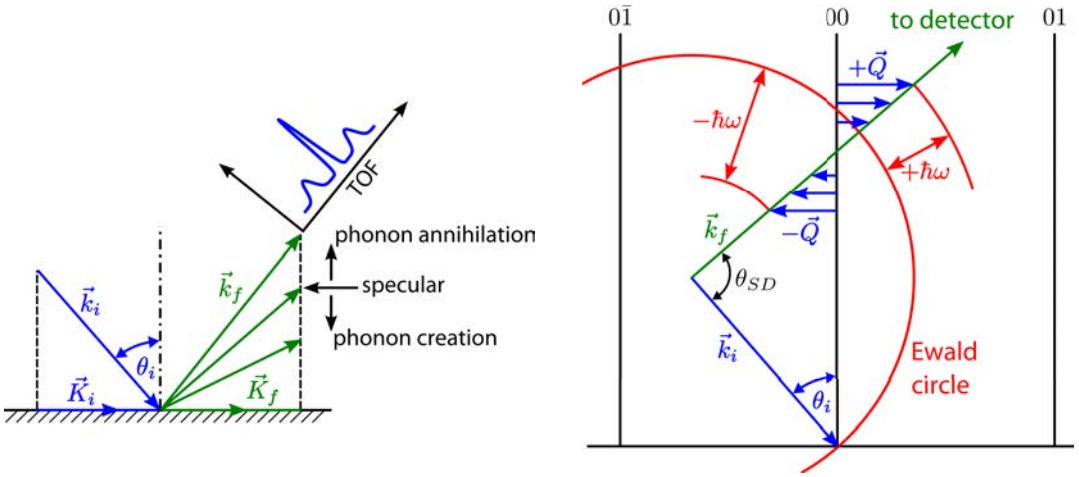

(a) Schematic illustration of elastic (specular peak) and inelastic scattering events.

(b) Ewald sphere for inelastic scattering from a surface with $G_{hk} = 0$.

Figure 3.8.: The left hand graph shows a schematic illustration of elastic and inelastic scattering events. The right hand graph shows the construction of the Ewald sphere for an inelastic process.

The conservation of parallel momentum is given by

$$\vec{K}_f = \vec{K}_i + \Delta\vec{K} \tag{3.13}$$

where $\Delta\vec{K}$ describes the momentum change of the helium atoms by the scattering process[4,11]. For scattering in the plane of the incident beam and the surface normal it simplifies to:

$$k_f \cdot \sin(\theta_f) = k_i \cdot \sin(\theta_i) + \Delta K \tag{3.14}$$

Combining both conservation of energy 3.12 and momentum 3.14 gives the energy ΔE of a phonon:

$$\Delta E = \hbar\omega(\Delta K) = \frac{\hbar^2}{2\ m \cdot \sin^2(\theta_f)}\Big[k_i \cdot \sin(\theta_i) + \Delta K\Big]^2 - E_i$$

Or in the more neatly arranged form:

$$\frac{\Delta E}{E_i} + 1 = \frac{\sin^2\theta_i}{\sin^2\theta_f}\left(1 + \frac{\Delta K}{K_i}\right)^2 \tag{3.15}$$

Equation 3.15 is the so-called scancurve for inelastic scattering of atoms by a surface. It determines the experimentally accessible phonon energy ΔE and momentum range ΔK for a given angle θ_i and beam energy E_i (see figure 3.9). To access different phonon momentum transfers ΔK the incident angle θ_i has to be varied. By varying θ_i it is possible to cover a wide range of ΔK which is shown in figure 3.10. This in turn allows the determination of the dispersion relation over the entire Brillouin zone[4,11].

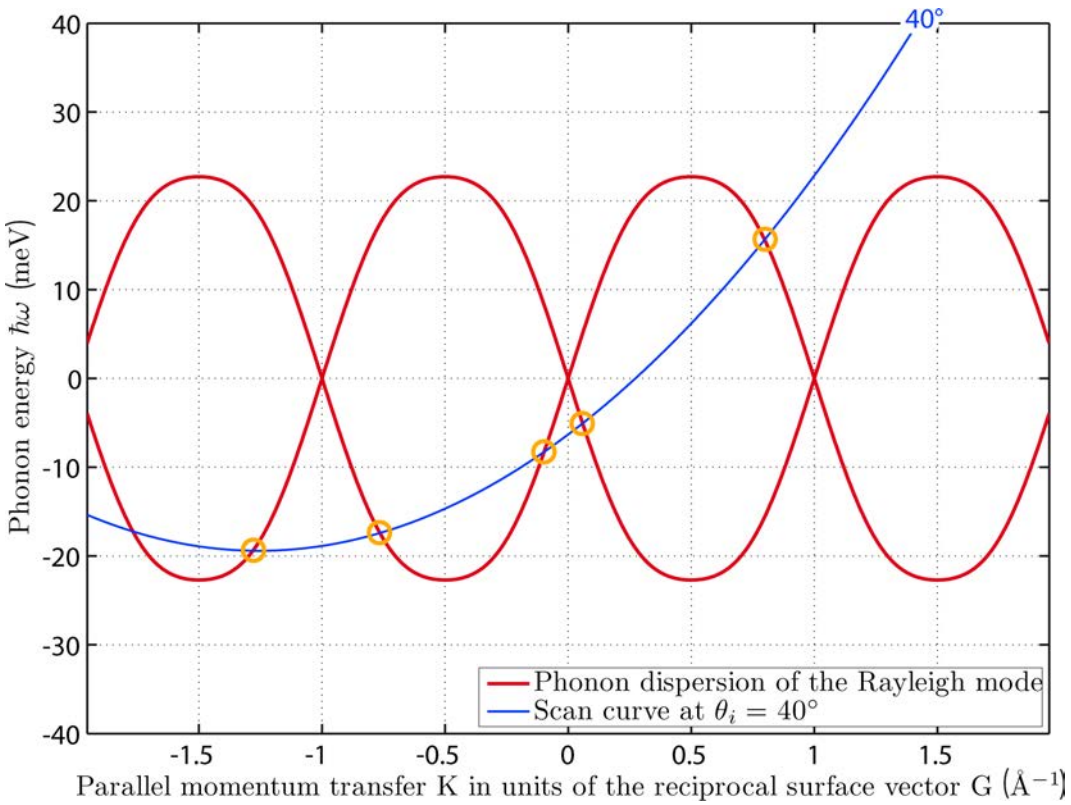

Figure 3.9.: Scan curve for scattering of He from LiF(001) along the ⟨100⟩ direction. The parabolic scan curve (according to equation 3.15 with a nozzle Temperature of 90 K and $\theta_i = 40°$) is superimposed on the phonon dispersion curves. The dispersion curves are plotted according to Brusdeylins et al.[48]. Each intersection of the scan curve with the phonon dispersion curve (highlighted by the orange circles) may give rise to an inelastic peak in the TOF measurement.

Inelastic peaks can be expected for positive as well as negative ΔK and ΔE: ΔE designates whether phonons are created or annihilated whereas the momentum exchange ΔK describes scattering in the forward (parallel to $\vec{K}_i$) or backward direction[11]. The resulting four possible events occur in different quadrants of the (ΔK,ΔE)-plane which is shown in figure 3.11.
According to this, phonon events are sometimes abbreviated using the following

notation: The energy exchange is labeled with A for annihilation and C for creation and the momentum exchange with F for forward and B for backward scattering. The phonon event may then be labeled as AF, AB, CF or CB[50].

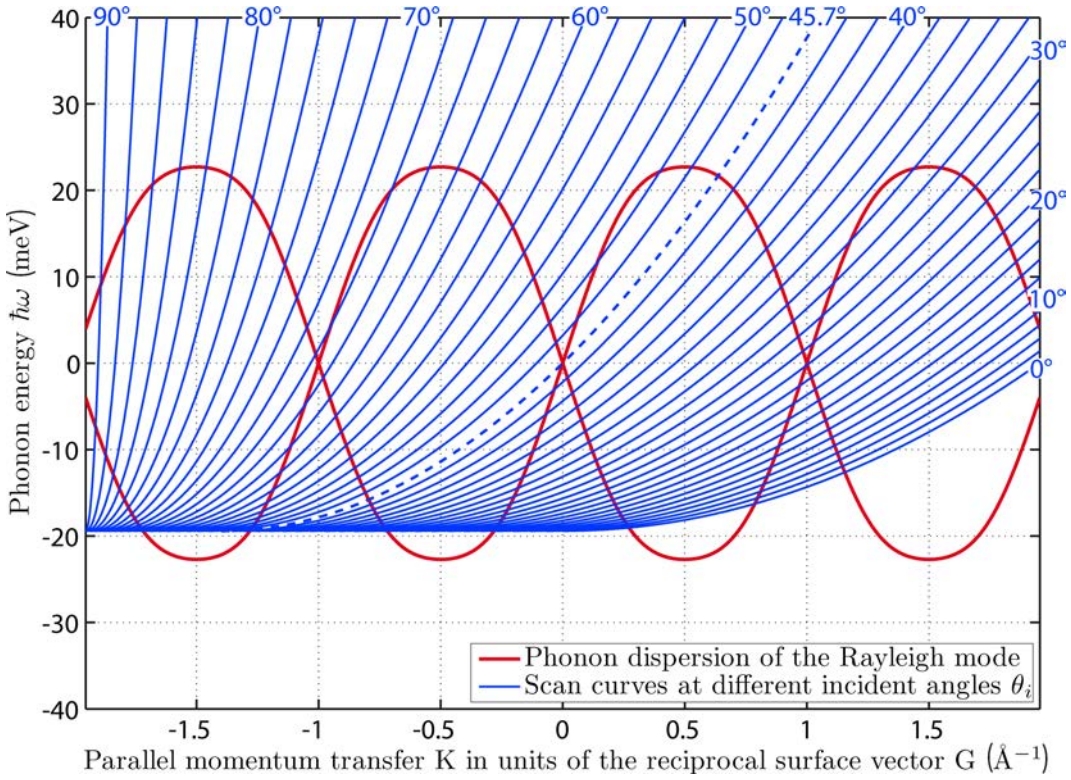

Figure 3.10.: Scan curves for scattering of He from LiF(001) along the ⟨100⟩ direction. The right branches of the scan curves with a nozzle temperature of 90 K and θ_i varying from 0° to 90° are again superimposed on the phonon dispersion curves determined by Brusdeylins et al.[48]

The common presentation of phonons is the dispersion curve where the phonon energy $\hbar\omega(\vec{Q})$ is plotted over the phonon wave vector $\vec{Q}$ as described in section 2.5. For this purpose the phonon energy is determined by time of flight measurements which will be described in the following section 3.3.3. The phonon wave vector $\vec{Q}$ or parallel momentum transfer ($\Delta\vec{K} = \vec{G}_{hk} + \vec{Q}$ for single phonon events) is then determined using the scan curve 3.15 rearranged in the following way:[7]

$$\frac{\Delta K}{K_i} = \sqrt{\frac{\sin^2\theta_f}{\sin^2\theta_i}\left(\frac{\Delta E}{E_i} + 1\right)} - 1 \tag{3.16}$$

At this point it shall be noted that these inelastic events appear also in elastic HAS measurements i.e. measurements that are not energy-analyzed. In particular, the background in the angular distribution which appears between the Bragg peaks

is caused by inelastically scattered atoms. At each incident angle, all phonons which are met by the scan curve contribute to the inelastic background in this direction[14].

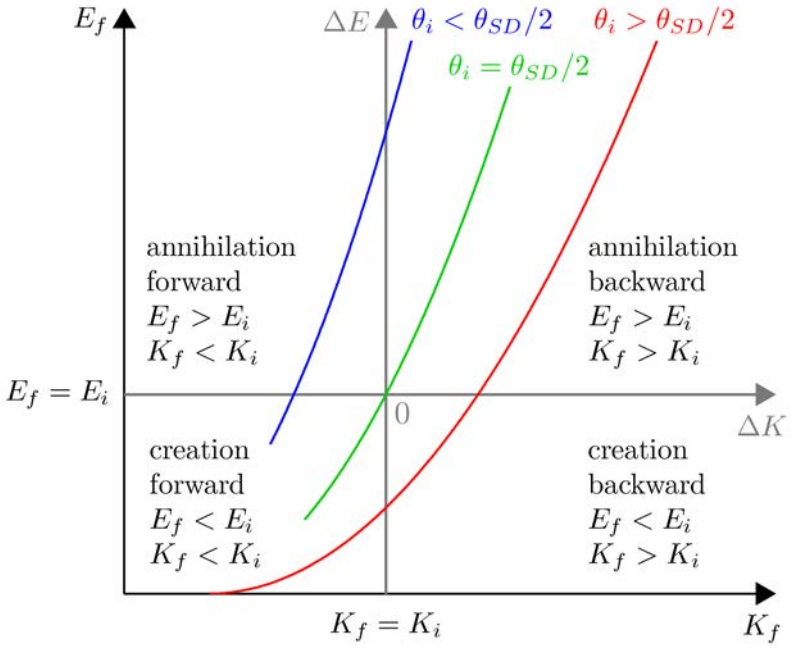

Figure 3.11.: Classification of inelastic scattering events according to their energy exchange ΔE and momentum exchange ΔK with respect to the incident atom with E_i and K_i. The (ΔK,ΔE)-plane is divided into four quadrants for phonon creation and annihilation processes in the forward or backward direction. The scan curves according to equation 3.15 are crossing through three of the four quadrants except the scan curve for the specular peak ($\theta_i = \theta_{SD}/2$) which passes through the origin.

3.3.3. From TOF to Phonon Energies

The phonon energies ΔE can be determined from the TOF spectra. The energy of a particle can easily be calculated for a given length and the corresponding time-of-flight TOF according to its kinetic energy:

$$E = \frac{m}{2}\left(\frac{\text{length}}{\text{TOF}}\right)^2 \tag{3.17}$$

The energy of a phonon is given via equation 3.11: $\Delta E = E_f - E_i$ where E_i is the energy of the incident beam and equals the energy of elastically scattered helium atoms. Hence one can use the elastic time of flight t_e (from chopper to detector) to calculate E_i. For inelastically scattered atoms the important distance is the target detector distance L_{TD} since the particles gain or loose energy after interaction with the surface (target):

$$E_f = \frac{m}{2}\left(\frac{L_{TD}}{t_{TD}}\right)^2 \tag{3.18}$$

where t_{TD} is the flight time of the inelastically scattered particles from the target to detector. t_{TD} can be readily obtained considering the fact the velocity of the He atoms traveling along the the chopper to detector distance L_{CT} is given by the elastic TOF t_e via:[11]

$$t_{TD} = t_{CD} - \frac{L_{CT}}{L_{CD}} t_e \tag{3.19}$$

Thus, if the HAS apparatus lengths L_{CD} (chopper to detector) and L_{TD} (target to detector) are known, the TOF spectra can be transformed into energy spectra by:[11]

$$\Delta E = E_f - E_i = E_i \left[\left(\frac{\frac{L_{TD}}{L_{CD}} t_e}{t_{CD} - \frac{L_{CT}}{L_{CD}} t_e} \right)^2 - 1 \right]. \tag{3.20}$$

The relation between ΔE and the TOF according to 3.20 is non-linear and hence introduces a distortion to the peak heights[11,50]. This non-linearity is clearly seen from figure 3.12 which shows a TOF spectrum and its transformation to the energy scale. The x-axis of the energy spectrum is plotted in reverse direction to maintain the same left-to-right ordering of the peaks with respect to the TOF spectrum.

In order to compensate for the non-linearity of the energy scale the intensity of the measured spectrum must be multiplied by the corresponding Jacobian determinant:[11,50]

$$\left| \frac{\mathrm{d}\, t_{TD}}{\mathrm{d}\, \Delta E} \right| = \frac{t_{TD}^3}{m \cdot L_{TD}^2} \tag{3.21}$$

The Jacobian scaling changes the height as well as the width of the peaks. However, it is necessary to maintain the overall intensity of the spectrum. The Jacobian scaling has been included in figure 3.12. On the annihilation side, peaks become wider and lower, whereas on the creation side the peaks are smaller and higher. Therefore the scaling also increases the height of experimental noise on the creation side, making it difficult to distinguish peaks from noise in the creation region with large energy loss[11,14,50].

This effect can be partly overcome by a simple approach first suggested by Bracco[51]. Usually noise in the TOF spectra is suppressed using the moving average method whereupon the sample width equals a quarter of the FWHM of the incident He-beam. However, on the energy scale the distance between two data points decreases with decreasing ΔE (the further going to the region of extreme creation energy loss in figure 3.12). Hence Bracco suggested to increase the sample width for the averaging as the creation side is approached.

Furthermore, the described non-linearity gives rise to another effect: Annihilation events are more likely observed than creation events since proportionally more intensity is compressed into a given TOF channel on the annihilation side[50].

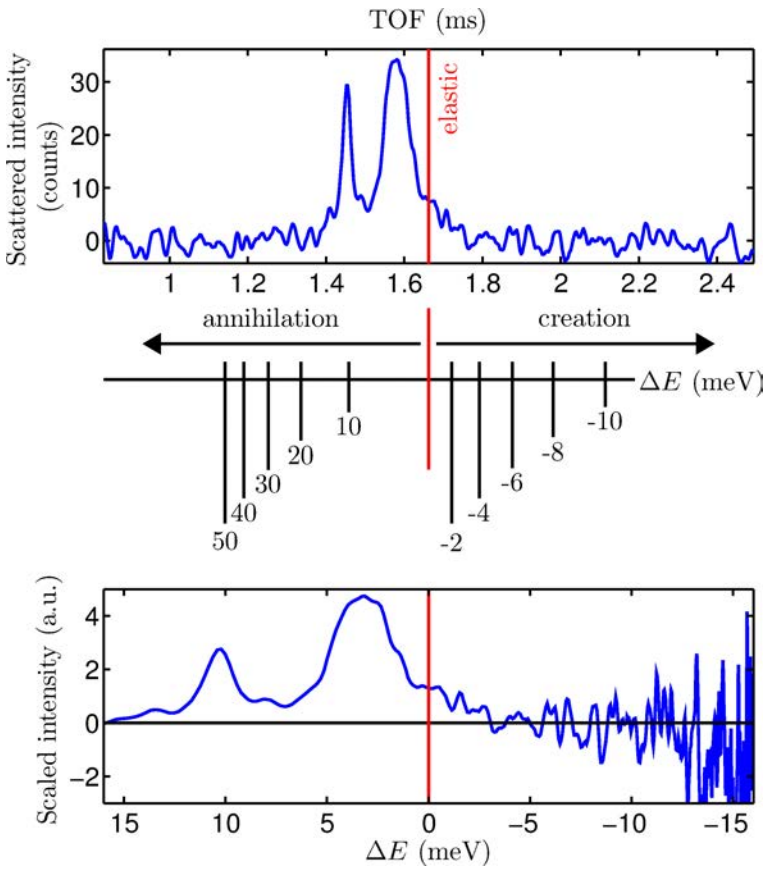

Figure 3.12.: Transformation of a TOF spectrum (upper graph) to the energy scale (lower graph) according to equation 3.20 and 3.21. The non-linearity of the energy transformation (illustrated in the middle graph) is compensated using the corresponding Jacobian. The Jacobian scaling increases the height of experimental noise on the creation side. The spectra show an inelastic measurement for LiF(001) along the $\langle 11 \rangle$ azimuth with $E_i = 20.4$ meV and $\theta_i = 27.5°$.

Finally, the width of the TOF peaks is governed by another effect: Strictly speaking, the scan curve is not a true line curve but has a finite width given by the velocity and angular spread of the He beam. Therefore the width of the TOF peaks should increase with increasing angle between the scan curve and the dispersion curve[11,50].
The extreme case is a tangency of the scan curve and the dispersion curve known as the kinematical focusing effect. This kinematical focusing effect can cause an intensity enhancement in the TOF spectrum at the kinematic focusing angle. At such a tangency point an extended section of the dispersion curve is sampled by the inelastic scattering and a broad but intense peak appears in the TOF spectrum[11,52,53].
Furthermore, it may even cause maxima in the angular distribution: The uniform

inelastic background is enhanced at the kinematic focusing angle since a larger fraction of He atoms is scattered inelastically at this position. These maxima exhibit typically an asymmetric wedge-like shape in the angular distribution. When the intersection between the scan curve and the dispersion curve approaches the tangency condition a smooth rise is visible in the angular distribution followed by an abrupt decrease in intensity at an angle where the scan curve does not intersect the dispersion curve any more[52,53].
In the angular distribution the features caused by kinematical focusing are often obscured by the tails of intense diffraction peaks and bound state resonance features (section 3.6). However, these disturbances can be reduced if the crystal is rotated to azimuthal angles a few degrees away from the high symmetry direction. This reduces the diffraction peak intensity but hardly affects the phonon dispersion and the kinematical focusing features[14,52,53].

3.3.4. The Weare Criterion and Thermal Population of Phonons

The analysis of TOF spectra, as it has been described so far, is based on the predominance of single phonon with respect to multi phonon processes. Descriptions on the analysis of multiple phonon inelastic scattering can be found in the literature[54]. In general, single phonon processes give rise to sharp peaks in the TOF-spectra while multi phonon processes produce broad structures. A criterion for the predominance of one phonon processes according to Weare is:[11,55]

$$\frac{m}{M}\frac{E_{iz}}{k_B\theta_D}\frac{T_S}{\theta_D} \lesssim 0.01 \tag{3.22}$$

where M is the mass of the surface atom, T_S the surface temperature, θ_D the surface Debye temperature and E_{iz} the energy perpendicular to the surface. The fulfillment of this criterion mainly depends on the thermal population of the surface phonons and the kinetic energy of the incident beam[11].
The occupation number for a given phonon energy is determined by the Bose-statistics:[19,56]

$$n\left(\hbar\omega\right) = \frac{1}{e^{\hbar\omega/k_BT} - 1} \tag{3.23}$$

The probability that either a phonon annihilation or creation occurs is then given by the Bose-factors $n(\hbar\omega)$ and $n(\hbar\omega) + 1$ respectively[11,14]. In figure 3.13 these Bose-factors are plotted versus the surface temperature.
According to this, there exists an ideal surface temperature T_S to observe phonon annihilation processes. At very low temperatures the thermal population of phonon states decreases giving rise to a declining amplitude of the annihilation peak.

However, if the surface temperature is too high (according to 3.22), multi phonon processes are beginning to deteriorate the sharp single-phonon peaks in the TOF signal.
On the other hand, the "freezing" of high frequency phonon modes at low temperatures does not affect the creation events. Hence their peak height is mainly determined by the deterioration due to multi-phonon events that increases steadily with increasing temperature. Therefore creation peaks are found to be sharp at low temperatures[11,50].

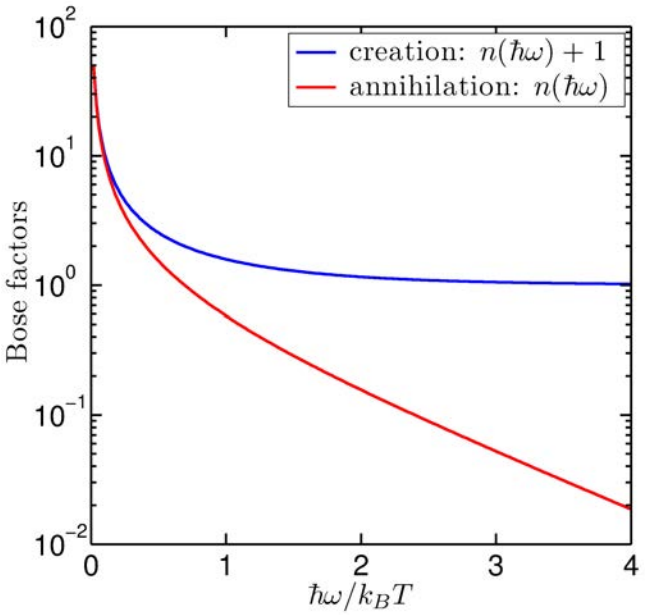

Figure 3.13.: Bose factors plotted versus the reduced inverse temperature $\hbar\omega/k_BT$. The Bose factors provide the probability for phonon creation and annihilation as a function of the surface temperature. For $T \ll \hbar\omega/k_B$ hardly any annihilation events are expected.

3.4. Calculation of Elastic Scattering Intensities

The interaction of a He atom with the surface can be described by means of an atom-surface interaction potential which has already been addressed in section 3.1. Since the He atoms are scattered by the electron distribution at the surface, a comparison of the measured diffraction peak intensities with calculations allows the determination of the surface charge distribution. However, due to the strong interaction of the He atoms with the surface electron distribution, HAS data is rather difficult to interpret[57].
Especially at low beam energies the scattering process can be described by quantum theory. According to this the diffraction of atoms from a surface can be treated by solving the Schrödinger equation[8,9,57]:

$$\left[\frac{\hbar}{2m}\nabla^2 + V(\vec{r})\right]\Psi(\vec{r}) = E\Psi(\vec{r}) \tag{3.24}$$

Due to the two-dimensional periodicity of the surface, the wavefunction $\Psi(\vec{r})$ will be of the form of Bloch waves parallel to the surface[3]:

$$\Psi(\vec{r}) = \Psi(z, \vec{R}) = e^{i\vec{K}_i\cdot\vec{R}} + \sum_{\vec{G}} e^{i\vec{G}\cdot\vec{R}}\Psi_G(z) \tag{3.25}$$

In order to solve the Schrödinger equation 3.24 a model of the atom-surface potential $V(\vec{r})$ is necessary. Thereby the turning point of a He atom scattered off the surface is determined by the locus where the atom surface potential $V(\vec{r}) = V(\vec{R}, z)$ equals the z-component of the incident energy:

$$V(\vec{R}, z) = E_{iz} \tag{3.26}$$

The solution of equation 3.26 is an equipotential surface which describes the closest approach of the He atom depending on the lateral position $\vec{R}$ (see also figure 3.2). Therefore, the position of the classical turning points follows a periodically modulated surface with constant total electron density[8].
To obtain now a complete description of the scattering process an exact solution of equation 3.24 is required. In the most general case this can be done using the close coupling method. However, under certain conditions the problem can be solved using approximate methods with a sufficient accuracy. Those methods have the advantage of less computational effort with respect to the close-coupling formalism[3,8].

3.4.1. The Hard Corrugated Wall Model

A simple approximate model of the atom-surface potential $V(\vec{r})$ is given by the hard corrugated wall (HCW)[8,9]. It describes the surface by an infinitely repulsive

barrier with a periodic corrugation according to the crystalline symmetry. Thereby the potential $V(\vec{R}, z)$ is represented as:

$$V(\vec{R}, z) = \begin{cases} 0 & \text{for } z > \xi(\vec{R}) \\ \infty & \text{for } z \leq \xi(\vec{R}) \end{cases} \tag{3.27}$$

with z representing the direction of the surface normal and $\vec{R}$ the lateral position parallel to the surface. $\xi(\vec{R})$ describes the spatial modulation of the surface that represents the surface structure and hence the periodicity given by $\vec{a}$ and $\vec{b}$ (see section 2.1). The HCW potential of a simple one-dimensional corrugation $\xi(x)$ with height h and periodicity a represented by a cosine is illustrated in figure 3.14.

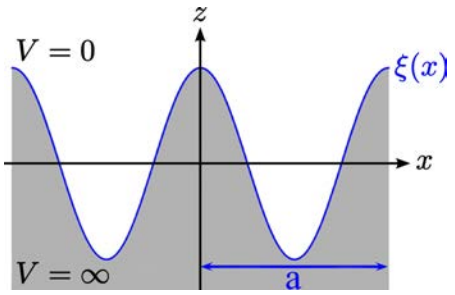

Figure 3.14.: Schematic image of the hard wall potential in one dimension: The potential represents a stationary periodic hard corrugated surface with the lattice parameter a and z being the direction perpendicular to the surface.

The function $\xi(\vec{R})$ holds the complete information that is obtainable from the surface in elastic scattering measurements. Strictly speaking $\xi(\vec{R})$ describes the spatial modulation of the surface electron density since the incoming He atoms are scattered due to the Pauli repulsion between the closed He shell and the electrons of the surface.
As a general trend, a strong modulation is expected for solids with a closed shell character (e.g. ionic crystals) whereas metallic surfaces should give rise to a rather smooth corrugation $\xi(\vec{R})$. This effect, known as the Smoluchowski effect[58], is attributed to the quasi-free valence electrons on metal surfaces which tend to smear out the electron distribution with respect to the position of the ion cores[32](see figure 3.15). To return to the problem of solving the Schrödinger equation 3.24, the atom-surface potential is approximated using the HCW-potential. Consequently, the Schrödinger equation has to fulfill the boundary condition given by 3.27: The wavefunction Ψ has to vanish as z approaches the hard corrugated wall:

$$\Psi\left[z = \xi(\vec{R}), \vec{R}\right] = 0 \tag{3.28}$$

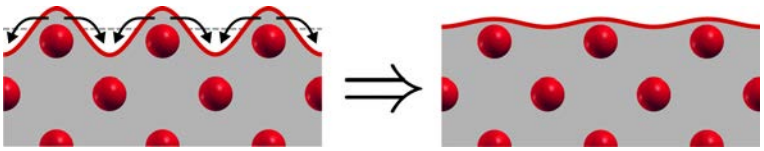

Figure 3.15.: Illustration of the Smoluchowski effect on metal surfaces: Redistribution of the quasi-free electrons gives rise to a smoothing of the electron density with respect to the sharp contour of the potential. This smoothing can be attributed to the attempt of the electrons to lower their kinetic energy[19,32].

3.4.2. The Rayleigh Ansatz

A simple procedure to calculate the diffraction peak intensities using the HCW starts with the so-called Rayleigh assumption[8]. In doing so the incoming and outgoing beams are treated as plane waves up to the surface, which is in principle only true far away from the surface. Hence the wavefunction $\Psi(z, \vec{R})$ becomes:

$$\Psi(z, \vec{R}) = e^{i\left(\vec{K}_i \vec{R} + k_{iz} \cdot z\right)} + \sum_{\vec{G}} A_{\vec{G}} \cdot e^{i\left[\left(\vec{K}_i + \vec{G}\right)\vec{R} + k_{Gz} \cdot z\right]} \tag{3.29}$$

Thereby the first term describes the incident beam and the second term describes the sum over all scattered beams corresponding to a reciprocal lattice vector $\vec{G}$. $A_{\vec{G}}$ are the scattering amplitudes for each reciprocal lattice vector $\vec{G}$. k_{Gz} is the z-component of the scattered/final wavevector.
By applying the boundary condition $\Psi[z = \xi(\vec{R}), \vec{R}] \equiv 0$ according to 3.27 we obtain for equation 3.29:

$$\sum_{\vec{G}} A_{\vec{G}} \cdot e^{i\left[\vec{G} \cdot \vec{R} + k_{Gz} \cdot \xi(\vec{R})\right]} = -e^{i\left[k_{iz} \cdot \xi(\vec{R})\right]} \tag{3.30}$$

Hence if the periodic surface corrugation $\xi(\vec{R})$ is known, the scattering amplitudes $A_{\vec{G}}$ can be directly obtained from these equation. Therefore equation 3.30 must be fulfilled for every point $\vec{R}$ in the unit cell which can be solved using different approaches that will be described in the following.
However, it should be noted that the convergence of the Rayleigh assumption is limited to a corrugation amplitude of $0.188a$ in the two-dimensional case with a being the lattice constant[9]. Though it has been shown that alternative methods give rise to a validity of the Rayleigh assumption much beyond this limit[59].

3.4.3. The Eikonal Approximation

By multiplying both sides of equation 3.30 by $\exp\{-i[\vec{G}' \cdot \vec{R} + k_{G'z} \cdot \xi(\vec{R})]\}$ and integration over the unit cell we obtain a matrix equation:

$$\begin{aligned} \sum_{\vec{G}} M_{\vec{G}\vec{G}'} &= A^0_{\vec{G}'} \\ M_{\vec{G}\vec{G}'} &= \frac{1}{S}\int_{u.c.} e^{i\left[(\vec{G}-\vec{G}')\vec{R}+(k_{Gz}-k_{G'z})\xi(\vec{R})\right]} d\vec{R} \\ A^0_{\vec{G}'} &= -\frac{1}{S}\int_{u.c.} e^{-i\left[\vec{G}'\vec{R}+(k_{G'z}-k_{iz})\xi(\vec{R})\right]} d\vec{R} \end{aligned} \tag{3.31}$$

where the integral is carried out over the unit cell ($u.c.$) and S denotes the area of the unit cell. In the case of the so-called eikonal approximation, the off-diagonal elements of $M_{\vec{G}\vec{G}'}$ are neglected and since the diagonal elements are unity, $A_{\vec{G}} = A^0_{\vec{G}'}$ [8,60]. Hence the scattering amplitudes can easily be calculated by evaluating the integral:

$$A_{\vec{G}} = -\frac{1}{S}\int_{u.c.} e^{-i\left[\vec{G}\vec{R}+(k_{Gz}-k_{iz})\xi(\vec{R})\right]} d\vec{R} \tag{3.32}$$

The eikonal approximation holds under the condition that the corrugation function $\xi(\vec{R})$ is smooth i.e. the corrugation height has to be smaller than $0.1a$. Furthermore, the angle of incidence must be small, so that all mainly contributing diffraction beams are far away from grazing incidence [8,9].

For some simple functions $\xi(\vec{R})$ the integration of equation 3.32 can be carried out analytically, whereas in the case of more complicated functions this has to be done numerically. However, the integration can also be replaced by a summation where $\xi(\vec{R})$ is evaluated at a set of special points $\vec{R}_i$ within the unit cell. [61]. For a periodic function $F(\vec{R})$ over the unit cell the integration can be replaced by a summation for these special points:

$$\int F(\vec{R}) d\vec{R} = \frac{1}{N}\sum_i F(\vec{R}_i) \tag{3.33}$$

Methods for the choice of these points can be found in the literature [61–63].

A drawback of the eikonal approximation is that it does not include multiple scattering events [8]. Hence the introduced approximation corresponds to a neglect of the contribution of evanescent waves ($k^2_{Gz} < 0$).

However, especially for large corrugation amplitudes and at grazing incidence angles (large θ_i) multiple scattering becomes important: A part of the incoming or outgoing beams is shadowed by the hard wall potential [57]. An example of such a multiple scattering event is illustrated in figure 3.16. Yet another approximative method which includes the contribution of these evanescent waves is the GR method.

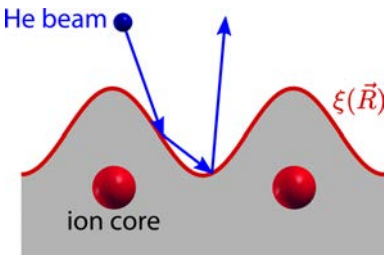

Figure 3.16.: Illustration of a multiple scattering event within the hard corrugated wall model.

3.4.4. The GR Method

The GR method is also based on the Rayleigh assumption. Starting again with equation 3.30, both sides are multiplied with $\exp[ik_{iz} \cdot \xi(\vec{R})]$ which gives rise to a matrix equation:

$$\begin{aligned} \sum_{\vec{G}} A_{\vec{G}} M_{\vec{G}\vec{R}} &= -1 \\ M_{\vec{G}\vec{R}} &= e^{i\left[(k_{Gz}-k_{iz})\xi(\vec{R})+\vec{G}\cdot\vec{R}\right]} \end{aligned} \tag{3.34}$$

which must be satisfied for every point $\vec{R}$ within the unit cell[8,9]. The principle of the GR method is to solve equation 3.34 for a set of n linear equations by matrix inversion for the $A_{\vec{G}}$'s.
Therefor a finite set of n vectors $\vec{R}_n$ which are uniformly distributed over the surface unit cell is chosen. Those are related to the same number of uniformly distributed reciprocal lattice vectors $\vec{G}$. This method which was developed by Garcia[64,65] has been implemented by Mayrhofer-Reinhartshuber[24,66] in a computational code.

3.4.5. The Close Coupling Approach

In the case of large corrugations or for scattering with low perpendicular momentum transfer a full quantum mechanical treatment must be used instead of the hard wall approximation. In contrast to the hard wall potential which is infinite, the real atom-surface potential is "soft". Hence the HCW model tends to limit the number of available multiple scattering channels. Under certain conditions these additional channels contribute significantly to the overall scattered intensity[57].
The close coupling approach accounts also for another effect which is neglected by the HCW model: The occurrence of resonance effects (see section 3.6). Due to the attractive part of the potential the incoming He atom can be temporarily trapped in a bound state under certain kinematical conditions which in turn can give rise to peaks and dips in the scattered intensity[57].

The principle of the close coupling approach is as follows: The two-dimensional potential 3.3 and the wavefunction 3.25 are inserted in the Schrödinger equation which results in a set of coupled second order differential equations. In contrast to the hard wall potential the boundary conditions are now that $\Psi_G(z)$ is an outgoing scattered wave far away from the crystal ($z \to +\infty$) and that $\Psi_G(z)$ becomes vanishingly small deep inside the crystal ($z \to -\infty$).
To solve the set of coupled equations, the infinite number of $\vec{G}$-vectors is truncated to a finite size N that is large enough to achieve the desired numerical accuracy[3]. Hence the coupled equations are solved for a set of N functions $\Psi_G(z)$.
It should be noted that there exists no general criterion for conditions under which the HCW model is accurate or whether the close coupling approach should be used instead. Certainly, if the well depth D of the attractive atom-surface potential is comparable to the energy of the incident beam, resonance effects will become more important requiring the application of the close coupling approach[57]. Furthermore, in the case of very large corrugations and grazing incidence angles HCW intensities should also be treated with care.

3.4.6. Determination of the Surface Corrugation from HAS Measurements

Since the scattered intensity maps the surface corrugation, measured HAS intensities can be used to determine the corrugation. So far only the scattering amplitudes $A_{\vec{G}}$ have been treated. The related scattered intensities $P_{\vec{G}}$ which are usually obtained in scattering experiments are[8]:

$$P_{\vec{G}} = \frac{k_{Gz}}{k_{iz}} |A_{\vec{G}}|^2 \tag{3.35}$$

where the ratio for the normal component of the incoming and outgoing momentum accounts for the cross section ratio of the incoming and outgoing beam. For elastic scattering the diffracted intensities have to satisfy the unitarity condition $\sum_{\vec{G}} P_{\vec{G}} = 1$ i.e., the incoming flux equals the outgoing flux[9].
The kinematical factor of equation 3.35 is valid for a scattering geometry according to the "classical Rutherford configuration". The definition of this configuration is that the incident beam illuminates a well-defined spot on the surface and that the detector acceptance angle is large enough that it "views" the entire illuminated spot[67].
The eikonal and GR method, discussed in the previous section dealt with the problem of calculating diffraction peak intensities for a given corrugation function $\xi(\vec{R})$. However, the experimentalist usually faces the problem of determining $\xi(\vec{R})$ from a set of measured diffraction intensities. Hence in order to relate the measured intensity to the surface corrugation a structural model must be proposed.

A possible approach is to assume $\xi(\vec{R})$ as a Fourier series expansion, i.e. a series of cosines and sines according to the geometry of the surface unit cell[8,57]. The coefficients and hence the amplitudes of the trigonometric functions are then varied until optimum agreement between the measured and the calculated intensities is obtained. The accuracy of the agreement is usually judged by evaluating a reliability factor[8]:

$$R = \frac{1}{N}\sqrt{\sum_{G}\left(P_G^{exp} - P_G^{calc}\right)^2} \tag{3.36}$$

where N denotes the number of experimentally observed diffraction peaks, and P_G^{exp} and P_G^{calc} are the experimental and calculated diffraction intensities for each G. Note that in the current form of the reliability factor all diffraction peaks are weighted equally, without considering their intensities. Therefore the reliability factor can be modified in a way that different peaks are weighted according to their intensities[9].

In principle, an exact determination of the surface corrugation requires measurements at different incident energies and at different surface temperatures. Firstly, realistic atom-surface potentials are not infinite. Hence the classical turning point depends on the energy of the incident He beam (equation 3.26). A He beam with a higher incident energy E_i will sample the charge distribution $\xi(\vec{R})$ slightly closer to the ion core than for lower E_i. Therefore, each set of measured intensities at a given incident energy yields a different corrugation $\xi(\vec{R})$[57].

Secondly, to exclude temperature effects, the corrugation $\xi(\vec{R})$ should be determined for $T_S = 0$ K. Consequently, the measured intensities must be linearly extrapolated to $T_S = 0$ K. This can be done by measuring the intensity of the specular peak as a function of the surface temperature (see section 3.4.7) and applying this correction to all diffraction peaks. However, for surface temperatures up to 300 K the corrugation function can be accurately determined without the application of temperature corrections implying an error of $\pm 10\%$ in the peak intensities[8,68].

3.4.6.1. The Beeby Correction

Although only the close coupling approach accounts for a realistic potential, a slightly better approximation of the HCW model can be achieved by inclusion of the attractive part of the atom-surface potential. The attractive part of the potential has the simple effect of first accelerating the incoming He atoms towards the HCW barrier and then decelerating the scattered atoms as they leave the surface[57]

This effect can be introduced in the previous treatment of the HCW model through a correction know as the Beeby correction. The attraction can be approximately

accounted for by adding the energy of the well depth D to the incident energy. Hence, the influence of the attractive well is considered by replacing the perpendicular momentum transfer Δk_z by[8,69]:

$$\Delta k_z^{'} = k_i \left[\sqrt{\cos^2(\theta_f) + \frac{D}{E_i}} + \sqrt{\cos^2(\theta_i) + \frac{D}{E_i}} \right] \tag{3.37}$$

In doing so the attractive part of the potential is included by assuming a spatially uniform well of depth D which is usually in the range of 4-10 meV for HAS[57]. The well depth can be accurately determined using resonant scattering phenomena which are described in section 3.6. However, the Beeby correction neglects the contribution of these bound state resonances to the scattered intensity.

3.4.7. The Debye-Waller factor

The theoretical models presented for the calculation of diffraction intensities assume that the atoms of the sample are at rest. This is not the case for real systems where zero-point motion and thermal vibrations of the surface atoms cause additional inelastic scattering of the incoming particles. This can be observed in the thermal attenuation of the coherent diffraction intensities without a change in the peak shapes.
The attenuation is described by the Debye-Waller factor which relates the diffraction intensity $I(T_S)$ of a sample at temperature T_S to the intensity I_0 of a sample at rest by[8]:

$$I(T_S) = I_0 \cdot e^{-2W(T_S)} \tag{3.38}$$

where $\exp[-2W(T_S)]$ is the Debye-Waller factor. The Debye-Waller factor is described using

$$2W(T_S) = \left\langle (\vec{u} \cdot \Delta\vec{k})^2 \right\rangle_{T_S}. \tag{3.39}$$

with $\vec{u}$, the displacement of a lattice atom out of its equilibrium position and $\Delta\vec{k}$ the momentum transfer during the scattering process. The outer brackets indicate that the thermal average has to be taken[8]. Assuming that the momentum transfer parallel to the surface equals zero, equation 3.39 reduces to:

$$2W(T_S) = \left\langle u_z^2 \right\rangle \cdot (\Delta k_z)^2 \tag{3.40}$$

where $\langle u_z^2 \rangle$ describes the average displacement of a crystal atom perpendicular to the surface. For a classical harmonic oscillator $1/2\ M\omega^2\langle u^2\rangle = 3/2\ k_B T$ holds. Using the Debye model and the definition of the Debye temperature[15] in terms of ω_D: $\hbar\omega_D/k_B T = \theta_D/T$, equation 3.40 becomes:

$$W(T_S) = \frac{3(\hbar^2 \Delta k_z^2) T_S}{2 M k_B \theta_D^2} \tag{3.41}$$

where M is the mass of the surface atom and θ_D the surface Debye-temperature. The effect of the attractive well near the surface can be taken into account using the Beeby correction. Consequently, the momentum transfer Δk_z is replaced by equation 3.37. In the case of the specular beam, $\theta_i = \theta_f$ holds and the Debye Waller factor (equation 3.41) together with the Beeby correction can be expressed as:

$$W(T_S) = \frac{12m\left[E_i \cos^2(\theta_i) + D\right] T_S}{2Mk_B\theta_D^2} \tag{3.42}$$

where m is the impinging particle mass. Although equation 3.42 is strictly valid only for the specular beam, it is also a reasonable approximation for final angles θ_f that are not too different from the incident angle θ_i.
In general the thermal attenuation of the diffraction intensities due to the vibration of the surface atoms can be described in a good approximation using the Debye Waller factor from equation 3.41 together with the Beeby correction (equation 3.37). However, for an exact description of the thermal attenuation multi-phonon processes have to be considered[8].

3.5. Inelastic Scattering Intensities

In order to describe inelastic scattering the full dynamical Hamiltonian has to be considered. The system can be described by

$$\begin{aligned} H &= H_0 + H_c + V(\vec{r}, t) \\ V(\vec{r}, t) &= V(\vec{r}) + \delta V(\vec{r}, t) \end{aligned} \tag{3.43}$$

where H_0 and H_c are the unperturbed operators of the incident free particle and the vibrating semi-infinite lattice respectively. $V(\vec{r}, t)$ describes the time-dependent atom-surface coupling potential and can be decomposed in the static atom-surface potential $V(\vec{r})$ (see section 3.1) and the time-dependent perturbation $\delta V(\vec{r}, t)$ due to the vibration of the lattice atoms. It is the static part which describes the elastic diffraction from the surface whereas the dynamic part $\delta V(\vec{r}, t)$ accounts for inelastic scattering[3,14,49].
Typically one starts with the transition rate w_{fi} from an initial to a final state of total energies E_i^{tot} and E_f^{tot}:

$$w_{fi} = \frac{2\pi}{\hbar} |T_{fi}|^2 \, \delta\left(E_f^{tot} - E_i^{tot}\right) \tag{3.44}$$

which is the generalized from of Fermi's golden rule. The subscripts f and i refer to the collective set of both the wavevector of the particle and the occupation number of phonons in each vibrational mode of the crystal. $|T_{fi}|^2$ are the matrix elements of the transition operator[3,49,56].

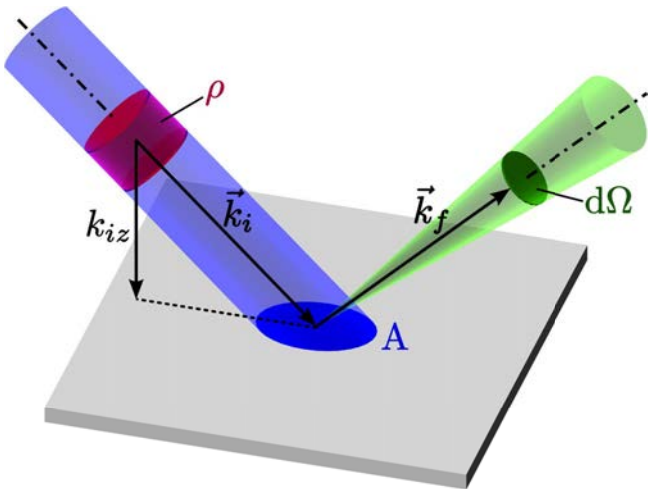

Figure 3.17.: Schematic illustration with the important parameters used in the definition of the reflection coefficient. The surface area A is illuminated by the incident beam with the density of particles ρ.

The experimentally relevant parameter is the transition rate of the particle with initial state $\vec{k}_i$ to the final state $\vec{k}_f$ in terms of the reflection coefficient $R(\vec{k}_f, \vec{k}i)$ divided by the incident particle flux[3,49]:

$$J_i = \frac{\hbar k_{iz}}{m}\rho \cdot A \tag{3.45}$$

with the surface area A, illuminated by the incident beam and the density ρ of particles above this area (see figure 3.17). The experimentally measured quantity is then obtained by multiplying the reflection coefficient with the available volume in phase space, i.e. the fraction of incident particles which are scattered into the solid angle $\mathrm{d}\,\Omega_f$ and the energy interval $\mathrm{d}\,E_f$ (momentum between $\vec{k}_f$ and $\vec{k}_f + \mathrm{d}\,\vec{k}_f$):

$$\frac{\mathrm{d}^2\,R}{\mathrm{d}\,E_f\,\mathrm{d}\,\Omega_f} = \frac{m^2}{8\pi^3\hbar^2\rho}\frac{|\vec{k}_f|}{J_i}w_{fi} = \frac{m^2}{8\pi^3\hbar^3\rho^2 A}\frac{|\vec{k}_f|}{k_{iz}}w_{fi} \tag{3.46}$$

In the experiment only differences in the phonon states are observed. Therefore, the transition rate (equation 3.44) summed over all final phonon states and averaged over all initial phonon states inserted in equation 3.46 yields:

$$\frac{\mathrm{d}^2\,R}{\mathrm{d}\,E_f\,\mathrm{d}\,\Omega_f} = \frac{m^2}{4\pi^2\hbar^4\rho^2 A}\frac{|\vec{k}_f|}{k_{iz}}\sum_{\{n_i\}\{n_f\}} p\left(\{n_i\}\right)|T_{fi}|^2\,\delta\left(E_f^{tot} - E_i^{tot}\right) \tag{3.47}$$

where the averaging over all initial phonon states is simply the sum over the initial states weighted by the temperature dependent distribution $p(\{n_i\})$ of initial phonons[14,49,56]. Consequently, all information on the scattered intensity depends upon the knowledge of the matrix elements T_{fi} of the transition operator. In

order to obtain these matrix elements the dynamical problem, expressed by the Hamiltonian (equation 3.43) that describes the interaction of the He atom with the vibrating surface, has to be solved.
Since in HAS the inelastic processes are usually small compared to the elastic processes the same holds for the dynamic and static components of the potential in equation 3.43. Hence it is usually sufficient to treat the static part $V(\vec{r})$ exactly and the dynamical part $\delta V(\vec{r},t)$ using first order perturbation theory. This approach is known as the distorted-wave Born approximation (DWBA)[14,49,70].
$\delta V(\vec{r},t)$ can be expanded in a Taylor series with respect to the time-dependent displacement of the atoms around their equilibrium position considering that the vibrational amplitudes are small with respect to the interatomic distances[14]. If merely one-phonon processes are considered, only the linear term to the first order will be involved and the occupation number changes by ± 1.

3.5.1. The Born Approximation

In the first-order Born approximation, which is even cruder than the DWBA, T_{fi} is replaced by V_{fi}, which means that multiple scattering and resonances with bound states, are neglected. In doing so, $V(r,t)$ is described as a sum of pairwise interactions. The differential reflection coefficient for one-phonon processes (corresponding to energies that differ by the phonon energy $\hbar\omega$) in the Born approximation is then:[3,56,71–73]

$$\begin{aligned}\frac{\mathrm{d}^2 R}{\mathrm{d}\, E_f\, \mathrm{d}\, \Omega_f} =& \frac{m^2}{4\pi^2\hbar^4\rho^2 A}\frac{|\vec{k}_f|}{k_{iz}}\sum_{\vec{Q}_\nu}\left|\vec{F}_{fi}\cdot\vec{u}_{\vec{Q}_\nu}\right|^2 \\ &\times\left\{\begin{array}{l} n[\hbar\omega(\vec{Q}_\nu)] \\ n[\hbar\omega(\vec{Q}_\nu)]+1 \end{array}\right\}\delta\left(E_f - E_i \mp \hbar\omega(\vec{Q}_\nu)\right)\end{aligned} \tag{3.48}$$

where $n(\hbar\omega)$ is the occupation number (according to equation 3.23) for annihilation and $n(\hbar\omega)+1$ for creation of a phonon. The conservation of energy is given by the δ-function. $\vec{F}_{fi}$ is the atom-phonon coupling force and $\vec{u}_{\vec{Q}_\nu}$ the planar displacement of the surface layer.[3,19,71,72] According to equation 3.48 the differential reflection coefficient is proportional to the surface-phonon spectrum which is weighted by $|\vec{F}_{fi}\cdot\vec{u}_{\vec{Q}_\nu}|^2$, the square of the coupling potential energy[72].
Although the Born-approximation is not a particularly good description for HAS, the structure of the differential reflection coefficient in equation 3.48 remains valid in further developments, as long as the linear atom-phonon coupling force $\vec{F}$ is given the appropriate form[19,72].
Since the occupation number $n(\hbar\omega)$ according to equation 3.23 enters the differ-

ential reflection coefficient 3.48 the intensities of phonon annihilation and creation events are related by:[19]

$$\frac{I_{an}}{I_{cr}} = \frac{n(\hbar\omega)}{n(\hbar\omega)+1} = e^{-\hbar\omega/k_BT} \tag{3.49}$$

Therefore, if the experimentally determined intensities of annihilation and creation events are compared, they have to be corrected for the Bose factor[14,32,70].

3.5.2. The Distorted-Wave Born Approximation

In both the distorted-wave Born approximation (DWBA) and the Born approximation the contribution of inelastic scattering is obtained by the matrix element of the time-dependent perturbing potential. For the "pure" Born approximation this matrix element is taken with respect to plane waves. However, in the DWBA the matrix element is now taken with respect to initial and final wavefunctions which are distorted by the reflection from the static surface potential[3,56,72,73].

3.5.3. The Cut-Off Factor

Due to the fact that the He atoms are scattered by the surface electron distribution several angstroms from the surface away, they tend to interact with more than one surface atom simultaneously. This gives rise to a strong damping in the intensity of surface phonons with large wavevectors $\vec{Q}$, described by the "cut-off" factor[4,14,74–76].
Thereby the He atom interacts with only one surface atom if the atom-surface interaction potential is short ranged. But with increasing interaction range the He atom will interact with several surface atoms simultaneously and the excitation of phonons with short wavelengths will be suppressed. Therefore the dependence of the intensity of single phonons with respect to the phonon wavevector $\vec{Q}$ can be described by[3,14]:

$$I(Q) = I_0 \cdot e^{-Q^2/Q_c^2} \tag{3.50}$$

with Q_c the cut-off value. The cut-off at $Q > Q_c$ is not absolute but exhibits a rapid decay of the phonon intensity with vectors Q beyond the cut-off Q_c.
Consequently, since the He atom can interact with several surface atoms at once according to the range of the atom-surface interaction, the inverse of Q_c describes the range of the lateral atom-surface interaction[76]. In general Q_c is found to be small on metallic surfaces (e.g.: $Q_c = 0.74$ Å^{-1} for Ag(111)) making it difficult to detected phonons beyond the first Brillouin zone. For closed-shell solids (e.g.: LiF) Q_c is typically much larger and phonon events are usually detected over

several Brillouin zones[32,74]. A comparison of the cut-off factor for Ag(111) and LiF(001) is shown in figure 3.18.
Within the classical picture of the He atom being a sphere scattered from an isotropic elastic continuum this effect can be understood as follows: The impinging atom produces a deformation of the surface with approximately the size of the atom. This deformation can be expanded in terms of a Fourier series of the normal vibration modes. The "large" and "slow" He atom will be unable to excite modes with high frequencies or short wavelengths, giving rise to a cut-off in the inelastic scattering beyond a certain phonon energy and wavevector[3].

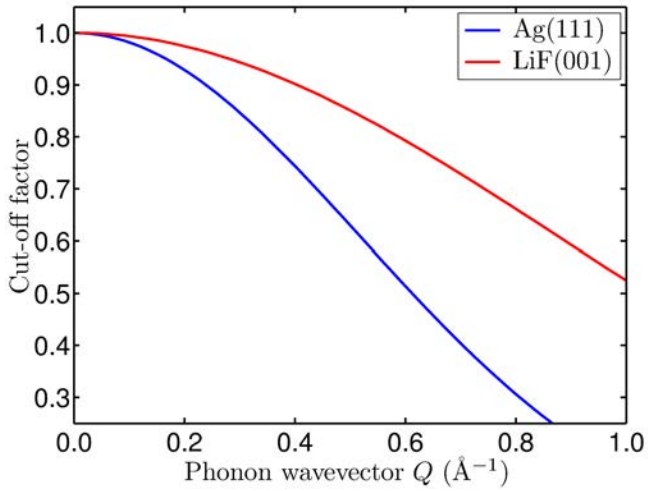

Figure 3.18.: Cut-off factor (equation 3.50) versus phonon wavevector for Ag(111) and LiF(001). The values of Q_c are according to Bortolani et al.[74].

Since the turning point depends on the energy of the incident He beam (equation 3.26), the cut-off effect can be partially counterbalanced by using higher beam energies. This is however limited by the onset of multi-phonon scattering processes (equation 3.22)[3,32].

3.6. Resonance Effects in HAS

In section 3.4 the intensities of diffraction peaks have been discussed for a given corrugation and scattering geometry. However, the influence of the surface potential has been neglected in this considerations so far. In cases where the incident beam energy E_i is comparable to the well depth D, the attractive well of the potential can give rise to selective adsorption resonances. These resonances can cause a disturbance in the intensities of the diffracted beams characterized by the sudden appearance of maxima (or minima)[8].
The appearance of a resonance can be explained in the following way: An incoming He-atom can be temporarily trapped in a bound state of the atom-surface potential. After some time the He-atom then leaves the bound state by interaction with a $\vec{G}$-vector and / or a phonon. Due to the interaction with the surface phonon the quantum-mechanical phase of the He atom is changed. Therefore, interference between a directly reflected He-atom and the He-atom that has been going through the bound state gives rise to an alteration of the scattered intensity[8,42]. The process is illustrated in figure 3.19.

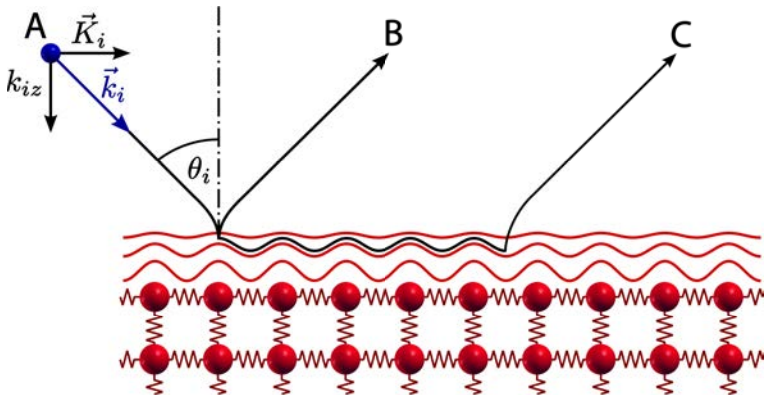

Figure 3.19.: Schematic illustration of the selective adsorption resonance process (according to[77]): The incoming He-atom (A) can either be scattered directly from the surface (B) or enter selective adsorption where it is temporarily trapped in one of the energy levels of the atom-surface interaction potential. The He-atom leaves the bound state by interaction with a G-vector and / or a phonon (C). Interaction with the surface phonon changes the quantum-mechanical phase of the He atom (C) with respect to the directly scattered atom (B) and interference occurs.

In general there exist various processes for the He atom to transit into a bound state or to leave the bound state which are summarized in figure 3.22. However, a modulation in the final beam intensity is always produced by the interference of a bound-state scattering channel with the respective direct scattering channel[50,78].

The involved temporary bound state can act as intermediate state causing a resonance behavior in the diffraction process which appears in the form of dips or peaks in the scattered intensity at specific, characteristic energies. Therefore the phenomenon is termed a selective adsorption resonance or a bound state resonance[3,8,79].
The transition of the incoming He-atom into a bound state is as follows: An incident He atom can be transferred to a bound state by diffraction. In this bound state the atom is bound normal to the surface in the gas-surface potential with a discrete binding energy $E_n < 0$. The process requires that the initial energy and angle are such that the total incident energy can be split into a negative bound state energy in the direction normal to the surface and a parallel kinetic energy. Therefore the energy E_i of the incident atom has to equal the kinetic energy of the atom moving on the surface plus the binding energy E_n of the adsorbed atom[8,42].

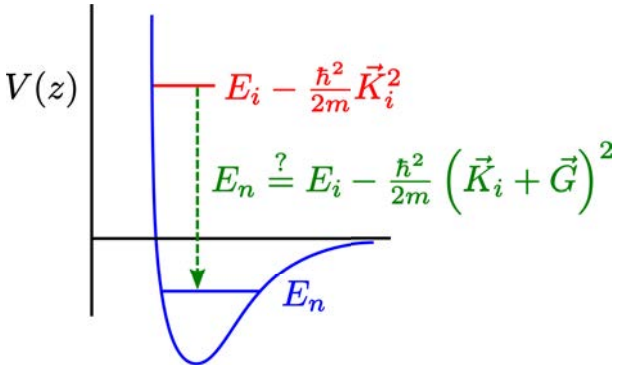

Figure 3.20.: Illustration of the resonance condition: The parallel kinetic energy of the He atom is increased from $\frac{\hbar^2}{2m}\vec{K}_i^2$ to $\frac{\hbar^2}{2m}(\vec{K}_i + \vec{G})^2$ by taking up a $\vec{G}$-vector. The normal energy (motion along z) is decreased by the same amount from $\frac{\hbar^2}{2m}k_{iz}^2$ to the bound state energy $-|E_n|$. This process is only possible if the final state after this transition matches a bound state E_n; hence it appears only at selected incident angles.

In other words: The initial kinetic energy is transferred into a bound state with negative energy and extra translational energy of the helium atom parallel to the surface by taking up a G-vector. Hence the energy of an atom moving parallel to the surface in the periodic gas-surface potential with the wave vector $\vec{K} + \vec{G}_{hk}$ surmounts the incident energy just by the binding energy[3,42].
The condition for this resonance into a bound state can be derived from the conservation of energy and parallel momentum[8,42,79]:

$$E_i = \frac{\hbar^2}{2m}k_i^2 = \frac{\hbar^2}{2m}\left(\vec{K}_i + \vec{G}_{hk}\right)^2 + E_n(\vec{K}_i, \vec{G}_{hk}) \tag{3.51}$$

which is illustrated in figure 3.20. Note that the kinematical condition known from

elastic scattering is "altered" due to the transition into the bound state. The Bragg condition states that $\Delta\vec{K} = \vec{G}_{hk}$ and the kinematically allowed reciprocal lattice vectors $\vec{G}_{hk}$ for scattering are found through conservation of energy. However, it is also possible for a particle to be diffracted temporarily into a channel which is kinematically forbidden via transition into a bound state: For certain diffraction angles the energy of the particle perpendicular to the surface becomes equal to the binding energy E_n of one of the bound states and resonant transitions into this state can occur without violating energy conservation[3].
Such selective adsorption processes give rise to sharp changes in the reflectivity as the resonance condition is passed, either as the scattering geometry is changed or as the incident helium energy changes. Thereby the resonance may cause either a maximum or a minimum depending on whether the interference is constructive or destructive, respectively. The sharp modulation of the peak intensity is due to the fact that the channel going through the bound state is only allowed at special angles, whereas the directly reflected part is continuously allowed at all angles[42,79,80].
The kinematical condition for the selective adsorption process 3.51 involves $\vec{K}_i$ and E_i of the incoming He atom; hence it affects the incident state. The reverse process, affecting the final state, is also possible in HAS and referred to as selective desorption. Consequently the corresponding kinematical condition involves $\vec{K}_f$ and E_f in the latter process[52]. To sum up, the inclusion of a bound state in a scattering process requires that two conditions are fulfilled simultaneously:

- The Bragg condition: The parallel component of the incident wavevector $\vec{K}_i$ or of the final wavevector $\vec{K}_f$ must be equal to $\vec{K} + \vec{G}_{hk}$ for a reciprocal lattice vector $\vec{G}_{hk} \neq 0$.
- For this value of $\vec{K}$ the total energy has to satisfy $E(\vec{K}) = \frac{\hbar^2}{2m}\vec{K}^2 - |E_n|$ where $E(\vec{K})$ is equal to either E_i or E_f.

These kinematic conditions can be satisfied in both elastic and inelastic surface scattering[52,81,82]. The different processes are illustrated in figure 3.22 and described below.

3.6.1. Elastic Resonant Scattering

For elastic resonant scattering (figure 3.22(c)) the incident He atom enters elastically into a bound state of energy E_n and exits elastically into a final state[3,8,52]. The interference is then caused between the directly scattered channel (figure 3.22(a)) and the part of the wave which passed through the bound state (figure 3.22(c)) and the intensity of either the specular or of Bragg peaks is modulated due to the resonant coupling to the bound state n.

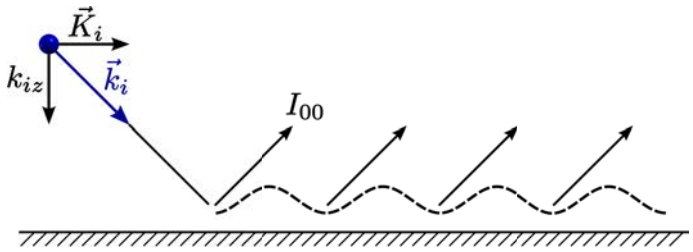

Figure 3.21.: Illustration of a selective adsorption process: The interference between the direct reflection and the reflection through bound states gives rise to a modulation in the intensity I_{00} of the specular beam.

Besides this effect, peaks or dips in the angular distribution may also occur due to interference between the direct inelastic channel (figure 3.22(b)) and the channel involving the bound state (figure 3.22(c)). Usually in the angular distribution of the scattered He beam (intensity vs. θ_i) the background in between the Bragg peaks is caused by inelastic scattering of He atoms[3,14].
Due to the fact that the final state can be reached via two channels - the direct inelastic and the one including the bound state - the intensity may sum up if the channels are in phase or decrease if they interfere negatively. This sharp peaks or dips in the angular distribution appear also at different angular positions as the diffraction peaks and can be used to identify the bound state energies[8,42]
In a precise treatment of the latter process, the trapped atom actually creates a phonon when it leaves the bound state. However, to cause an interference this has to be the same phonon as in the direct inelastic process. Hence the phonon energy or wavevector does not affect the kinematical resonance condition which is why the effect is still regarded as elastic resonance. The phonon causes the phase shift of the bound atom and therefore determines whether a maximum or minimum occurs but the position of the elastic resonance is independent of the exchanged phonon[50,78]

Finally, as the name suggestes, elastic resonance scattering events do not have any effect on the time-of-flight distribution. It was shown by Doak et al.[50] that the lifetime of the atom in the bound state is in the order of 10^{-12} s which cannot be resolved in the TOF distribution[50,83].
However, apart from the modulation of the intensity, a broadening of scattering features due to the finite lifetime of the atom in the bound state can occur. Indeed the angular width of resonant scattering events can even be related to the lifetime of the atoms in the bound states. Therefore the measured width Δ_{tot} has to be corrected for the finite angular resolution of the apparatus Δ_{app} using the simple formula for two folded Gaussian distributions[50,83]: $(\Delta_{res})^2 = (\Delta_{tot})^2 - (\Delta_{app})^2$.

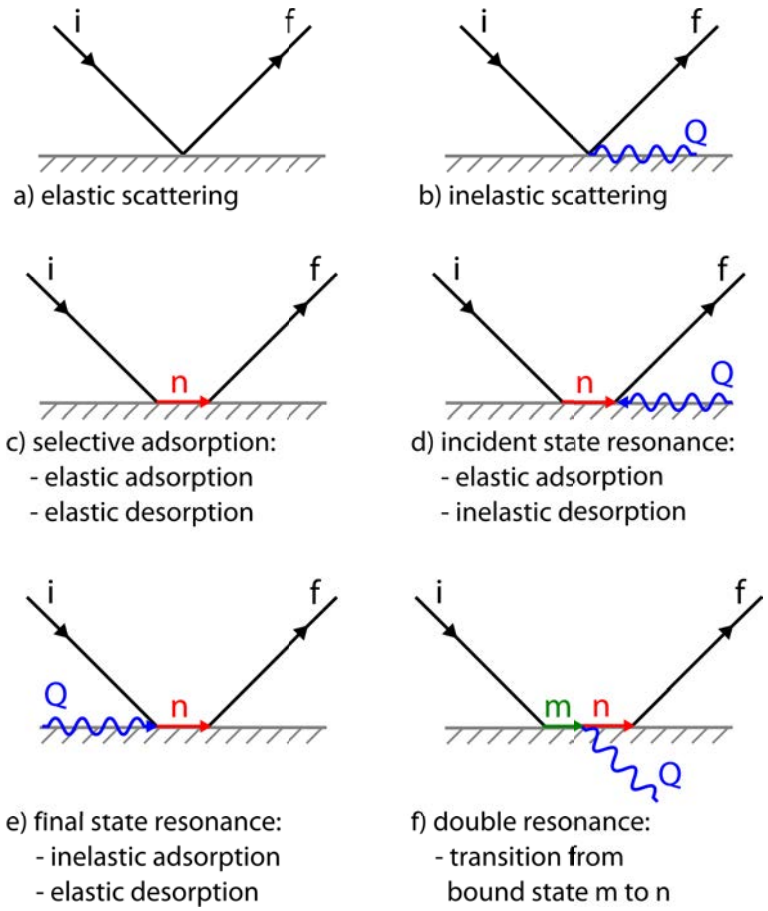

Figure 3.22.: Diagram showing different resonance processes. Features in the intensity of the scattered beam are due to the interference of the part of the wave which is going through a bound-state (c,d,e,f) with the direct scattering channel (a,b).

3.6.2. Inelastic Resonant Scattering

Inelastic resonance processes involve the contribution of a phonon, either in transition to the bound state (figure 3.22(d)) or when leaving the bound state (figure 3.22(e)). Consequently a single surface phonon with energy $\hbar\omega$ and parallel wavevector $\vec{Q}$ is involved in the kinematical conditions[78].

If the incident atom enters the bound state inelastically in which it is elastically resonant with the final state the process is called final-state resonance. On the other hand, if the incident atom is elastically resonant with a bound state and exits inelastically into the final state it is known as an incident-state resonance[3,46,52,78,82,84].

Final state resonances do not give rise to any features in the angular distribution. Since the He atom enters the bound state inelastically it can always "find" the ap-

propriate phonon out of the continuum spectrum which fits the energy and there is no definite incident angle at which the resonance occurs. Therefore this effect contributes to the inelastic background in the angular distribution. Otherwise, incident-state resonances cause features in the angular distributions sometimes also known as phonon assisted selective adsorption resonances[82,84].
Yet the effect on the TOF spectrum in the case of incident-state resonances is just a uniform enhancement. Final-state resonances however, can give rise to a resonance enhancement of inelastic events at specific positions of the $(\Delta\vec{K}, \omega)$-plane. To identify such an event for the involved phonon a relation similar to the scan curve can be derived and superimposed onto the dispersion relation. A phonon can then participate in such an event if it lies simultaneously on a resonance curve, a scan curve and a phonon dispersion curve[50,52,81].
Furthermore, there exists also the possibility that signatures of this final state resonance occur in the angular distribution as selective desorption peaks. This is the case if the surface phonon involved in the process has a large weight in the differential reflection coefficient which is the case for the Rayleigh wave[84].

Finally, figure 3.22(e) shows a further resonance process that can appear under special kinematical conditions: If the kinematical conditions are fulfilled for two surface phonons simultaneously, with the first one meeting a bound state E_m and the second fulfilled for a bound state E_n, a double resonance occurs with a transition of the trapped atom from a bound state to another due to the annihilation or creation of a surface phonon. This double resonance can be viewed as a final-state resonance which is reinforced by an initial-state resonance and is therefore expected to cause an intense feature in the angular distribution[3,50].
If a double resonance occurs at the same angle as a focused inelastic resonance (if the curve representing the resonance condition is tangent to the scan curve and the tangency point falls within the surface phonon spectrum) a huge peak occurs in the angular distribution comparable to the intensity of an elastic peak[85,86].

A careful analysis of angular distributions and time-of-flight measurements usually allows to sort out the exact nature of resonance processes. In particular, resonance processes can be separated from competing phenomena such as kinematical focusing effects[50,52,87].
At this juncture it is also important to keep in mind that equation 3.51 only holds within the framework of the free atom approximation: The motion of the atom trapped in the bound state is treated as free and unrestricted in the direction parallel to the surface (according to the dispersion relation $E(\vec{K}) = \frac{\hbar^2}{2m}\vec{K}^2 - |E_n|$). Strictly speaking, this case only applies in the limit of zero corrugation whereupon the resonantly scattered atom experiences only a laterally averaged poten-

tial. Therefore the approximation is analogous to the free electron model but with resonantly scattered atoms instead of electrons in solids[88].
Yet this is somewhat contrary to the occurrence of bound state resonances: In order to enter a bound state elastically the atom needs to exchange a $\vec{G}$-vector, consequently it is necessary that the surface potential has a G-component. In other words, the surface must be corrugated. In a more general treatment this corrugation yields band-structure effects i.e. there appear gaps in the bound state dispersion curves. To include this effect in the description of the bound states so called Celli diagrams are used[82,89].

Further descriptions regarding resonance processes and examples can be found throughout the literature[3,8,29,30,42,52,78,79,82,84,85,87–93].

3.6.3. Measurement of Resonance Effects

The measurement of resonance effects in HAS is of prominent importance since they contain information about the interaction potential (figure 3.24) via the bound state energy levels. Thereby, if the binding energies of at least two bound states are known then the potential parameters can be determined[3,8,42].
Therefore the condition for elastic resonances can be illustrated in a geometrical way similar to the concept of the Ewald-sphere: Using equation 3.51 the sum of the incident surface wave vector $\vec{K}_i$ and the lattice vector $\vec{G}_{hk}$ lies on a circle with the radius:

$$\left|\vec{K}_i + \vec{G}_{hk}\right| = \sqrt{\frac{2m}{\hbar^2}\left(E_i + |E_n|\right)} \tag{3.52}$$

In figure 3.23 the resonance circle is illustrated. The figure clearly shows that the resonance condition can only be fulfilled at certain conditions of incidence. Hence the investigation of resonance effects can be performed via variation of the following experimental parameters:

(a) Variation of the angle of incidence θ_i changes the length of $K_i = k_i \sin\theta_i$ so that at certain values of θ_i a $\vec{G}_{hk}$ vector coincides with a resonance circle.

(b) Variation of the azimuthal angle ϕ at fixed θ_i by rotating the crystal around the surface normal corresponds to rotating the reciprocal lattice around the origin of the resonance circle.

(c) Variation of the incident energy E_i gives rise to a similar effect as in case (a) however, it also changes the radius of the resonance circle[42].

It should be noted that from an experimental point of view (a) is the easiest to apply. In addition, a useful set of rules describing the effect of resonances on the specular beam can be found in Engel et al.[9] or Krzyzowski et al.[94].

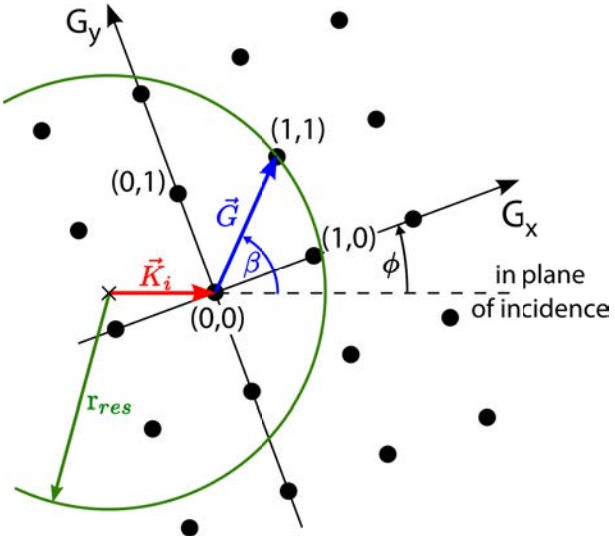

Figure 3.23.: Geometrical representation of the resonance condition according to equation 3.52. The situation for a cubic lattice in the reciprocal space is shown. The resultant vector $\vec{K}_i + \vec{G}_{hk}$ that leads to a resonant transition lies on a circle with the radius $\mathrm{r}_{\mathrm{resonance}} = \sqrt{2m/\hbar^2\,(E_i + |E_n|)}$.

3.6.4. The 9-3 Potential

The energies E_n and the number of bound states depends on the actual shape of the potential. In a first attempt the atom-surface interaction potential has been addressed in section 3.1. Thereby it has already been mentioned that an effective atom-surface potential is achieved by summation over the two-body potentials between the He atom and the atoms of the solid.
In case of the Lennard-Jones potential (equation 3.2) this can be done by replacing the surface lattice with a continuum giving rise to an integral instead of the sum. The resulting atom-surface potential is the so-called 9-3 potential:[8,42,95]

$$V(z) = \left(3^{3/2}\frac{D}{2}\right)\left[\left(\frac{\sigma}{z}\right)^9 - \left(\frac{\sigma}{z}\right)^3\right] \tag{3.53}$$

where, D denotes the well depth, σ the distance at which the potential vanishes and $z = 3^{1/6}\sigma$ is the equilibrium position of a bound atom.
The atom-surface potential is now only dependent on z whereupon the origin of the z-dependence can be understood in the following manner: The z-dependence of the Lennard-Jones 12-6 potential (equation 3.2) is reduced by the integration. Thereby the first integration yields the potential for a He-atom interacting with a one-dimensional continuous string of atoms and the second yields the interaction with a two-dimensional plane. Finally the third integration is performed along the depth of the solid giving rise to the 9-3 z-dependence.

The eigenvalue spectrum of this potential can be calculated using the distorted wave Born approximation[95]:

$$E_n = -D\left[1 - \frac{\pi\hbar}{3.07}\frac{n+\frac{1}{2}}{\sigma\sqrt{2mD}}\right]^6 \tag{3.54}$$

with E_n, the bound state energy of the probe atom in the level with quantum number n. n varies from zero up to a maximum value for which 3.54 remains negative ($E_n < 0$)[42] In figure 3.24 the 9-3 interaction potential for He-LiF(001) is given which also shows the discrete energy states which are represented by the horizontal lines.
The 9-3 potential as well as the corresponding eigenvalue spectrum are determined by an analytical formula and the potential reflects the correct asymptotic form of the attractive part. However, the z^{-9} repulsion term is somewhat arbitrary for an interatomic interaction[42].

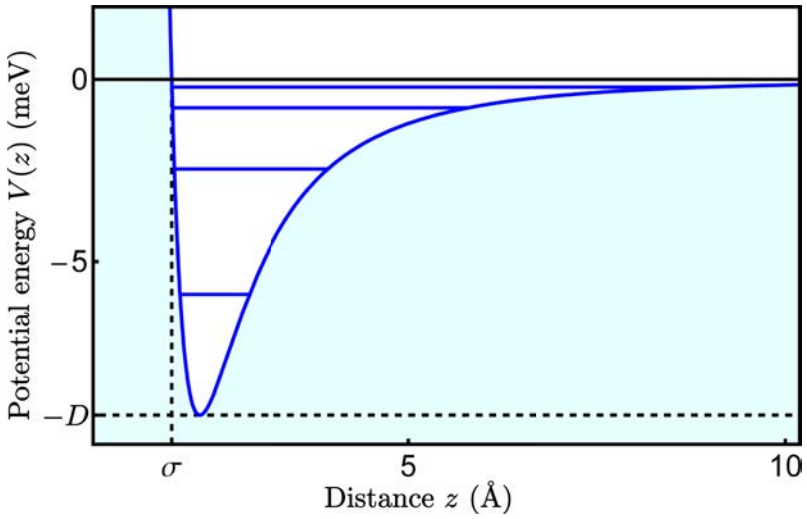

Figure 3.24.: The 9-3 interaction potential (equation 3.53) for the system He-LiF(001) according to the parameters by Celli et al.[45]. As the atom approaches the surface (along z) it experiences first the attractive part of the potential and may be bound in one of the discrete energy states E_n which are represented by the horizontal lines. Hereby the He-atom is then bound normal to the surface with the binding energy E_n

3.6.5. The Corrugated Potential

In section 3.1 the dependence of the potential energy on the lateral position at which the impinging He atom approaches the surface has been described. Consequently the potential follows the corrugation at the surface and $V(\vec{R}, z)$ is usually

written according to a Fourier series (equation 3.3). Figure 3.25 shows a plot of such a corrugated atom-surface potential.

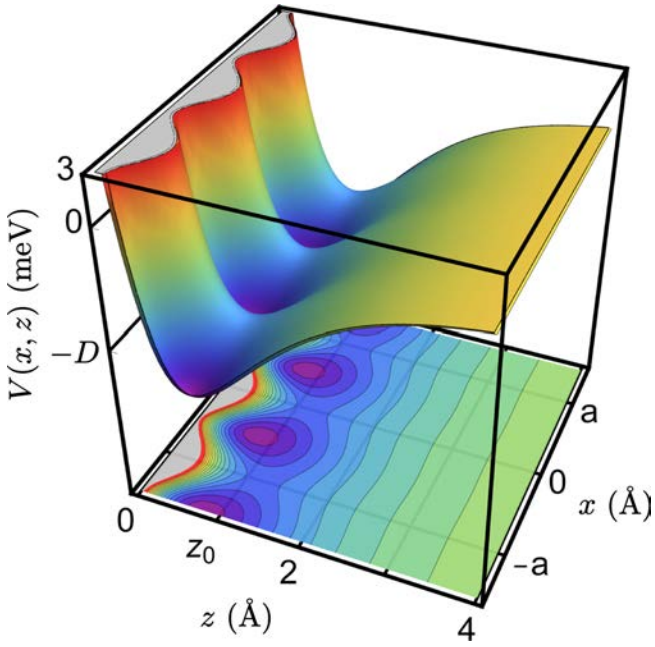

Figure 3.25.: Corrugated 9-3 interaction potential for the the system He-LiF according to the parameters by Celli et al.[45]. The typical dependence along the direction z normal to the surface is modulated by the surface corrugation along the lateral direction x. Consequently at the position of a surface atom ($x = \pm$a) the potential is slightly higher.

However, in the experiment it is not possible to detect a single He atom that approaches the surface on a specific lateral site. Actually, the He beam illuminates a rather large area on the sample surface. Therefore the potential which is determined via HAS reflects the lateral average of the atom-surface interaction.
This laterally averaged potential $V_{00}(z)$, which depends only on the distance z to the surface, is the first term ($\vec{G} = 0$) of the Fourier series expansion 3.3 according to the surface periodicity[47]:

$$V(\vec{R}, z) = V_{00}(z) + \sum_{\vec{G}\neq 0} V_{\vec{G}}(z) \cdot e^{i\vec{G}\vec{R}} \tag{3.55}$$

4. Experimental Setup

4.1. Construction of the Apparatus

Figure 4.1 provides a 3-dimensional illustration of the whole helium atom scattering apparatus. The experiments are performed under high and ultra high vacuum conditions. High vacuum conditions are needed to provide the appropriate mean free path for the He beam and to maintain the supersonic expansion (2.2). Furthermore, to keep the surfaces on which the measurements take place clean, UHV is needed. This is necessary to avoid an unintentional coverage of particles in the residual gas during the required timescales of the experiment[96]. Therefore, the sample is mounted in a separately evacuated chamber.
In particular, the used vacuum system consists of three separately evacuated chambers which are shown in figure 4.1: The source chamber, the main or scattering chamber and the detector chamber. The He-beam is generated in the source chamber. The sample holder and all necessary devices that are used to perform sample preparations are situated in the main chamber. Scattered He-atoms are finally monitored in the detector chamber using a quadrupole mass spectrometer.
The experimental setup of most HAS machines is usually similar and detailed descriptions about the design and setup can be found throughout the literature[9,12]. Hence the reader who is not interested in the experimental details of the apparatus may skip the following parts of this chapter. The apparatus described in this work was actually constructed at the FU Berlin and then transfered to Graz University of Technology. However, a detailed description of most parts of the apparatus is missing so far which is why a few parts of the apparatus will be described in greater depth in the following sections.

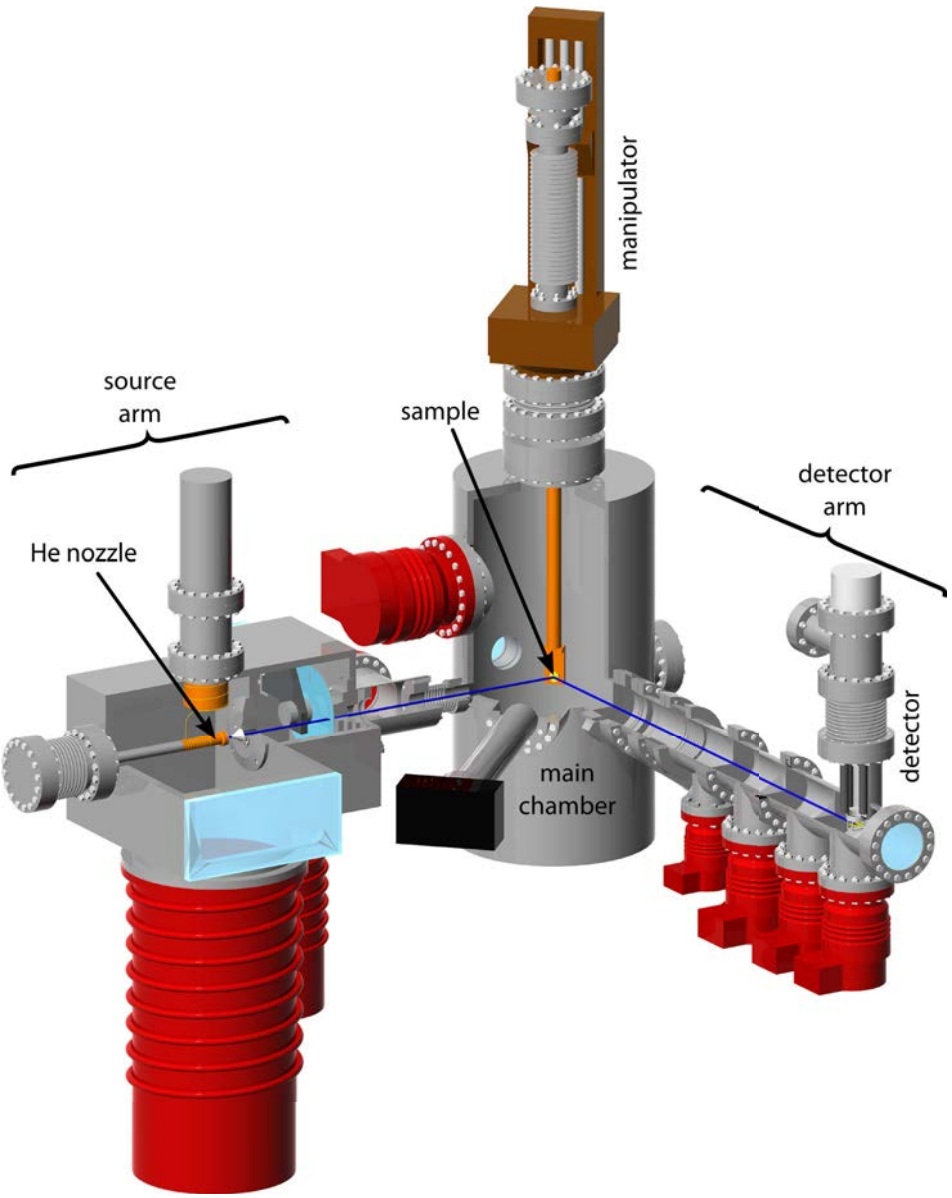

Figure 4.1.: 3-dimensional illustration of the experimental setup showing the main components: The He-beam (symbolized by the blue line) is generated in the source chamber, interacts with the sample in the main chamber and is then monitored in the detector chamber using a quadrupole mass spectrometer. The sample is mounted on a manipulator in the main chamber which allows movements around 6 axes. The red parts represent the vacuum pumps.

4.1.1. The Source Arm

The He beam is generated in a supersonic expansion of helium gas of typically 50 bar pressure through a 10 μm nozzle. The central part of the beam is then

selected using a 380 μm skimmer. The He nozzle can be cooled using a cold head according to the Gifford McMahon-process (Leybold RGD 510). Therefore, the pipe supplying the He gas is first wound around the cold head and the cold head is connected thermally with the He nozzle using oxygen-free copper braids (not shown in the figure).

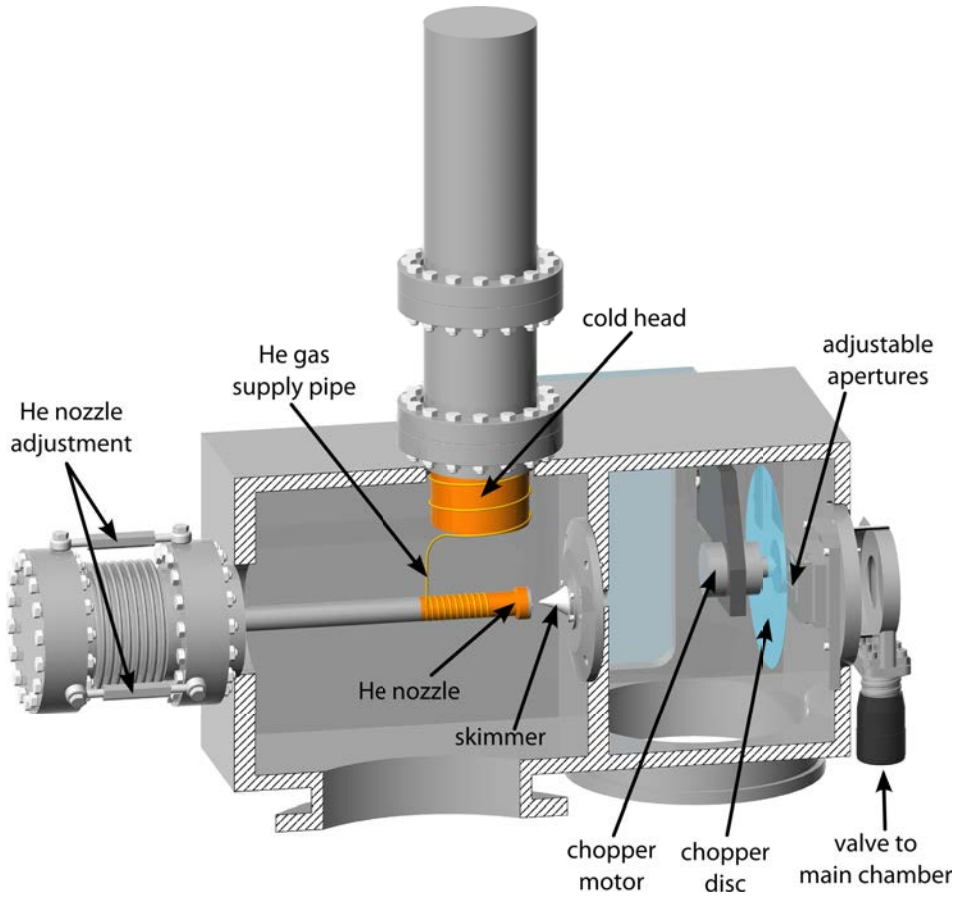

Figure 4.2.: 3-dimensional cut of the source arm. The He beam is generated in the source chamber via supersonic expansion through a 10 μm nozzle. The central part of the beam is transfered using a skimmer into the chopper chamber where the beam can be chopped in order to allow time-of-flight measurements.

The temperature of the cold head is determined using a Si-diode (LTC 60 temperature controller) and the temperature of the nozzle is measured using a Pt100 resistance thermometer. The nozzle can also be heated resistively. Typical intermediate nozzle temperatures ($70 - 140$ K) are obtained by both cooling the nozzle and heating it. Furthermore, the nozzle is wrapped with a superinsulation foil to ensure minimal thermal losses due to radiative heating.
The position of the nozzle and the distance with respect to the skimmer can be varied via a flexible bellow. In order to allow time-of-flight measurements a chop-

per is situated in the 2nd stage (chopper chamber) after the source chamber. Both a single slit chopper disk and a pseudo random chopper are available whereupon a pseudo random sequence with 511 bits is used in the latter case (see section 2.4).

4.1.1.1. The chopper chamber

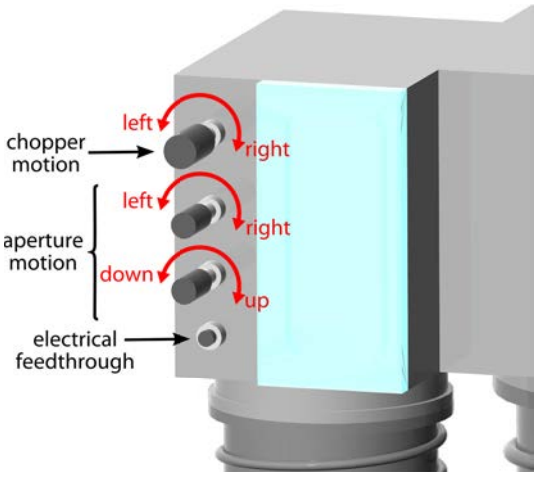

(a) View of the chopper chamber with the feedthroughs. The topmost feedthrough is responsible for the motion of the chopper disc whereas the 2nd and 3rd ones enable the motion of the apertures that is shown in (b).

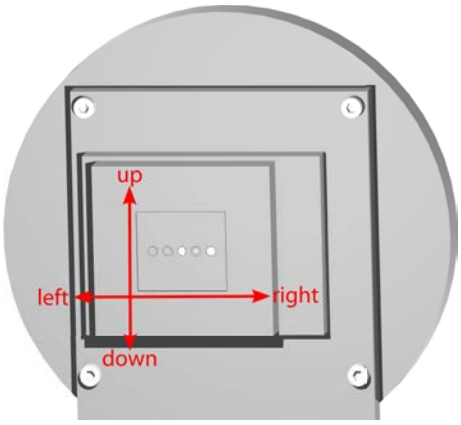

(b) The spot size of the helium beam can be manipulated using one of the 5 apertures. Lateral motion of the apertures, indicated by the red arrows, is possible via the feedthroughs in (a)

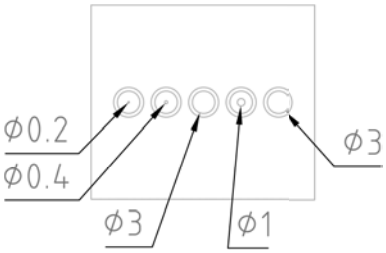

(c) The apertures that can be introduced into the helium beam (diameters given in mm).

Figure 4.3.: Motion of the chopper disc and the apertures in the chopper chamber via mechanical feedthroughs from outside the vacuum chamber. The designated directions in the figure are always with respect to the incident helium beam.

In the 2nd stage after the source chamber the chopper is located together with a plate with different apertures. The chopper disc can be moved into the beam or out of the helium beam using a mechanical feedthrough from outside the chopper chamber (see figure 4.3(a)). Furthermore the spot size of the helium beam can be manipulated using different apertures. Therefore a plate with 5 apertures of

different diameters is available. This plate is placed at the backside of the vacuum chamber (behind the chopper) and its lateral position may be changed using two feedthroughs outside the vacuum chamber.
In figure 4.3 the motion of these apertures together with the diameter of the apertures is illustrated. Note that the designated directions in the figure are always with respect to the incident He beam. In the movement of the apertures one full turn of the mechanical feedthrough corresponds to a lateral motion of 0.5 mm. However, the best way is to monitor the He-signal using the QMS in the main chamber for guidance during the motion of the apertures.

4.1.2. The Main Chamber

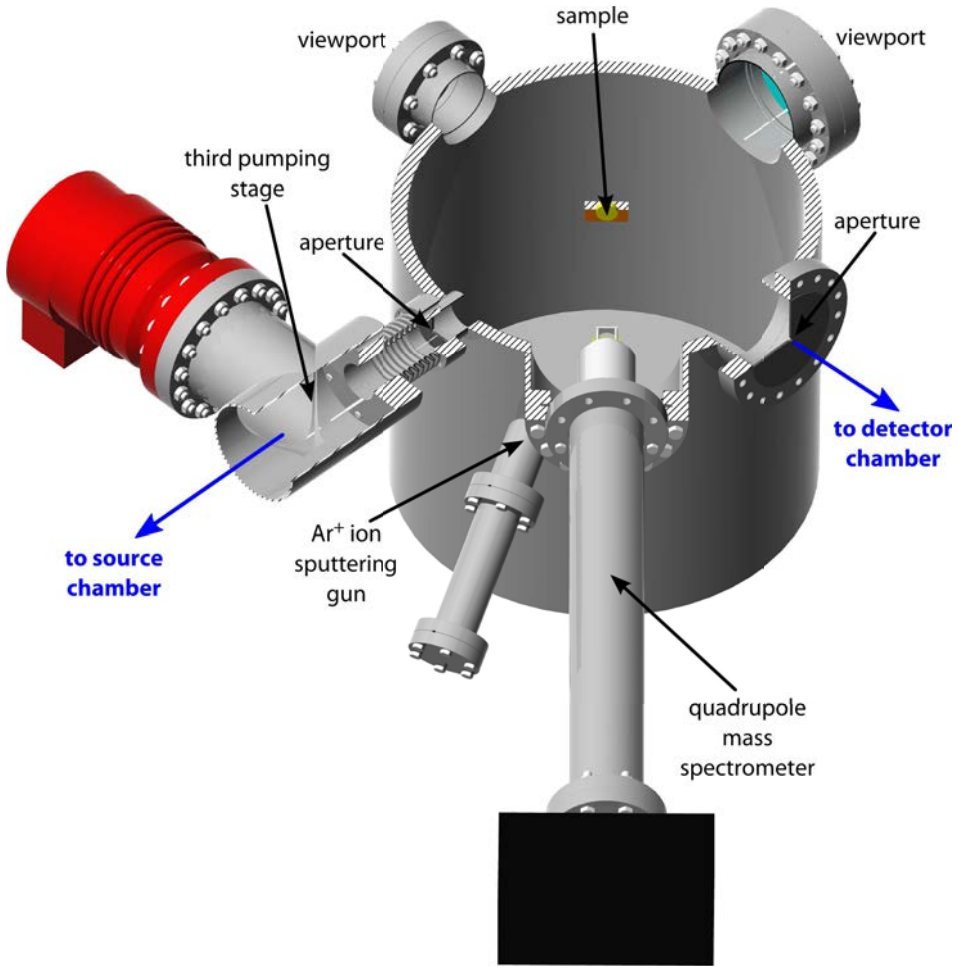

Figure 4.4.: Illustration of the lower level of the main chamber. Despite the sample the ion sputtering gun and a QMS for residual gas analysis are situated at this level.

In the main chamber or scattering chamber the sample is situated together with additional devices that are necessary to prepare and analyze the sample. Most mounting flanges of the main chamber are arranged at two levels of the z direction. The lower level is shown in figure 4.4. It includes the He scattering plane whereupon the angle between the source and the detector arm θ_{SD} is 91.5°.
In addition, an ion sputtering gun (Omicron ISE 10) and a quadrupole mass spectrometer (Hiden Analytical) are mounted onto the lower level. The sputtering gun is used to clean the surface in situ by Ar^+ ions. The QMS allows to determine the composition of the residual gas and to measure the partial pressure in the main chamber.
The upper level provides two further surface analysis methods: A LEED (low energy electron diffraction) and an XPS (X-ray photoelectron spectrometer). The LEED (Omicron Spectaleed) is mainly used to obtain additional information about the surface structure and to align the sample. The XPS (Specs RQ 20/38 X-ray tube with a Mg anode and a VG Scientific CLAM 2 hemispherical electron energy analyzer) permits the determination of the surface composition e.g. whether the surface is clean. A short description of the different analyzing methods is given at the end of this chapter (section 4.3).

4.1.2.1. The Sample Holder

The sample is mounted on the sample holder in the main chamber with the sample holder itself being attached to a 6-axes manipulator. Most parts of the manipulator are shown in figure 4.5. The manipulator allows motions in the 3 lateral directions, a tilt around the x- and y-axis and a rotation around the z-axis. Furthermore the sample can be rotated around the surface normal (azimuthal rotation).
The sample temperature can be measured using a chromel-alumel thermocouple and it may be either heated resistively using a button heater (HeatWave Labs, UHV Button Heater 101137) or cooled down using liquid nitrogen (LN_2). Therefore, a small reservoir at the lower end of the manipulator is filled with liquid nitrogen which is connected via a cooper braid to the sample holder. Thus the sample can be cooled down to −170°C. Moreover, the liquid nitrogen reservoir can also be heated by a Thermocoax wire which is wound around the reservoir.
Parts of the sample holder were actually rebuilt after a vacuum leak had appeared (the figure shows the current version). During this reconstruction several improvements were introduced including an enhanced liquid nitrogen cooling and the azimuthal rotation of the sample. Originally, the azimuthal motion was carried out via a wheel and rope system which had a considerable lack of reproducibility. It was replaced by a gear-wheel system which is also illustrated in figure 4.5.

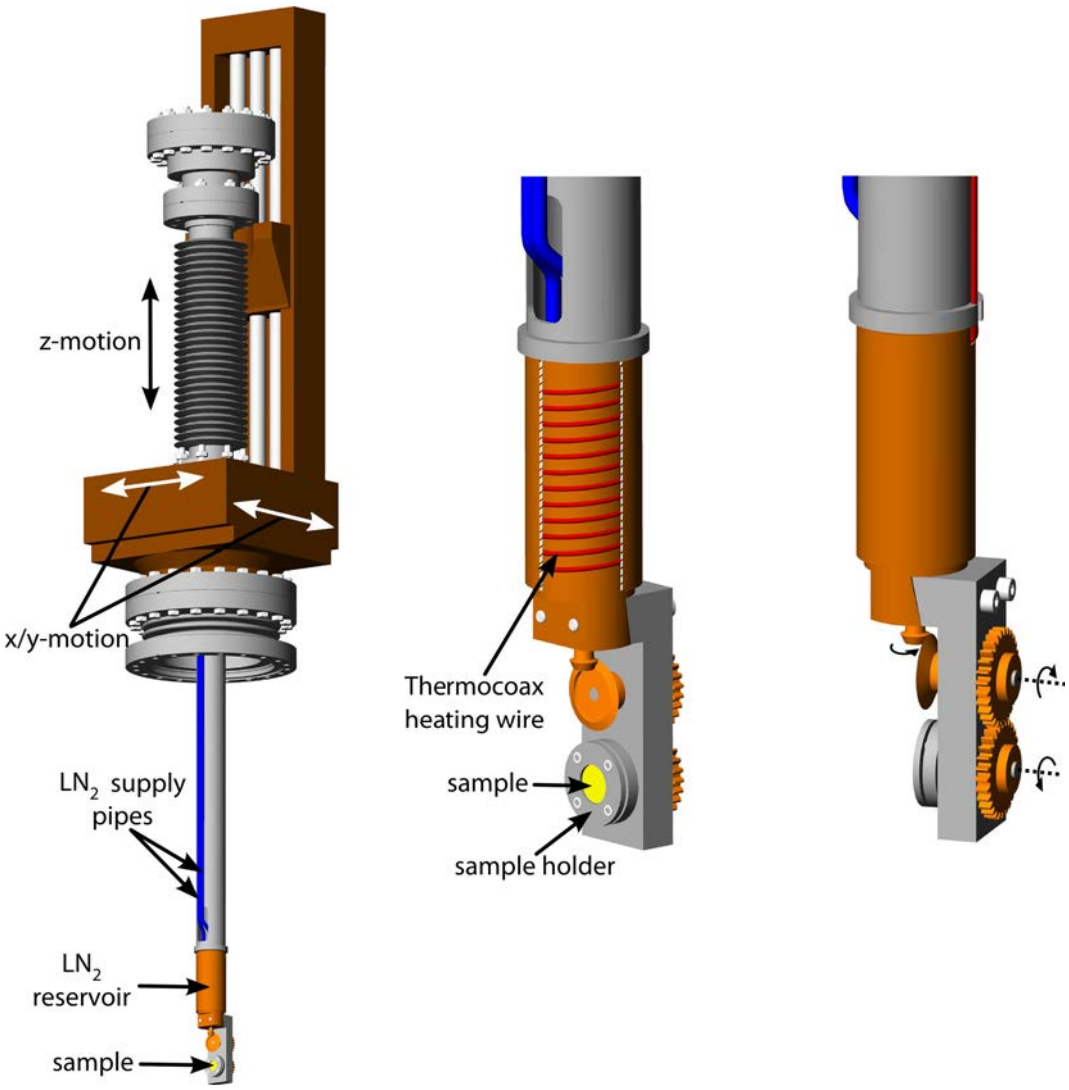

Figure 4.5.: Drawing of the manipulator. The leftmost image shows the manipulator which enables the lateral motion along the x- y- and z-axis. Both images on the right display the lowest part of the manipulator: The liquid nitrogen cooling reservoir and the sample holder together with the sample. The rightmost image shows the azimuthal motion of the sample via a gear-wheel system.

The z-motion and the rotation of the sample around the z-axis are performed via stepper motors. These stepper motors are controlled using a home-built interface that is connected to the serial port of a computer. Therefore these manipulator motions are operated using a number of MATLAB programs that communicate via serial port with the stepper motors. This enables an automatic realization of various HAS measurements e.g. of an angular distribution.
The realization of the control and measurement system and the implementation of the MATLAB programs were part of this work. However, it will not be addressed

here since it is of no scientific relevance.

4.1.3. The Detector Arm

The detector chamber with the quadrupole mass spectrometer is connected to the main chamber using several apertures and differential pumping stages which allows to distinguish between He-atoms that are scattered directly from the sample and background particles.

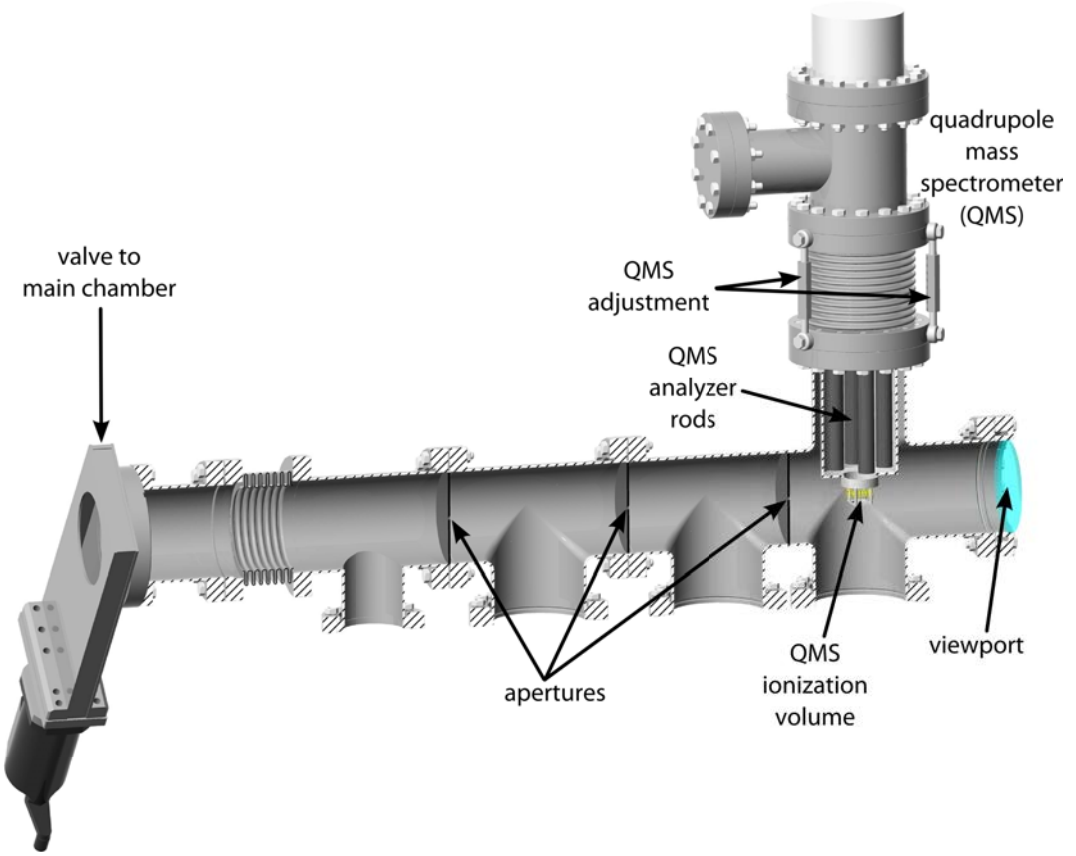

Figure 4.6.: A cut of the detector arm. It exhibits four differentially pumped stages which are separated by small apertures. He atoms are detected using a QMS with a cross-beam ion source and a quadrupole mass analyzer.

The He atoms are detected using a commercial QMS (Balzers QMA 400 with a cross beam ion source and a 90° off axis secondary electron multiplier). The ECL output signal from the QMS is converted to a TTL signal which is then recorded using a home-built multi-channel analyzer (MCA). The position of the QMS can be adjusted via a flexible bellow as to allow the He beam to enter the ionization volume.

4.1.4. Beam-defining Geometry

The geometry of the beam is mainly defined by the dimensions of the apertures. Figure 4.7 shows all apertures of the apparatus in mm together with their lateral positions. In addition, the relevant distances for the time-of-flight measurements (chopper - target - detector) are given. Note that the aperture dimensions in the drawing have been expanded relative to the distances.

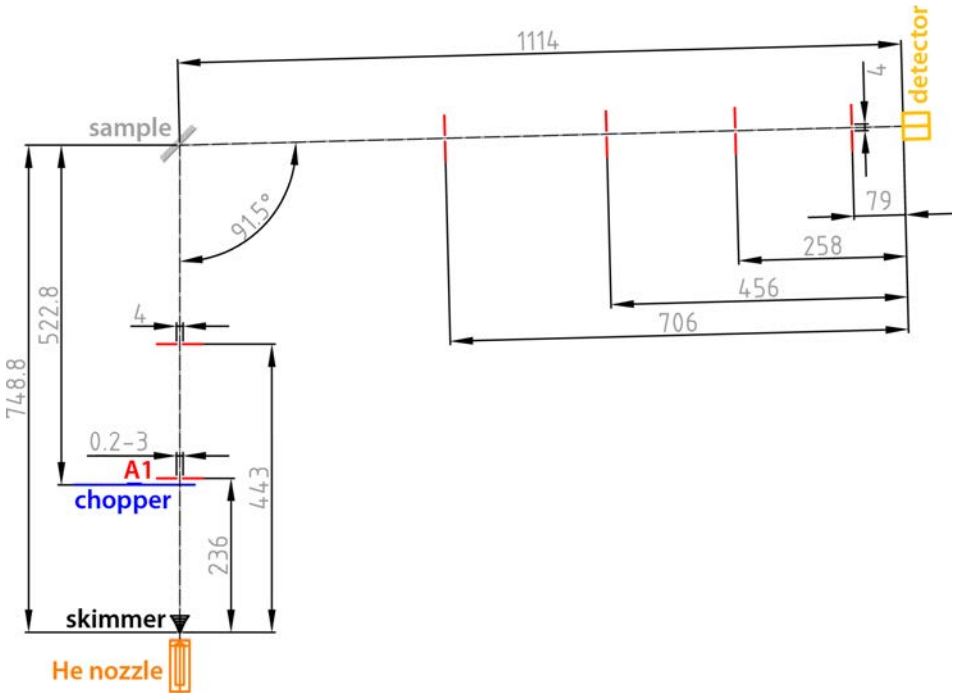

Figure 4.7.: Schematic drawing with the significant dimensions of the apparatus in mm. All apertures which are drawn in red have a diameter of approximately 4 mm. The only exception is the aperture right behind the chopper labeled with A1. This aperture can be varied between 0.2 mm and 3 mm (see figure 4.3).

4.2. Vacuum Setup

The whole vacuum system is illustrated in figure 4.8. All vacuum pumps and pressure gauges are listed in detail in the following tables 4.1, 4.2 and 4.3. The abbreviations that are used in the tables are:

S (N_2)	...	nominal pumping speed (based on N_2)
cbp	...	critical backing pressure
diff. pump	...	oil diffusion pump
TMP	...	turbo molecular pump
i.g.	...	inspection glass
DC	...	Dow Corning (diffusion pump oil)

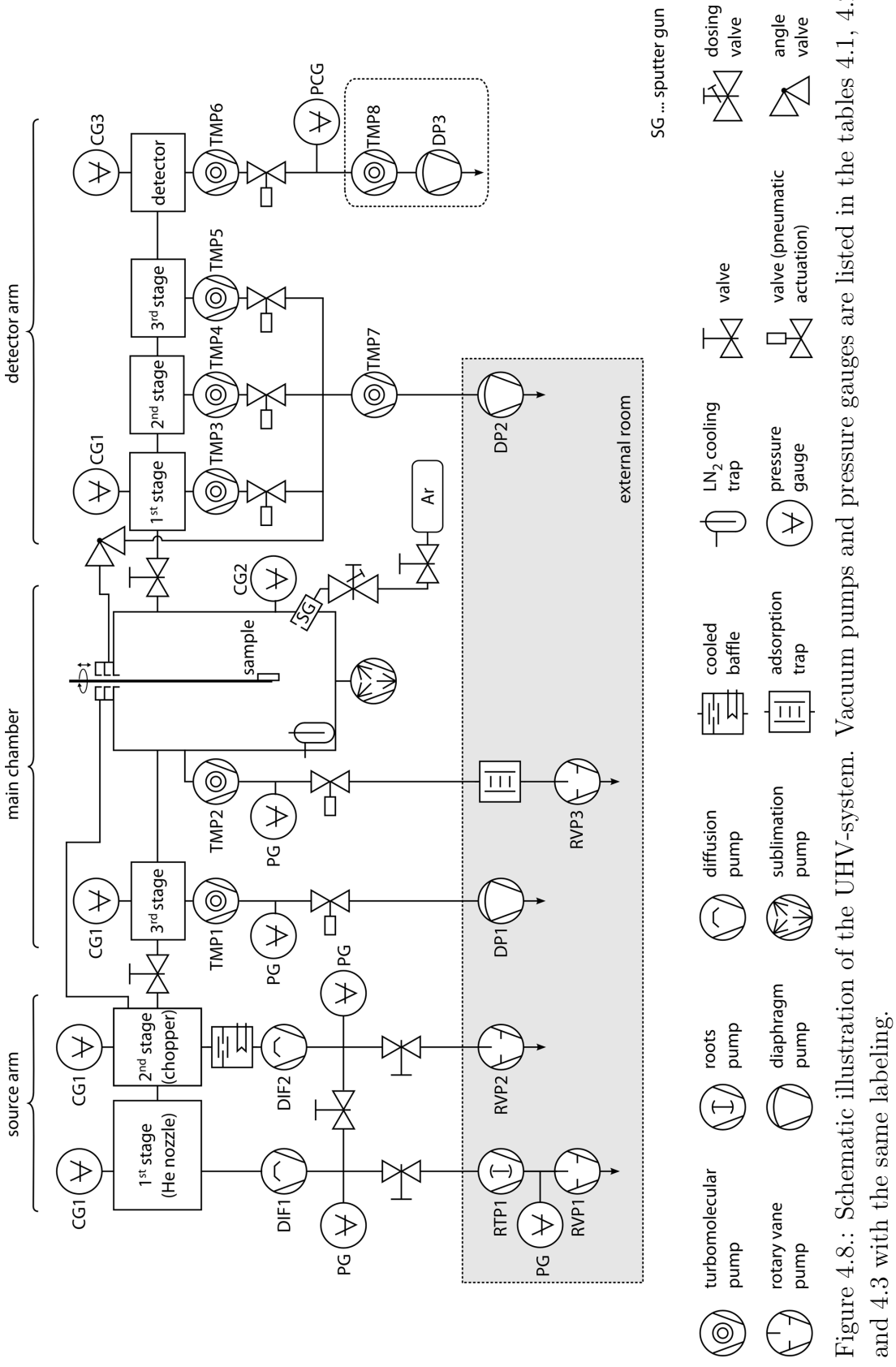

Figure 4.8.: Schematic illustration of the UHV-system. Vacuum pumps and pressure gauges are listed in the tables 4.1, 4.2 and 4.3 with the same labeling.

Table 4.1.: Vacuum pumps of the source arm and the main chamber

	Backing pump			Main pump		
1st stage (nozzle)	**RTP1**	Rotary vane pump	Pfeiffer DUO 030 A	**DIF1**	diff. pump	Balzers DIF 320
		S (N_2)	38 m^3/h		S (N_2)	3500 l/s
		Oil	P3, 5.0 l		cbp	0.5 mbar
		ultimate pressure	$< 1 \cdot 10^{-4}$ mbar		oil	DC 704, 1.8 l
		oil level	upper half of i.g.			
	RVP1	roots pump	WKP 250 A			
		S (N_2)	270 m^3/h			
		ultimate pressure	$< 5 \cdot 10^{-3}$ mbar			
		oil	P3, 1.3 l			
		oil level	0-10 mm under middle of i.g.			
2nd stage (chopper)	**RVP2**	rotary vane pump	Pfeiffer DUO 20	**DIF2**	diff. pump	Balzers DIF 200
		S (N_2)	21 m^3/h		S (N_2)	2000 l/s
		ultimate pressure	$< 5 \cdot 10^{-4}$ mbar		cbp	0.6 mbar
		oil	P3, 1.1 l		oil	DC 704, 0.75 l
		oil level	between marks at i.g.		baffle	HSR BFA 200MF
					S (N_2) (with baffle)	1270 l/s
3rd stage	**DP2**	diaphragm pump	Vacuubrand MD4	**TMP1**	TMP	Balzers TPU 180 H
		S (N_2)	3.3 m^3/h		S (N_2)	180 l/s
		ultimate pressure	2 mbar		cbp	20 mbar
					controller	TCP 380
					display	TCP 380
					lubricant reservoir	PM 063 265 -T
main chamber	**RVP2**	rotary vane pump	Leybold Trivac D8B	**TMP1**	TMP	Pfeiffer TMU 521 YP
		S (N_2)	8.5 m^3/h		S (N_2)	510 l/s
		ultimate pressure	$< 2 \cdot 10^{-3}$ mbar		cbp	13 mbar
		oil	N62, 0.5 l		controller	TC600 PM C01 690 C
		oil level	middle of i.g.		display	DCU 300
		zeolite trap	manufacturer unkn.		lubricant reservoir	PM 063 266 AT

Table 4.2.: Vacuum pumps of the detector arm

	Backing pump			Main pump		
1st stage	**TMP7**			**TMP3**	TMP	Pfeiffer TMU 071 P
					S (N_2)	60 l/s
					cbp	18 mbar
					controller	TC600 PM C01 720 A
					display	DCU 100
					lubricant reservoir	PM 103 593 AT
2nd stage		diaphragm pump	Pfeiffer MVP 055-3	**TMP4**		
		S (N_2)	3.3 m^3/h		TMP	Pfeiffer TMU 261 P
		ultimate pressure	≤ 2 mbar		S (N_2)	210 l/s
		TMP	Pfeiffer TMH 071 P		cbp	10 mbar
		S (N_2)	33 l/s		controller	TC600 PM C01 720
		cbp	18 mbar		display	DCU 200
		controller	TC600 PM C01 720 A		lubricant reservoir	PM 063 265 -T
		display	DCU 100			
3rd stage		lubricant reservoir	PM 103 593 AT	**TMP5**	TMP	Pfeiffer TMU 261
					S (N_2)	210 l/s
					cbp	10 mbar
					controller	TC600 PM C01 690 A
					display	DCU 200
					lubricant reservoir	PM 063 265 -T
detector chamber	**DP3 + TMP8**	diaphragm pump combined w. TMP	Pfeiffer TSH 065 D	**TMP6**	TMP	Pfeiffer TMU 261 P
		S (N_2)	30 l/s		S (N_2)	210 l/s
		ultimate pressure	< $1 \cdot 10^{-8}$ mbar		cbp	10 mbar
		diaphragm pump	Pfeiffer MZ 2T		controller	TC600 PM C01 720 A
		TMP	Pfeiffer TMH 065		display	DCU 200
		lubricant reservoir	PM 103 593 AT		lubricant reservoir	PM 063 265 -T

Table 4.3.: Pressure gauges

abbreviation	type	product name	measurement range	
			max (mbar)	min (mbar)
PG	penning	Pfeiffer TPR 010	1000	$5.6 \cdot 10^{-4}$
CG1	cold cathode	Pfeiffer IKR 050	$5 \cdot 10^{-3}$	$2.0 \cdot 10^{-9}$
CG2	cold cathode	Pfeiffer IKR 070	$5 \cdot 10^{-3}$	$1.0 \cdot 10^{-11}$
CG3	cold cathode	Pfeiffer IKR 060	$5 \cdot 10^{-3}$	$1.0 \cdot 10^{-10}$
PCG	full range (penning + cold cathode)	Pfeiffer PKR 251	1000	$5.0 \cdot 10^{-9}$

In the main and the detector chamber several additional actions are performed to obtain pressures in the range of $p = 1 \cdot 10^{-10}$ mbar. Thus, each time after the vacuum system has been opened the evacuation process is followed by a bake-out of the chambers. Therefore the whole system is held at a temperature of about 130°C for at least 24 hours, mainly to reduce the amount of water in the chambers[96].

Vapor Pressure

Materials used inside the vacuum system evolve vapors of their constituent parts whereupon these vapors add to the gas load in the system. Therefore the vapor pressure of these materials has to be considered[97].

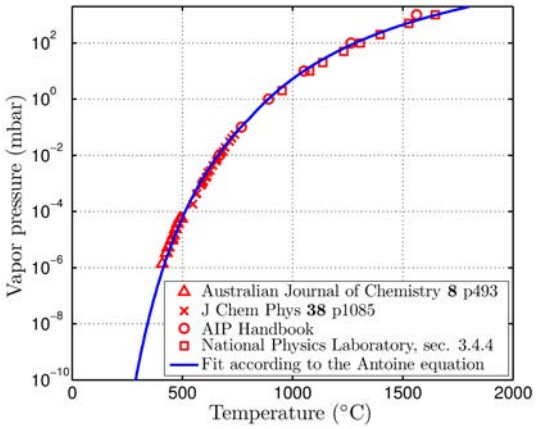

(a) Vapor pressure of Bi (fitted below and above 800 °C)

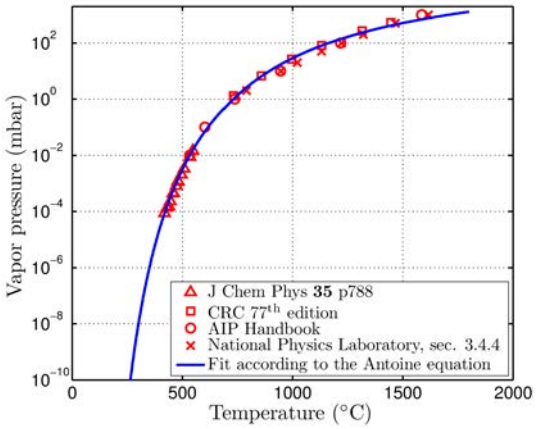

(b) Vapor pressure of Sb (fitted below and above 700 °C)

Figure 4.9.: Vapor pressure of bismuth and antimony versus temperature: Several experimental data points have been fitted using the Antoine equation. To cover the whole temperature range this was done using two adjacent fits.

If the vapor pressure of a material is higher than the required ultimate pressure of the vacuum system the material will limit the achievable ultimate pressure. Since the vapor pressure is a function of temperature the material's vapor pressure must remain low at the highest applied temperature (e.g. during the baking procedure)[97].
This is not only relevant for the construction of the vacuum chamber but also for materials used inside the chamber and hence also for the sample. Thus the vapor pressure of bismuth and antimony are shown in figure 4.9. Both Bi and Sb exhibit a vapor pressure that remains low enough in the relevant temperature range.

4.3. Additional Measuring Equipment

As already mentioned, the upper level of the main chamber provides a LEED and an XPS system. The principle of both surface analysis methods is described in the following together with the principle of a QMS and an ion sputtering gun.

4.3.1. QMS

Quadrupole mass spectrometers are used to detect particles according to their mass and to determine the partial pressure. In general, a mass spectrometer consists of an ion source, an analyzer and a detector. The particles are fist ionized in the ion source followed by a separation according to their mass to charge ratio in the analyzer.
In case of a QMS, the analyzer is built of four parallel electrodes in such a way that opposite electrodes have the same potential. A voltage of $U(t) = \pm U + V\cos(\omega t)$ is applied between two opposed electrodes. Consequently, the voltage determines the trajectories of the ions, that are moving along the center of the four electrodes. Thus for each voltage only particles with a certain mass to charge ratio are moving along a stable track and reach the detector where they are finally detected by a secondary electron multiplier[19,96].

4.3.2. Ion Sputter gun

Surface contaminants can be sputtered off together with the top layers of the sample by bombardment of the surface with noble gas ions (e.g. Ar^+). Therefore, a beam of ions is produced using an ion gun: Argon gas is admitted through a dosing valve into the ionization chamber of the gun, where the gas atoms are ionized via electron impact. The produced ions are then accelerated and directed towards the sample surface.
A side effect of the ion bombardment is the degradation of the smooth surface.

Hence subsequent annealing is required to restore the surface crystallography and to remove embedded and adsorbed Ar atoms. During this annealing process the sample is heated and then maintained at a suitable temperature for an appropriate time[17,96]

4.3.3. LEED

The main elements of a four-grid LEED system are shown in figure 4.10.

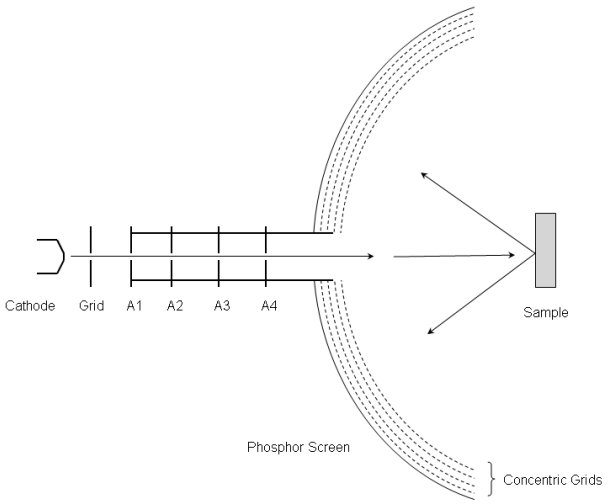

Figure 4.10.: Schematic diagram of a four-grid LEED

An electron gun is used to produce a beam of collimated low-energy electrons in the energy range of 30-500 eV. These electrons are directed towards the sample surface, where they are scattered. The de Broglie wavelength of the electrons is then given by[17]

$$\lambda[\text{Å}] \approx \sqrt{\frac{150}{E(\text{eV})}} \tag{4.1}$$

which corresponds to a wavelength ($\approx 1 - 2$ Å) of the order of the interatomic distances and hence satisfies the atomic diffraction condition.
In a four grid LEED system the sample and the first grid are at earth potential. Consequently, after the scattering process the electrons propagate through the field-free space towards the grid. In order to reject the inelastically scattered electrons, the potential of the second and the third grid is close to that of the cathode but somewhat lower in magnitude. Finally, the fourth gird is at earth potential again to screen other grids from the field of the fluorescent screen. After

passing the retarding field, the elastically scattered electrons are then reaccelerated towards the fluorescent screen, where they cause a light spot and the diffraction pattern is observed[2,17,96].

4.3.4. XPS

X-ray photoelectron spectroscopy is based on the photoelectric effect, where electrons are emitted from matter after the absorption of electromagnetic radiation such as X-rays (see figure 4.11(a)). The electron with an initial binding energy

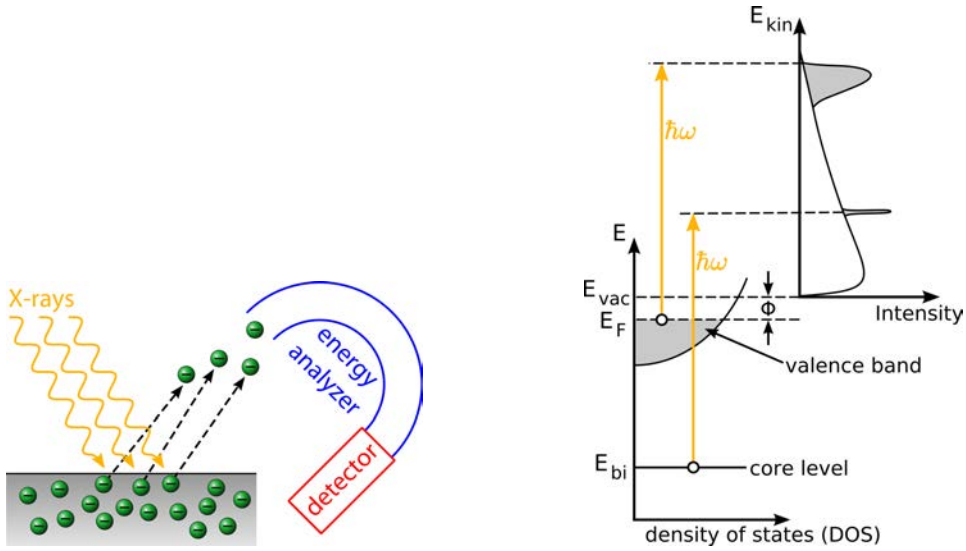

(a) Principle of an XPS

(b) Schematic illustration of the photoemission process

Figure 4.11.: Illustration of the principle of an X-ray photoelectron spectrometer

E_{bi} absorbs a photon of energy $\hbar\omega$ and leaves the solid with a kinetic energy E_{kin} according to:

$$E_{\text{kin}} = \hbar\omega - E_{bi} - \phi \tag{4.2}$$

where $\phi = E_{\text{vacuum}} - E_{\text{Fermi}}$ is the work function of the material (see figure 4.11(b))[1,17]. The X-rays are generated in a tube where a Mg anode is bombarded with high-energy electrons which gives rise to the emission of X-ray radiation with the characteristic $K_{\alpha 1,2}$ radiation at 1253.6 eV. A hemispherical electron energy analyzer is used to record the spectra of the photoemission electrons.

5. Characterization of the Apparatus

Although the apparatus described in this work was actually constructed at the FU Berlin, no HAS measurements were performed on it, before it was transferred to Graz. This fact and the reconstruction in Graz made it necessary to perform a number of measurements to characterize the apparatus and to ensure that it is running properly.
Most measurements were performed on LiF(001) since it is one of the most extensively studied surfaces by means of HAS[48,79,82–84,87,90,98,99] and it is easy to keep the surface clean even under poor vacuum conditions. In addition, some measurements were also conducted on Bi(111) which will be described in greater detail later on.

5.1. First Measurements on LiF and Calibration

5.1.1. Structure of LiF and Preparation

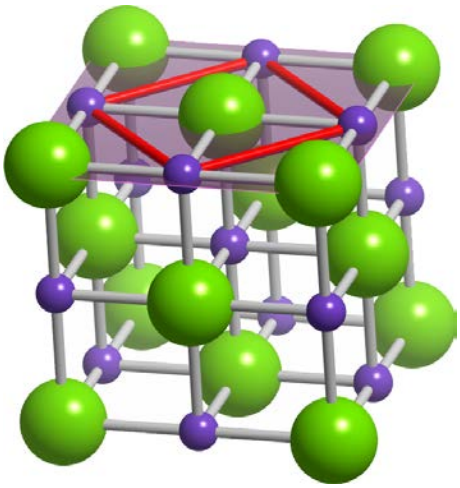

Figure 5.1.: Structure of the LiF crystal, purple spheres: Li, green spheres: F. The shaded area shows the (001) plane of the crystal whereupon the highlighted red square indicates the surface unit cell.

The structure of LiF and the (001) plane are illustrated in figure 5.1. Note that the surface unit cell (the red square) is rotated with respect to the bulk direction by 45° so that the ⟨110⟩ bulk direction corresponds to the ⟨10⟩ direction at the surface. The labeling of measurements on LiF(001) within this work always refers to the surface unit cell: A square with a side length of $a = 2.84$ Å[45].
The LiF(001) single crystal used for the HAS measurements was purchased from MaTecK. $3-4$ mm slices were cleaved from the single crystal with a cross-section of 10×10 mm^2 in air and mounted onto the manipulator. The cleavage results in an atomically flat surface with large terraces suitable for HAS experiments[100].
Active sites on the surface can be removed by annealing the crystal in vacuum at 430°C for several hours[100]. Hence the adsorption of water from the residual gas inside the vacuum chamber is prevented. The presence of sharp diffraction peaks as seen in figure 5.2 can also be regarded as evidence for a well-ordered and clean surface[48].

5.1.2. First Elastic Measurements

Figure 5.2 shows an angular distribution for He scattered from LiF(001) along the ⟨11⟩ azimuth. The angular position of the diffraction peaks (equation 3.10) is determined by the incident wavevector k_i (or the incident energy E_i) of the He beam. Using equation 2.22 and 2.23 k_i is given by the temperature of the nozzle T_N according to:

$$k_i = \frac{\sqrt{5mk_BT_N}}{\hbar}$$

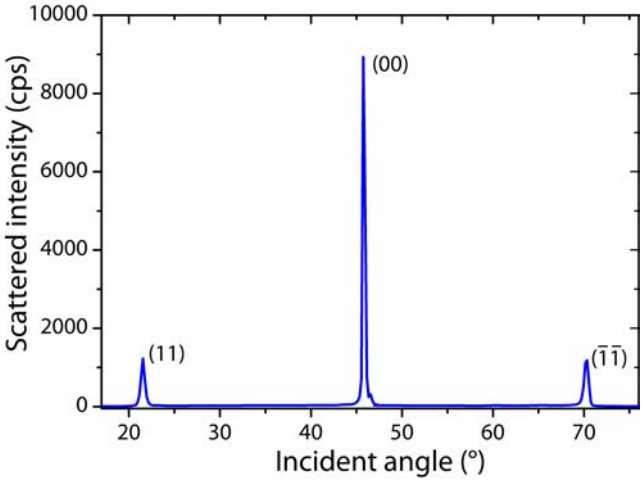

Figure 5.2.: He diffracted from LiF(001) along the ⟨11⟩ azimuth with $E_i = 15.5$ meV and the crystal at room temperature.

Although the nozzle temperature is measured using a Pt100 the actual temperature of the helium beam may differ from this value since the Pt100 is positioned next to the opening of the nozzle.
Therefore, an exact value for the incident energy E_i is best obtained either by using the position of diffraction peaks from a well-known surface structure or the time-of-flight of the elastic peak. To employ the TOF measurement for this purpose, an exact knowledge of the flight length is essential (section 5.1.4).

5.1.3. Determination of θ_{SD}

The construction of the apparatus is such that the mounting flanges that are connecting the main chamber with the source arm and the detector arm respectively, enclose an angle of approximately 90°. However, HAS measurements on a well defined surface structure can be used to obtain a more accurate value for the fixed angle θ_{SD} between source and detector.
According to equation 3.10 the incident angle θ_i of a diffraction peak is given by θ_{SD}, the incident wavevector k_i and the reciprocal lattice vector $\vec{G}_{hk}$. Hence the measurement of the angle θ_i at which a diffraction peak occurs can be used to calculate θ_{SD} if k_i and the involved $\vec{G}$-vector are known. Thus θ_{SD} can be readily calculated from equation 3.10.

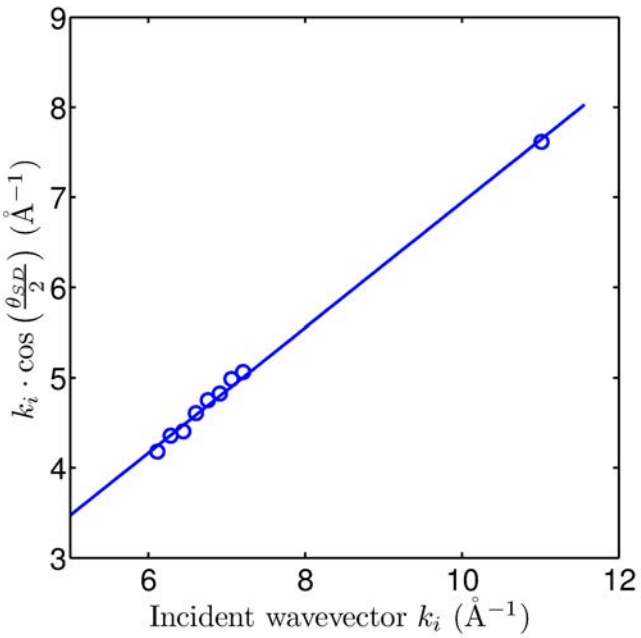

Figure 5.3.: Calibration of the fixed source detector angle θ_{SD}: $k_i \cdot \cos(\theta_{SD}/2)$ is plotted versus the incident wavevector k_i.

However, to exclude any uncertainties introduced by the measurement of the noz-

zle temperature, several measurements at different nozzle temperatures were performed. θ_{SD} was then calculated from the measured values of θ_i and $k_i \cdot \cos(\theta_{SD}/2)$ which was plotted versus k_i as shown in figure 5.3. Consequently, the slope of this plot determines θ_{SD}. From a linear fit, the fixed angle between source and detector is determined to be:

$$\theta_{SD} = (91.5 \pm 0.6)^\circ$$

5.1.4. Determination of L_{CD}

In addition to the source-detector angle the length between chopper and detector can also be determined experimentally with the aid of time-of-flight measurements. Therefore, a series of TOF spectra with varying nozzle temperature T_N were recorded. In figure 5.4(a) a few of the spectra are displayed. It clearly shows that the peak shifts to smaller times with increasing nozzle temperature. Since $v = L_{CD}/\mathrm{TOF}$, this can be used to determine L_{CD}.

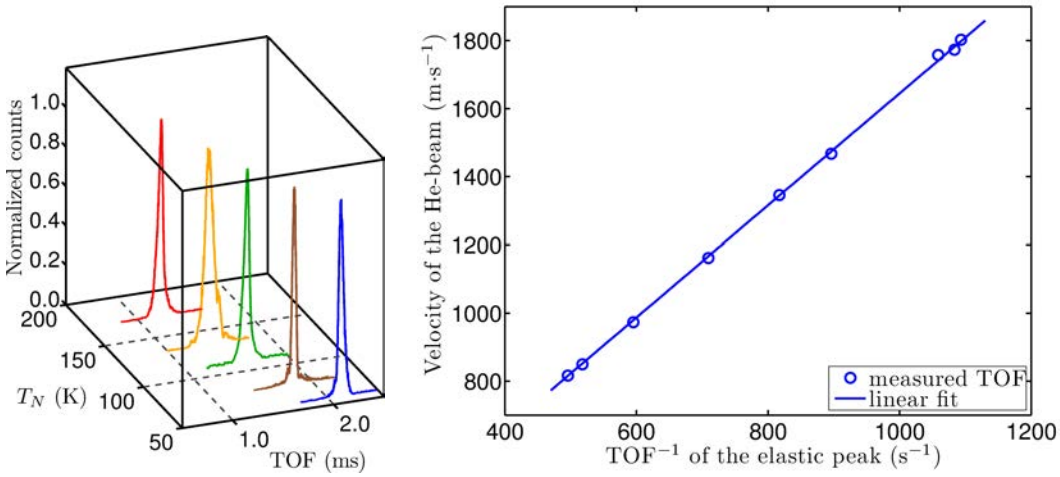

(a) Shift of the elastic TOF with increasing T_N

(b) Velocity of the He-beam as a function of the inverse TOF on the specular position

Figure 5.4.: Determination of L_{CD} using TOF measurements at different nozzle temperatures T_N: In a plot of the He velocity versus the inverse time-of-flight (figure (b)), the slope determines the chopper detector distance L_{CD}.

The TOF spectra were then fitted using a Gaussian function and the inverse time-of-flight was plotted versus the He velocity (figure 5.4(b)). Using a linear fit L_{CD} is determined by the slope according to $v = L_{CD}/\mathrm{TOF}$:

$$L_{CD} = (1643 \pm 5)\ \mathrm{mm}$$

Since this requires an exact knowledge of the velocity, elastic measurements were recorded previous to each time-of-flight measurement. The position of the diffrac-

tion peaks in the elastic measurement was then used to calculate the corresponding velocity.

5.2. Calibration of Time-of-Flight Measurements

The restraints to the resolution of a TOF spectrum have already been discussed in section 2.4.1 and it was shown that the TOF spectrum can be approximated by a Gaussian function with adequate accuracy.
Figure 5.5 shows a TOF spectrum of the elastic peak due to He scattered from LiF(001) using a single slit chopper disc. From the Gaussian fit of the data, the center of the peak $t_p = (2.0300 \pm 0.0002)$ ms and the full width at half maximum FWHM= (44 ± 1) μs is obtained. Note that the FWHM equals $2\sqrt{2\ln(2)} \cdot \sigma$ where σ^2 is the variance of the fitted Gaussian function.

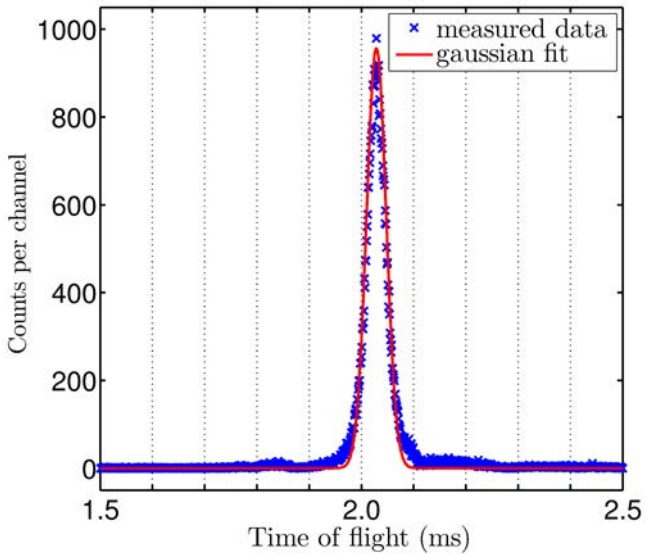

Figure 5.5.: TOF spectrum of the specular peak on LiF(001) surface. Nozzle temperature $T_N = 64$ K, chopper frequency $\nu_{Ch} = 253$ Hz, channel width $t_{mc} = 1$ μs, number of channels $N_{mc} = 1000$.

The true flight time t_f may be calculated according to $t_f = t_p + t_c - t_{ch}/2$ (equation 2.27) whereupon the correction according to the channel width $t_{mc}/2$ is negligible for $t_{mc} = 1$ μs. However, the correction time t_c is necessary due to the triggering of the chopper which causes a slightly altered time-of-flight [47]:
The time-of-flight measurement starts with a trigger signal which is caused when the emitted light of a diode passes through the chopper slit and is detected by a phototransistor. Due to the fact that the measurement starts with the falling edge of the trigger signal the measured flight time is slightly shorter than the true

flight time which is illustrated in figure 5.6.

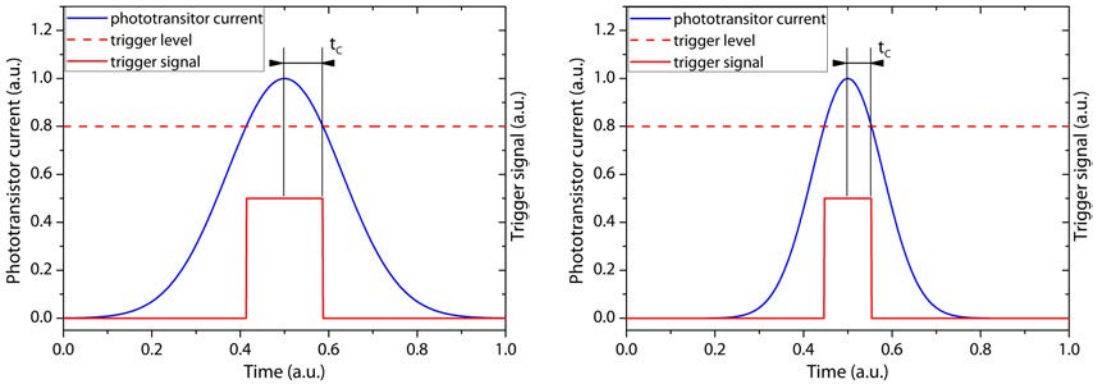

(a) Triggering at the falling edge causes a measurement of the flight time that is slightly shorter (by t_c) than the true flight time.

(b) With increasing chopper frequency ν_{ch} (compared to graph (a)) the correction time t_c decreases.

Figure 5.6.: Schematic illustration of the correction time t_c for the time-of-flight peaks due to the triggering.

Figure 5.6(a) and 5.6(b) show a comparison of the effect with increasing chopper frequency ν_{ch}. Thus t_c decreases with increasing ν_{ch}, whereby for $\nu_{ch} \to \infty$ the correction time approaches zero: $t_c \to 0$. In general

$$t_c = \alpha \cdot \frac{1}{\nu_{ch}} \tag{5.1}$$

holds[47]. Hence when measuring the peak time t_p at different ν_{ch}, α can be determined by calculating the slope in a plot of t_p versus $1/\nu_{ch}$. In figure 5.7 a plot of the described measurement on the LiF(001) specular position is shown. Therefore, a series of TOF spectra recorded with different ν_{ch} have been fitted using a Gaussian function and the center t_p was plotted versus $1/\nu_{ch}$. The slope of the linear fit gives a value of:

$$\alpha = -(5.4 \pm 1.2)\ \text{ms/s}$$

Thus with α the correction time $t_c(\nu_{ch})$ can be calculated according to equation 5.1 for any chopper frequency ν_{ch}.
With the knowledge of the flight time t_f (according to equation 2.27) and an exact knowledge of the flight length L_{CD} the beam velocity v and the beam energy E_i for figure 5.5 can be calculated:

$$v = \frac{L_{CD}}{t_f} = (801 \pm 15)\ \text{m/s}$$

$$E_i = \frac{mv^2}{2} = (13.3 \pm 0.5)\ \text{meV}$$

Note that the determined broadening of the velocity and the incident energy is not the same as the broadening due to the velocity spread of the incident beam. The velocity spread of the supersonic beam is much smaller and it is the resolution of the apparatus which adds to the initial spread of the beam. This broadening effects will be addressed in section 5.3.4.

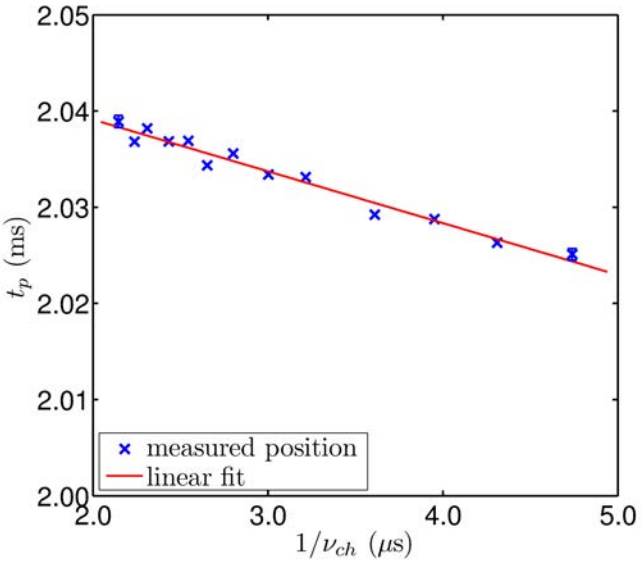

Figure 5.7.: Measured TOF peak position t_p against inverse chopper frequency $1/\nu_{ch}$. $T_N = 65$ K, $t_{mc} = 1$ μs, $N_{mc} = 1000$.

5.3. Resolution of the Apparatus

5.3.1. Influence of the Scattering Geometry on the Intensities

The scattered intensities in HAS measurements were addressed in section 3.4 from a theoretical point of view. However, the intensities that are measured in the experiment are also influenced by the geometry of the apparatus e.g. the diameter of the He beam or the acceptance angle of the detector.
So far, only the geometrical situation of a "classical Rutherford" scattering experiment has been considered. In this scattering configuration the incident He beam illuminates an area on the surface which is smaller than the area "seen" by the detector[67]. This situation is illustrated in figure 5.8 for the fixed source-detector geometry. In this case the illuminated area of the incident beam is so small with respect to the acceptance angle of the detector that $A_f^{'} > A_i^{'}$ holds[14].
However, the reverse configuration can also be realized. In particular if the illuminated area is considerably large and the detector arm is rather long the detector only "views" a small area within the illuminated spot, i.e. $A_f^{'} < A_i^{'}$. This situation is mainly the case for many HAS machines constructed by Toennies in Göttingen which is why this type will be regarded as the Toennies-type[67].

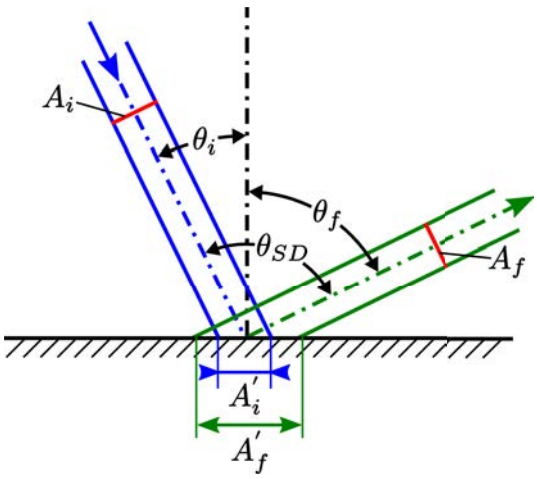

Figure 5.8.: Schematic graph illustrating the geometrical reduction of the surface area "seen" by the detector. In the displayed situation the area on the surface which is illuminated by the He beam ($A_i^{'}$) is smaller than the area "seen" by the detector ($A_f^{'}$) since $A_f^{'} > A_i^{'}$ holds. Note that $A_i^{'}$ and $A_f^{'}$ are functions of the scattering angles θ_i and θ_f.

Equation 3.35 introduced in section 3.4 which relates the scattered intensities $P_{\vec{G}}$ with the scattering amplitudes $A_{\vec{G}}$ via $P_{\vec{G}} = \frac{k_{Gz}}{k_{iz}}|A_{\vec{G}}|^2$ is only correct for the

Rutherford scattering configuration.
For such a scattering configuration in the case of a fixed source-detector geometry, a surface corrugation that is symmetric in the scanning direction would give rise to $|A_{+G}|^2 = |A_{-G}|^2$. That is, $|A_{\vec{G}}|^2$ is the same e.g. for $\vec{G}_{11}$ and $\vec{G}_{1\bar{1}}$ which is a consequence of the time reversal invariance of the Schrödinger equation[67].
However, the diffraction peaks corresponding to $+G$ and $-G$ do not have the same intensity. This is because the scattered intensity $P_{\vec{G}}$ at position $+G$ is not the same as it is at position $-G$ due to the kinematical factor $\frac{k_{Gz}}{k_{iz}}$ which is different at the two positions.
The conclusions made above hold for the Rutherford scattering configuration but for a Toennies-type HAS apparatus the situation is altered by the fact that the detector only "views" a small portion of the illuminated He spot on the surface. It can be seen from figure 5.8 that the effective surface areas are determined by $A_i^{'} = A_i \cdot \cos(\theta_i)$ and $A_f^{'} = A_f \cdot \cos(\theta_f)$.
Now, in order to compensate for the intensity of the illuminated spot as a function of incident angle, the intensity $P_{\vec{G}}$ must be multiplied by $\cos(\theta_i)$. The area within the illuminated spot that is "seen" by the detector increases with increasing θ_f, hence the intensity must be divided by $\cos(\theta_f)$ for compensation. Since $\cos(\theta_i)/\cos(\theta_f) = k_{iz}/k_{Gz}$ this factor exactly cancels the kinematical prefactor of equation 3.35 ($P_{\vec{G}} = \frac{k_{Gz}}{k_{iz}}|A_{\vec{G}}|^2$) and the measured intensity becomes simply $|A_{\vec{G}}|^2$. Therefore, in a Toennies-style apparatus with fixed source-detector geometry, the intensity of the $+G$ and $-G$ diffraction peak should give rise to the same scattered intensity in the case of a symmetric surface corrugation[67].

According to this conclusions the distinction between a Toennies-type apparatus and a classical Rutherford configuration can be simply made by carrying out a diffraction measurement on a surface that exhibits a symmetric corrugation. If the sample is properly aligned, the corresponding positive and negative diffraction peak intensities should be equal in case of a Toenneis type apparatus whereas the intensities should differ by the the kinematical prefactor for a Rutherford type apparatus[67].
In addition it shall also be noted that for a purely spectroscopic analysis e.g. if only the surface structure and the phonon dispersion curves are of interest the configuration of the machine is not important. While the position of the diffraction peaks gives rise to the surface structure, the phonon dispersion is determined via the position of the inelastic peaks relative to the diffuse elastic peak and the intensities do not come into play[67].

5.3.2. Broadening of the Angular Distribution

The finite width of the diffraction peaks in the angular distribution is mainly governed by two effects: The velocity spread and the angular width of the incident beam. The angular distribution which is recorded at the detector is a convolution of both broadening effects[50] which is illustrated in figure 5.9. For this consideration the detector width shall be treated as negligible fist.

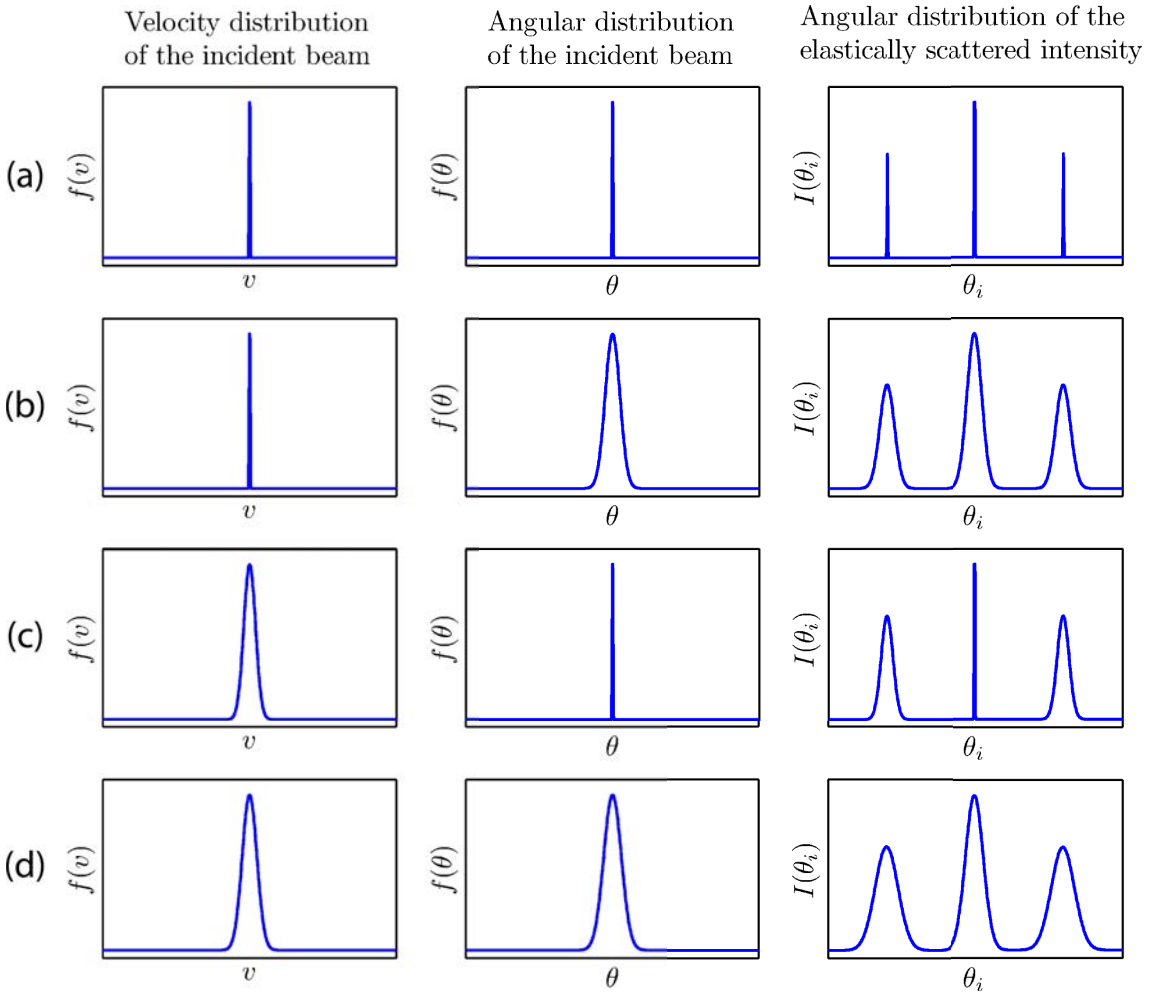

Figure 5.9.: A schematic illustration of the broadening effects due to the velocity and the angular spread of incident beam on the angular distribution. While the velocity spread affects only the diffraction peaks (c), the angular spread affects the specular peak as well (b). The angular distribution at the detector is the convolution of both effects (d).

In the case of an infinitesimally small velocity and angular spread the diffraction peaks would be small delta-like functions if a perfectly flat surface is provided

(case (a) of figure 5.9).
If an angular spread of the incident beam is introduced (case (b) of figure 5.9) both the diffraction and the specular peaks are broadened. This is a consequence of the fact that the angular width of the incident beam $\Delta\theta_i$ influences both the angle at which diffraction peaks appear (via equation 3.10) as well as the mirror reflection.
However, the broadening due to the finite velocity spread Δv (case (c) of figure 5.9) affects only the diffraction peaks but not the specular peak. This is because the velocity does not enter the condition for the mirror reflection ($\vec{G} = 0$), whereas it affects the position of the Bragg peaks according to equation 3.10 via k_i. In the picture of the Ewald construction the Ewald sphere is no longer a distinct sphere but a spherical shell due to Δv of the incident beam.
The final angular distribution shown in case (d) of figure 5.9 is the convolution of both effects[50].
In order to address this question from an experimental point of view, several angular distributions have been recorded using different apertures to manipulate the spot size. Figure 5.10 shows the angular distribution for He scattered from Bi(111) along the $\langle 11 \rangle$ azimuth. The slight asymmetry in the angular scans is likely to be caused by alignment problems.
The upper trace of figure 5.10 displays the elastic peaks with the x-axis greatly expanded to show the angular half-widths. Apparently, the angular distribution corresponds to case (d) of figure 5.9 where the broader width of the diffraction peaks with respect to the specular peak is caused by the velocity spread of the incident beam.
To gain further insight, the peaks were fitted with the sum of two Gaussian functions to account for the narrow coherent elastic contribution and for the broad diffuse elastic and multiphonon contribution[9]. The peak width of the narrow elastic contribution was then used to describe the broadening of the diffraction peaks. In particular, the angular width of the specular peak can be used to estimate the size of the He spot on the surface.

5.3.2.1. Angular Width of the Specular Peak

In order to estimate the size of the He spot on the surface the peak widths from the angular distribution can be used. For this purpose it makes sense to have a look at the specular peak rather than the diffraction peaks, since the specular peak is not affected by the velocity spread of the incident beam. It is solely the angular distribution which determines the width of the specular peak[50,67].
Figure 5.11 displays the fitted coherent elastic contribution that was extracted from figure 5.10. Obviously the diffraction peaks (graph (a) and (c)) are hardly

influenced by the aperture dimensions since their width is mainly governed by the energy spread of the incident beam. However, the angular width of the specular peak (b) clearly shows a decrease in the width for the smaller apertures.

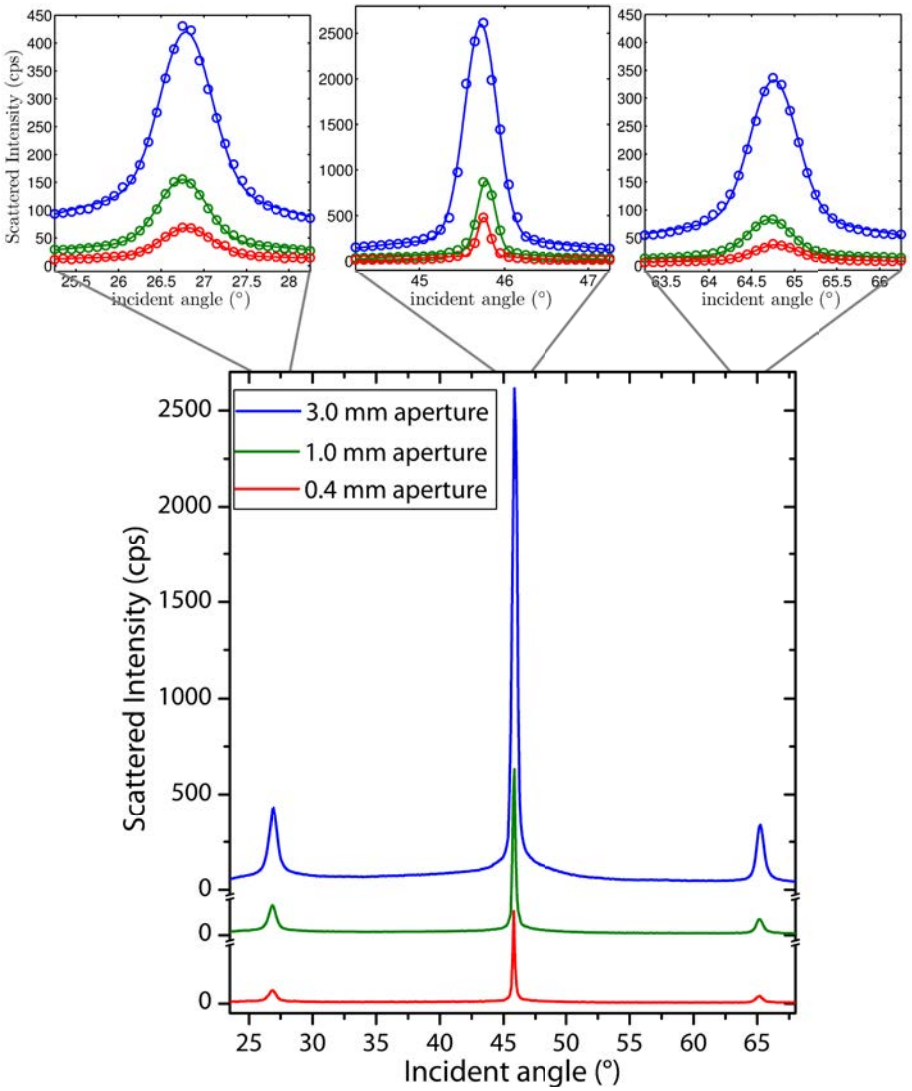

Figure 5.10.: Angular distributions for He scattered from Bi(111) along the ⟨11⟩ azimuth with $E_i = 19.4$ meV and $T_S = 300$ K. The three spectra were recorded using different apertures A1 (see figure 4.7) to manipulate the spot size. The upper trace displays a magnification of the elastic peaks which have been fitted with a sum of two Gaussian functions to account for the narrow coherent elastic contribution and for the broad diffuse elastic and multiphonon contribution.

Since the specular peak is to a first approximation simply mirror scattering, its size at the detector can be extrapolated back by using the distance from the sample to the detector to estimate the size of the illuminated spot on the sample

from the angular distribution measurement. This can be done using simple linear geometry according to the dimensions of the apparatus in figure 4.7.
Using FWHM= 0.45° for the specular peak monitored with the 3 mm aperture at the detector the extrapolated spot size at the position of the sample is 9 mm. The spot size on the sample is then enlarged by $1/\cos(\theta_f)$ giving rise to an area with a diameter of approximately 13 mm.
On the other hand, the approximate beam diameter on the sample as seen from the source can also be calculated using simple geometrical considerations. Therefore, the beam diameter at the position of the sample is given by the size of aperture A1 and its distance with respect to the source and the sample.
The actual spot size on the sample gets enlarged by the inverse cosine of the incident angle θ_i (see figure 5.8) yielding a value of approximately 10 mm. Consequently the estimated value of the spot size is comparable to the size extrapolated back from the measurement.

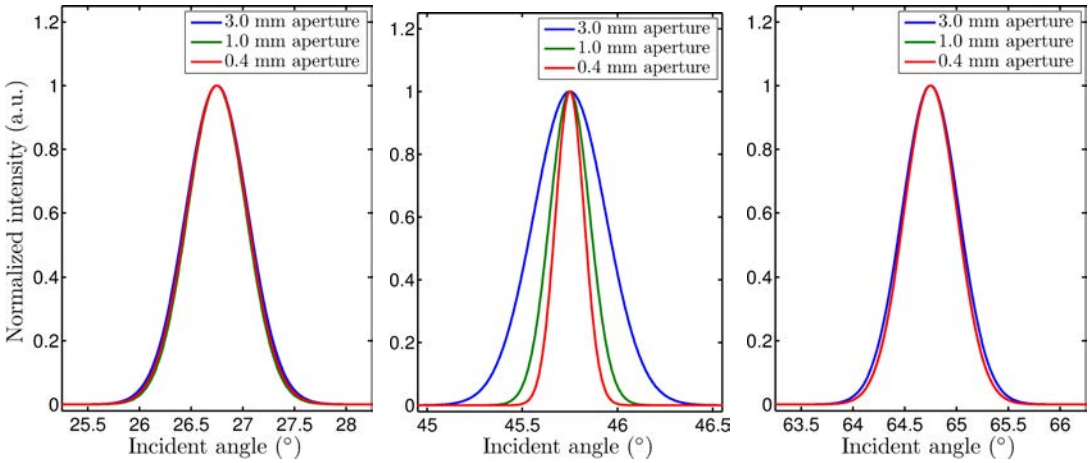

(a) (11) diffraction peak (b) Specular peak (c) $(\bar{1}\bar{1})$ diffraction peak

Figure 5.11.: Fitted coherent elastic contribution for the angular distributions of figure 5.10. The maximum of the peaks has been normalized to one in order to compare the measurements with different apertures.

Furthermore, the acceptance angle of the detector can be estimated using the distance between the detector and the aperture closest to the sample. Using this acceptance angle the area on the surface that is "seen" by the detector can be calculated. For the specular geometry this corresponds to an effective area with a diameter of 9 mm on the sample.
Notably, this value is also comparable to the two estimates of the illuminated spot size calculated above. Hence the surface area illuminated by the He beam may not always be wholly within the confines of the detector acceptance angle. In fact this suggests that the geometry in this case is neither a pure "Rutherford" type,

nor a "Toennies" type, but in a region in between the two[67].
Applying the same geometrical considerations for the remaining two apertures, it is only the 0.4 mm aperture which gives rise to an estimated spot size that is small enough to be completely within the acceptance angle of the detector. This geometrical situation would correspond to the "classical Rutherford configuration", at least for values of θ_i not too far away from the specular position.
However, by using this aperture, the overall intensity decreases giving rise to a trade-off between resolution and intensity. Thus in most measurements the 3 mm aperture was used since this issue is not important in a purely spectroscopic analysis as mentioned above.

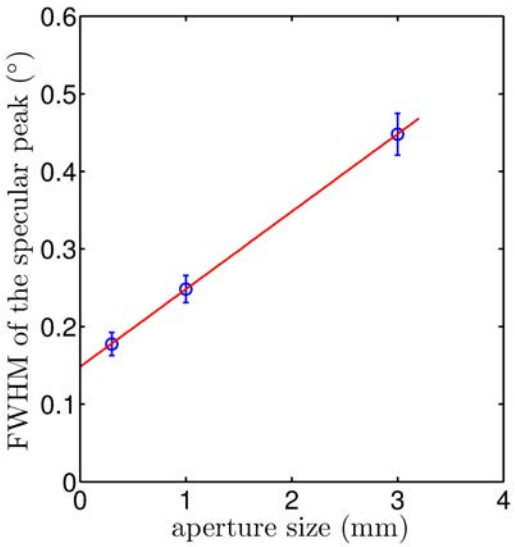

Figure 5.12.: FWHM of the specular peak from (figure 5.11(b)) as a function of the aperture diameter.

The above described crude estimate of the detector acceptance angle does not include the possibility of misalignments e.g. of the apertures in the detector arm. Therefore, it shall be tried to extract an estimated value of the acceptance angle from the experimentally measured widths that have been recorded with different apertures.
Plotting the FWHM of the specular peak (from figure 5.11(b)) versus the aperture size gives rise to a straight line as shown in figure 5.12. Assuming that an aperture size approaching zero corresponds to a beam width of vanishing diameter, the width at the detector would solely be determined by the acceptance angle of the latter.
In doing so, the intersection of the linear fit in figure 5.12 with the y-axis yields an acceptance angle $\Delta\theta_{det} = (0.15 \pm 0.01)°$. Certainly, this estimated value should be treated with care, in particular its use for quantitative conclusions.

5.3.2.2. Angular Width of the Diffraction Peaks

The angular width of the diffraction peaks is governed by both the angular width and the velocity spread of the incident beam. According to Valbusa the angular width of the diffraction peaks due to the velocity spread of the incident beam is determined by[55]:

$$\Delta\theta = \frac{G}{k_i \cos(\theta_f)} \frac{\Delta v}{v} \tag{5.2}$$

where the angular broadening of the incident beam is neglected. In a more realistic consideration of the experimental setup, the angular width of the incident beam has to be considered as well as the dimensions of the apparatus.
According to Doak the angular distribution as it is recorded in figure 5.10 suggests a geometrical situation where the beam width w_b is larger than the detector width w_d: $w_b > w_d$. This is supported by the fact that in the reverse case the angular broadening would be determined by w_d and the effect of velocity broadening would not be seen in the diffraction peaks[50].
Based on $w_b > w_d$ an expression for the beam width w_b at the detector position can be derived using the final scattering angle θ_f according to the Bragg equation 3.7: $\theta_f = \arcsin[G/k_i + \sin(\theta_i)]$. For each reciprocal lattice vector G, w_b is then calculated via[50]:

$$w_b = \Delta\theta_i \cdot L_{SD} + \left(\left| \frac{\partial \theta_f}{\partial \theta_i} \right| \cdot \Delta\theta_i + \left| \frac{\partial \theta_f}{\partial k_i} \right| \cdot \Delta k_i \right) L_{TD} \tag{5.3}$$

where $\Delta\theta_i$ is the angular broadening of the incident beam and L_{SD} is the distance from source to detector. The first term of equation 5.3 describes the angular broadening of the incident beam along L_{SD} and the second term describes the broadening of the scattered beam due to Δk_i and $\Delta\theta_i$ along L_{TD}.
Indeed, equation 5.3 assumes that the respective contributions add linearly whereas they actually correlate in a rather complex fashion and effects that are associated with the clipping of the beam by target edges or apertures are neglected[11]. Nonetheless equation 5.3 can be used to calculate an approximate value for w_b. The relative angular width of the diffraction peaks at the detector is then given by w_b associated with the diffraction peak relative to w_b of the specular peak.
The experimentally determined FWHM (using the coherent elastic contribution) in the angular distribution of figure 5.10 recorded with the 3 mm apertures are:

(11): FWHM $= (0.71 \pm 0.05)^\circ$
(00): FWHM $= (0.45 \pm 0.03)^\circ$
($\bar{1}\bar{1}$): FWHM $= (0.64 \pm 0.04)^\circ$

By applying 5.3 with $\Delta k_i / k_i = 0.01$ to this measurement, the predicted angular broadenings are $(0.80 \pm 0.08)^\circ$ for the (11) diffraction peak and $(0.48 \pm 0.03)^\circ$ for

the $(\bar{1}\bar{1})$ peak. Although the angular broadening of the (11) peak is somewhat over-estimated and the $(\bar{1}\bar{1})$ is under-estimated the overall trend in the angular distribution is reproduced. The deviations may be attributed to clipping effects introduced by the target edges or the apertures in combination with enlargement of the effective surface area (figure 5.8) at the diffraction angles.

5.3.3. Transfer Width and Surface Coherence Length

The transfer width is a quantum length, describing the size of the quantum mechanical wave packet assigned to an individual He atom[67]. As described in chapter 3 diffraction patterns in HAS are caused due to the superposition of individual diffraction events. Each diffraction event corresponds to the interference of an incoming particle with itself, whereupon the measured signal is a superposition of many individual diffraction events in a given time interval[8]. Therefore, the coherence of the helium beam as well as the perfection of the crystal surface are essential.
Comsa[101] addressed the question of the angular width of the peaks and whether they are limited by the apparatus itself or the surface imperfections. Thereby the transfer width represents the minimum lateral dimension over which the surface must be perfect to give rise to diffraction peaks which are limited in width solely by the resolution of the instrument[8]. According to Comsa the angular spread at the detector which is caused by the geometry of the apparatus is given approximately by[9,46,101]:

$$(\Delta\theta \cdot \theta_f)^2 \approx \left(\frac{\cos\theta_i}{\cos\theta_f}\frac{\delta_s}{D_S}\right)^2 + \left(\frac{\cos\theta_i}{\cos\theta_f}\frac{\delta_a}{D_a}\right)^2 + \left(\frac{\cos\theta_f}{\cos\theta_i}\frac{D_s}{D_d}\frac{\delta_a}{D_a}\right)^2 + \left(\frac{\delta_d}{D_d}\right)^2 \quad (5.4)$$

The four terms represent the contribution of the source dimension, of the aperture, of the spot size and of the detector opening[101]. Figure 5.13 illustrates the relevant geometrical dimensions which can be found in section 4.

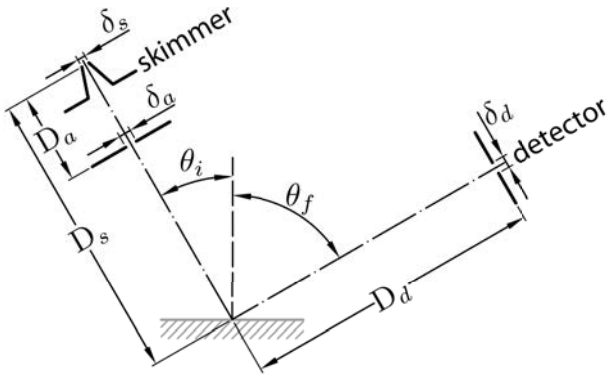

Figure 5.13.: Schematic diagram illustrating the geometrical parameters used to calculate the angular broadening according to equation 5.4.

The contribution to the transfer width due to this geometrical factor is then given by[9,46]:

$$w_\theta \approx \frac{\lambda}{\Delta\theta \cdot \theta_f \cos(\theta_f)} \tag{5.5}$$

Using equations 5.4 and 5.5 with the same parameters as in the measurement shown in figure 5.14, $\Delta\theta = 1.1°$ and $w_\theta \approx 100$ Å are calculated. However, the experimentally determined angular broadening of the peak exhibits only a FWHM of $(0.26 \pm 0.02)°$.
This suggests that equation 5.5 cannot be applied to the geometry of the used HAS apparatus in the current form. The origin of the smaller than expected angular width could be caused due to a clipping of the He beam by an improper alignment of the apertures.
Furthermore, Comsa has received criticism on how he develops the idea of a transfer width[67,102,103]. In particular John Pendry who derived a formula for the correlation length in LEED measurements concludes that it cannot be used to predict any specific broadening[103]. Hence equation 5.4 should be treated carefully in the prediction of any angular broadening.

Nevertheless, Comsa obtains an important result for the transfer width w in atom diffraction in analogy to LEED experiments. Depending on the angular and the energy spread, w is given by[8,9,46]:

$$w \approx \frac{\lambda}{\sqrt{(\Delta\theta \cdot \theta_f)^2 \cos^2(\theta_f) + [\sin(\theta_i) - \sin(\theta_f)]^2 \, \overline{(\Delta E)^2}/E^2}} \tag{5.6}$$

where $\overline{(\Delta E)^2}$ is the mean square energy spread of the beam. Certainly, equation 5.6 requires an accurate determination of $\Delta\theta$ but it is widely excepted by the community since it can be derived in analogy to concepts known from LEED[103]. Note that the contribution of the energy spread disappears for the mirror geometry $\theta_i = \theta_f$. Hence it has no influence on the angular width of the specular beam[101].
In order to obtain a large transfer width, the angular divergence of the incident beam has to be minimized and a small acceptance angle of the detector is desirable. However, these steps will also give rise to a reduction of the intensity at the detector[8,9].

While the transfer width describes the limitations that are imposed by the apparatus on the diffraction experiment, an additional broadening originates from the so-called surface coherence length. This dimension describes the part of the broadening which is caused by surface imperfections rather than the restraints of the apparatus[9].
Usually, all real surfaces exhibit a finite concentration of defect sites e.g. steps

and terraces which adds the broadening $\Delta\theta_w$ to the peak width[104]. The measured overall width in the angular distribution $\Delta\theta_{tot}$ is then given by the formula for two folded Gaussian distributions:

$$\Delta\theta_{tot}^2 = \Delta\theta_w^2 + \Delta\theta_{app}^2 \tag{5.7}$$

where $\Delta\theta_{app}$ is the contribution due to the instrumental limitations discussed above and $\Delta\theta_w$ is the broadening caused by the finite domain sizes of the crystal. Thereby the crystal can be thought of as being composed of perfectly ordered domains which have however, only a finite diameter and are separated by grain boundaries and steps. Consequently, the trajectories of He atoms scattered from two domains, e.g. from an upper and a lower terrace will interfere which adds in the case of destructive interference to a broadening of the peak width[3].
Assuming that the trajectories from various domains add incoherently, the peak broadening is proportional to the average domain size l_c also known as the surface coherence length[3,9,105].

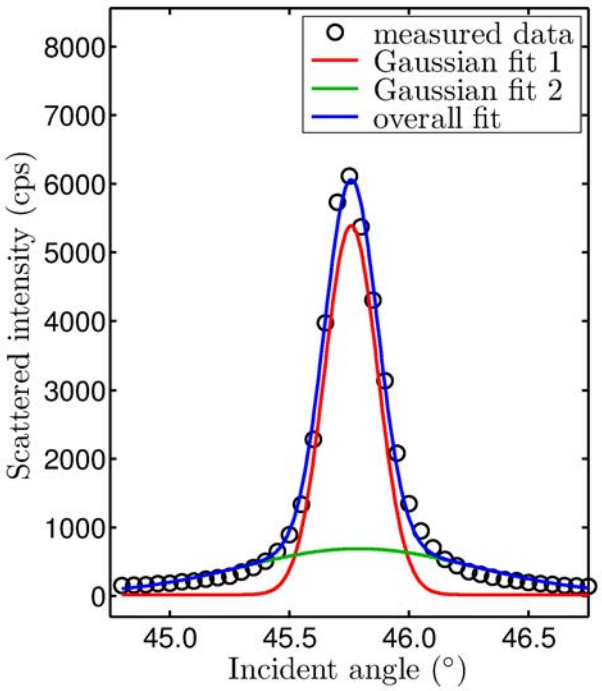

Figure 5.14.: Specular peak for He scattered from Bi(111) with $E_i = 17.7$ meV and $T_S = -110$°C. The data points (open circles) were fitted with the sum of two Gaussians to account for the coherent elastic peak (red curve) and the broad diffuse elastic/multiphonon background (green curve). The blue line is the overall fit to the measured data. The full width at half maximum of the narrow coherent elastic peak is FWHM= (0.26 ± 0.02)°.

Using equation 5.7 $\Delta\theta_w$ can be readily calculated form the measured width of the diffraction peak if $\Delta\theta_{app}$ is known. $\Delta\theta_w$ can then be used to determine the average domain size l_c by[69,104,105]:

$$l_c = \frac{5.54}{\Delta\theta_w \cdot k_i \cos(\theta_f)} \tag{5.8}$$

This equation can be applied to determine l_c for Bi(111) from the measurement of the specular peak which is shown in figure 5.14. Therefore, the measured data was fitted with two Gaussian functions in order to account for the narrow coherent elastic contribution and the broad diffuse elastic/multiphonon contribution[9,69]. A FWHM= 0.26° was determined from the fit of the coherent elastic contribution. Since we are dealing with the broadening of the specular peak, the velocity spread does not come into play. In a first estimate we will use the acceptance angle of the detector determined in section 5.3.2.1 for the broadening of the apparatus $\Delta\theta_{app} = 0.15°$.
Therefore, the FWHM of the specular peak $\theta_{tot} = 0.26°$ gives rise to an average domain size of approximately 400 Å as calculated from equation 5.7 and 5.8. This value is reasonable in comparison with other experimentally determined surface coherence lengths[69,104], although it should be treated with care if used for any quantitative conclusions.

5.3.4. Resolution of TOF Measurements

The question of resolution effects in TOF measurements was addressed shortly in section 2.4.1. According to equation 2.26 the halfwidth (FWHM) of the measured TOF peaks Δt_G is caused by several contributions[11,14,47]:

Δt_g^2 velocity distribution of the He beam
Δt_C^2 finite width of the chopper slit
Δt_D^2 finite ionization length of the QMS

To extract the true width of the TOF distribution a precise knowledge of the broadening caused by the mechanical restraints (Δt_C and Δt_D) is essential. The broadening effects may be estimated according to[11,14,23]:

$$\Delta t_g = L_{CD} \cdot \frac{\Delta v}{v^2} \tag{5.9}$$

$$\Delta t_D = \frac{X_D}{v} \tag{5.10}$$

$$\Delta t_C = \frac{w_{ch} + w_{be}}{2\pi \cdot r_{ch} \cdot \nu_{ch}} \tag{5.11}$$

with the beam velocity v, Δv the FWHM of the velocity distribution and X_D the ionization length of the QMS detector. The broadening due to the chopper opening

5.11 is described using a trapezoidal shape rather than a Gaussian function due to the fact that the He beam width w_{be} is larger than the slit width w_{ch} of the chopper. In this case Δt_C is determined by w_{ch}, w_{be}, r_{ch} the radius of the chopper disk at the position of the entering He beam and ν_{ch} the frequency of the chopper[23].
The width of the He beam at the position of the chopper is calculated using geometrical considerations according to figure 4.7) giving rise to $w_{be} = (2.9 \pm 0.1)$ mm. For the single chopper disc and the ionization length of our detector the following values hold:

$$r_{ch} = (84 \pm 1) \text{ mm}$$
$$w_{ch} = (0.55 \pm 0.05) \text{ mm}$$
$$X_D = (8 \pm 1) \text{ mm}$$

For the measurement shown in figure 5.5 the broadening according to equations 5.10 and 5.11 becomes:

$$\Delta t_D = (10 \pm 1) \ \mu\text{s}$$
$$\Delta t_C = (26 \pm 1) \ \mu\text{s}$$

It is important to note that the broadening due to the finite ionization length $\Delta t_D(v)$ is a function of the beam velocity v i.e. with increasing nozzle temperature T_N, $\Delta t_D(v)$ will consequently become smaller due to the increasing v.
If the fact that the chopper gating function is not a true Gaussian is neglected, the broadening Δt_T of the apparatus according to equation 2.26 becomes :

$$\Delta t_T = \sqrt{\Delta t_C^2 + \Delta t_D^2} = (27.6 \pm 1.5)\mu\text{s}$$

The broadening due to the finite chopper opening can also be determined experimentally. Therefore a series of time-of flight spectra with varying chopper frequency ν_{ch} is recorded. The TOF spectra are fitted using a Gaussian and the FWHM Δt_G is then plotted versus the inverse chopper frequency $1/\nu_{ch}$ (figure 5.15).
Using equation 5.11 for $\nu_{ch} \to \infty (1/\nu_{ch} \to 0)$, the chopper broadening approaches zero: $\Delta t_C \to 0$. Hence the broadening of the TOF peak Δt_G according to equation 2.26) simplifies to:

$$\Delta t_G(\nu_{ch} \to \infty) \to \sqrt{\Delta t_g^2 + \Delta t_D^2}$$

From the linear fit in figure 5.15 the value for $1/\nu_{ch} = 0$ is determined to be $\Delta t_G(1/\nu_{ch} = 0) = (33 \pm 1) \ \mu$s. Using this value the experimentally determined broadening for $\nu_{ch} = 253$ Hz is:

$$\Delta t_C = \sqrt{\Delta t_C^2(\nu_{ch} = 253 \text{ Hz}) - \Delta t_C^2(\nu_{ch} \to \infty)} = (29.1 \pm 2.5) \ \mu\text{s}$$

The broadening of the apparatus becomes:

$$\Delta t_T = \sqrt{\Delta t_C^2 + \Delta t_D^2} = (30.8 \pm 2.8)\ \mu\text{s}$$

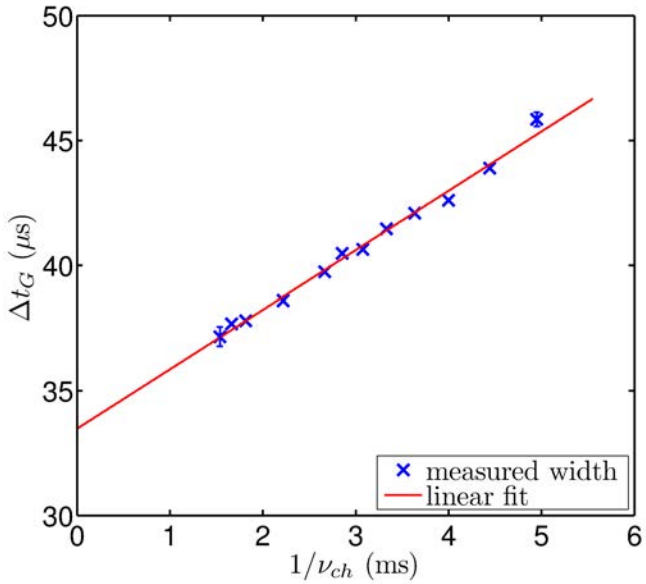

Figure 5.15.: FWHM Δt_G of the TOF peak on the specular position against $1/\nu_{ch}$. $T_N = 65$ K, $t_{mc} = 1$ μs, $N_{mc} = 1000$.

Once the broadening of the apparatus is known the broadening of the velocity distribution of the He beam Δt_g^2 is calculated using equation 2.26:

$$\Delta t_g^2 = \Delta t_G^2 - \Delta t_T^2 = \Delta t_g^2 - \underbrace{\left(\Delta t_C^2 + \Delta t_D^2\right)}_{=\Delta t_T^2}$$

Using the calculated value for the broadening of the chopper Δt_g becomes:

$$\Delta t_g = (34 \pm 2)\ \mu\text{s}$$

$$\Delta v/v = (1.7 \pm 0.1)\ \%$$

The experimentally determined value of Δt_C gives rise to:

$$\Delta t_g = (32 \pm 4)\ \mu\text{s}$$

$$\Delta v/v = (1.5 \pm 0.2)\ \%$$

The broadening introduced due to non ideal components of the apparatus according to equation 5.9-5.11 can in principle be minimized. Hence it is advantageous to minimize L_{CT} and X_D and to maximize L_{TD}. However, from an experimental point of view the minimization is limited by the need of accessibility and vacuum pumping considerations and L_{TD} is limited by the intensity loss with increasing length[106].

5.3.5. Resolution of Phonon Dispersion Measurements

In the previous section the resolution of TOF measurements was addressed. In determination of the phonon dispersion from TOF measurements this resolution as well as additional aspects that will be discussed in in the following come into play.

According to Doak[11] a feature in the TOF spectrum with the energy transfer $\hbar\omega$ and a time of flight broadening Δt gives rise to an energy spread ΔE_f of the final energy by:

$$\frac{\Delta E_f}{E_i} = 2\left(1+\frac{\hbar\omega}{E_i}\right)^{3/2}\frac{\Delta t}{t^e_{TD}} \tag{5.12}$$

where t^e_{TD} is the elastic target-to-detector flight time. Equation 5.12 describes the effective energy resolution of the apparatus for a certain phonon energy and TOF broadening. According to this the resolution becomes best if $\frac{\Delta E_f}{E_i}$ approaches zero, i.e. for extreme creation events ($\hbar\omega < 0$, $\hbar\omega \approx E_i$). However, due to the conversion from TOF to phonon energy this is hardly accessible for reasons described in section 3.3.3. On the other hand, the resolution becomes very poor for extreme annihilation events or very low beam energies[14].

In order to deal with the energy resolution the broadening shall be treated on the energy scale. Assuming the individual broadening components to be Gaussian distributions, the energy spread that is made up of four components is given by:[14,106]:

$$\Delta E_f^2 = \Delta E_C^2 + \Delta E_D^2 + \Delta E_{CT}^2 + \Delta E_{en}^2 \tag{5.13}$$

The first three terms describe the resolution of the apparatus in TOF measurements (see section 5.3.4) and appear also in the case of an energy analyzed elastic event.

They can be readily calculated from the corresponding contributions in the TOF broadening (equations 5.9, 5.10, 5.11) with ΔE_C the broadening of the chopper opening function, ΔE_D the broadening due to the ionizer length and ΔE_{CT} the broadening caused by the velocity spread of the incident beam along the chopper target distance[11,106].

In contrast to this, the last term ΔE_{en} of equation 5.13 is inherent to any inelastic scattering event that involves surface phonons. It adds an additional broadening after the phonon creation or annihilation process, due to the dispersion in the passage time from target to the detector and is composed of two components[106]:

$$\Delta E_{en} = dE_i + d\hbar\omega \tag{5.14}$$

where dE_i accounts for the dispersion resulting from the velocity spread in the incident beam. $d\hbar\omega$ describes the so-called kinematic smearing effect.

As described in section 3.3.3, the observation of phonon events is restricted to

intersection points between the scan curve and the phonon dispersion relation. Therefore, the term $d\hbar\omega$ describes the uncertainty in the phonon energy at this intersection point[106].

In the case of an ideal beam with zero velocity and angular spread, the scan curve is a narrow line. In this case the uncertainty is mainly given by the angle of intersection between the scan curve and the dispersion curve. Hence the resolution is worst at angles where kinematic focusing appears[14], i.e. when the scan curve is tangent to the dispersion curve. This is illustrated by the green curve in figure 5.16.

Therefore, the scattering geometry should be chosen in a way that the scan curve crosses the dispersion curve as close to right angles as possible. The effect of kinematic focusing can be mainly avoided by measuring only annihilation-backward and creation-forward phonons[14,106].

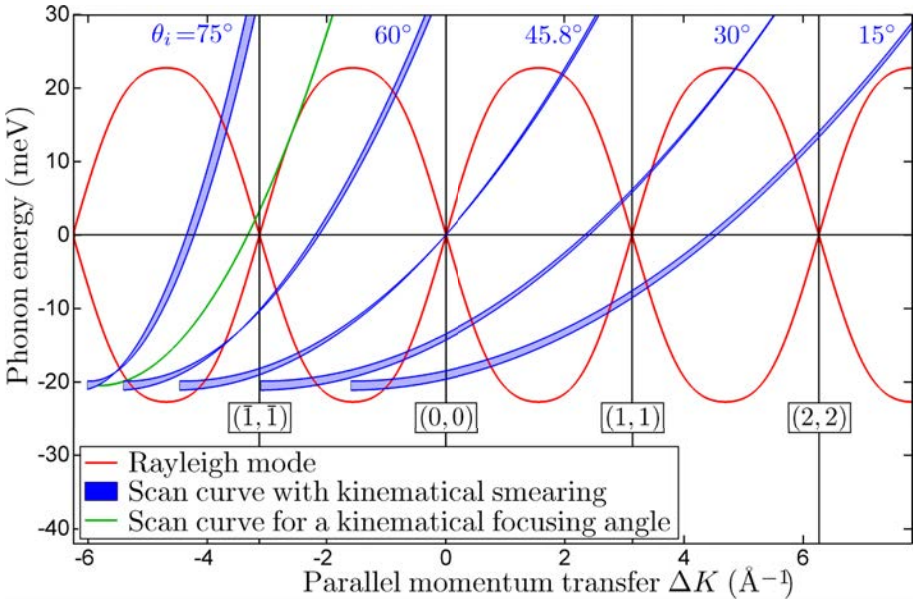

Figure 5.16.: Illustration of the kinematic smearing effect due to the velocity spread of the incident beam. Scan curves at different θ_i with k_i ranging from 6.18 Å^{-1} to 6.38 Å^{-1} are superimposed onto the dispersion relation according to[48]. In addition, the scan curve for a kinematical focusing angle (green curve) is plotted.

For a "real" beam the scan curve is no longer a narrow line. Depending on the velocity and angular spread of the incident beam the scan curve is smeared out over a certain region. An intersection of this scan curve with the phonon dispersion relation occurs if the scan curve S according to equation 3.15 equals the phonon energy $\hbar\omega$:

$$\hbar\omega = S\left[k_i, \theta_i, \theta_f, \Delta K\left(\hbar\omega\right)\right] \tag{5.15}$$

The uncertainty $d\hbar\omega$ at this intersection point is then given by[14,106]:

$$d\hbar\omega = \frac{\partial S}{\partial k_i}dk_i + \frac{\partial S}{\partial \theta_i}d\theta_i + \frac{\partial S}{\partial \theta_f}d\theta_f + \frac{\partial S}{\partial \Delta K}\frac{\partial \Delta K}{\partial \hbar\omega}d\hbar\omega \tag{5.16}$$

where the last term accounts for the kinematical focusing effect described above. The first three terms account for the velocity and angular spread of the incident beam.
The consequence of this fact on the uncertainty of the intersection point can be visualized graphically. In figure 5.16 the influence of the velocity spread is shown: A number of scan curves are plotted for an incident beam with $k_i \pm \Delta k_i$ (somewhat exaggerated with respect to the actual velocity spread). The intersection with the dispersion relation is no longer a single point but a range of phonon energies and wave vectors.
Despite this smearing due to the velocity spread, the angular spread of the incident beam has a similar effect. However, it can be seen from 5.16 that it is generally possible to pick scattering angles at which kinematic smearing is not a major concern in terms of resolution[3].
Finally, an explicit expression for the kinematical smearing given in terms of the angular spread $\Delta\theta_i$, $\Delta\theta_f$ and the velocity spread ΔE_i can be found in the publication of Smilgies et al.[106].

In addition to resolution considerations, resonance effects described in section 3.6 can be used to enhance inelastic processes under certain kinematic conditions. Thereby phonon modes to which HAS is less sensitive, e.g. optical modes, can be amplified using final-state inelastic resonances or focused inelastic resonances[85,86].

5.3.6. Elastic Effects in Inelastic Measurements

The analysis of TOF measurements has to be carried out carefully since the TOF spectrum may contain peaks that appear to be phonons but are not. In the literature those events are called deceptons or spurions due to their deceptive / spurious nature[11,99]
One of the most commonly observed effects is due to an elastic scattering event that is falsely assigned as an inelastic event. These deceptons are caused due to elastic diffraction from the wings of the incident velocity distribution[99]. It is evident that the elastic diffraction of He atoms with a velocity v^* that differs significantly from the most probable speed v_0 gives rise to a flight time that is considerably shifted from the median elastic scattering flight time by:[14]

$$\Delta t_{TOF} = L_{CD}\left(\frac{1}{v_0} - \frac{1}{v^*}\right) \tag{5.17}$$

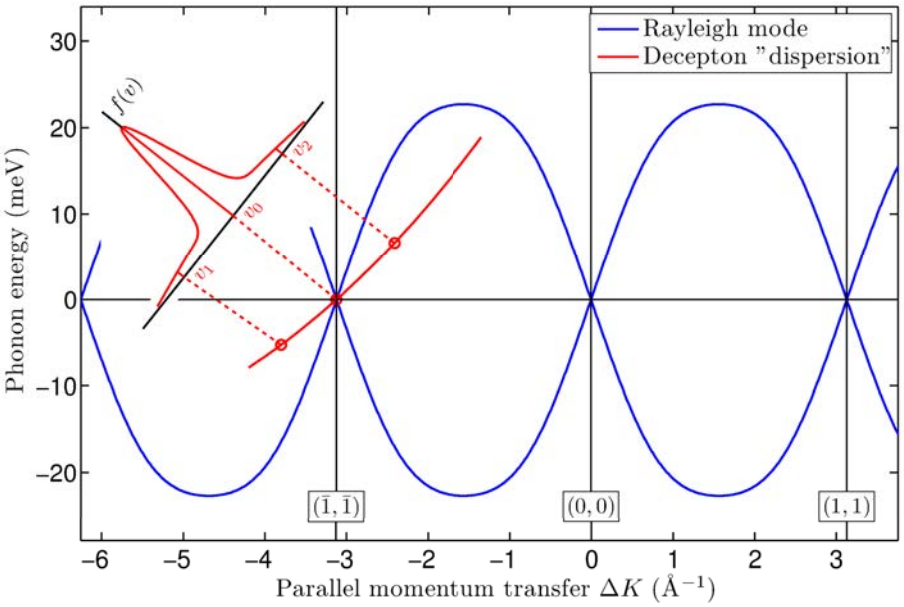

(a) Elastic diffraction of the low-intensity tails of the incident beam that could be mistaken as phonons (red dots) .

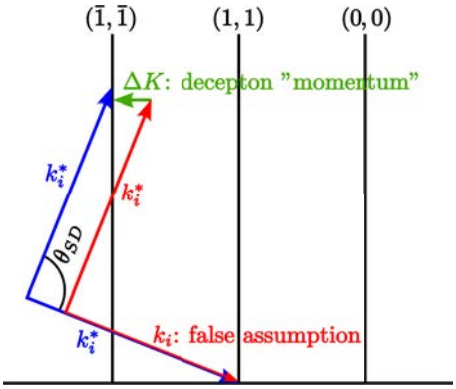

(b) The origin of a decepton due to elastic diffraction of helium with k_i^* illustrated in k-space. The false assumption of an incident wavevector k_i yields to a deceptive phonon event with the momentum transfer ΔK

Figure 5.17.: Appearance of deceptons in TOF measurements and the origin of the peaks illustrated in reciprocal space.

Hence assigning this peak in the TOF spectra falsely to an inelastic event and determining the dispersion relation using the usual scan curve gives rise to an "anomalous" dispersion which is illustrated in figure 5.17.
The intensity of these decepton peaks in the TOF measurements is comparable to the intensity of true phonon features. Thus the tails that give rise to them must be only about 10^{-3} of the peak intensity[11,107]. For that reason the undesired

elastic components can be explained due to the presence of a very weak additional beam component with a broad Maxwellian velocity distribution[14].
However, once knowing the origin of the deceptons it is relatively easy to distinguish between deceptons and "real" phonons in the dispersion relation. Since the deceptons are due to diffraction they only occur in the vicinity of diffraction peaks and not near the specular peak[11].
Furthermore a pseudo "dispersion" of the deceptons can be plotted together with the phonon dispersion relation whereupon points that lie on this decepton "dispersion" curve are likely due to the undesired elastic components. Therefore, the energy exchange ΔE and the parallel momentum transfer ΔK are calculated for a range of velocities v^* in the following way:
The typical conversion from TOF to ΔE and ΔK for each v^* is determined. Thereby the energy exchange ΔE is calculated according to equation 3.20 using the flight time $t_{CD} = L_{CD}/v^*$. The actual scattering angle θ_i is determined using the Bragg condition, given k^* and G_{hk} (which is the reciprocal lattice vector in whose vicinity the deceptons are visible) via equation 3.10. Finally, the parallel momentum transfer can be calculated with the aid of equation 3.16 whereupon the just mentioned values of θ_i and ΔE have to be used.

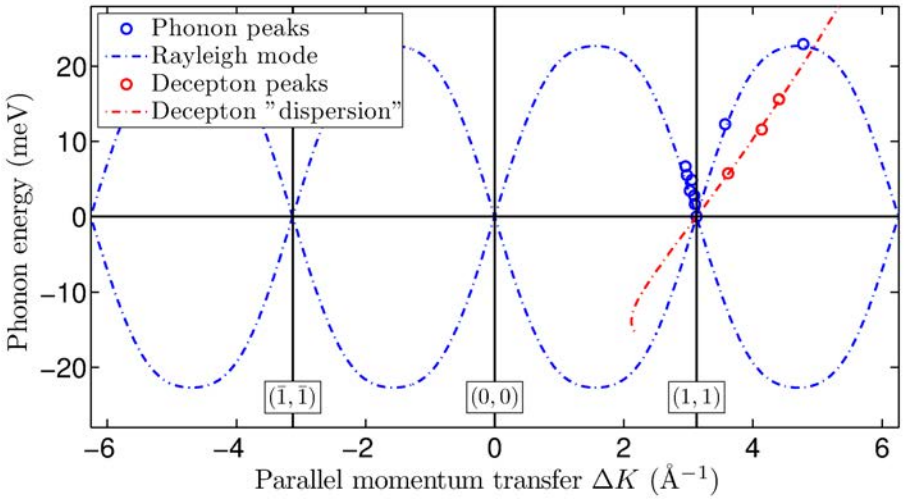

Figure 5.18.: Dispersion relation for a few inelastic measurements on LiF(001) with $E_i = 10.6$ meV and the crystal at room temperature. The blue circles correspond to phonon modes; they fit the Rayleigh mode (according to Brusdeylins et al.[48]) very well. The measured decepton peaks (red circles) in the vicinity of the $(1, 1)$ peak can be described by the plotted "dispersion" in a good way.

In figure 5.18 the dispersion relation for a set of inelastic measurements on LiF(001) at room temperature with a beam energy of 10.6 meV is shown. The blue circles correspond to phonon modes which is confirmed by the fact that they fit the

Rayleigh mode (blue dash-dotted line, according to Brusdeylins et al. [48]) very well. The plotted "dispersion" relation of the deceptons in the vicinity of the $(1, 1)$ peak gives a very good fit to the measured decepton peaks.
It is remarkable that the measured decepton peaks correspond to a range of velocities v^* that go even up to to 1.2 v_0. Compared to the usual halfwidth of the incident beam with $\Delta v/v \approx 0.01$ the spread is much larger. This has already been noticed by Doak[11].
Therefore, the origin of the beam component that gives rise to the deceptons is not fully understood yet. Toennies concludes that the undesired component must originate in vacuum chambers used for differential pumping further downstream from the source chamber[14].

6. HAS from Bi(111)

There has been an increasing interest in bismuth in the recent years since it turned out to be a prime candidate for the study of quantum size effects in solids[108–113]. In particular a phase transition in Bi involving electron pockets that host Dirac electrons has received much attention[109,114,115]. Despite anisotropies in conductivity measurements of bismuth with increasing magnetic field strength or decreasing temperature[5,116], oscillations of the Nernst coefficient in bismuth have been observed[108,117–121].
While the strong spin-orbit interaction in bismuth remains challenging from a theoretical point of view, it is a promising property of Bi surfaces and interfaces with respect to applications in spintronics[111]. Furthermore, superconductivity of Bi cluster films, nanowires and Bi bicrystals has been observed[122–126].
Over the past decades HAS has been widely used to investigate the surfaces of ionic crystals, semiconductors and metals but so far no attention has been given to semimetal surfaces, with the only exception of graphite[127–129]. This is a bit surprising since the diffraction patterns in HAS contain information about the electronic structure, i.e. it reflects the surface electron density at the scattering turning point[8,9,12].
Although semimetal surfaces are usually conducting it is expected that contrary to ordinary metals, semimetals exhibit corrugated surface profiles due to the fact that their surface electrons and holes at the Fermi level are concentrated into fairly narrow pockets in the surface Brillouin zone (SBZ)[111,130].
In this respect the Bi(111) surface also plays a central part in the question what marks the transition to a metal since its surface has been reported to be a much better metal than the bulk[111,112,131]. Moreover, the present interest in topological insulators (e.g.: Bi_2Se_3) has been a stimulus for helium scattering measurements[132–134].

6.1. Structure and properties of Bi(111)

Bismuth crystallizes in the rhombohedral A7 structure with two atoms per unit cell as displayed in figure 6.1(a). The side view of the Bi(111) surface in figure

6.2(a) shows that the crystal consists of puckered bilayers of atoms perpendicular to the [111] direction. The covalent bonding within each of these bilayers is much stronger than the Van der Waals character of the interbilayer bonding. Due to those weak bonds the crystal is easily cleaved along the [111] direction[111,135,136].

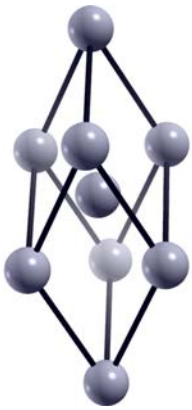

(a) Rhombohedral unit cell (drawn with the aid of XCrySDen[137])

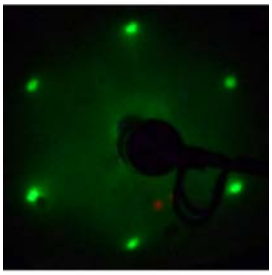

(b) LEED pattern of Bi(111)

Figure 6.1.: Rhombohedral unit cell of bismuth with 2 atoms per unit cell on the left and a LEED pattern of the Bi(111) surface with a beam energy of 29.4 eV on the right-hand side.

The first LEED patterns of Bi(111) was reported by Jona et al.[138] and Mönig et al.[139] investigated the detailed structural parameters using LEED and ab-initio calculations. They showed that the only relaxation on the surface is a rather small deviation of the interlayer distances with respect to the bulk values.

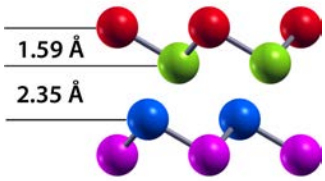

(a) Side view

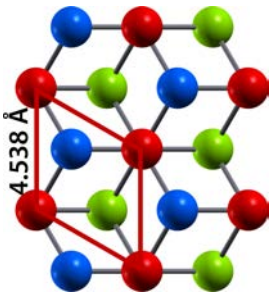

(b) Top view

Figure 6.2.: Side and top view of the Bi(111) surface structure (structural parameters according to[139]). Atoms in different layers are indicated using different colors with red, green, blue and pink for the 1^{st}, 2^{nd}, 3^{rd} and 4^{th} layer respectively[135]. The plot was generated with the aid of XCrySDen[137].

A model of the geometric surface structure is shown in figure 6.2. Alternatively to the rhombohedral structure, Bi may also be described using a hexagonal structure

with six atoms per unit cell or as a pseudocubic structure with one atom per unit cell[111,138]. Thereby the hexagonal lattice is the natural choice when labeling the Bi(111) surface since it describes its first layer in an intuitive way. The unit cell in using this notation is a rhombus with $a = 4.538$ Å (according to Mönig et al.[139]) which is highlighted in red in figure 6.2(b).
The majority of previous experimental investigations concerning the Bi(111) surface concentrates on photoemission studies[112,113,131,140–144]. One of the most important conclusions of this work was that the number of surface charge carriers is much higher than the corresponding number of bulk carriers[111] giving rise to the fact that the surface is a much better metal than the bulk. Koroteev et al. showed that this metallic character of the Bi(111) surface can be explained in terms of a strong spin-orbit splitting[135,140].

6.1.1. Sample Preparation

The Bi(111) single crystal used in this study was obtained from Metal Crystals & Oxides Ltd. in the shape of a circular disk with a diameter of 15 mm and a thickness of 2 mm. Prior to the measurements the surface was cleaned by Ar^+ sputtering (1.5 kV, 2 μA) and annealing to 423 K.

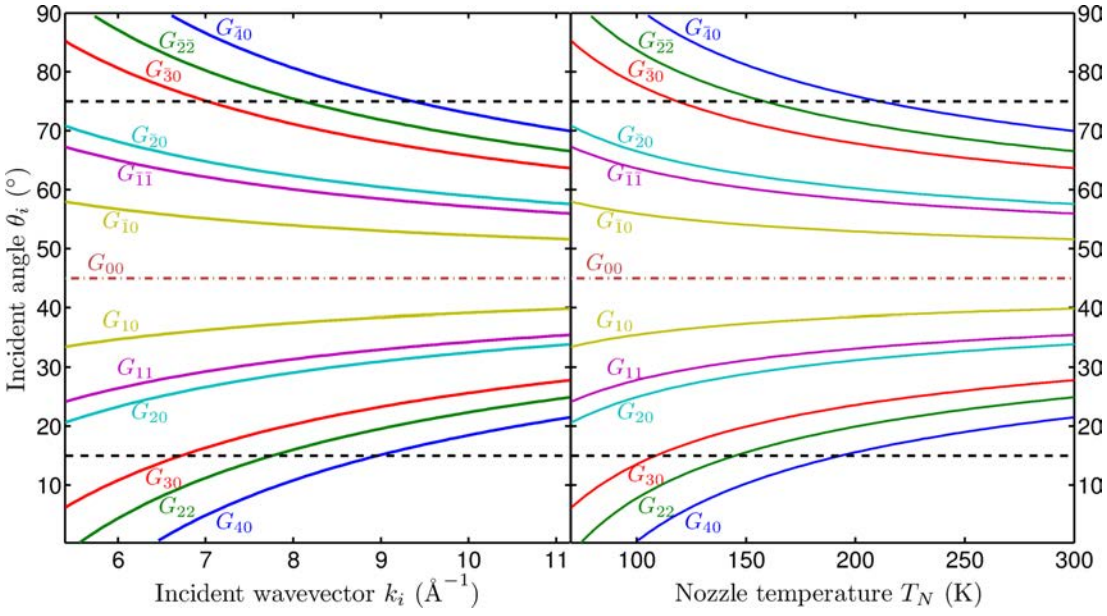

Figure 6.3.: Diagram showing the incident angle θ_i of diffraction peaks on Bi(111) versus the incident wavevector k_i (left plot) and the nozzle temperature T_N (right plot) respectively. For incident angles $\theta_i < 15°$ and $\theta_i > 75°$ the helium beam is shadowed by the sample holder which is designated by the dashed lines.

LEED was used to determine the azimuthal alignment of the crystal (see figure 6.1(b)). Figure 6.3 shows which diffraction peaks should be observable. Therefore the calculated incident angle for various diffraction peaks on Bi(111) is plotted as a function of the incident wavevector and the nozzle temperature, respectively.

6.2. Elastic Scattering on Bi(111)

Figure 6.4 shows a scan of the He intensity scattered from Bi(111) along the ⟨10⟩ azimuth. The measurement that was carried out at an incident energy E_i = 25.5 meV with the Bi surface at room temperature, displays sharp diffraction peaks up to second order.

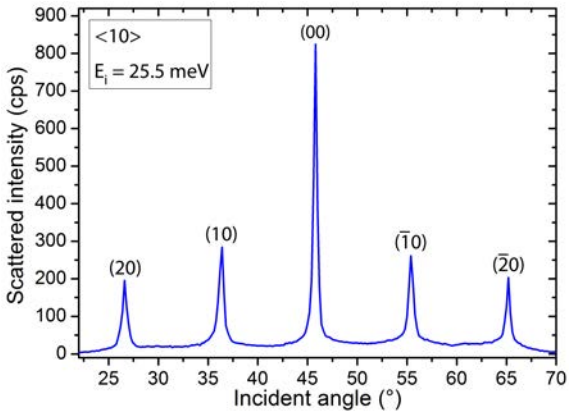

Figure 6.4.: Scattered intensity of He vs. incident angle for He diffracted from Bi(111) along the ⟨10⟩ azimuth with the sample at room temperature.

According to Bragg's law (equation 3.7) for elastic in-plane scattering the reciprocal lattice vector G_{hk} can be readily obtained from the momentum transfer parallel to the surface. Thereby the structural parameters determined from the scattering angles agree very well with those determined by Mönig et al.[135,139].
In figure 6.5(a) the ⟨10⟩ and the ⟨11⟩ scanning directions are displayed. Note that those are the only low-index directions with a different spacing of atoms as long as only the top-most atomic layer is considered. This is a consequence of the sixfold symmetry of the first atomic layer[136].
However, if the second layer is taken into account, the ⟨11⟩-direction is no longer a mirror plane (see figure 6.5(a)). Hence the sixfold symmetry is reduced to a threefold symmetry and diffraction intensities along the ⟨10⟩ azimuth would no longer be expected to be symmetric about the specular direction[136].
Usually in HAS measurements only the top-most atomic layer is considered since the He atoms are scattered by the surface electron density due to the Pauli repulsion (see section 3.4). Since the turning point depends on the energy of the

incident He beam (equation 3.26) He atoms tend to penetrate deeper into the surface electron corrugation with increasing incident energy. To tackle the problem of a possible interaction with second layer atoms ab-initio calculations were performed by D. Campi and G. Benedek[145].
Their calculations are summarized in figure 6.5 which shows the He turning point due to the surface electron density for two different incident energies. For a He beam with $E_i = 60$ meV a small difference in the calculated corrugation of $\approx 4\%$ appears. However, for He atoms with an incident energy of 17 meV (which was the case for the measurements performed to determine the corrugation function) the difference in the turning points is so small that it is reasonable to neglect any influence of the second layer in the scattering of He atoms at this beam energy.

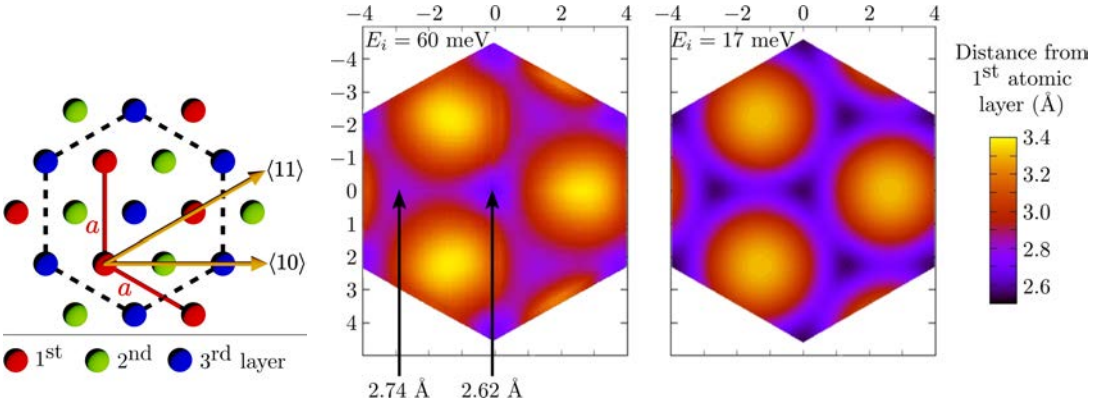

(a) ⟨10⟩ and ⟨11⟩ scattering direction for Bi(111)

(b) Ab-initio surface charge density corrugation for different beam energies calculated by Davide Campi[145].

Figure 6.5.: Ab-initio calculation of the He turning point due to the surface electron density for two different incident energies. The dashed hexagon in (a) represents the region for which the turning point in (b) was calculated. For $E_i = 60$ meV the turning point at the two hollow sites indicated by the arrows is 2.74 Å at the position of a second layer atom and 2.62 Å at the position of a third layer atom, respectively. With respect to a maximum of 3.4 Å this gives rise to a difference of $\approx 4\%$. For $E_i = 17$ meV the difference between the two sites is just 0.04 Å and can thus be neglected.

By cooling the sample down to a temperature of 123 K and using incident energies of $E_i = 31.7$ meV (⟨10⟩ azimuth) and $E_i = 24.1$ meV (⟨11⟩ azimuth) of the helium beam diffraction patterns with peaks up to third order were observable[136]. They are shown in figure 6.6 as a function of the incident angle with the zero-order diffraction peak at $\theta_i = 45.75°$.
The positions of the peaks are again in excellent agreement with the already known structure[136,139]. As an advantage of the cooling, much higher intensities compared to the measurements with the sample at room temperature could be

achieved. There is a slight asymmetry in the angular scans which is likely to be caused by steps in the Bi(111) surface[146] and alignment problems[136]. In a few measurements the bad alignment was caused by the following effect: While trying to align the sample in a way that yields the same peak height of both second order diffraction peaks, it turned out later, that the angular position of one of the second order diffraction peaks coincides with a surface resonance condition. Thus the peak height was influenced by this resonance and the sample alignment was somewhat incorrect.

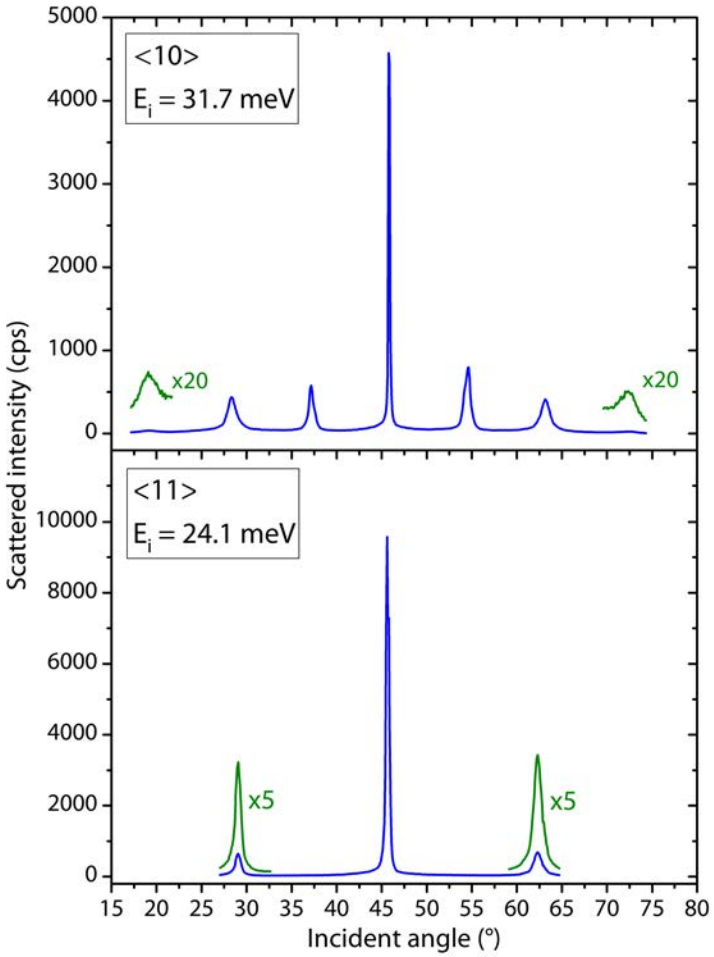

Figure 6.6.: Scattered intensity of He vs. incident angle for He diffracted from Bi(111) along the ⟨10⟩ azimuth (upper part) and along the ⟨11⟩ azimuth (lower part). The crystal has been cooled down to 123 K.

The angular distribution measurements illustrate that a large fraction of the scattered He atoms is found in the diffraction peaks which is unusual for a surface with metallic character. As seen from the view of the Bi(111) surface in figure 6.2b) the ion cores of the first bilayer exhibit a corrugation of 1.59 Å. Due to this

highly corrugated surface one would expect strong diffraction peaks which is indeed confirmed by our measurements. However, considering the reported metallic character of the surface one would expect a smoothing of the contour due to the Smoluchowski effect[58], yet the large diffraction peaks imply an increased importance of the surface corrugation for HAS on Bi(111) compared to other metals. To provide a more thorough investigation of this effect a detailed analysis of the diffraction peak intensities has been carried out[135,136].

6.2.1. The Surface Corrugation

In order to determine the corrugation of the He-Bi(111) surface interaction potential, intensity calculations based on the hard corrugated wall model were performed. Therefore, the assumptions of the eikonal approximation[8,9] as well as the GR-method[64,147] as described in section 3.4 were used. The surface was modeled using the simple two-parameter Fourier ansatz for the surface corrugation function

$$\xi(x,y) = \xi_{01} \cdot \left\{ \cos\left[\frac{2\pi}{a}\left(x - \frac{y}{\sqrt{3}}\right)\right] + \cos\left[\frac{2\pi}{a}\left(x + \frac{y}{\sqrt{3}}\right)\right] + \cos\left[\frac{2\pi}{a} \cdot \frac{2y}{\sqrt{3}}\right] \right\} + \xi_{11} \cdot h.o. \tag{6.1}$$

with x and y being rectangular coordinates with respect to the oblique geometry of the surface and $h.o.$ corresponding to higher order Fourier terms. Hard wall intensities were calculated for various ξ_{01} and ξ_{11} and compared to the relative experimental diffraction possibilities. The best-fit coefficients have then been determined by varying the amplitudes ξ_{01} and ξ_{11} until optimum agreement between the measured and the calculated intensities was reached[135,136].
For this purpose the diffraction peak intensities for each G are normalized by dividing by the intensity of the specular peak. The accuracy of the agreement was judged by evaluating a reliability factor R according to equation 3.36. Both azimuthal directions were included in the determination of the corrugation function. The fitting procedure has been applied to angular HAS scans with the Bi crystal at room temperature and cooled down to 123 K to account for dynamic effects that may be related to the structure. As described in section 3.4 this approach for fitting hard wall corrugation functions is sufficiently accurate[8,68,136].
Figure 6.7 shows the corresponding angular scans along the $\langle 10 \rangle$ and the $\langle 11 \rangle$ azimuth with a beam energy $E_i = 17.7$ meV. In the appendix A.1 a tabular listing of all diffraction peak intensities on Bi(111) that have been measured in the framework of this thesis can be found.
For comparison with the calculated intensities the experimental peak areas were determined. The reason for using the peak areas is due to the broadening of the elastic peaks caused by the energy spread of the He beam and the broadening

caused by the apparatus and the domain size of the crystal surface[101,105]. Therefore the elastic peaks were fitted with two Gaussian functions to account for the narrow coherent elastic contribution and for the broad diffuse elastic and multiphonon contribution[69,136].
The area of the narrow coherent elastic peaks was then compared with the calculations. The asymmetries in the measurements were attributed to a poor alignment and peak areas of corresponding peaks were averaged. In figure 6.7 the peak areas are indicated as circles while the solid curves show the experimental count rates versus the incident angle. Figure 6.7 also shows the calculated intensities obtained by the eikonal approximation, indicated by the triangles and those obtained by the GR method designated by the squares[136].

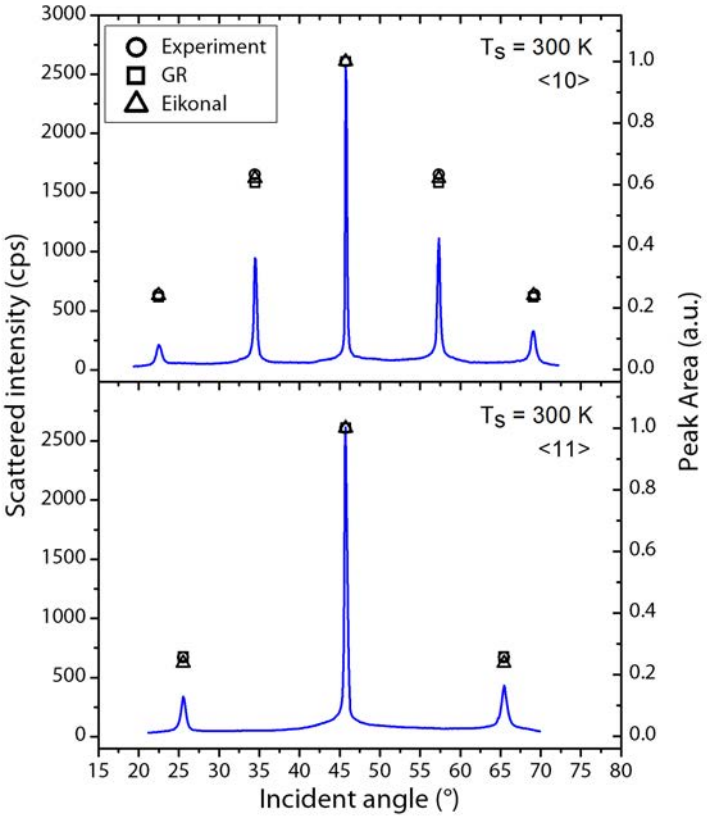

Figure 6.7.: Scattered intensity of He vs. incident angle for He diffracted from Bi(111) along the ⟨10⟩ and ⟨11⟩ azimuth for $E_i = 17.7$ meV. The shown measurements were performed with the crystal at 300 K. The circles correspond to the experimentally determined peak areas, the triangles indicate the calculation using the eikonal approximation and the squares show the results using the GR method.

To account approximately for the attractive well near the surface, the Beeby correction has been applied in the calculations[8]. In both cases (GR and eikonal

approximation), a Beeby correction of 8 meV was found to provide a good fit[136] which is also confirmed by bound state resonance measurements that will be described section 6.4[130].
The best fits to the data are summarized in table 6.1 with the reliability factor according to (3.36) and the peak-to-peak corrugation in percentage of the surface lattice constant a. The experimental results agree well with the calculations; in terms of R the deviation is smaller than 2.8% for the GR method and smaller than 4.0% using the eikonal approximation[136].
However, it should be mentioned that the application of the eikonal approximation for such a large corrugation should be treated with caution whereas the GR method has proven its reliability for corrugations as large as $0.18a$[8].

Table 6.1.: Best fit corrugations in percent of the lattice constant a corresponding to the experimental measurements at $T_S = 123$ K and $T_S = 300$ K. The results were obtained with the eikonal approximation and the GR method by modeling the surface with the Fourier ansatz (6.1). All calculations were performed with the Beeby correction ($D = 8$ meV).

	R-factor (%)		corr. height/a (%)	
T_S (K)	Eikonal	GR	Eikonal	GR
123	4.0	2.8	10.6	9.7
300	1.6	1.4	11.2	10.1

The obtained corrugation height at both surface temperatures is ≈10% of the lattice constant. This rather large value is by no means expected at a metal-like surface[142]. The reported metallic character of the surface should give rise to a smoothing of the contour due to the Smoluchowski effect. This would imply a nearly flat surface charge density corrugation as it has been reported for (111) metal surfaces such as Ag(111) or Pt(111) whose spatial modulation is one to two orders of magnitude smaller[91,135,148].
Indeed such a large corrugation height is comparable to those obtained for semimetals such as graphite[149]. Although this is somewhat in contradiction to the reported metallic character of the Bi(111) surface, the actual corrugation due to the ion core positions seems to be the dominant effect for helium scattering[135].
In figure 6.8 a surface plot together with a density plot of the best fit corrugation is shown. At a closer look it is quite remarkable that a linearly shaped enhancement of the electron density between the positions of the Bi atoms seems to appear. This is not due to any contribution of atoms in the second layer since the interaction of He atoms with the second layer can be neglected for an incident energy of 17.7 meV.

Furthermore it should be mentioned that the calculation of the corrugation shows a slight increase of the corrugation height with increasing surface temperature. While this tendency is still within the uncertainty of the calculations both calculation methods, the eikonal approximation as well as the GR method show the same trend. However, this effect could also be caused by a slight difference in the Debye temperatures of the diffraction peaks[8,68,136].

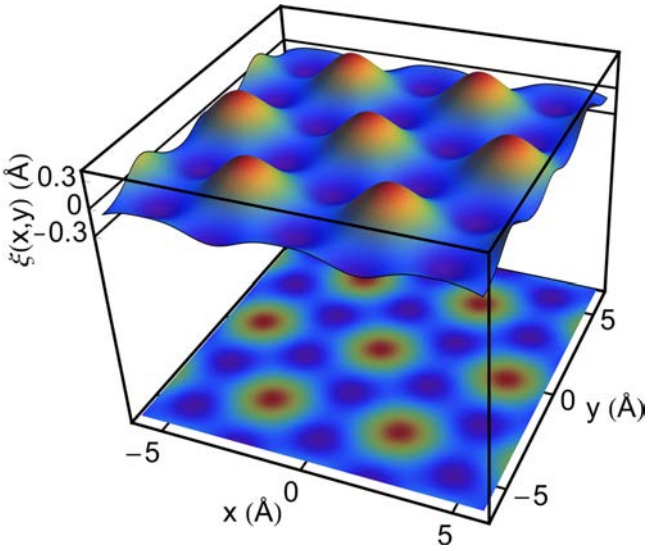

Figure 6.8.: Plot of the hard-wall potential surface for the Bi(111) surface at an incident energy of $E_i = 17.7$ meV and a temperature of 300 K. The corrugation was obtained by fitting the observed helium diffraction intensities within the eikonal approximation. The peak to peak amplitude is 0.51 Å.

6.3. Surface Debye Temperature of Bi(111)

The thermal attenuation of the diffraction peaks provides insight into the surface vibrational dynamics[8]. Figure 6.9 shows the decay of the specular peak intensity with increasing surface temperature T_S. Therefore scans of the scattered intensity around the zero order peak were collected for an incident energy of $E_i = 17.7$ meV while the Bi surface temperature was varied between 118 K and 408 K.
The thermal attenuation of the diffraction peak intensities is caused by vibrations of the surface atoms giving rise to inelastic scattering of the incoming atoms. This attenuation is described by the Debye-Waller factor which has been addressed in section 3.4.7.
According to (3.38) and (3.41) a plot of $\ln(I(T_S)/I_0)$ versus the surface temperature T_S gives rise to a linear decay within the Debye model whereupon the surface Debye temperature can be calculated from the slope. In figure 6.10 the decay of

the specular and the first order diffraction peak intensity versus temperature are depicted. Both measurements have been carried out at an incident beam energy $E_i = 17.7$ meV.
The experimental data perfectly fits a linear decay over the experimental range consistent with the Debye model. The intensity of the first order diffraction peak shows small deviations which could be the effect of a slightly misaligned symmetry axis due to elongation effects when cooling down the sample with liquid nitrogen.

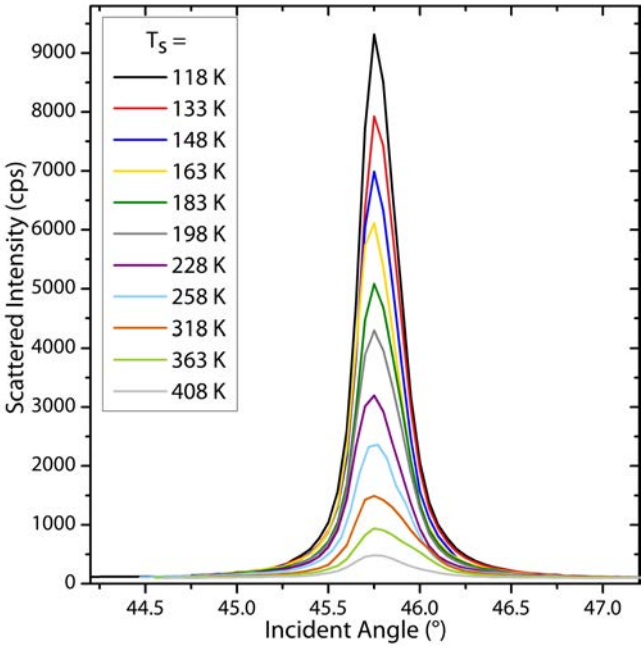

Figure 6.9.: Plot of the attenuation of the specular peak with increasing surface temperature T_S of the Bi(111) sample. The scattered intensity of the helium beam with an incident energy of $E_i = 17.7$ meV is shown.

The slopes obtained from the linear fits of figure 6.10 are $-12.1 \cdot 10^{-3}$ K^{-1} for the decay of the specular peak intensity and $-15.8 \cdot 10^{-3}$ K^{-1} for the first order diffraction peak. Using equation 3.41 - 3.42 the surface Debye temperature θ_D can be calculated from the slope if the mass of the helium atom scatterer M and the potential well depth D are known[136].
Due to the enhanced metallic character of the Bi(111) surface a considerable well depth can be expected[150,151]. Therefore, a value of $D = 8$ meV was used for the calculation of the Debye temperature. This value was also found to provide a good fit for the calculations of the surface corrugation and is confirmed by bound state resonance measurements (section 6.4)[130,136].
With M equal to the mass of a single Bi atom, the Debye temperature θ_D was determined to be (84 ± 8) K from the measurements of the specular peak and (75 ± 8) K from the measurements of the first order peak. Hence the surface Debye

temperature of Bi(111) is reduced significantly with respect to the bulk value which is 120 K[152,153]. This is in good agreement with the theoretical approximation of van Delft[154] that estimates a reduction of the surface Debye temperature by a factor of $1/\sqrt{2}$ with respect to the bulk value[136].

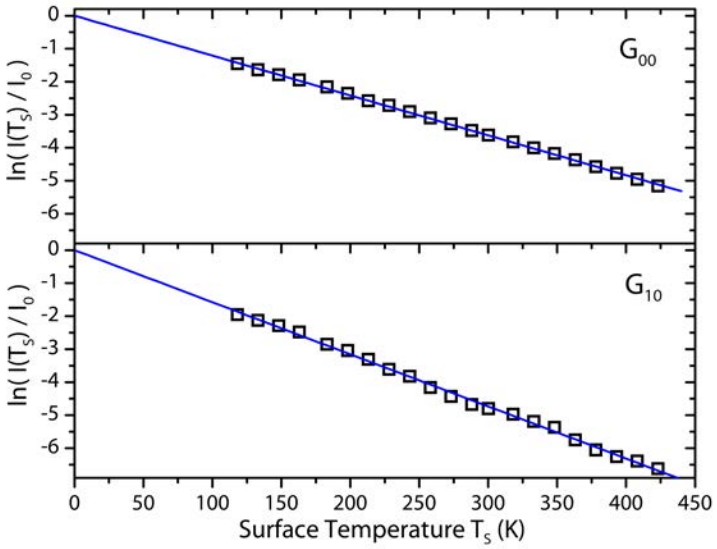

Figure 6.10.: Decay of the specular and first order diffraction peak intensity $I(T_S)$ versus surface temperature T_S for an incident beam energy $E_i = 17.7$ meV. In both cases the natural logarithm of $I(T_S)/I_0$ exhibits a linear slope.

Even though the determination of the surface Debye temperature using LEED measurements usually includes the measurement of scattered electrons that are penetrating into the first layers of the bulk, it shall be tried to compare the LEED results with the HAS measurements. Mönig et al.[139] determined a surface Debye temperature of Bi(111) with $\theta_D = 71(+7/-5)$ K for the first layer using LEED experiments, which is slightly smaller in comparison[136]
Considering collisions of the impinging helium atom with more than one surface atom due to the cooperative motion of the surface atoms would give rise to a helium scatterer mass M greater than that of a single Bi atom and consequently a lower θ_D[155,156]. However, the uncertainty in our calculation of the Debye temperature results primarily from the well depth D.
Yaginuma et al.[157] reported a decrease of the surface Debye temperature above 350 K which they attribute to a softening transition of the outermost interbilayer bonds accompanied by a hardening of the topmost intrabilayer bonds. Using LEED experiments they determined the surface Debye temperature of a bismuth nanofilm that adopts the same structure as the bulk truncated Bi(111) surface. Thereby θ_D decreases from 76 K to 50 K for $T_S > 350$ K[157].
However, in the HAS measurements there is no evidence for such a drop in the

surface Debye temperature. The fact that this transition is not observed in the measurements of the bulk truncated surface may be caused by different properties of the nanofilm or a signature of the substrate[136].
However, it has been shown that the nanofilm surface takes the same atomic configuration with a lattice constant that is almost the same as the one of the bulk truncated surface[158]. Therefore the reason for the different behavior of the surface Debye temperature is likely due to the different nature of the LEED experiments in comparison to HAS where the helium atoms are scattered at the surface electron density[136].

6.4. Selective Adsorption Resonances

Besides the elastic diffraction peaks, which contain information about the surface structure and the associated surface electron density, small features can occur in the angular distribution of HAS measurement at angular positions different to the diffraction peak positions. They necessarily correspond to inelastic processes involving single surface phonons and can be caused either by kinematical focusing or due to phonon assisted selective adsorption resonances (see section 3.6).
Figure 6.11a displays the angular distribution for He with $E_i = 15.1$ meV scattered from Bi(111) along the $\langle 11 \rangle$ azimuth. The y-axis is greatly magnified which shows several small additional features. The position of these additional features due to bound state resonances, which can be either peaks or dips, allows the determination of the bound state energies.
The features observed at $\theta_i = 32°$, $37°$, $42°$ and $51°$ in the angular regions between the specular and the first order diffraction peaks are attributed to selective adsorption. The bound state energies of these resonances are calculated using the resonance condition (equation 3.51). Therefore, the curve corresponding to the resonance condition (equation 3.51) as a function of θ_i is superimposed onto the angular distribution for different $\vec{G}$-vectors[130].
The two broken lines plotted in figure 6.11a correspond to the smallest $\vec{G}$-vectors indexed by $(1, 1)$ and $(1, 0)$. The three resonances on the left-hand side of the specular peak are clearly associated with the $(1, 1)$ channel (in-plane resonances) and three different bound states. The large resonance at $51°$ can be associated with the (1,0) channel (out-of-plane resonance) and the same bound state energy as the feature at $32°$. The (1,0)-channel provides two further resonances associated with deeper bound state energies that are expected at $58°$ and $66°$. The corresponding signatures in the angular distribution could correspond to the broad bump and the small sharp peak in figure 6.11a which are however, hardly detectable above the background noise[130].

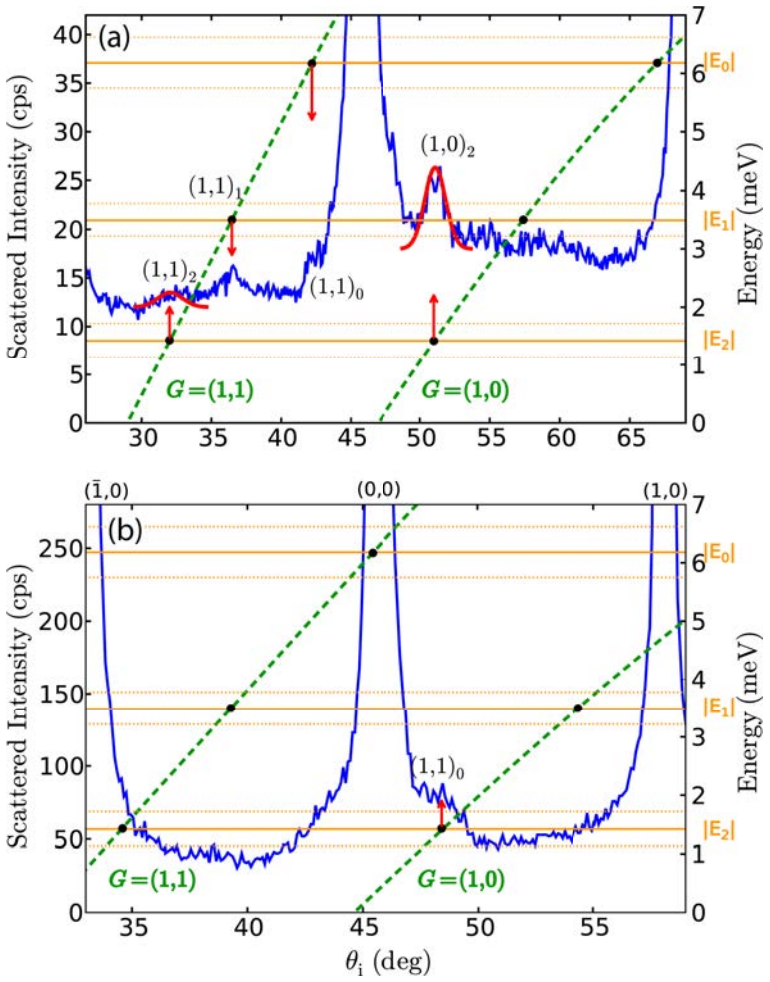

Figure 6.11.: (a): Angular distribution of the scattered intensity (ordinate scale on the left-hand side) for He scattered from Bi(111) along the $\langle 11 \rangle$ azimuth. Besides the specular and the two first order diffraction peaks, the angular distribution shows additional features corresponding to selective adsorption resonances. The bound state energies that may give rise to a feature in the angular distribution are plotted as functions of the incident angle (broken lines) for the two smallest $\vec{G}$-vectors indexed by $(1,1)$ and $(1,0)$. The vertical arrows associate the resonant features with the energies of three bound states whereupon the ordinate on the right-hand side corresponds to the bound state energy.
(b): Same as (a) for the $\langle 10 \rangle$ azimuth

The binding energies determined from these resonance features in figure 6.11 are:

$$\begin{aligned} E_0 &= (6.18 \pm 0.55)\ \text{meV} \\ E_1 &= (3.49 \pm 0.28)\ \text{meV} \\ E_2 &= (1.42 \pm 0.30)\ \text{meV} \end{aligned} \tag{6.2}$$

After the energy values have been calculated from the most prominent resonances, other weaker features can eventually be assigned to other combinations of reciprocal lattice vectors $\vec{G}_{hk}$ with bound states n: $(\vec{G}_{hk})_n$. Those are for example $(1,1)_2$ and $(1,0)_1$ along the $\langle 10 \rangle$ azimuth (fig. 6.11b)[130].
In contrast to the $\langle 10 \rangle$ azimuth the measurement along the $\langle 11 \rangle$ azimuth (figure 6.11b shows only one strong resonance feature that appears right next to the specular peak. This peak can be identified as the $(1,0)_2$ resonance.

6.4.1. He-Bi(111) Interaction Potential

The experimentally determined bound state energies can be used to evaluate the He-Bi(111) interaction potential. A good description of this interaction potential is given in terms of the 9-3 potential (equation 3.53 in section 3.6.4). The eigenvalue spectrum provided by the 9-3 potential according to equation 3.54 is fitted with the experimentally determined bound state energies by a least-squares method. The potential parameters resulting from the fit are[130]:

$$\begin{aligned} D &= (8.32 \pm 0.73) \text{ meV} \\ \sigma &= (0.297 \pm 0.012) \text{ nm} \end{aligned} \tag{6.3}$$

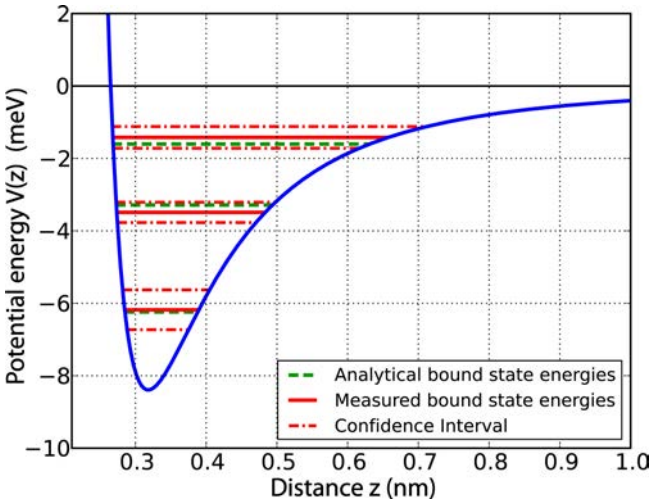

Figure 6.12.: Best fit 9-3-potential (equation 3.53) for the He-Bi(111) atom-surface interaction with $D = 8.32$ meV and $\sigma = 0.297$ nm. The red lines indicate the experimentally determined bound state energies and their uncertainties, the green lines correspond to the analytical bound state values from equation 3.54

Figure 6.12 displays the 9-3-potential according to the best fit parameters, together with its three bound states and the respective confidence intervals. The

calculated potential well depth D is consistent with previously determined values for noble metal vicinal (corrugated) surfaces such as $D = 7.41$ meV for Cu(117)[159] and $D = 9.3$ meV for Ag(111)[130,160].
Note that in a more general treatment as shortly outlined in section 3.6 the potential follows the corrugation at the surface which gives rise to band structure effects such as gaps in the bound-state dispersion relation. These effects are more pronounced for deeper bound states, i.e., for atoms moving closer to the surface[89]. Nonetheless, they are sufficiently small and the restraints of the experimental measurements allow only the determination of a laterally averaged potential[130].

6.4.2. Resonance Effects in the Specular Intensity

In addition to the measurement of resonances in the angular distribution two further experimental approaches are possible (3.6): While the intensity variation with the azimuthal rotation of the crystal is difficult to perform in the apparatus, variation of the incident energy E_i is easily applied. Therefore, the intensity of the specular peak is recorded as a function of the incident energy E_i or the corresponding incident momentum k_i.
The resonant features which are expected to occur in this measurement are calculated by solving the resonance condition (equation 3.51) with respect to k_i for the specular θ_i and for a given $\vec{G}$ and $|E_n|$. The nozzle temperatures T_N corresponding to the values of k_i at which resonances in the intensity of specular peak can occur are summarized in table 6.2.

Table 6.2.: Nozzle temperatures T_N at which bound-state resonances are expected to cause a dip in the intensity of the specular peak with the sample aligned along the $\langle 10 \rangle$ azimuth. Resonances are labeled by $(\vec{G})_n$

Resonance	T_N(K)
$(0,2)_0$	33
$(1,1)_0$	70
$(0,2)_1$	83
$(0,2)_2$	114
$(1,1)_1$	127
$(1,1)_2$	163

In principle this measurement could be performed at any angular position θ_i, but fixing the incident angle at the specular peak provides the best signal-to-noise

ratio. Figure 6.13 shows the peak height of the specular peak recorded while the nozzle temperature was varied between 60 K and 200 K ($4.5 < k_i < 9$ Å^{-1})[130]. Since the flux of He atoms through the nozzle is a function of the nozzle temperature via $T_N^{-\frac{1}{2}}$ according to Miller[6], the specularly reflected intensity should exhibit a similar continuous decay with increasing nozzle temperature if resonance effects are not considered and the sample is held at a constant temperature. However, besides this expected continuous decrease of the intensity, figure 6.13 shows some clear and intense dips at 76, 86 and a broad feature at 116 K.
According to the predictions of table 6.2, the observed dips can be associated to the $(1,1)_0$, the $(0,2)_1$ and the $(0,2)_2$ resonances. Hence the measurement of resonance feature in the specular intensity confirms the values of the 9-3 potential that have been determined from the resonances in the angular distribution[130].

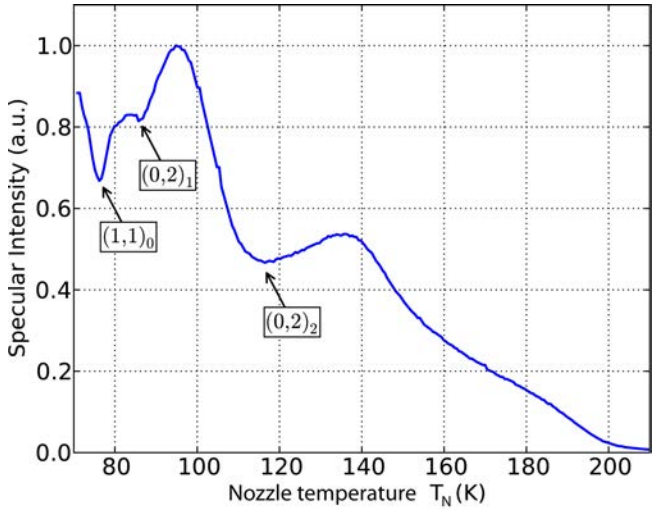

Figure 6.13.: Peak height of the specularly reflected helium beam vs. the nozzle temperature in the $\langle 1,0\rangle$ scattering plane. The dips at 76 K, 86 K and the broad feature at 116 K can be explained with the aid of bound state resonances.

The knowledge of the He-Bi(111) interaction potential does not only provide fundamental information about the atom surface interactions and the main trends of surface phenomena. Bound-state resonances can also be applied to enhance inelastic HAS intensities e.g. of optical surface phonon modes[85,86,130].

6.5. Determination of the Phonon Dispersion Relation

As opposed to the electronic structure nothing is known about the surface phonons on Bi(111) so far which is where HAS plays fully on its strength. Inelastic HAS measurements are of particular interest on Bi surfaces since the phonon energies are too low to be accessible for other scattering techniques such as electron scattering[111] and HAS has been demonstrated to be a method of choice for the study of surface phonons in the low energy regime with resolutions better than 0.1 meV[10].

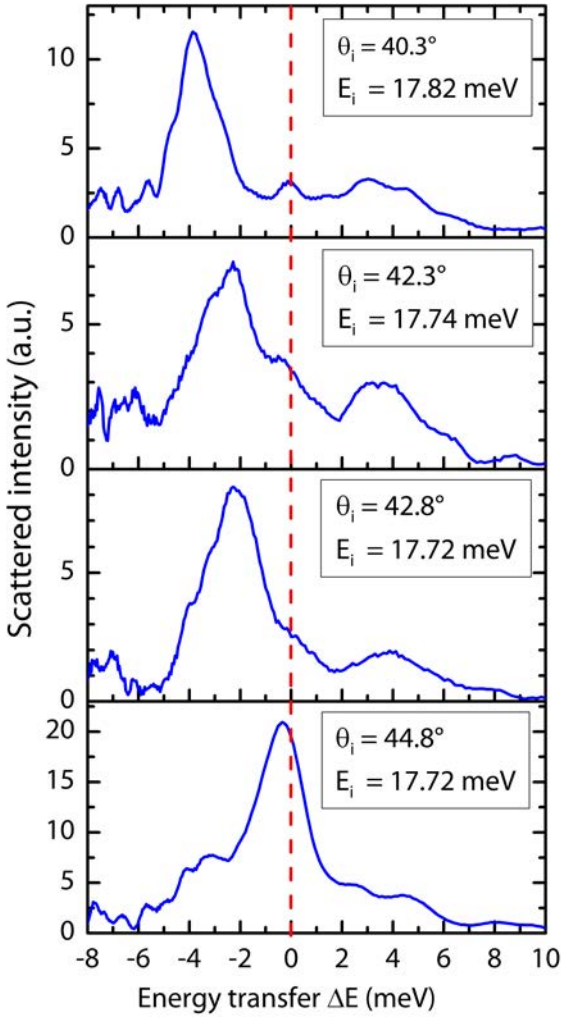

Figure 6.14.: Time-of-flight spectra converted to energy transfer spectra for helium atoms scattered from the Bi(111) surface along the ⟨11⟩ azimuth ($\overline{\Gamma M}$). The crystal was cooled down to $T_S = 103$ K

In figure 6.14 a series of TOF spectra that have been converted to the energy scale is shown. The measurements have been carried out with the Bi crystal

cooled down to 103 K at different incident angles θ_i along the $\langle 11 \rangle$ azimuth. The energy transfer spectra reveal several peaks on the creation and annihilation side. In order to identify the peak maxima and to resolve merged peaks, the spectra were least squares fitted by multiple Gaussian peaks whereupon an example is shown in figure 6.15.
The diffuse elastic peak at $\Delta E = 0$ in figure 6.14 is due to the small concentration of surface defects which are even found on perfectly structured surfaces[161]. The small magnitude of this diffuse elastic peak approves the good quality of the surface.
Peaks at positions corresponding to bound state resonances (illustrated by the vertical red lines in figure 6.15 have not been included in the surface phonon dispersion since they may correspond to resonance-enhanced bulk modes and are thus no longer localized on the surface.

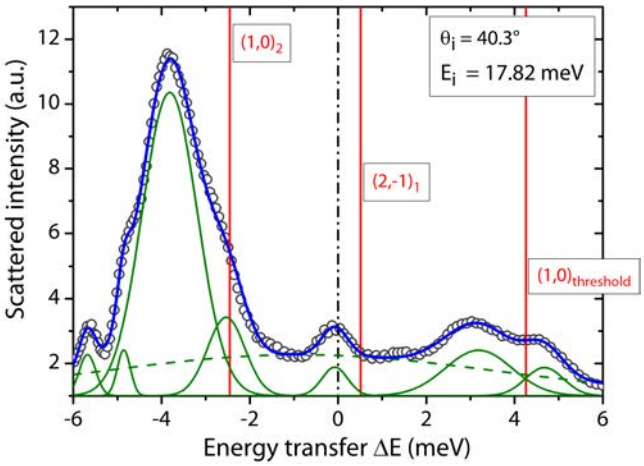

Figure 6.15.: Energy transfer spectra for helium atoms scattered from the Bi(111) surface along the $\langle 11 \rangle$ azimuth at $\theta_i = 40.3°$ and $T_S = 103$ K. The blue line represents a least squares fit of the experimental data (gray circles) with a sum of Gaussian peaks whereupon the green lines correspond to the individual Gaussian peaks. The vertical red lines illustrate the position of bound state resonances according to the 9-3 potential with the parameters from equation 6.3 and are labeled by $(\vec{G})_n$.

To determine the entire phonon dispersion curve up to the Brillouin zone boundary a series of time-of-flight spectra was measured at incident angles between the first-order diffraction peaks. The phonon dispersion was then obtained by transforming each TOF spectrum into an energy spectrum from which the phonon energy $\Delta E = \hbar\omega$ was extracted. The phonon wave vector $\vec{Q}$ was calculated from the conservation of parallel momentum and energy known as the scan curve (equation

3.16). Finally, wavevectors extending beyond the fist Brillouin zone were folded into the first Brillouin zone.
Using the measurement of a few hundred time-of-flight spectra, the surface phonon dispersion relations for both high symmetry directions as well as for the cooled sample and the sample at room temperature were obtained. The phonon dispersion relation for the cooled sample is shown in figure 6.16.

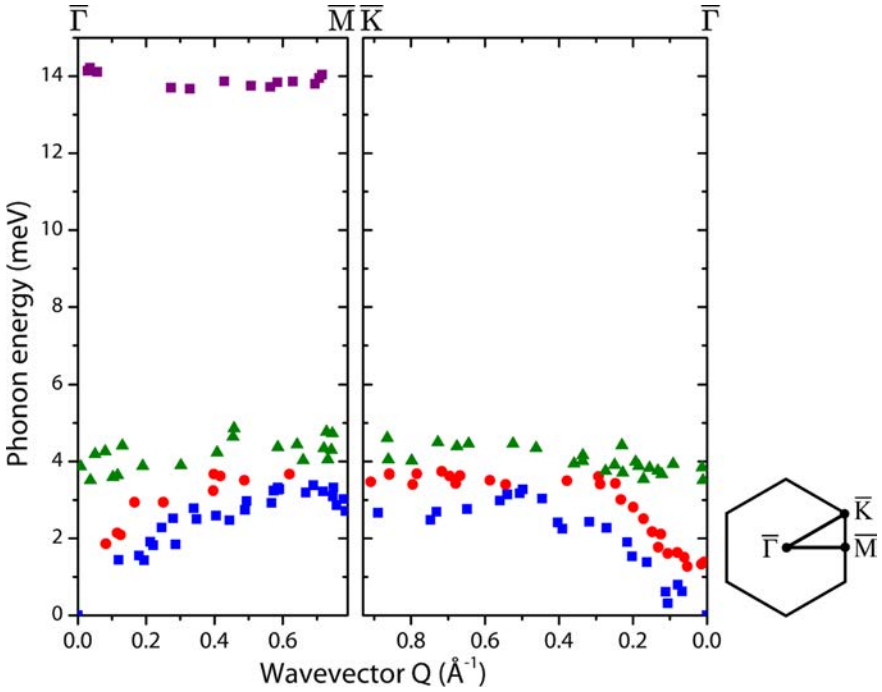

Figure 6.16.: Measured surface phonon dispersion relation for Bi(111). The crystal was cooled down to $T_S = 123$ K for the measurement along the $\overline{\Gamma M}$-azimuth and to $T_S = 103$ K for the $\overline{\Gamma K}$-azimuth. Different colors represent possible different modes.

The different colors of the data points represent a first attempt to attribute them to different modes. The blue squares, which correspond to the mode with the lowest energy are likely to be due to the Rayleigh mode.
In the measurement along $\overline{\Gamma M}$ there appears a flat mode at approximately 14 meV plotted as purple squares in figure 6.16. In comparison to the phonon dispersion of the bulk from Díaz-Sánchez et al.[30] which is displayed in figure 6.17 this mode is situated somewhat above the bulk edge. This suggests that it is an optical surface mode.
While the mode is detected along $\overline{\Gamma M}$, where it is barely recognizable above the noise in the TOF measurements, there is no hint for this mode along $\overline{\Gamma K}$. This is probably due to the fact that surface optical modes are usually less sensitive to HAS[86].

There appear to be two further modes in the dispersion relation: The red circles which appear in an energy region that is typical for a longitudinal resonance, a common feature on metal surfaces[39] and a mysterious mode displayed by the green triangles. In order to gain further insight into the nature of these modes, the measured dispersion shall be compared with calculations of the surface phonons on Bi(111).

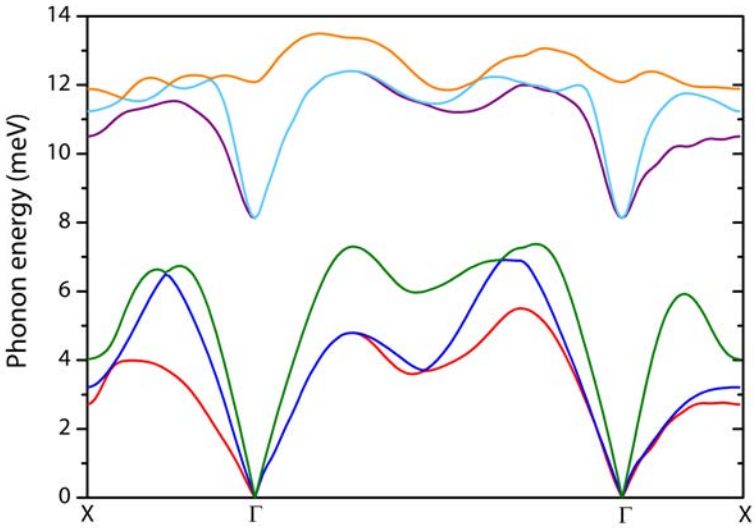

Figure 6.17.: Bulk phonon dispersion of bismuth according to the calculation of Diaz-Sanchez et al.[30].

The dispersion curves of Bi(111) which are shown in figure 6.18 have been calculated by Davide Campi[145] from DFPT (density functional perturbation theory). The calculations were performed using a 6-layer slab without the spin orbit interaction since the calculation of the complete dispersion is computationally expensive. Campi performed also a calculation at the $\overline{\Gamma}$-point including the spin orbit interaction which gives rise to a softening of the phonon modes of approximately 8% with respect to the calculation without spin orbit coupling. This can be seen as a rough trend for the entire phonon dispersion although an exact calculation is required for definitive conclusions[145].
In order to compare the calculated surface lattice dynamics with the measured surface phonon dispersion the experimental data in the energy region of the acoustic modes is plotted in figure 6.19. The data for both the cooled sample and the sample at room temperature are shown to account for temperature dependent effects related to the phonon dispersion.
Obviously the data measured at room temperature shows a larger variation which can be attributed to the peak broadening due to the increasing multi-phonon contribution with higher temperature[11]. Furthermore, significantly shorter TOF

measurement times were used along the $\overline{\Gamma M}$-azimuth at room temperature.

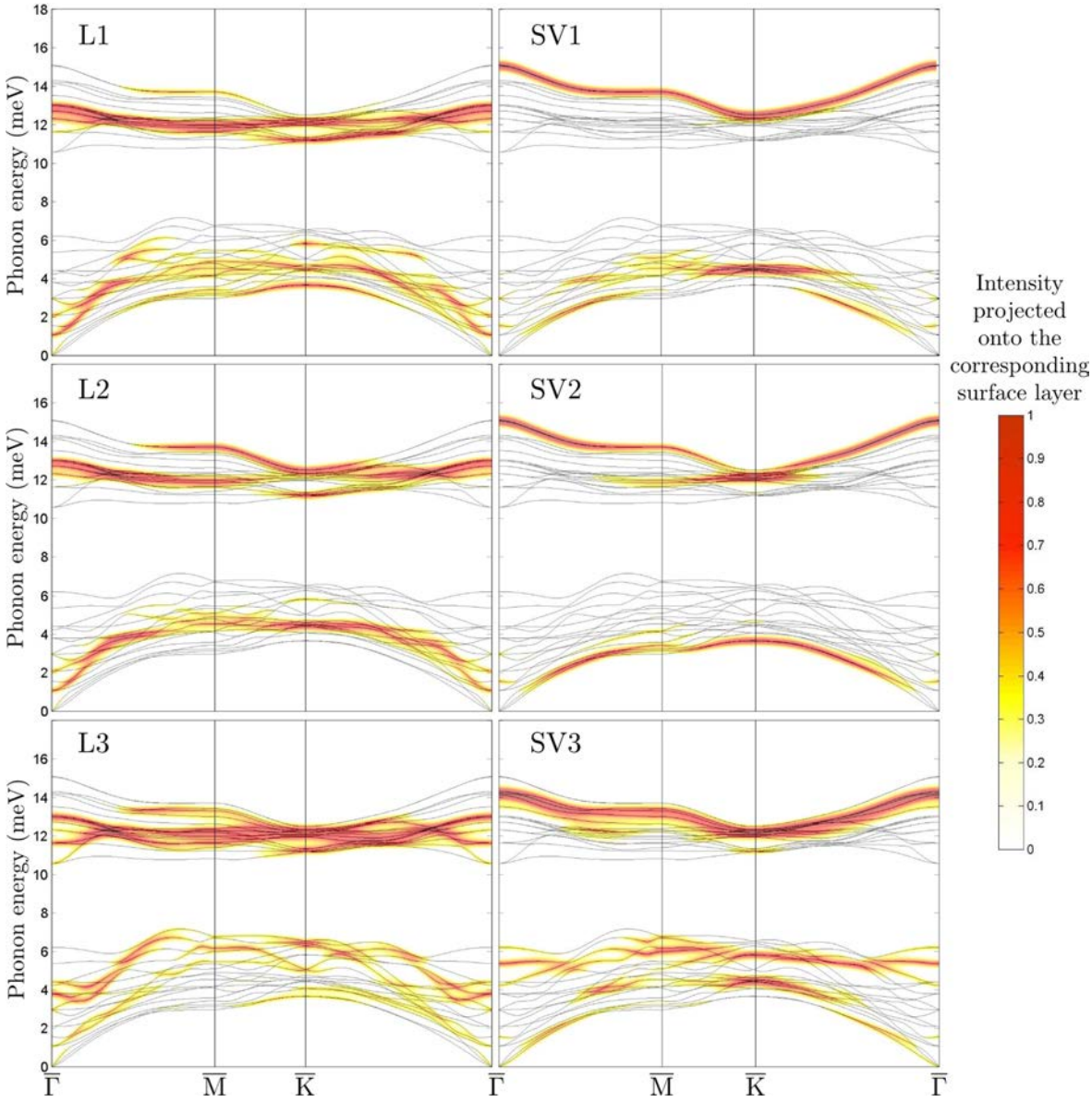

Figure 6.18.: Dispersion curves of a Bi(111) 6-layer slab from a DFPT calculation without spin orbit coupling performed by D. Campi[145]. Highlighted branches represent surface localized modes and resonances. The left hand graph shows modes with longitudinal polarization of the first three layers (L1-L3). The right hand graph displays modes with shear vertical polarization (SV1-SV3). The intensity projected onto the corresponding layer is given by the color coding.

The Rayleigh mode (blue squares) was fitted using a simple force constant model considering only the first atomic layers with nearest and next nearest neighbor

interactions. The fitted curves are illustrated by the solid blue lines in figure 6.19. From these fits the group velocity was determined which is illustrated by the dashed lines in figure 6.19.
Along the the $\overline{\Gamma K}$-azimuth a group velocity of 9.0 meV is obtained for the cooled sample and 8.0 meV for the sample at room temperature. Along $\overline{\Gamma M}$ the group velocity changes from 8.7 meV for the crystal at low temperature to 7.9 meV at room temperature. This decrease in the phonon energy with increasing temperature is a common effect in the phonon dispersion[33].

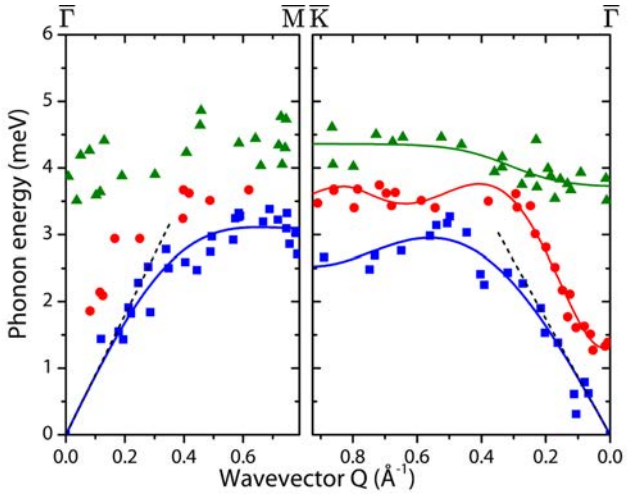

(a) Sample at 123 K for the measurement along the $\overline{\Gamma M}$-azimuth and at 103 K for the $\overline{\Gamma K}$-azimuth

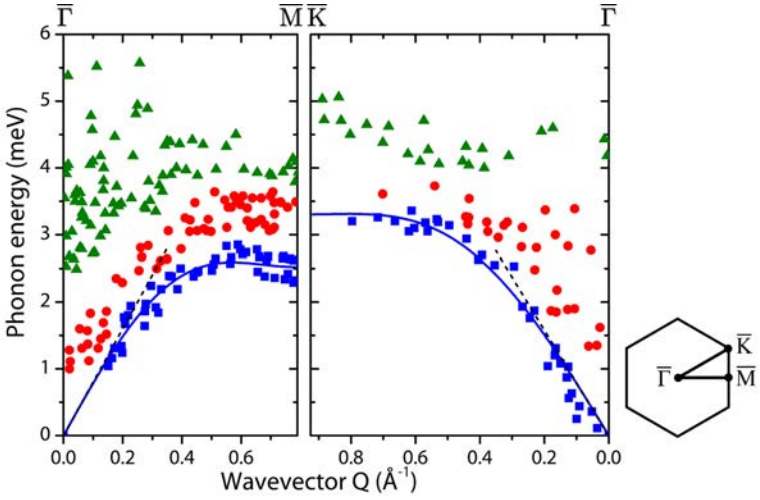

(b) Sample at room temperature

Figure 6.19.: Measured surface phonon dispersion of Bi(111). The solid blue lines were fitted using a simple force constant model of the first atomic layer. The black dashed lines represent the corresponding group velocities of the Rayleigh mode. The solid red and green lines serve as a guide to the eye.

Due to the pseudocubic character of the Bi(111) surface it is reasonable to compare the data with those of fcc(111) metals e.g. measurements of the surface phonon dispersion on Pt(111) by Harten et al.[35]. Using the proportion of the surface Debye temperatures on Bi(111) and Pt(111)[139,162] and the data by Harten et al. one would expect a group velocity between 6 meV and 6.8 meV for Bi(111). The actual group velocity determined from the phonon dispersion of Bi(111) is significantly larger, which is however confirmed by the DFPT calculations of D. Campi[145] shown in figure 6.18.
The DFPT calculations also illustrate that the intensity of the Rayleigh mode is rather weak, in particular in the vicinity of $\overline{\Gamma}$ it exhibits hardly any intensity. Indeed this is confirmed in the measurements where the Rayleigh mode cannot be observed for small wavevectors along $\overline{\Gamma M}$ up to approximately 0.2 Å (figure 6.19). Furthermore, the calculations also show the existence of the strong longitudinal resonance (red circles in figure 6.19). According to the calculations this mode is located in the first bilayer and exhibits the largest amplitude in the second layer (L2 in figure 6.18). The high intensity of this mode also confirms the fact that the corresponding peak in the TOF spectra is higher than the one of the Rayleigh mode.
Interestingly for the cooled sample (figure 6.19(a)) the Rayleigh mode tends to bend down before reaching the zone edge. In particular, the zone edge energy of the Rayleigh mode is even lower at the $\overline{\text{K}}$-point than it is at the $\overline{\text{M}}$-point which is in contrast to the calculations. This behavior and the phonon dispersion along $\overline{\Gamma K}$ in figure 6.19(a) look very much as in the case of an avoided crossing.
A similar avoided crossing has been observed in the phonon dispersion of metal surfaces such as Cu(111) and Al(001)[39]. Thereby on Cu(111) a large avoided crossing between the Rayleigh branch and the longitudinal resonance is observed which has been attributed to an intrinsic feature of metal surface dynamics[39,163]. Moreover, in the phonon dispersion of Cu(111) there appears also an avoided crossing between the longitudinal resonance with a 2nd-layer surface optical mode[163] which shows a behavior quite similar to the flat mode represented by the green triangles in figure 6.19(a).
In the following the longitudinal resonance and the flat mode at approximately 4 meV shall be discussed in greater detail and in particular, why they can be observed using HAS.

6.5.1. The Longitudinal Resonance

The DFPT calculations of the Bi(111) phonon dispersion (figure 6.18) clearly show the presence of a strong mode with longitudinal polarization in the first and the second layer which appears in the same energy region as the mode represented by

the red dots in the measured dispersion curve (figure 6.19).
This fact may again be an indication of the reported metallic character of Bi(111) since the existence of a surface acoustic phonon branch which is not predicted by the continuum theory is a common feature on metal surfaces. This so-called longitudinal resonance has only recently been discussed for surfaces such as Cu(111) and Al(001)[39,163]. While Heid et al.[34] first conjectured that this acoustic longitudinal resonance is an artifact of HAS it could be shown that this resonance is an intrinsic feature of the surface dynamics on metals[38,39].
Indeed this is quite intriguing since the displacement field of this phonon mode is located subsurface to a large extent and the question arises how HAS, a strictly surface-sensitive technique, can measure these modes with intensities that are often exceeding those of the Rayleigh wave[38,39].
However, HAS does not measure the phonon amplitudes but the corresponding surface charge density oscillations. Therefore, the intensities in inelastic HAS measurements can only be explained via the calculation of these charge density oscillations. These calculations showed that certain surface modes, that exhibit a negligible displacement in the surface layer, can nevertheless induce large charge density oscillations on the surface and give rise to large inelastic HAS amplitudes[38,39,163].
Notably, via this charge density oscillations, HAS intensities contain even information on the surface electron-phonon interaction[163].

6.5.2. The S3 Mode

Phonon modes with a similar dispersion as the flat mode at approximately 4 meV (green triangles in figure 6.19) have been observed for the vibration of adsorbates on surfaces. Those nearly dispersionless branches appear in a similar energy region and have been attributed to a collective motion of the adsorbate layer[164–166].
However, the influence of adsorbates on the Bi(111) surface can be excluded, since the diffuse elastic peak remains small during the timescale of the experiment. Furthermore, this mode cannot be explained by means of surface resonances, since the position of the peaks in the energy transfer spectra does not coincide with any resonance features with probable G-vectors.
The calculation of the surface phonon dispersion of Sb(111) by Campi et al.[167] already showed a flat strong resonance that appears in exactly the same energy region as on Bi(111) if the phonon dispersion of Sb is scaled accordingly. Interestingly, this branch appears in the projection onto the third layer (second bilayer).
As pointed out above, even though the He atoms are scattered by oscillations of the surface electron density about $2-3$ Å away from the first atomic layer, it has been shown that such subsurface modes are accessible for HAS. In the case

of a strong electron-phonon interaction the electron charge density above the first layer can oscillate up and down due to movement of the atoms in subsurface layers. Thereby it was shown that in the case of Pb(111) overlayers on Cu(111) even deep subsurface modes that are localized at the seventh layer could be observed by HAS[161,168].
Indeed, the calculations of the Bi(111) surface phonons seem to confirm the localization of this mode in the third layer. In particular, in the vicinity of the $\overline{\Gamma}$-point a strong longitudinally polarized mode appears at 4 meV (L3 in figure 6.18). Furthermore, there appears a strong shear vertical mode at approximately 5 meV, localized on the third layer, which extends nearly dispersionless over the entire Brillouin zone (SV3 in figure 6.18). Yet the SV mode is a little too high in comparison with the experiment, but this could be compensated by the expected softening if the spin orbit coupling were included in the calculations.
Therefore, the experimentally measured points in this energy region are likely to be caused due to the modes localized in the third layer. This is also supported by calculations which show that the SV3 mode produces an important surface charge density oscillation, which is of the same size as the highest optical mode[145].

6.5.3. Indication for a Kohn Anomaly

Figure 6.20 shows a magnification of the Rayleigh mode along $\overline{\Gamma\mathrm{K}}$ for the measurement with the crystal cooled down to 103 K. Although there are unfortunately only a few points available the dispersion curve exhibits distinct anomalies along $\overline{\Gamma\mathrm{K}}$: There appear two drops in the energy of the Rayleigh mode at the position of 0.11 Å^{-1} and 0.39 Å^{-1}. Such a softening of the phonons at a discrete value of Q can be caused by a so-called Kohn-anomaly[169].
It was Kohn who showed that dips in the phonon dispersion, known as Kohn anomalies, can be caused by electron-hole excitations which appear across the Fermi-surface with $2k_F$[170,171]. The alternating compressions and expansions of the lattice caused by a phonon propagating through a metal can give rise to the excitation of an electron-hole pair. Due to this process each electron subtracts the energy that is necessary for the transition from the energy and momentum of the phonon.
Under so-called nesting conditions this is the case for a multitude of electrons and a strong coupling between phonons and electron-hole excitations occurs. Therefore at values of Q, where this nesting condition is fulfilled, a dip appears in the phonon dispersion[10]
At $T = 0$ K the drop-off in the phonon energy is proportional to $\ln|\frac{q+2k_F}{q-2k_F}|$, hence the dip appears exactly at $q = 2k_F$. However, as demonstrated by Kröger[169] this static approximation also holds at higher temperatures for the phonon energies

which are considered in this work. Consequently, the behavior of the phonon dispersion at $q = 2k_F$ is related to the topology of the involved Fermi surface.[169]

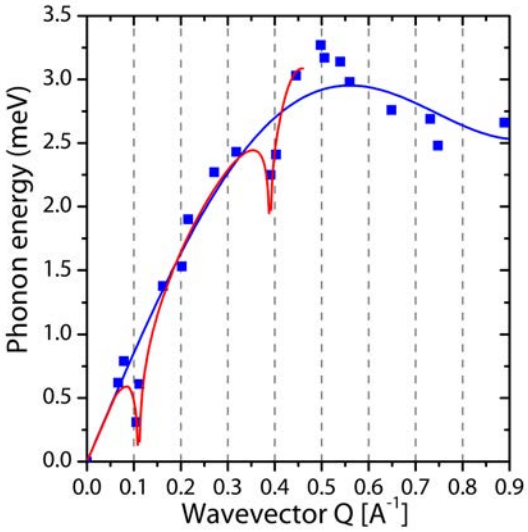

Figure 6.20.: Measured surface phonon dispersion for Bi(111) along $\overline{\Gamma K}$ with the crystal at 103 K. The solid blue line was fitted using a simple force constant model of the first atomic layer. The red line acts as a guide to the eye with the typical shape of a Kohn anomaly at $Q = 0.11$ Å^{-1} and $Q = 0.39$ Å^{-1}.

From the ARPES intensity map at the Fermi level (figure 6.21) which was measured by Ast et al[112] it can be seen that a good nesting region along $\overline{\Gamma K}$ appears for a transition between the two opposite sides of the small hexagon representing the electron pockets. The nesting vector for the small hexagon was determined to be $2k_F = 0.106$ Å^{-1} by Kim et al.[172]. Since the position of the Kohn anomaly in the phonon dispersion is related to the Fermi surface via the condition $Q = 2k_f$ this corresponds perfectly to the first dip in figure 6.20.
Note that the hexagonal element of the Fermi surface as shown in figure 6.21, is rotated by 30° with respect to the surface Brillouin zone which corresponds to a strong nesting in the $\overline{\Gamma K}$-direction[172]. This confirms also the fact that along $\overline{\Gamma M}$ no dips appear in the measurement. In particular, along $\overline{\Gamma K}$ the contours of the Fermi surface exhibit parallel segments, hence the necessary condition is fulfilled by various electronic states[169].
Another evidence for the existence of a Kohn anomaly is found in the temperature dependence, since the indentation of the dispersion curve due to the Kohn anomaly should decrease with increasing temperature[169]. While there appears no clear indication for any dips in the measurement at room temperature, they emerge in the dispersion determined with the crystal at 103 K.
Furthermore, theory predicts that the dip in the phonon dispersion increases as

the dimensionality of the system is reduced[169]. Therefore, the rather large dip in the phonon dispersion may be a hint towards a two-dimensional system.
The second anomaly observed at 0.39 $Å^{-1}$ in the phonon dispersion could be caused by transitions between the drop-like hole-pockets in figure 6.21. In contrast to the former intraband process the nesting condition involves now an interband transition whereupon there are four different ways along $\overline{\Gamma K}$ for this nesting.

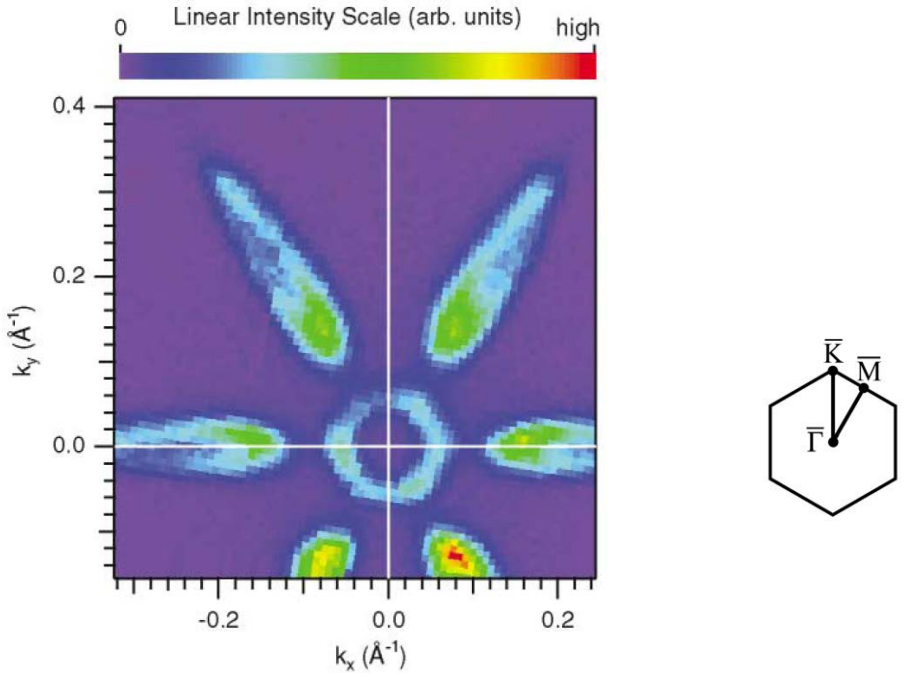

(a) Intensity map at the Fermi level from[112]

(b) Surface Brillouin zone

Figure 6.21.: ARPES intensity map at the Fermi level of Bi(111) from Ast et al.[112]†. The small hexagon corresponds to electron pockets whereas the drop-like contours are hole pockets.

It is important to note that, if there exist Kohn anomalies, those are non-adiabatic Kohn anomalies. As demonstrated by Kim et al.[172], the two opposing electron states on the hexagon of the Fermi surface exhibit opposing spin. Hence a transition between those two states would require a spin flipping process which can no longer be explained in terms of an adiabatic process.
Therefore, the anomaly observed in the phonon dispersion must be related to a non-adiabatic effect such as the sharp anomalies in hydrogen covered systems e.g. W(110):H and Mo(110):H[39,169,173].
Non-adiabatic anomalies can be attributed to an avoided crossing between the surface phonon branch with the quasi-1D electron-hole excitation branch. In this case HAS does no longer create a phonon but an electron-hole excitation due to a

† Copyright (2001) by the American Physical Society

strong electron-phonon coupling. In general, these non-adiabatic anomalies can be measured with HAS which is sensitive to charge density oscillations whereas EELS (electron-energy-loss-spectroscopy) is relatively insensitive to the charge density oscillations[39,174].

7. Summary

The present work describes the experimental technique of helium atom scattering (HAS) from surfaces to gain information on both surface structure and surface dynamics. While one part of the work concentrates on a first characterization of the apparatus, the novel findings on the structure and dynamics of Bi(111) are summarized below.

Surface Structure

Elastic HAS measurements on Bi(111) at a surface temperature of 123 K exhibit diffraction peaks up to third order whose positions are in an excellent agreement with the structural data previously obtained by Mönig et al.[139]. The high intensities of the diffraction peaks indicate a large corrugation both at surface temperatures of 123 K and 300 K.
With the eikonal approximation and the GR method a corrugation function was determined with a corrugation height of approximately 10% of the surface lattice constant. This is somewhat surprising since the reported metallic character of Bi(111) would imply a smoothing of the charge density corrugation by the Smoluchowski effect and hence a nearly flat corrugation. However, the observed corrugation height is comparable to those obtained for semimetals and may also be a consequence of the surface electron pocket states at the Fermi level.
Thermal attenuation effects in the intensities of the diffraction peaks were studied in a temperature range between 118 K and 408 K. A typical Debye-Waller behavior revealed surface Debye temperatures of (84 ± 8) K from the measurements of the specular peak and (75 ± 8) K from the measurements of the first order peak. In contrast to LEED measurements of a Bi nanofilm with a similar structure the surface Debye temperature measured with HAS remains constant over the whole temperature range, probably due to the different nature of electrons and helium atoms in scattering experiments.
Moreover, the corrugated Bi(111) surface allows also the observation of bound state resonances from which the corresponding surface potential profile can be determined. From the angular distribution three bound state levels were identified with binding energies of 6.18, 3.49 and 1.42 meV. These bound states were fitted with a 9-3 atom-surface interaction potential giving rise to a well depth

of $D = (8.32 \pm 0.73)$ meV. The determined values of the 9-3 potential could be confirmed by the measurement of resonance features in the specular intensity. The well depth D is consistent with previously determined values for noble metals[130,160].

Surface Dynamics

Using inelastic helium atom scattering the surface phonon dispersion of Bi(111) has been determined for the first time. Notably, due to the low energies the surface phonons on Bi(111) are hardly accessible for other scattering techniques such as electron scattering.
The surface phonon dispersion curve up to the Brillouin zone boundary was determined from a series of time-of-flight spectra. Thereby the phonon dispersion was measured at surface temperatures of 123 K and at room temperature. In both high-symmetry directions the phonon dispersion exhibits a Rayleigh mode, a longitudinal resonance and a nearly dispersionless branch at approximately 4 meV.
The group velocity of the Rayleigh mode gives rise to values between 7.9 meV $\cdot$ Å and 9.0 meV $\cdot$ Å depending on the azimuthal direction and the surface temperature whereupon the group velocity shows the typical decrease with increasing surface temperature. A comparison of the dispersion with DFPT (density functional perturbation theory) calculations by D. Campi[145] confirms the rather weak intensity of the Rayleigh mode in particular close to the $\overline{\Gamma}$-point.
Furthermore, the calculations also show the existence of the strong longitudinal resonance which exceeds the intensity of the Rayleigh mode. The appearance of such a phonon branch is a common feature on metal surfaces[39] which is again an indication of the metallic character of the Bi(111) surface. Interestingly, the DFPT calculations show that this mode exhibits the largest amplitude in the second layer. However, since HAS measures the surface charge density oscillations corresponding to the phonon amplitudes this mode can cause a large inelastic HAS amplitude via the electron-phonon interaction.
At first sight the origin of the flat phonon branch at approximately 4 meV, which appears in the energy region of the acoustic bulk modes, seems even more puzzling. While the influence of adsorbates on the surface can be excluded, scaled calculations of the surface phonon dispersion of Sb(111) already showed such a mode in the projection onto the third layer[167]. Indeed, the DFPT calculations for Bi(111) are able to reproduce the localization of this mode in the third layer (the second bilayer).
Thereby this branch is likely to be caused by a longitudinally polarized mode in the vicinity of $\overline{\Gamma}$ which turns into a shear vertical mode that extends nearly dispersionless over the entire Brillouin zone. In particular the DFPT calculations show

that the shear vertical mode produces a surface charge density oscillation, which is of the same size as the highest optical mode[145]. The underlying mechanism is the electron phonon-coupling which causes the electron charge density above the first layer to oscillate up and down due to the movement of the atoms in subsurface layers. Whereas such subsurface modes have already been observed with HAS in the case of Pb(111) overlayers on Cu(111)[161], this effect is observed for the first time on a single crystal surface.
Finally, the Rayleigh mode shows an indication for a Kohn anomaly along $\overline{\Gamma K}$. While the position of this anomaly coincides with nesting vectors across the Fermi surface involving the electron pockets and hole pockets, the anomaly must be related to a non-adiabatic effect which cannot be reproduced by DFPT. To confirm this indication of a Kohn anomaly, further measurements are on their way whereupon it should even be possible to calculate the dimensionless electron-phonon coupling parameter from the temperature dependence[169].

8. Bibliography

[1] H. Lüth, *Solid Surfaces, Interfaces and Thin Films* (Springer, 2001), 4th ed.

[2] A. Zangwill, *Physics at Surfaces* (Cambridge University Press, UK, 1996).

[3] E. Hulpke, *Helium Atom Scattering from Surfaces* (Springer, 1992).

[4] S. A. Safron, Adv. Chem. Phys. **95**, 129 (1996).

[5] S. A. Parameswaran and V. Oganesyan, Nat. Phys. **8**, 7 (2012), ISSN 1745-2473, URL http://dx.doi.org/10.1038/nphys2189.

[6] D. R. Miller, *Free jet source* (Oxford University Press, 1983), vol. 1, chap. 2, pp. 15–53, Atomic and Molecular Beam Methods.

[7] F. Traeger, ChemPhysChem **7**, 1006 (2006), ISSN 1439-7641, URL http://dx.doi.org/10.1002/cphc.200500599.

[8] D. Farias and K.-H. Rieder, Rep. Prog. Phys. **61**, 1575 (1998), URL http://stacks.iop.org/0034-4885/61/1575.

[9] T. Engel and K. Rieder, in *Structural Studies of Surfaces* (Springer Berlin / Heidelberg, 1982), vol. 91 of *Springer Tracts in Modern Physics*, pp. 55–180, URL http://dx.doi.org/10.1007/BFb0041342.

[10] G. Benedek and J. Toennies, Surf. Sci. **299-300**, 587 (1994), ISSN 0039-6028, URL http://dx.doi.org/10.1016/0039-6028(94)90683-1.

[11] R. B. Doak, *Single-Phonon Inelastic Helium Scattering* (Oxford University Press, 1983), vol. 2, chap. 14, pp. 385–441, Atomic and Molecular Beam Methods.

[12] J. P. Toennies, J. Phys.: Cond. Matt. **5**, A25 (1993), URL http://stacks.iop.org/0953-8984/5/i=33A/a=003.

[13] B. M. Murphy, M. Müller, J. Stettner, H. Requardt, J. Serrano, M. Krisch, and W. Press, J. Phys.: Cond. Matt. **20**, 224001 (2008), ISSN 0953-8984, URL http://stacks.iop.org/0953-8984/20/i=22/a=224001.

[14] J. P. Toennies, *Surface Phonons* (Springer, 1991), vol. 21 of *Springer Series in Surface Sciences*, chap. Experimental Determination of Surface Phonons by Helium Atom and Electron Energy Loss Spectroscopy, pp. 111–166.

[15] C. Kittel, *Introduction to Solid State Physics* (John Wiley & Sons Inc, 2005).

[16] W. N. Unertl, in *Physical Structure*, edited by W. Unertl (North-Holland, 1996), vol. Volume 1, pp. 3–49, URL http://www.sciencedirect.com/science/article/pii/S1573433196800060.

[17] K. Oura, V. G. Lifshits, A. A. Saranin, A. V. Zotov, and M. Katayama, *Surface Science: An Introduction* (Springer, 2003).

[18] L. P. Bouckaert, R. Smoluchowski, and E. Wigner, Phys. Rev. **50**, 58 (1936), URL http://link.aps.org/doi/10.1103/PhysRev.50.58.

[19] H. Ibach, *Physics of Surfaces and Interfaces* (Springer, 2006).

[20] H. Pauly, *Atom, Molecule, and Cluster Beams I* (Springer, 2000).

[21] T. Reisinger, G. Bracco, S. Rehbein, G. Schmahl, W. E. Ernst, and B. Holst, J. Phys. Chem. A **111**, 12620 (2007).

[22] D. J. Auerbach, *Velocity measurements by Time-of-Flight methods* (Oxford University Press, 1983), vol. 1, chap. 14, pp. 363–379, Atomic and Molecular Beam Methods.

[23] H. Pauly, *Atom, Molecule, and Cluster Beams II* (Springer, 2000).

[24] M. Mayrhofer-Reinhartshuber, Master's thesis, Graz University of Technology (2010).

[25] C. A. Visser, J. Wolleswinkel, and J. Los, J. Phys. E **3**, 483 (1970), URL http://stacks.iop.org/0022-3735/3/i=7/a=302.

[26] R. B. Doak, *Experimental Limitations and Opportunities in Single Phonon Inelastic Helium Scattering* (Springer, 1992), vol. 27 of *Springer Series in Surface Sciences*, chap. 2, pp. 5–39, Helium Atom Scattering from Surfaces.

[27] F. Huisken, Ph.D. thesis, Georg-August-Universität Göttingen (1978).

[28] C. V. Nowikow and R. Grice, J. Phys. E **12**, 515 (1979), URL http://stacks.iop.org/0022-3735/12/i=6/a=017.

[29] P. Kraus, Master's thesis, Graz University of Technology (2011).

[30] L. E. Díaz-Sánchez, A. H. Romero, and X. Gonze, Phys. Rev. B **76**, 104302 (2007), URL http://dx.doi.org/10.1103/PhysRevB.76.104302.

[31] F. W. de Wette, *Surface Phonons* (Springer, 1991), vol. 21 of *Springer Series in Surface Sciences*, chap. Study of Surface Phonons by the Slab Method, pp. 67–109.

[32] K. Kern and G. Comsa, *Helium-Scattering Studies of the Dynamics and Phase Transitions of Surfaces* (John Wiley & Sons, Inc., 1989), pp. 211–280, ISBN 9780470141250, URL http://dx.doi.org/10.1002/9780470141250.ch5.

[33] J. Xie, S. de Gironcoli, S. Baroni, and M. Scheffler, Phys. Rev. B **59**, 965 (1999), URL http://link.aps.org/doi/10.1103/PhysRevB.59.965.

[34] R. Heid and K.-P. Bohnen, Physics Reports **387**, 151 (2003), ISSN 0370-1573, URL http://www.sciencedirect.com/science/article/pii/S0370157303003247.

[35] U. Harten, J. P. Toennies, and C. Woll, Faraday Discuss. Chem. Soc. **80**, 137 (1985), ISSN 0301-7249, URL http://dx.doi.org/10.1039/DC9858000137.

[36] C. Kaden, P. Ruggerone, J. P. Toennies, G. Zhang, and G. Benedek, Phys. Rev. B **46**, 13509 (1992), URL http://link.aps.org/doi/10.1103/PhysRevB.46.13509.

[37] C. S. Jayanthi, H. Bilz, W. Kress, and G. Benedek, Phys. Rev. Lett. **59**, 795 (1987), URL http://link.aps.org/doi/10.1103/PhysRevLett.59.795.

[38] V. Chis, B. Hellsing, G. Benedek, M. Bernasconi, and J. P. Toennies, J. Phys.: Cond. Matt. **19**, 305011 (2007), ISSN 0953-8984, URL http://stacks.iop.org/0953-8984/19/i=30/a=305011.

[39] G. Benedek, M. Bernasconi, V. Chis, E. Chulkov, P. M. Echenique, B. Hellsing, and J. P. Toennies, J. Phys.:Cond. Matt. **22**, 084020 (2010), URL http://stacks.iop.org/0953-8984/22/i=8/a=084020.

[40] A. A. Maradudin and G. I. Stegeman, eds., *Surface Phonons* (Springer, 1991), vol. 21 of *Springer Series in Surface Sciences*, chap. Surface Acoustic Waves, pp. 5–35.

[41] J. T. Lewis, A. Lehoczky, and C. V. Briscoe, Phys. Rev. **161**, 877 (1967), URL http://link.aps.org/doi/10.1103/PhysRev.161.877.

[42] H. Hoinkes, Rev. Mod. Phys. **52**, 933 (1980), URL http://rmp.aps.org/abstract/RMP/v52/i4/p933_1.

[43] G. P. Brivio and M. I. Trioni, Rev. Mod. Phys. **71**, 231 (1999), URL http://link.aps.org/doi/10.1103/RevModPhys.71.231.

[44] M. I. Trioni, G. Fratesi, S. Achilli, and G. P. Brivio, J. Phys.:Cond. Matt. **21**, 264003 (2009), URL http://stacks.iop.org/0953-8984/21/i=26/a=264003.

[45] V. Celli, D. Eichenauer, A. Kaufhold, and J. P. Toennies, J. Chem. Phys. **83**, 2504 (1985), URL http://link.aip.org/link/?JCP/83/2504/1.

[46] G. Boato, *Elastic Scattering of Atoms* (Oxford University Press, 1983), vol. 2, chap. 12, pp. 340–365, Atomic and Molecular Beam Methods.

[47] A. Apfolter, Master's thesis, Graz University of Technology (2005).

[48] G. Brusdeylins, R. B. Doak, and J. P. Toennies, Phys. Rev. B **27**, 3662 (1983), URL http://link.aps.org/abstract/PRB/v27/p3662.

[49] J. R. Manson, Phys. Rev. B **43**, 6924 (1991), URL http://link.aps.org/abstract/PRB/v43/p6924.

[50] R. B. Doak, Ph.D. thesis, Massachusettes Institute of Technology (1981).

[51] G. Bracco, Ph.D. thesis, University of Genova (??).

[52] G. Benedek, G. Brusdeylins, J. P. Toennies, and R. B. Doak, Phys. Rev. B **27**, 2488 (1983), URL http://link.aps.org/doi/10.1103/PhysRevB.27.2488.

[53] G. Benedek, G. Brusdeylins, R. Bruce Doak, J. G. Skofronick, and J. P. Toennies, Phys. Rev. B **28**, 2104 (1983), URL http://link.aps.org/doi/10.1103/PhysRevB.28.2104.

[54] D. J. Auerbach, *Multiple-Phonon Inelastic Scattering* (Oxford University Press, 1983), vol. 2, chap. 15, pp. 444–462, Atomic and Molecular Beam Methods.

[55] U. Valbusa, *General Principles and Methods* (Oxford University Press, 1983), vol. 2, chap. 11, pp. 327–339, Atomic and Molecular Beam Methods.

[56] R. Manson and V. Celli, Surf. Sci. **24**, 495 (1971), ISSN 0039-6028, URL http://www.sciencedirect.com/science/article/pii/0039602871902779.

[57] E. Conrad, in *Physical Structure*, edited by W. Unertl (North-Holland, 1996), vol. 1 of *Handbook of Surface Science*, pp. 271 – 360, URL http://www.sciencedirect.com/science/article/pii/S1573433196800126.

[58] R. Smoluchowski, Phys. Rev. **60**, 661 (1941), URL http://link.aps.org/doi/10.1103/PhysRev.60.661.

[59] J. Wauer and T. Rother, Opt. Commun. **282**, 339 (2009), ISSN 0030-4018, URL http://www.sciencedirect.com/science/article/pii/S0030401808010122.

[60] J. R. Manson and K.-H. Rieder, Phys. Rev. B **62**, 13142 (2000), URL http://link.aps.org/doi/10.1103/PhysRevB.62.13142.

[61] D. Kaufman, R. James, and T. Engel, Surf. Sci. **148**, 72 (1984), ISSN 0039-6028, URL http://www.sciencedirect.com/science/article/pii/0039602884900311.

[62] B. Salanon and G. Armand, Surf. Sci. **112**, 78 (1981), ISSN 0039-6028, URL http://www.sciencedirect.com/science/article/pii/0039602881903356.

[63] S. L. Cunningham, Phys. Rev. B **10**, 4988 (1974), URL http://link.aps.org/doi/10.1103/PhysRevB.10.4988.

[64] N. Garcia, J. Chem. Phys. **67**, 897 (1977), URL http://link.aip.org/link/?JCP/67/897/1.

[65] N. García and N. Cabrera, Phys. Rev. B **18**, 576 (1978), URL http://link.aps.org/doi/10.1103/PhysRevB.18.576.

[66] M. Mayrhofer-Reinhartshuber, Ph.D. thesis, Graz University of Technology (unpublished).

[67] J. R. Manson, E-mail correspondence (2011).

[68] E. H. Conrad, D. S. Kaufman, L. R. Allen, R. M. Aten, and T. Engel, J. Chem. Phys. **83**, 5286 (1985), URL http://link.aip.org/link/?JCP/83/5286/1.

[69] J. S. Becker, R. D. Brown, E. Johansson, N. S. Lewis, and S. J. Sibener, J. Chem. Phys. **133**, 104705 (pages 8) (2010), URL http://link.aip.org/link/?JCP/133/104705/1.

[70] D. Eichenauer, U. Harten, J. P. Toennies, and V. Celli, J. Chem. Phys. **86**, 3693 (1987), URL http://link.aip.org/link/?JCP/86/3693/1.

[71] G. Benedek and N. Garcia, Surf. Sci. Lett. **103**, L143 (1981), ISSN 0167-2584, URL http://www.sciencedirect.com/science/article/pii/0167258481906307.

[72] G. Benedek and G. Seriani, Jpn. J. Appl. Phys. **2S2**, 545 (1974), URL http://jjap.jsap.jp/link?JJAPS/2S2/545/.

[73] G. Benedek and N. Garcia, Surf. Sci. **80**, 543 (1979), ISSN 0039-6028, URL http://www.sciencedirect.com/science/article/pii/0039602879907155.

[74] V. Bortolani, A. Franchini, N. Garcia, F. Nizzoli, and G. Santoro, Phys. Rev. B **28**, 7358 (1983), URL http://link.aps.org/doi/10.1103/PhysRevB.28.7358.

[75] G. Witte, J. Toennies, and C. Wöll, Surf. Sci. **323**, 228 (1995), ISSN 0039-6028, URL http://www.sciencedirect.com/science/article/pii/0039602894005931.

[76] N. S. Luo, P. Ruggerone, J. P. Toennies, and G. Benedek, Phys. Scr. **1993**, 584 (1993), URL http://stacks.iop.org/1402-4896/1993/i=T49B/a=036.

[77] A. Jardine, H. Hedgeland, G. Alexandrowicz, W. Allison, and J. Ellis, Prog. Surf. Sci. **84**, 323 (2009), ISSN 0079-6816, URL http://www.sciencedirect.com/science/article/B6TJF-4X0MP7F-1/2/4b3a9cac32140a526ede2c1e79325b49.

[78] S. Miret-Artés, Surf. Sci. **366**, L735 (1996), ISSN 0039-6028, URL http://www.sciencedirect.com/science/article/B6TVX-3VXHPHX-5B/2/b0d4fc6453a1e5253d055d861843f124.

[79] D. J. Riley, A. P. Jardine, S. Dworski, G. Alexandrowicz, P. Fouquet, J. Ellis, and W. Allison, J. Chem. Phys. **126**, 104702 (2007), URL http://link.aip.org/link/?JCP/126/104702/1.

[80] H. Hoinkes, H. Nahr, and H. Wilsch, Surf. Sci. **30**, 363 (1972), ISSN 0039-6028, URL http://www.sciencedirect.com/science/article/B6TVX-46SXKGY-HK/2/aad013d856232360818b6523a0d4286c.

[81] D. Evans, V. Celli, G. Benedek, J. P. Toennies, and R. B. Doak, Phys. Rev. Lett. **50**, 1854 (1983), URL http://link.aps.org/doi/10.1103/PhysRevLett.50.1854.

[82] G. Lilienkamp and J. P. Toennies, J. Chem. Phys. **78**, 5210 (1983), URL http://link.aip.org/link/?JCP/78/5210/1.

[83] G. Brusdeylins, R. B. Doak, and J. P. Toennies, Phys. Rev. Lett. **46**, 437 (1981), URL http://link.aps.org/abstract/PRL/v46/p437.

[84] G. Brusdeylins, R. B. Doak, and J. P. Toennies, J. Chem. Phys. **75**, 1784 (1981), URL http://link.aip.org/link/?JCP/75/1784/1.

[85] G. Benedek and S. Miret-Artés, Surf. Sci. **339**, L935 (1995), ISSN 0039-6028, URL http://www.sciencedirect.com/science/article/pii/0039602895800611.

[86] G. Benedek, R. Gerlach, A. Glebov, G. Lange, S. Miret-Artes, J. G. Skofronick, and J. P. Toennies, Phys. Rev. B **53**, 11211 (1996), URL http://link.aps.org/doi/10.1103/PhysRevB.53.11211.

[87] G. Benedek, J. P. Toennies, and R. B. Doak, Phys. Rev. B **28**, 7277 (1983), URL http://link.aps.org/doi/10.1103/PhysRevB.28.7277.

[88] G. Lee, Ph.D. thesis, University of Cambridge (2004).

[89] V. Celli, N. Garcia, and J. Hutchison, Surf. Sci. **87**, 112 (1979), ISSN 0039-6028, URL http://www.sciencedirect.com/science/article/pii/0039602879901730.

[90] G. Derry, D. Wesner, S. V. Krishnaswamy, and D. R. Frankl, Surf. Sci. **74**, 245 (1978), ISSN 0039-6028, URL http://www.sciencedirect.com/science/article/B6TVX-46P3R5M-K5/2/4ab61e2145038224748l4e48e5d45991.

[91] H. Jonsson and J. H. Weare, J. Chem. Phys. **86**, 3711 (1987), URL http://link.aip.org/link/?JCP/86/3711/1.

[92] J. Perreau and J. Lapujoulade, Surf. Sci. **122**, 341 (1982), ISSN 0039-6028, URL http://www.sciencedirect.com/science/article/B6TVX-46T379Y-FH/2/a5e9e740b361fbde374c5a40dd820f4e.

[93] G. Boato, P. Cantini, C. Guidi, R. Tatarek, and G. P. Felcher, Phys. Rev. B **20**, 3957 (1979), URL http://link.aps.org/doi/10.1103/PhysRevB.20.3957.

[94] M. A. Krzyzowski, P. Zeppenfeld, and G. Comsa, J. Chem. Phys. **103**, 8705 (1995), URL http://link.aip.org/link/?JCP/103/8705/1.

[95] M. W. Cole and T. Tsong, Surf. Sci. **69**, 325 (1977), ISSN 0039-6028, URL http://www.sciencedirect.com/science/article/pii/0039602877901777.

[96] A. Tamtögl, Master's thesis, Graz University of Technology (2008).

[97] J. F. O'Hanlon, *A Users's Guide to Vacuum Technology* (John Wiley & Sons, Inc., 2003).

[98] J. P. Toennies, J. Vac. Sci. Technol., A **2**, 1055 (1984), URL http://link.aip.org/link/?JVA/2/1055/1.

[99] W. Allison, R. F. Willis, and M. Cardillo, Phys. Rev. B **23**, 6824 (1981), URL http://link.aps.org/doi/10.1103/PhysRevB.23.6824.

[100] J. Estel, H. Hoinkes, H. Kaarmann, H. Nahr, and H. Wilsch, Surf. Sci. **54**, 393 (1976), ISSN 0039-6028, URL http://www.sciencedirect.com/science/article/pii/0039602876902338.

[101] G. Comsa, Surf. Sci. **81**, 57 (1979), ISSN 0039-6028, URL http://www.sciencedirect.com/science/article/pii/0039602879905053.

[102] D. R. Frankl, Surf. Sci. **84**, L485 (1979), ISSN 0039-6028, URL http://www.sciencedirect.com/science/article/pii/0039602879901511.

[103] J. B. Pendry (1978), Reply to "Coherence Length and/or Transfer Width?".

[104] B. Poelsema, R. L. Palmer, G. Mechtersheimer, and G. Comsa, Surf. Sci. **117**, 60 (1982), ISSN 0039-6028, URL http://www.sciencedirect.com/science/article/pii/003960288290485X.

[105] J. Lapujoulade, Y. Lejay, and G. Armand, Surf. Sci. **95**, 107 (1980), ISSN 0039-6028, URL http://www.sciencedirect.com/science/article/pii/0039602880901314.

[106] D. Smilgies and J. P. Toennies, Rev. Sci. Instrum. **59**, 2185 (1988), URL http://dx.doi.org/10.1063/1.1139984.

[107] R. B. Doak, in *Proceedings of the Werner Brandt Workshop* (1984), URL www.osti.gov/bridge/servlets/purl/5749002-58nAE4/.

[108] K. Behnia, L. Balicas, and Y. Kopelevich, Science **317**, 1729 (2007), URL http://dx.doi.org/10.1126/science.1146509.

[109] L. Li, J. G. Checkelsky, Y. S. Hor, C. Uher, A. F. Hebard, R. J. Cava, and N. P. Ong, Science **321**, 547 (2008), URL http://www.sciencemag.org/content/321/5888/547.abstract.

[110] B. Fauqué, H. Yang, I. Sheikin, L. Balicas, J.-P. Issi, and K. Behnia, Phys. Rev. B **79**, 245124 (2009), URL http://link.aps.org/doi/10.1103/PhysRevB.79.245124.

[111] P. Hofmann, Prog. Surf. Sci. **81**, 191 (2006), ISSN 0079-6816, URL http://dx.doi.org/10.1016/j.progsurf.2006.03.001.

[112] C. R. Ast and H. Höchst, Phys. Rev. Lett. **87**, 177602 (2001), URL http://dx.doi.org/10.1103/PhysRevLett.87.177602.

[113] F. Patthey, W.-D. Schneider, and H. Micklitz, Phys. Rev. B **49**, 11293 (1994), URL http://dx.doi.org/10.1103/PhysRevB.49.11293.

[114] K. Behnia, Science **321**, 497 (2008), http://www.sciencemag.org/content/321/5888/497.full.pdf, URL http://www.sciencemag.org/content/321/5888/497.short.

[115] B. Seradjeh, J. Wu, and P. Phillips, Phys. Rev. Lett. **103**, 136803 (2009), URL http://link.aps.org/doi/10.1103/PhysRevLett.103.136803.

[116] Z. Zhu, A. Collaudin, B. Fauque, W. Kang, and K. Behnia, Nat. Phys. **8**, 89 (2012), ISSN 1745-2473, URL http://dx.doi.org/10.1038/nphys2111.

[117] K. Behnia, M.-A. Méasson, and Y. Kopelevich, Phys. Rev. Lett. **98**, 166602 (2007), URL http://dx.doi.org/10.1103/PhysRevLett.98.166602.

[118] Y. V. Sharlai and G. P. Mikitik, Phys. Rev. B **79**, 081102 (2009), URL http://dx.doi.org/10.1103/PhysRevB.79.081102.

[119] M. Matsuo, A. Endo, N. Hatano, H. Nakamura, R. Shirasaki, and K. Sugihara, Phys. Rev. B **80**, 075313 (2009), URL http://dx.doi.org/10.1103/PhysRevB.80.075313.

[120] Y. V. Sharlai and G. P. Mikitik, Phys. Rev. B **83**, 085103 (2011), URL http://link.aps.org/doi/10.1103/PhysRevB.83.085103.

[121] Z. Zhu, B. Fauqué, Y. Fuseya, and K. Behnia, Phys. Rev. B **84**, 115137 (2011), URL http://link.aps.org/doi/10.1103/PhysRevB.84.115137.

[122] B. Weitzel and H. Micklitz, Phys. Rev. Lett. **66**, 385 (1991), URL http://dx.doi.org/0.1103/PhysRevLett.66.385.

[123] C. Vossloh, M. Holdenried, and H. Micklitz, Phys. Rev. B **58**, 12422 (1998), URL http://dx.doi.org/10.1103/PhysRevB.58.12422.

[124] M. Tian, N. Kumar, M. H. W. Chan, and T. E. Mallouk, Phys. Rev. B **78**, 045417 (2008), URL http://dx.doi.org/10.1103/PhysRevB.78.045417.

[125] F. Muntyanu, A. Gilewski, K. Nenkov, A. Zaleski, and V. Chistol, Solid State Commun. **147**, 183 (2008), ISSN 0038-1098, URL http://dx.doi.org/10.1016/j.ssc.2008.05.024.

[126] M. Tian, J. Wang, Q. Zhang, N. Kumar, T. E. Mallouk, and M. H. W. Chan, Nano Lett. **9**, 3196 (2009), ISSN 1530-6984, URL http://dx.doi.org/10.1021/nl901431t.

[127] G. Benedek, G. Brusdeylins, C. Heimlich, J. Toennies, and U. Valbusa, Surf. Sci. **178**, 545 (1986), ISSN 0039-6028, URL http://www.sciencedirect.com/science/article/pii/0039602886903316.

[128] G. Boato, P. Cantini, C. Salvo, R. Tatarek, and S. Terreni, Surf. Sci. **114**, 485 (1982), ISSN 0039-6028, URL http://www.sciencedirect.com/science/article/pii/0039602882907002.

[129] P. Cantini and R. Tatarek, Surf. Sci. **114**, 471 (1982), ISSN 0039-6028, URL http://www.sciencedirect.com/science/article/pii/0039602882906999.

[130] P. Kraus, A. Tamtögl, M. Mayrhofer-Reinhartshuber, W. E. Ernst, and G. Benedek, unpublished (2012).

[131] M. Hengsberger, P. Segovia, M. Garnier, D. Purdie, and Y. Baer, Eur. Phys. J. B **17**, 603 (2000), URL http://dx.doi.org/10.1007/s100510070097.

[132] L. A. Wray, S.-Y. Xu, Y. Xia, D. Hsieh, A. V. Fedorov, Y. S. Hor, R. J. Cava, A. Bansil, H. Lin, and M. Z. Hasan, Nat. Phys. **7**, 32 (2011), ISSN 1745-2473, URL http://dx.doi.org/10.1038/nphys1838.

[133] D. Hsieh, Y. Xia, D. Qian, L. Wray, J. H. Dil, F. Meier, J. Osterwalder, L. Patthey, J. G. Checkelsky, N. P. Ong, et al., Nature **460**, 1101 (2009), ISSN 0028-0836, URL http://dx.doi.org/10.1038/nature08234.

[134] X. Zhu, L. Santos, R. Sankar, S. Chikara, C. . Howard, F. C. Chou, C. Chamon, and M. El-Batanouny, Phys. Rev. Lett. **107**, 186102 (2011), URL http://link.aps.org/doi/10.1103/PhysRevLett.107.186102.

[135] A. Tamtögl, M. Mayrhofer-Reinhartshuber, N. Balak, W. E. Ernst, and K. H. Rieder, J. Phys.: Cond. Matt. **22**, 304019 (2010), URL http://stacks.iop.org/0953-8984/22/i=30/a=304019.

[136] M. Mayrhofer-Reinhartshuber, A. Tamtögl, P. Kraus, K. H. Rieder, and W. E. Ernst, J. Phys.: Cond. Matt. **24**, 104008 (2012), ISSN 0953-8984, URL http://stacks.iop.org/0953-8984/24/i=10/a=104008.

[137] A. Kokalj, Comput. Mater. Sci. **28**, 155 (2003), ISSN 0927-0256, URL http://www.sciencedirect.com/science/article/B6TWM-49H73N8-9/2/4671dde62e473bc4f7aa7822e61b6231.

[138] F. Jona, Surf. Sci. **8**, 57 (1967), ISSN 0039-6028, URL http://dx.doi.org/10.1103/10.1016/0039-6028(67)90073-8.

[139] H. Mönig, J. Sun, Y. M. Koroteev, G. Bihlmayer, J. Wells, E. V. Chulkov, K. Pohl, and P. Hofmann, Phys. Rev. B **72**, 085410 (2005), URL http://dx.doi.org/10.1103/PhysRevB.72.085410.

[140] Y. M. Koroteev, G. Bihlmayer, J. E. Gayone, E. V. Chulkov, S. Blügel, P. M. Echenique, and P. Hofmann, Phys. Rev. Lett. **93**, 046403 (2004), URL http://dx.doi.org/10.1103/PhysRevLett.93.046403.

[141] C. R. Ast and H. Höchst, Phys. Rev. B **70**, 245122 (2004), URL http://dx.doi.org/10.1103/PhysRevB.70.245122.

[142] C. R. Ast and H. Höchst, Phys. Rev. B **67**, 113102 (2003), URL http://dx.doi.org/10.1103/PhysRevB.67.113102.

[143] G. Jezequel, J. Thomas, and I. Pollini, Phys. Rev. B **56**, 6620 (1997), URL http://dx.doi.org/10.1103/PhysRevB.56.6620.

[144] G. Jezequel, Y. Petroff, R. Pinchaux, and F. Yndurain, Phys. Rev. B **33**, 4352 (1986), URL http://dx.doi.org/10.1103/PhysRevB.33.4352.

[145] D. Campi and G. Benedek, E-mail correspondence (2012).

[146] C. Wöll and A. M. Lahee, *Helium Atom Scattering from Surfaces* (Springer, 1992).

[147] E. Stoll, M. Baumberger, and N. Garcia, J. Chem. Phys. **81**, 1496 (1984), URL http://link.aip.org/link/?JCP/81/1496/1.

[148] J. Lee, J. Cowin, and L. Wharton, Surf. Sci. **130**, 1 (1983), ISSN 0039-6028, URL http://dx.doi.org/10.1016/0039-6028(83)90256-X.

[149] G. Boato, P. Cantini, and R. Tatarek, Phys. Rev. Lett. **40**, 887 (1978), URL http://dx.doi.org/10.1103/PhysRevLett.40.887.

[150] N. Esbjerg and J. K. Nørskov, Phys. Rev. Lett. **45**, 807 (1980), URL http://link.aps.org/doi/10.1103/PhysRevLett.45.807.

[151] J. Harris and A. Liebsch, J. Phys. C **15**, 2275 (1982), URL http://stacks.iop.org/0022-3719/15/i=10/a=027.

[152] R. M. Goodman and G. A. Somorjai, J. Chem. Phys. **52**, 6325 (1970), URL http://dx.doi.org/10.1063/1.1672946.

[153] K. G. Ramanathan and T. M. Srinivasan, Phys. Rev. **99**, 442 (1955), URL http://dx.doi.org/10.1103/PhysRev.99.442.

[154] F. van Delft, Surf. Sci. **251-252**, 690 (1991), ISSN 0039-6028, URL http://www.sciencedirect.com/science/article/pii/003960289191080H.

[155] D. Velic and R. J. Levis, Chem. Phys. Lett. **269**, 59 (1997), ISSN 0009-2614, URL http://www.sciencedirect.com/science/article/pii/S0009261497002509.

[156] E. K. Grimmelmann, J. C. Tully, and M. J. Cardillo, J. Chem. Phys. **72**, 1039 (1980), URL http://link.aip.org/link/?JCP/72/1039/1.

[157] S. Yaginuma and T. Nagao, Phys. Rev. B **82**, 045422 (2010).

[158] S. Yaginuma, T. Nagao, J. Sadowski, M. Saito, K. Nagaoka, Y. Fujikawa, T. Sakurai, and T. Nakayama, Surf. Sci. **601**, 3593 (2007), ISSN 0039-6028, URL http://www.sciencedirect.com/science/article/pii/S003960280700739X.

[159] J. Lapujoulade, Y. Lejay, and N. Papanicolaou, Surf. Sci. **90**, 133 (1979), ISSN 0039-6028, URL http://www.sciencedirect.com/science/article/pii/0039602879900165.

[160] J. M. Horne, S. C. Yerkes, and D. R. Miller, Surf. Sci. **93**, 47 (1980), ISSN 0039-6028, URL http://www.sciencedirect.com/science/article/pii/003960288090045X.

[161] I. Y. Sklyadneva, G. Benedek, E. V. Chulkov, P. M. Echenique, R. Heid, K.-P. Bohnen, and J. P. Toennies, Phys. Rev. Lett. **107**, 095502 (2011), URL http://link.aps.org/doi/10.1103/PhysRevLett.107.095502.

[162] H. B. Lyon and G. A. Somorjai, J. Chem. Phys. **44**, 3707 (1966), URL http://dx.doi.org/10.1063/1.1726523.

[163] V. Chis, B. Hellsing, G. Benedek, M. Bernasconi, E. V. Chulkov, and J. P. Toennies, Phys. Rev. Lett. **101**, 206102 (2008), URL http://link.aps.org/doi/10.1103/PhysRevLett.101.206102.

[164] G. Witte and J. P. Toennies, Phys. Rev. B **62**, R7771 (2000), URL http://link.aps.org/doi/10.1103/PhysRevB.62.R7771.

[165] L. W. Bruch, A. P. Graham, and J. P. Toennies, J. Chem. Phys. **112**, 3314 (2000), URL http://dx.doi.org/10.1063/1.480914.

[166] A. P. Graham, M. F. Bertino, F. Hofmann, J. P. Toennies, and C. Woll, J. Chem. Phys. **106**, 6194 (1997), URL http://dx.doi.org/10.1063/1.473242.

[167] D. Campi, M. Bernasconi, and G. Benedek, Phys. Rev. B **submitted** (2012).

[168] J. Braun, P. Ruggerone, G. Zhang, J. P. Toennies, and G. Benedek, Phys. Rev. B **79**, 205423 (2009), URL http://link.aps.org/doi/10.1103/PhysRevB.79.205423.

[169] J. Kröger, Rep. Prog. Phys. **69**, 899 (2006), URL http://stacks.iop.org/0034-4885/69/i=4/a=R02.

[170] E. Plummer, J. Shi, S.-J. Tang, E. Rotenberg, and S. Kevan, Prog. Surf. Sci. **74**, 251 (2003), ISSN 0079-6816, URL http://www.sciencedirect.com/science/article/pii/S0079681603000807.

[171] W. Kohn, Phys. Rev. Lett. **2**, 393 (1959), URL http://link.aps.org/doi/10.1103/PhysRevLett.2.393.

[172] T. K. Kim, J. Wells, C. Kirkegaard, Z. Li, S. V. Hoffmann, J. E. Gayone, I. Fernandez-Torrente, P. Häberle, J. I. Pascual, K. T. Moore, et al., Phys. Rev. B **72**, 085440 (2005), URL http://dx.doi.org/10.1103/PhysRevB.72.085440.

[173] J. Kröger, J. Phys.: Cond. Matt. **20**, 224015 (2008), ISSN 0953-8984, URL http://stacks.iop.org/0953-8984/20/i=22/a=224015.

[174] G. Benedek, M. Pardo, and P. Toennies, J, in *Highlights on Spectroscopies of Semiconductors and Nanostructures*, edited by G. Guizzetti, C. Andreani, A, F. Marabelli, and M. Patrini (2007), vol. 94, pp. 151–67.

A. Appendix

A.1. Tabular Listing of the Measured Diffraction Intensities on Bi(111)

Table A.1.: Diffraction peak intensities for He scattered from Bi(111) along the $\langle 11 \rangle$ azimuth at different incident energies E_i and surface temperatures T_S.

E_i (meV)	T_S (K)	$\vec{G}_{hk}$ h	k	Peak intensity (cps)	Peak area (° cps)	Relative intensity	Relative area
		1	1	1390	957	0.14	0.22
17.9	113	0	0	10141	4437	1.00	1.00
		-1	-1	1262	830	0.12	0.19
		1	1	1387	1054	0.10	0.20
21.4	113	0	0	13271	5308	1.00	1.00
		-1	-1	885	627	0.07	0.12
		1	1	688	541	0.07	0.14
24.1	113	0	0	9574	3903	1.00	1.00
		-1	-1	645	369	0.07	0.09
		1	1	2072	1211	0.17	0.33
15.5	123	0	0	12229	3635	1.00	1.00
		-1	-1	902	588	0.07	0.16
		1	1	86	89	0.02	0.07
39.7	122	0	0	3918	1199	1.00	1.00
		-1	-1	46	28	0.01	0.02
		1	1	153	97	0.04	0.07
31.7	197	0	0	4113	1366	1.00	1.00
		-1	-1	97	88	0.02	0.06

Table A.2.: Diffraction peak intensities for He scattered from Bi(111) along the ⟨11⟩ azimuth at different incident energies E_i and the crystal at room temperature ($T_S = 300$K).

E_i (meV)	T_S (K)	$\vec{G}_{hk}$ h	k	Peak intensity (cps)	Peak area (° cps)	Relative intensity	Relative area
		1	1	494	318	0.20	0.29
16.8	300	0	0	2477	1082	1.00	1.00
		-1	-1	394	236	0.16	0.22
		1	1	431	259	0.16	0.27
17.9	300	0	0	2615	976	1.00	1.00
		-1	-1	337	198	0.13	0.20
		1	1	379	239	0.13	0.20
20.3	300	0	0	2999	1203	1.00	1.00
		-1	-1	230	119	0.08	0.10
		1	1	260	161	0.14	0.22
22.4	300	0	0	1865	736	1.00	1.00
		-1	-1	177	106	0.09	0.14
		1	1	165	84	0.11	0.14
24.8	300	0	0	1549	584	1.00	1.00
		-1	-1	134	66	0.09	0.11
		1	1	127	66	0.09	0.13
27.2	300	0	0	1347	527	1.00	1.00
		-1	-1	87	51	0.06	0.10
		1	1	107	47	0.10	0.12
29.3	300	0	0	1048	408	1.00	1.00
		-1	-1	72	31	0.07	0.08
		1	1	72	20	0.10	0.08
31.7	300	0	0	702	261	1.00	1.00
		-1	-1	47	19	0.07	0.07

Table A.3.: Diffraction peak intensities for He scattered from Bi(111) along the ⟨10⟩ azimuth at different incident energies E_i and surface temperatures T_S.

E_i (meV)	T_S (K)	$\vec{G}_{hk}$ h	k	Peak intensity (cps)	Peak area (° cps)	Relative intensity	Relative area
		2	0	783	432	0.07	0.24
		1	0	5074	1458	0.47	0.81
17.7	123	0	0	10730	1805	1.00	1.00
		-1	0	2784	1004	0.26	0.56
		-2	0	531	341	0.05	0.19
		3	0	37	27	0.01	0.03
		2	0	413	328	0.09	0.35
		1	0	797	577	0.17	0.61
30.8	123	0	0	4572	945	1.00	1.00
		-1	0	578	323	0.13	0.34
		-2	0	439	328	0.10	0.35
		-3	0	26	33	0.01	0.04
		1	0	1558	613	0.24	0.63
15.5	203	0	0	6592	978	1.00	1.00
		-1	0	1465	584	0.22	0.60
		2	0	214	125	0.13	0.30
		1	0	582	272	0.36	0.64
15.5	303	0	0	1606	422	1.00	1.00
		-1	0	695	317	0.43	0.75
		-2	0	99	47	0.06	0.11
		2	0	329	170	0.13	0.28
		1	0	1113	401	0.43	0.66
17.7	300	0	0	2580	605	1.00	1.00
		-1	0	943	364	0.37	0.60
		-2	0	211	124	0.08	0.21
		2	0	182	83	0.24	0.54
		1	0	189	90	0.25	0.58
30.8	300	0	0	748	155	1.00	1.00
		-1	0	168	82	0.23	0.53
		-2	0	157	76	0.21	0.49